Marcos António Martins Bento

Licenciado em Química

CO_2 Reduction with Formate Dehydrogenase mimetic compounds

Dissertação para obtenção do Grau de Mestre em
Química Bioorgânica

Orientador: Doutor Paulo Nuno Barradas Pereira Martinho
Co-orientadora: Doutora Luísa Bernardina Lopes Maia

Júri
Presidente: Professora Doutora Paula Cristina de Sério Branco
Arguente(s): Doutora Clara Sofia Barreiro Gomes
Vogal: Doutor Paulo Nuno Barradas Pereira Martinho

FACULDADE DE CIÊNCIAS E TECNOLOGIA
UNIVERSIDADE NOVA DE LISBOA

Dezembro de 2020

CO_2 REDUCTION WITH FORMATE DEHYDROGENASE MIMETIC COMPOUNDS

Acknowledgements

First, I would like to thank the Doctor Paulo Nuno Martinho for all the opportunities given in his research group, as long as all the time and dedication spent to improve my capacities and my way of thinking, not only as a researcher but also as a person capable of accepting any challenge proposed. I want also to thank Doctor Luísa Maia for accepting this challenge, to leave her comfort zone and for sharing with my new knowledge, for teaching me how to think in a "biochemical way" and for all the availability over this year.

I want to thank Doctor Sara Realista for all the discussions that we had, for an answer always to my questions about electrochemistry and to help me understand how this technique works and for the advice given over the last years.

To professor Maria José Calhorda, I want to thank all the knowledge transmitted during the classes and for make inorganic chemistry interesting and for all the availability and opportunities given during all my course.

To Doctor Marta Saraiva for all the knowledge about molybdenum chemistry and of inert atmosphere reactions. I also want to thank my laboratory colleagues Catarina Caetano e, Rafaela Marques, for the great lab environment and some adventures.

To Professor and Doctor Paula Branco, for being always available for questions especially about organic chemistry, and for helping me to do a reverse column chromatography.

To my family and friends, especially to my parents for all the support that they gave me and to let me do the things that I love. Finally, I want to thank my girlfriend Ana Rita Reis for never give up on me, for all the strength and motivation that she gave me especially in the hard times and for making me one of the most happier persons in the world.

Resumo

A concentração de dióxido de carbono (CO_2) na atmosfera tem vindo a aumentar muitíssimo nas últimas décadas, em grande parte devido ao uso excessivo de combustíveis fósseis. O nível crescente deste gás com efeito de estufa está a modificar o clima, o que terá efeitos dramáticos e irreversíveis no nosso planeta. Soluções eficientes e inovadoras são necessárias urgentemente para resolver este problema. Vários investigadores em todo o Mundo estão a desenvolver novas estratégias para capturar e converter o CO_2 em combustíveis inovadores e outros produtos químicos com elevado valor comercial. Com este fim, diferentes metodologias eletro- e fotoquímicas têm sido exploradas, usando uma grande variedade de complexos metálicos como catalisadores.

Neste trabalho, inspirámo-nos no centro ativo das enzimas formato desidrogenase dependentes de molibdénio para desenvolver novos catalisadores inorgânicos baseados em molibdénio que convertam o CO_2 em formato ou outros produtos interessantes de valor acrescentado. Os dois principais objetivos deste trabalho foram (i) sintetizar dez complexos de molibdénio e (ii) estudar a sua capacidade para catalisar a redução do CO_2 eletroquimicamente. A escolha dos ligandos dos complexos foi inspirada no ditioleno presente no cofactor que coordena o molibdénio nestas enzimas e também em diferentes compostos descritos na literatura. Todos os complexos sintetizados foram caracterizados por análise elementar e métodos espectroscópicos (NMR, FTIR e UV-vis), assim como por eletroquímica (voltametria cíclica). Estudos de eletrólise a potencial controlado mostraram que quatro dos novos complexos preparados são seletivos para a redução do CO_2 a formato. Estes compostos promissores serão em breve estudados com maior detalhe e novos compostos, melhorados, serão preparados com base nestes.

Palavras-chave: dióxido de carbono; molibdénio; compostos biomiméticos; eletro-redução; formato; coordenação rica em enxofre

Abstract

The atmospheric carbon dioxide (CO_2) concentration has greatly increased in the last decades, mainly due to the excessive use of fossil fuels. The rising levels of this greenhouse effect gas are changing the climate, which will have irreversible and dramatic effects on our planet. Efficient and innovative solutions to tackle this problem are urgently needed. Several researchers around the world are developing new approaches to capture and convert CO_2 into novel fuels and other chemicals with economical value. For that, different electro- and photochemical methodologies have been explored, using a variety of metal complexes as catalysts.

In this work, we took inspiration from the active site of molybdenum-containing formate dehydrogenase enzymes to develop new inorganic molybdenum-based catalysts that convert CO_2 into formate or other interesting added-value compounds. Our two main goals were to (i) synthesise ten molybdenum complexes and (ii) study their ability to catalyse the reduction of CO_2 electrochemically. The complex ligands chosen were inspired in the dithiolene moiety of the cofactor that coordinates the molybdenum ion within the enzymes (dithiolene and derivative compounds) and also in different compounds previously described in literature (pincer-type and salen-type units). All complexes synthesised were characterised by elemental analysis and spectroscopic methodologies (NMR, FTIR and UV-vis), as well as, electrochemically (cyclic voltammetry). Controlled potential electrolysis experiments showed that four of the new compounds synthesised are selective for the CO_2 reduction to formate. These promising CO_2 reduction catalysts will be further studied and improved in the near future.

Keywords: carbon dioxide; molybdenum; biomimetic compounds; electroreduction; formate; sulfur-rich coordination

Symbols and notations

ACN	Acetonitrile
aq	Aqueous
BNAH	1-Benzyl-1,4-dihydronicotinamide
COSY	Homonuclear correlation spectroscopy
CPE	Controlled potential electrolysis
CV	Cyclic voltammetry
D_2O	Deuterium oxide
DBU	1,8-Diazabicyclo[5.4.0]undec-7-ene
DCM	Dichloromethane
dmb	4,4’-dimethyl-2,2-bipyridine
DMF	Dimethylformamide
DMSO	Dimethyl sulfoxide
DMSO-d_6	Deuterated dimethyl sulfoxide
DPPAS2	Bis(diphenylphosphino)amide-disulfide
EA	Elemental analysis
EPR	Electron paramagnetic resonance
equiv	Equivalents (stoichiometric relation)
EtOH	Ethanol
Et_2O	Diethyl ether
FDH	Formate dehydrogenase
FE	Faradaic efficency
FTIR	Fourier-transform infrared spectroscopy
GC-TCD	Gas chromatography with thermal conductivity detector
H_2QDT	Quinoxaline-2,3-dithiolate
H_2salen	*N*,*N′*-Bis(salicylidene)ethylenediamine
HMBC	Heteronuclear multiple bond correlation
HSQC	Heteronuclear single quantum coherence spectroscopy
I1	2-bromo-1-(4-fluorophenyl)prop-1-en-1-ol
I2	1-(4-fluorophenyl)-1-oxopropan-2-yl dimethylcarbamodithioate
I3	*N*-(4-(4-fluorophenyl)-5-methyl-1,3-dithiol-2-ylidene)-*N*-methylmethanaminium hydrogen sulfate
I4	2,6-bis(chloromethyl)pyridine

IR	Infrared radiation
L1	H_2QDT
L2	Disodium (*Z*)-1-(4-fluorophenyl)prop-1-ene-1,2-bis(thiolate)
L3	5,5'-methylenebis(1,3-dihydro-2*H*-benzo[*d*]imidazole-2-thione)
L4	Bis(diphenylphosphino)amide-disulfide
L5	H_2salen
L6	2,6-bis(mercaptomethyl)pyridine
LEDs	Light Emitting Diode
LiOTf	Lithium triflate
MeOH	Methanol
MeOD	Deuterated methanol
MOF	Metal organic framework
NADH	Hydrogen nicotinamide adenine dinucleotide
NMR	Nuclear magnetic resonance
Q	Charge
R	Gas constant
r.t	Room Temperature
SCE	Saturated calomel electrode
SHE/NHE	Standard hydrogen electrode/normal hydrogen electrode
T	Temperature
$TBAPF_6$	Tetrabutylammonium hexafluorophosphate
TEOA	Triethanol-amine
TFE	2,2,2-trifluoroethanol
TOF	Turnover frequency
TON	Turnover number
UV-vis	Ultaviolet-visible spectroscopy
Δ	Heat
ΔG^{o}	Standard free Gibbs energy
δ	Chemical shift
e^-	Electron
^{o}C	Degree Celsius

Table of contents

Figure index

Schemes index

Table index

1. Introduction

1. Introduction

1.1. The carbon dioxide emergency

In recent years, climate change has received considerable attention, being considered one of the greatest threats for Life on Earth as we know it and the probable responsible for the next great species mass extinction. The present climate crisis is directly related to the anthropogenic emission of greenhouse effect gases, such as carbon dioxide (CO_2), methane (CH_4) and nitrous oxide (N_2O), which, once trapped in the atmosphere, absorb and emit infrared radiation towards Earth's surface, warming the planet.[1–5]

The atmospheric CO_2 levels have greatly increased in the last decades (Figure 1.1). The atmospheric CO_2 concentration is dependent on the balance between CO_2 emission and uptake.[6] The most significant sources of CO_2 are fossil fuel combustion, oxidations from other energy and industrial processes and deliberate activities on land (mainly deforestation); natural processes, such as volcanic eruptions and biological activity, also contribute to CO_2 emissions. On the other hand, CO_2 uptake is mainly provided by physicochemical and biological processes in oceans and land, including CO_2 fixation by plants, algae and other living organisms. Because the CO_2 emissions are so huge, the natural Carbon Biogeochemical Cycle[a] is no longer able to maintain the equilibrium (that is, remove the excess of CO_2 from the

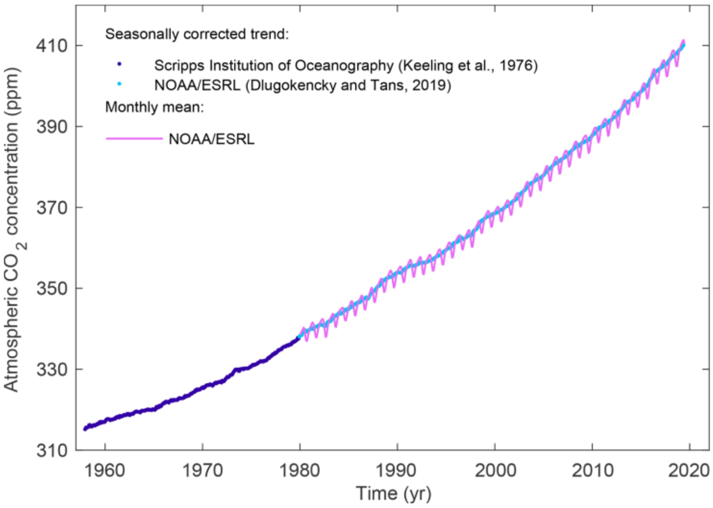

Figure 1.1: Surface average atmospheric CO_2 concentration from the last 60 years. *Reproduced from*[2].

---

[a] The Carbon Biogeochemical Cycle is the global process responsible by the flow of carbon between the atmosphere, lithosphere, hydrosphere and biosphere; it works through physicochemical and biological processes, that is, with the intervention of living organisms in Earth's biosphere.

atmosphere) and the atmospheric CO_2 levels are steadily increasing. Yet, this massive excess of CO_2 presents itself as a huge carbon feedstock and many researchers around the world are searching for innovative materials and catalysts to convert CO_2 into added-value compounds, such as chemical feedstocks or fuels (Figure 1.2).

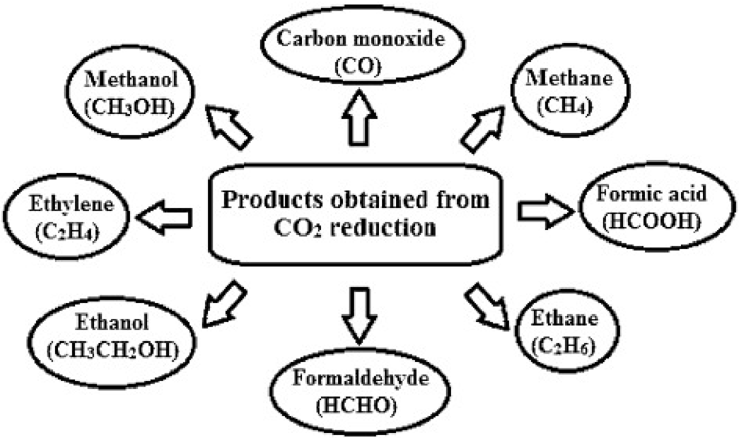

Figure 1.2: Some added-value compounds that can be obtained from CO_2 conversion.
Reproduced from[3].

1.2. Carbon dioxide conversion

CO_2 is a kinetically and thermodynamically stable molecule (ΔG^o = -400 kJ mol^{-1}), with two linear-configured double bonds between the carbon and oxygen atoms, where the carbon is on the most oxidised form (4+). As result, its activation and reduction to compounds with a higher added-value without using a catalyst or an input of energy became a challenging task. Also challenging is the CO_2 capture, separation and purification, which must be efficient and affordable. Despite these challenges, CO_2 reduction is feasible and very promising regarding energy production (innovative fuels) and energy storage (provides a way to storage "intermittent" renewable energies). It is also very promising regarding chemical feedstocks production (which are essential for making all the modern-world chemical commodities, from bulk chemicals to plastics, fertilisers or pharmaceuticals).

To reduce CO_2 and convert it into added-value compounds, one needs a catalyst, that can be a nanomaterial or a metal complex, and electrons (energy), that can be provided by an electrode or a light source (photons). Accordingly, most strategies to handle CO_2 are based on electrochemical and photocatalytic approaches.[7,8]

1.2.1. Catalytic electroreduction

The electrochemical CO_2 conversion has received considerable attention, as it presents several advantages: the process can be controlled by electrode potentials and reaction temperature; the supporting electrolytes can be fully recycled; the electricity used to drive the process can be obtained from renewable sources, including solar, wind and hydropower; the electrochemical reaction systems are compact, modular, on-demand, and easy for scale-up applications.[9,10]

Electrochemical techniques, such as cyclic voltammetry (CV), are very useful to get mechanistic insights in the catalytic process and to study the intrinsic properties of the catalyst (complemented with spectroscopic studies, like electron paramagnetic resonance (EPR) spectroscopy).[11] Electrochemical reduction of CO_2 can occur through several electron reduction pathways (usually involving 2, 4, 6 or 8 electrons) (Table 1.1) and in gaseous, aqueous, and non-aqueous phases with different temperatures. The most common reduction products are carbon monoxide (CO), methane (CH_4), formic acid/formate ($HCOOH$ / $HCOO^-$, depending on medium pH), oxalic acid/oxalate ($H_2C_2O_4$ / $C_2O_4^{2-}$, depending on pH), methanol (CH_3OH; MeOH) and ethanol (CH_3CH_2OH; EtOH); in some cases, several of these products are produced

Table 1.1: Standard reduction potentials of selected half-reactions of CO_2 reduction in aqueous solutions at 1 atm and 25ºC. *Reproduced from* [9].

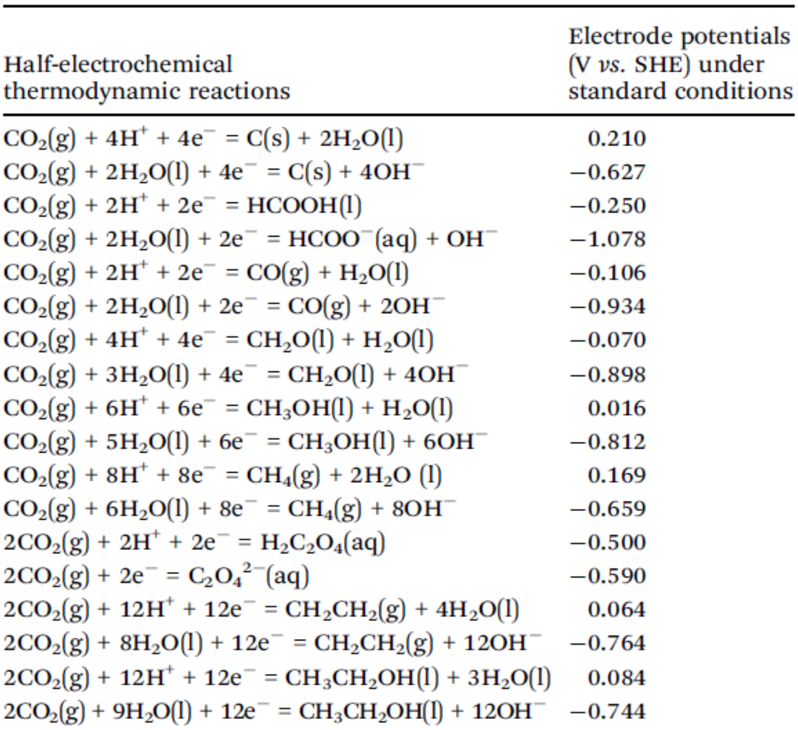

Half-electrochemical thermodynamic reactions	Electrode potentials (V *vs.* SHE) under standard conditions
$CO_2(g) + 4H^+ + 4e^- = C(s) + 2H_2O(l)$	0.210
$CO_2(g) + 2H_2O(l) + 4e^- = C(s) + 4OH^-$	−0.627
$CO_2(g) + 2H^+ + 2e^- = HCOOH(l)$	−0.250
$CO_2(g) + 2H_2O(l) + 2e^- = HCOO^-(aq) + OH^-$	−1.078
$CO_2(g) + 2H^+ + 2e^- = CO(g) + H_2O(l)$	−0.106
$CO_2(g) + 2H_2O(l) + 2e^- = CO(g) + 2OH^-$	−0.934
$CO_2(g) + 4H^+ + 4e^- = CH_2O(l) + H_2O(l)$	−0.070
$CO_2(g) + 3H_2O(l) + 4e^- = CH_2O(l) + 4OH^-$	−0.898
$CO_2(g) + 6H^+ + 6e^- = CH_3OH(l) + H_2O(l)$	0.016
$CO_2(g) + 5H_2O(l) + 6e^- = CH_3OH(l) + 6OH^-$	−0.812
$CO_2(g) + 8H^+ + 8e^- = CH_4(g) + 2H_2O\ (l)$	0.169
$CO_2(g) + 6H_2O(l) + 8e^- = CH_4(g) + 8OH^-$	−0.659
$2CO_2(g) + 2H^+ + 2e^- = H_2C_2O_4(aq)$	−0.500
$2CO_2(g) + 2e^- = C_2O_4^{2-}(aq)$	−0.590
$2CO_2(g) + 12H^+ + 12e^- = CH_2CH_2(g) + 4H_2O(l)$	0.064
$2CO_2(g) + 8H_2O(l) + 12e^- = CH_2CH_2(g) + 12OH^-$	−0.764
$2CO_2(g) + 12H^+ + 12e^- = CH_3CH_2OH(l) + 3H_2O(l)$	0.084
$2CO_2(g) + 9H_2O(l) + 12e^- = CH_3CH_2OH(l) + 12OH^-$	−0.744

simultaneously. The number and the amount of each species generated (specificity, selectivity and yield) are factors strongly dependent on the electrocatalyst used and electrode potential applied during the reduction reaction (Table 1.1).[9,11,12]

To accomplish the electrochemical reduction of CO_2, several authors used catalysts based on complexes of Earth-abundant transition metals of the 4th Period of the Periodic Table, like nickel (Ni), cobalt (Co), iron (Fe), manganese (Mn) and copper (Cu); most of these use ligands like polypyridyl, cyclam, aza-macrocyclic, and phosphine derivative ligands, as well as, porphyrins, phthalocyanines and related macrocycles (Figure 1.3).[11,13]

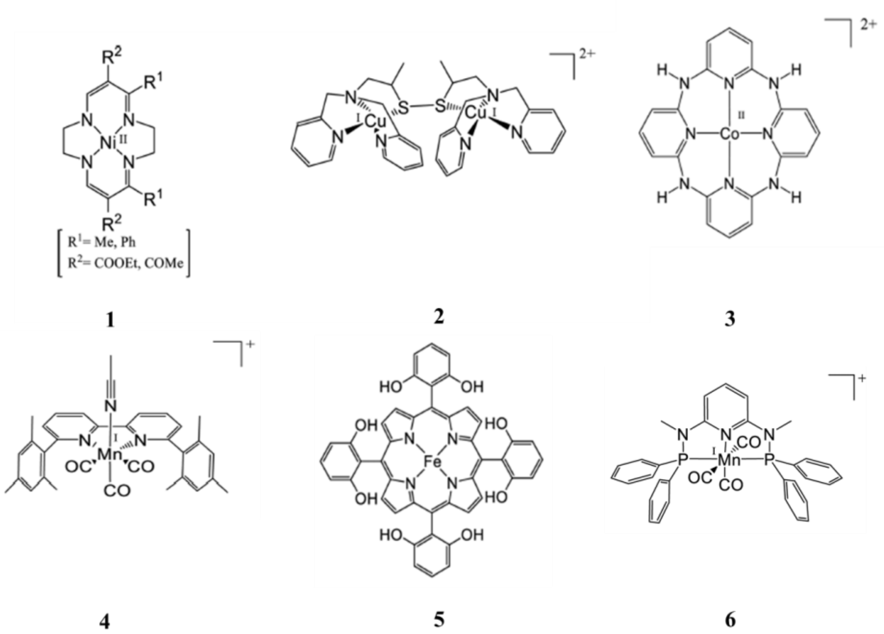

Figure 1.3: Selected examples of complexes used in electrochemical systems to reduce CO_2.
See text for details and references.

The nickel complex 1 (Figure 1.3) was shown to reduce CO_2 to oxalate with a faradaic yield of 90% upon electrolysis at a potential close to -2.5V vs SCE in acetonitrile (ACN), with a CO_2 saturated solution.[14] The binuclear copper complex 2 (Figure 1.3) was also able to reduce CO_2 to oxalate with a very good yield (approximately 96%), but using, in this case, a considerably lower potential of -0.27V vs SCE (7h electrolysis in ACN solution saturated with CO_2).[15] Other complexes (structures 3, 4 and 5 - Figure 1.3) were shown to reduce CO_2 into CO with high efficiency and selectivity. The cobalt complex 3 (Figure 1.3) catalysed this conversion with a faradaic yield of 98%, in the presence of a weak Brønsted acid, like 2,2,2-trifluoroethanol (TFE), in dimethylformamide (DMF), after 2h electrolysis.[16] Complex 4 (Figure 1.3) based in manganese showed a faradaic yield of 98% for the CO formation (electrolysis during 25h, with TFE in ACN, saturated with CO_2).[17] Spectroscopic and mechanistic studies demonstrated that the metal is reduced by two electrons, but the ligand prevents the dimerization of the complex.[18] The iron complex 5 (Figure 1.3) converted CO_2 into CO in a quantitative yield (around 90%-100%) in DMF solution saturated with CO_2, in the presence of phenol.[19] Complex 6 was based on a PNP ligand and obtained in a tentative of searching new types of catalysts for CO_2 conversion. This complex produces CO with excellent efficiency (close to 100%) in electrolysis during 5h in dry acetonitrile. The electrolysis experiments realised with an addition of a small percentage of water (5%) showed H_2 evolution suggesting a competitive pathway for CO_2 conversion.[20] Several of these catalysts showed also promising results regarding CO_2 photoreduction. [11,15,21–24]

1.2.2. Catalytic photoreduction

Photogenerated electrons can be used to drive chemical reactions, including the CO_2 reduction. In this case, the light/solar energy is converted into chemical bonds; for example, conversion into a new C-H bond when CO_2 is reduced to formate. This light-to-chemical energy conversion is usually called “artificial photosynthesis”, as it is a mimic of the photosynthetic process used by a living organism to fix CO_2. A CO_2 photochemical-reducing system needs to include (i) a light source that can be solar light or artificial light derived from LEDs, (ii) a light absorber/photosensitizer and electron donor (for light harvest, charge separation and charge transfer) to transfer electrons to the catalyst, and (iii) a catalyst to catalyse the CO_2 reduction (Figure 1.4). The catalyst should have high activity and stability and operate at low overpotential; it must be able to catalyse the transfer of at least two electrons to CO_2 to form new products, but it can also promote the multi-electron reduction using a photoredox cycle.[3,11]

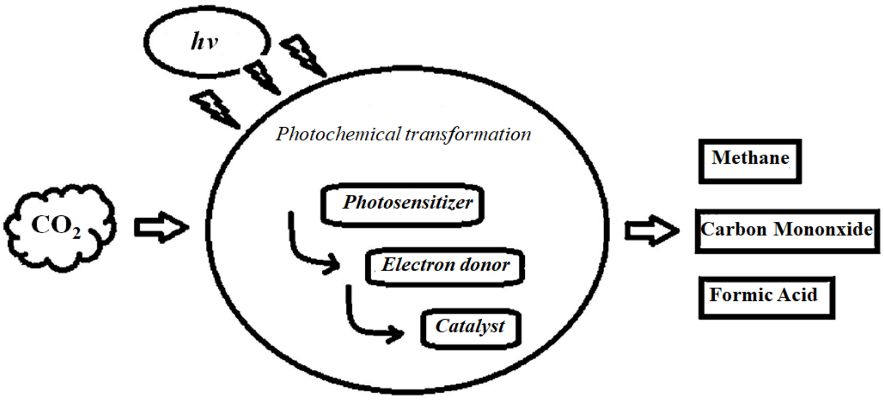

Figure 1.4: Schematic representation of a photochemical process for CO_2 conversion.
Reproduced from[3].

In the last decades, several researchers aimed to mimic photosynthesis to achieve the CO_2 conversion into added-value compounds. For this propose, Kubiak and co-workers[25] synthesised a doped metal-organic framework (MOF) to produce formate using solar energy (Figure 1.5). The synthesis of this new material was performed inserting specific ligands in the MOF structure that can coordinate to a metal ion (Figure 1.5 - top panel). The doped MOF-catalysed CO_2 reduction into formate occurred irradiating the structure with visible light (420nm) for 18h, in a mixed solution of DMF/triethanol-amine (TEOA), and using $[Ru(dmb)_3]^{2+}$ as photosensitizer and 1-benzyl-1,4-dihydronicotinamide (BNAH) as a sacrificial reductant. The formate formation was suggested to occur through a radical on the metal centre (Figure 1.5 - bottom panel).[7,16,25,26]

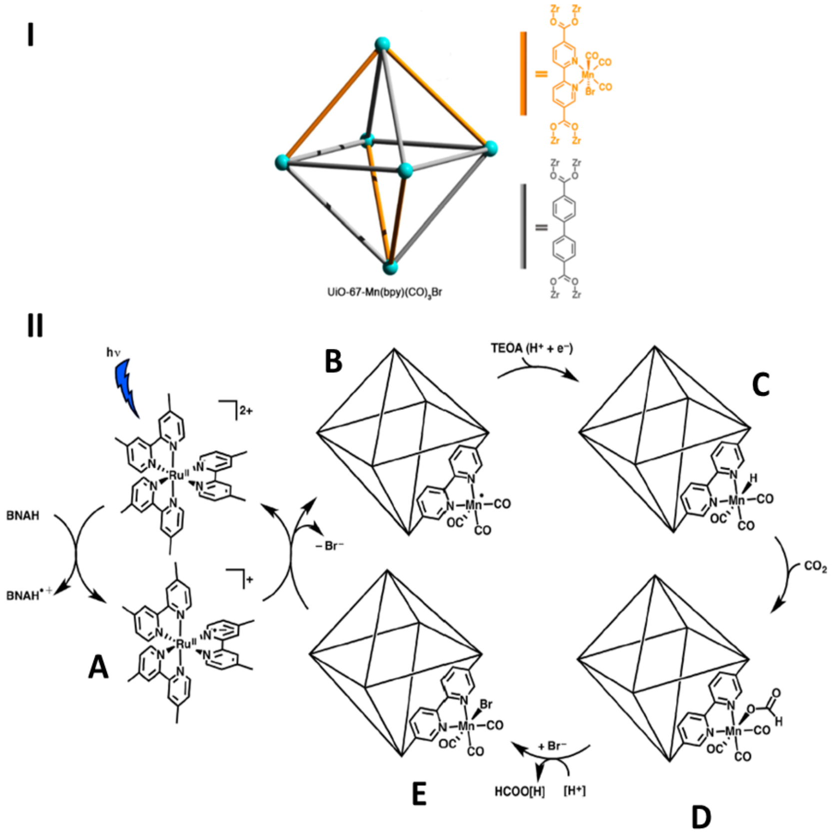

Figure 1.5: Doped metal-organic framework used by Kubiak and co-workers[25] to produce formate using solar energy. *Panel I (top): Schematic representation of the MOF. Panel II (bottom): proposed mechanism for the photochemical CO_2 reduction. (A), ruthenium complex (PS) reduction by BNAH; (B), electron transfer to the MOF catalytic metal centre; (C) electron and proton donation by TEOA, facilitating the hydride formation; (D) hydride transfer and CO_2 coordination to the metal centre; (E) catalyst regeneration and formate release. Adapted from[25].*

1.3. Carbon dioxide conversion - the biological way

Biology has evolved several ways to handle CO_2 to fulfil the living organisms needs. To activate CO_2 and convert it into products of interest, organisms use different enzymes, such as: (i) ribulose-1,5-bisphosphate carboxylase/oxygenase that forms a new C-C bond by the addition of CO_2 (carboxylation) to ribulose-1,5-bisphosphate, to yield two molecules of glycerate-3-phosphate (Equation 1); (ii) carbonic anhydrase which accelerates the conversion of CO_2 into hydrogenocarbonate (Equation 2) and, in this way, increases the CO_2 bioavailability; (iii) carbon monoxide dehydrogenase that catalyses the cleavage of the C-O bond to produce carbon monoxide (Equation 3); (iv) formate dehydrogenase (FDH) that catalyses the formation of a new C-H bond to produce formate (Equation 4). [27–30]

$$\text{ribulose-1,5-bisphosphate} + H_2O + CO_2 \longrightarrow 2\ \text{glycerate-3-phosphate} + 2\ H^+ \quad \text{(Equation 1)}$$

$$CO_2 + H_2O \rightarrow HCO_3^- + H^+ \quad \text{(Equation 2)}$$

$$CO_2 + 2e^- + 2\,H^+ \rightarrow CO + H_2O \quad \text{(Equation 3)}$$

$$CO_2 + 2e- + H^+ \rightleftharpoons HCOO^- \quad \text{(Equation 4)}$$

1.3.1. Formate dehydrogenases

FDH enzymes, whose active site this work aims to mimic, catalyse the reversible reduction of CO_2 into formate (Equation 4). These enzymes can be separated into two classes, which are distinguished by their composition. One class, the metal-independent FDH, comprises enzymes that do not have redox active cofactors or metal ions.[31,32] In these enzymes the CO_2 reduction is carried out by hydride transfer from the pyridine ring of NADH to the carbon atom of CO_2 (or the reverse for formate oxidation; Equation 5)[33], as is illustrated in Figure 1.6.

$$CO_2 + NADH \rightleftarrows HCOO^- + NAD^+ \quad \text{(Equation 5)}$$

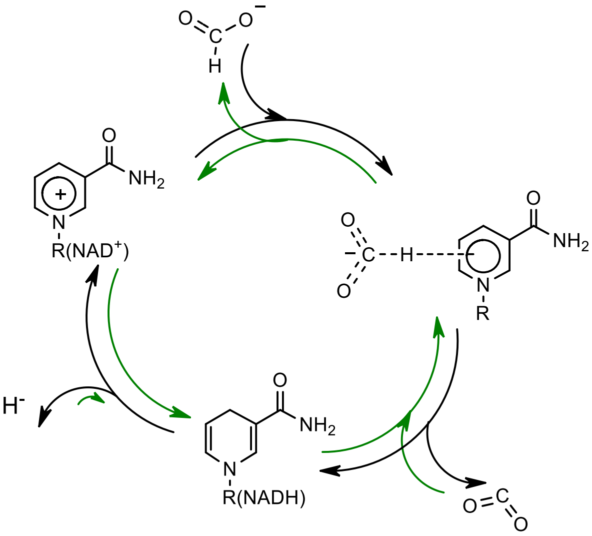

Figure 1.6: Mechanism of CO_2 reduction to formate catalysed by metal-independent FDH.

The other class comprises the metal-dependent FDH, whose active site (the place where the CO_2 reduction or formate oxidation takes place) harbours one molybdenum (Mo) or tungsten (W) ion. [31,32]During the catalytic cycle, the metal cycles between the 6+ and 4+ oxidation state. In the oxidised state (Mo^{6+} or W^{6+}), the metal is coordinated by the cis-dithiolene (–S–C=C–S–) group of two pyranopterin cofactor molecules, plus one terminal sulfido group (Mo/W=S) and one sulfur or selenium atom from a cysteine or selenocysteine residue (Mo/W-S(Cys) or Mo/W-Se(SeCys)), in a distorted trigonal prismatic geometry (Figure 1.7). The active site also contains two conserved arginine and histidine residues, close to the metal centre, that are thought to be essential for the catalytic cycle. In the reduced state (4+), the terminal sulfido group becomes protonated (Mo/W-SH). [31,32]

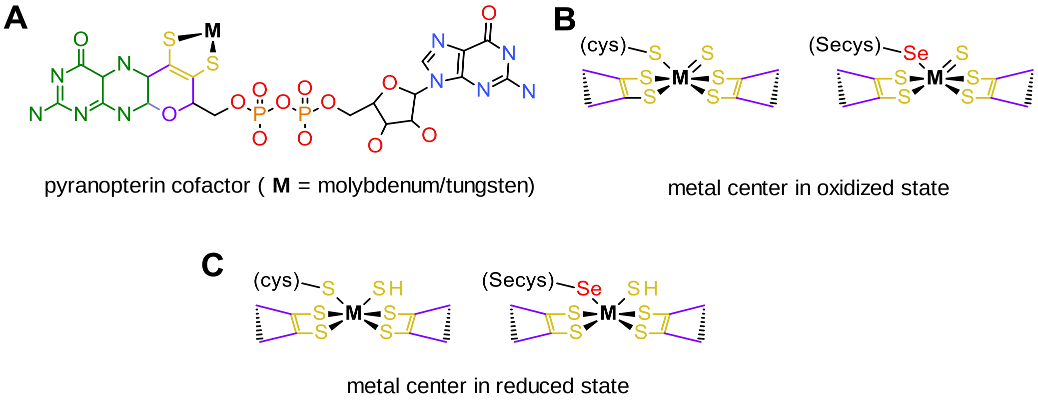

***Figure 1.7: Active site of metal-dependent formate dehydrogenases. (A)** Complete structure of the pyranopterin cofactor. **(B)** Structure for the metal centre in the oxidised state (6+ oxidation state) **(C)** Structure of the catalytic centre in the reduced state (4+ oxidation state).*

The reaction mechanism of the reversible CO_2 reduction to formate has been extensively studied, with different hypothesis been proposed during the last two decades.[31,32] Presently, it is accepted that the CO_2 molecule does not bind directly to the metal and that the reaction proceeds in the metal second coordination sphere by direct hydride transfer, as initially proposed by Maia *et al.* (2016)[34] and Niks *et al.* (2016)[35] (Figure 1.8). Accordingly, in a first step, CO_2 binds in the active site by interaction with an arginine residue (via hydrogen bridges). The following step consists on the direct hydride transfer from the terminal sulfido group of the reduced metal centre (Mo^{4+}/W^{4+}-SH) to the CO_2, with the metal being oxidised in the process (Mo^{4+}/W^{4+}-SH to Mo^{6+}/W^{6+}=S). Finally, the catalytic cycle is closed by the re-reduction of the metal centre (Mo^{6+}/W^{6+}=S to Mo^{4+}/W^{4+}-SH) and formate release. The electrons necessary to re-reduce the metal are provided by the physiological partners of the enzyme. Formate oxidation is proposed to follow the reverse mechanism, with formate binding to the same site (via hydrogen bridges to the arginine residue) and the reaction proceeding by direct hydride transfer from the formate molecule to the terminal sulfido group of the oxidised metal centre.[34,35]

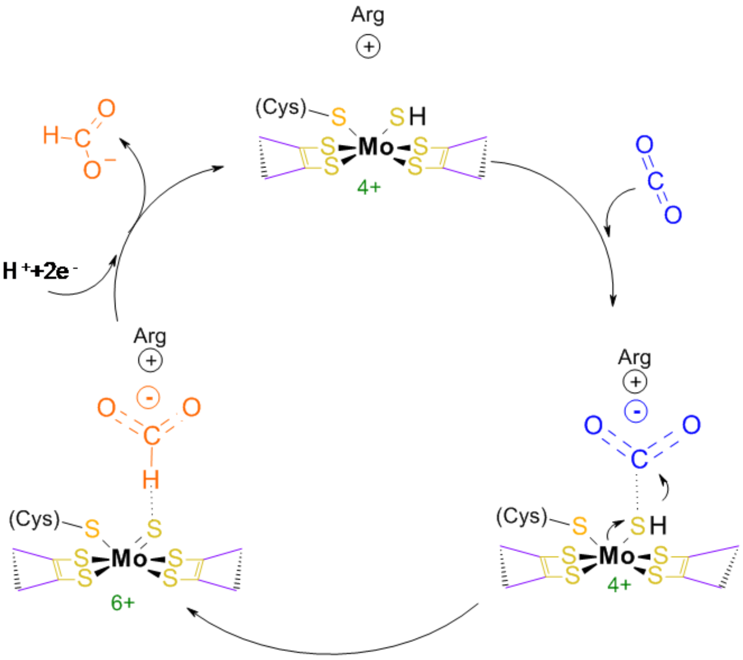

Figure 1.8: Mechanism of CO_2 reduction to formate catalysed by metal-dependent FDH*, as proposed by Maia et al. (2016)[34] and Niks et al. (2016)[35]. Formate oxidation should proceed by the reverse mechanism. The reaction is represented with a molybdenum-containing FDH harbouring a cysteine residue, but the mechanism should be the same for enzymes having instead a selenocysteine residue or for tungsten-dependent enzymes. "6+" and "4+" represent the metal oxidation state.*

1.4. Carbon dioxide conversion – Biomimetic compounds

Enzymes are very interesting from a catalytic point of view. These natural catalysts offer several key advantages, namely substrate (reagent) and product specificity because the enzymes have the ability to discriminate the substrate in a complex mixture and to produce only the product of interest for the organism. Another important advantage is the enzymes ability to catalyse the reactions at ambient temperature and pressure and neutral pH, that is, under "green" conditions. For these reasons, many researchers are trying to develop metal complexes that mimic the enzymes active site, aiming to convert CO_2 with the same selectivity and yield as enzymes do and in an innovative and clean way.

In the search for innovative biomimetic catalysts, in the last decade, heavier transition metals (5th and 6th Period of the Periodic Table), like Mo and rhenium (Re), started to be exploited for CO_2 reduction. Kubiak and Fontecave are some of the researchers who influenced this area and produced new catalysts with these metals (Figure 1.9). Kubiak and co-workers[36] studied different molybdenum complexes based in two different pyridine monoimine ligands (Figure 1.9 - A). The molybdenum complex 6 was capable of producing CO with 10% of faradaic yield, when submitted to a 1h electrolysis, in CO_2 saturated ACN. Interesting, the molybdenum complex 7 was not tested as a catalyst for CO_2 reduction by electrolysis, but it was confirmed by CV experiments that this complex displays catalytic behaviour.[36] Fontecave and co-workers synthesised the molybdenum compounds 8 and 9 (Figure 1.9 - B), with the purpose of mimicking the molybdenum-containing FDH active site and photochemically reduce CO_2 to formate.[37] The photochemical assays were performed using a mixture of CO_2 saturated ACN and TEOA; $[Ru(bpy)_3]^{2+}$ was used as the photosensitizer and 1,3-dimethyl-2-phenyl-2,3-dihydro-1*H*-benzoimidazole (BIH) as the sacrificial electron donor; the two complex isomers (8 and 9; Figure 1.9 - B) were not isolated and, consequently, the assays were carried out in the presence of a mixture of both. The catalysts mixture was active and formate and CO were produced with a faradaic yield of 39% and 19% respectively. The CO_2 reduction was found to be competitive with the proton (H^+) reduction reaction to dihydrogen (H_2) and about 40% of H_2 was produced in the photochemical experiments.[37]

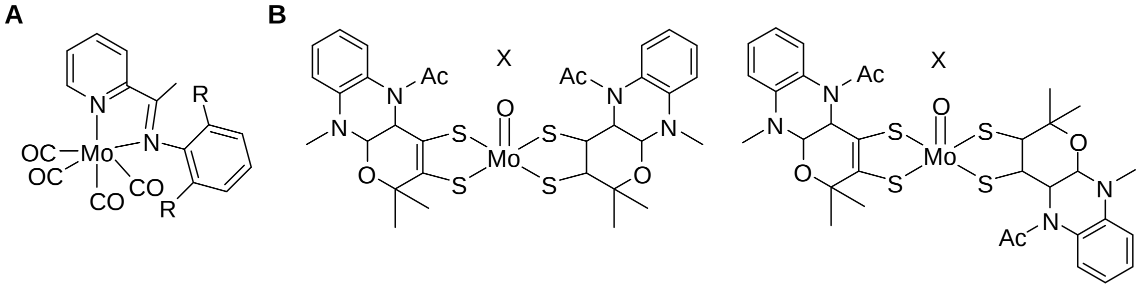

R = H (**6**), iPr (**7**) **8** X=$NBut_4^+$ **9**

Figure 1.9: Selected molybdenum complexes studied in CO_2 reduction assays. *Reproduced from* [36,37].

Berke and co-workers[38] studied pincer-molybdenum complexes to carry out the CO_2 hydrogenation with H_2, in presence of different types of bases. The complexes 10 (Figure 1.10) were able to reduce CO_2, however, with very low yields, varying between 0.14% - 5%.[38] Bernskoetter and co-workers[39] also studied pincer-molybdenum complexes (complex 11; Figure 1.10). Their catalysts can activate CO_2 by directly coordinating it to the metal. The resulting complexes are then able to reduce the coordinated CO_2 to formate, after treatment with a tetrahydrofuran solution with 100 equiv of 1,8-diazabicyclo[5.4.0]undec-7-ene (DBU) and a 1:1 mixture of 69 atm of H_2 and CO_2, at 100 °C, for 16 h, in an autoclave reactor. After different assays with several bases and solvents, they selected lithium triflate (LiOTf) as a co-catalyst. The addition of 50 equiv of LiOTf, along with 100 equiv of DBU and 69 atm of a 1:1 mixture of H_2 and CO_2, at 100 ºC, for 16 h, enabled the production of formate with a turnover number (TON) of 16(2); this value was further improved to 35(5) by changing the solvent to 1,4-dioxane.[39]

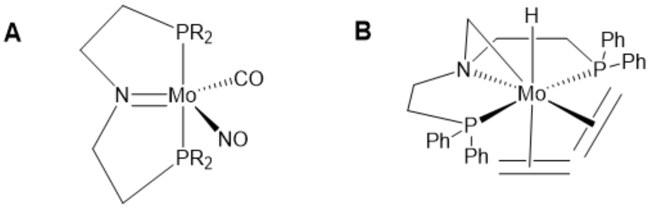

10 **11**

Figure 1.10: Selected molybdenum-pincer catalysts. *Reproduced from* [38,39]

1.5. Aim of the work

In this work, we aimed to take inspiration from the active site of molybdenum-containing FDH enzymes to develop a new catalyst that converts CO_2 into formate or other interesting added-value compounds, such as, carbon monoxide, methane, methanol, oxalate and ethane. For that, we set two main goals: (i) synthesise ten molybdenum complexes and (ii) study their ability to catalyse the reduction of CO_2 electrochemically.

The complex ligands were chosen to mimic the sulfur-rich coordination sphere of the FDH molybdenum centre (Figure 1.7), namely, dithiolene and derivative compounds and one pincer-type unit; one salen-type unit (no sulfur coordination) was also included in the list of ligands to study. The six ligands chosen were quinoxaline-2,3-dithiolate (H_2qdt; **L1**), disodium (*Z*)-1-(4-fluorophenyl)prop-1-ene-1,2-bis(thiolate) (**L2**), 5,5'-methylenebis(1,3-dihydro-2*H*-benzo[*d*]imidazole-2-thione) (**L3**), bis(diphenylphosphino)amide-disulfide, (DPPAS2; **L4**), H_2salen (**L5**) and 2,6-bis(mercaptomethyl)pyridine (**L6**) (Figure 1.11). The ten molybdenum complexes were designed to be mono-substituted (**M1**, **M3**, **M5**, **M7** and **M10**) and di-substituted (**M2**, **M4**, **M6** and **M8**), with one binuclear complex (**M9**) (Figure 1.12).

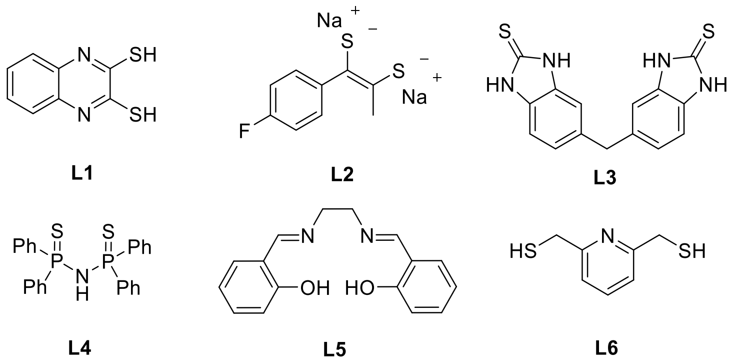

Figure 1.11: Ligands synthesised for the preparation of the molybdenum complexes studied in this work.

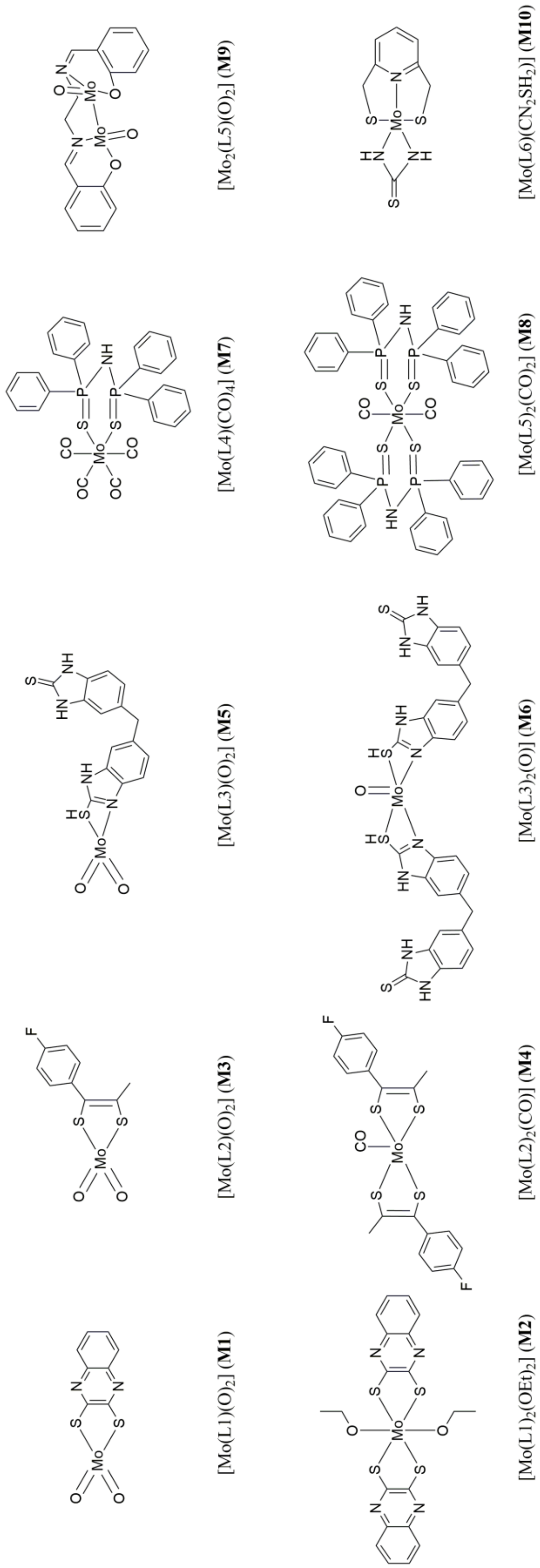

[Mo(L1)(O)$_2$] (**M1**)

[Mo(L2)(O)$_2$] (**M3**)

[Mo(L3)(O)$_2$] (**M5**)

[Mo(L4)(CO)$_4$] (**M7**)

[Mo$_2$(L5)(O)$_2$] (**M9**)

[Mo(L1)$_2$(OEt)$_2$] (**M2**)

[Mo(L2)$_2$(CO)] (**M4**)

[Mo(L3)$_2$(O)] (**M6**)

[Mo(L5)$_2$(CO)$_2$] (**M8**)

[Mo(L6)(CN$_2$SH$_2$)] (**M10**)

Figure 1.12: Molybdenum complexes studied in this work.

2. Materials and Methods

2. Materials and Methods

2.1. Reagents

All chemicals were purchased from TCI, Sigma Aldrich, Fluorochem and Acros Organics and were of the highest purity available and were directly used as purchased (except solvents). Solvents were purified as described elsewhere [40], being distilled under inert atmosphere in the presence of a drying agent (e.g. $CaCl_2$ or metallic sodium) and some of these solvents were pre dried according to the procedures described in [40].

2.2. Spectroscopic and electrochemical measurements

NMR spectra were obtained on a Bruker Advance 400 MHz spectrometer using deuterated solvents from Sigma Aldrich. IR spectra were obtained on a Nicolet Nexus 6700 FTIR spectrophotometer in the 400-4000 cm^{-1} range with 4 cm^{-1} resolution using KBr pellets. UV-vis spectra were measured in the Shimadzu UV-visible 1601 spectrophotometer with standard 1 cm quartz cells in DMSO solutions. For the electrochemical experiments, a potentiostat PGSTAT 12 AUT71019 controlled by NOVA 2.0 software was used. For CV, a three-electrode electrochemical cell with working, a counter and a reference electrode, which was separated by a glass frit, was used. Glassy carbon (3 mm diameter) and platinum wire were used as working and counter electrodes, respectively. Ag/AgCl 3 M KCl (0.278V vs NHE) electrode was used as reference electrode. The working electrode was polished before each CV experiment using 1, 0.5 and 0.03 µm alumina suspensions (Al_2O_3, Buehler) and washed with Milli-Q water. All CV experiments were performed at $0.1Vs^{-1}$, in DMF (solvent), with 1 mM solutions of the catalyst, using 0.1 M of tetrabutylammonium hexafluorophosphate ($TBAPF_6$) (Acros Organics, 98%, which was recrystallised from hot ethanol) as supporting electrolyte. Before the measurements, the solutions were deoxygenated and saturated with CO_2 by bubbling first with N_2 and then with CO_2, both gases for 30 minutes. Controlled-potential electrolysis (CPE) experiments were carried out using the same type of electrochemical cell and reference electrode as for CV. The scan rate used to set the potential at which the CPE experiment was performed was 0.01 Vs^{-1}. A glassy carbon plate (Sigradur® G) with 3 cm^2, was used as working electrode. The reference electrode was merged in the solution (5 mL) while the counter electrode (platinum wire) was placed in a different compartment (with 5 mL of solution) separated by a glass frit. Before the CPE experiments, the solutions were purged by bubbling CO_2 from 45 minutes to 1 hour.

2.3. Formate, CO and H_2 detection and elemental analysis

For formate detection and quantification, an NMR multiple solvent suppression assay was used. Before each experiment, an NMR tube was prepared with 0.250µL of a solution (in D_2O) containing 43mM of maleic acid and 0.2M HCl (used as internal standard) and 0.250µL of the bulk electrolysis solution from the CPE experiment. Multiple solvent suppression routine (LC1DCWPS) was used and the product was quantified through the calculation of relative integrations of the internal standard solution (maleic acid solution). After the formate quantification, a solution of 53mM of formic acid in D_2O (240µL) was added to the NMR tube (spiking) to confirm the presence of formic acid in bulk electrolysis solution.

For gas quantification, a gas chromatography equipment was used from Agilent Technology (GC-TCD 7820A) controlled by OpenLAB CemStation edition software. This equipment was fitted with a thermal conductivity detector and Carboxen®-1006 PLOT Capillary GC Column (L × I.D. 30 m × 0.53 mm, average thickness 30 µm) that was used for H_2, CO and CO_2 detection. The carrier gas was Ar flowing at 3 mL min^{-1} and injections were performed with gas tight syringes (500 µL) previously purged with CO_2. Temperature was held at 230 ºC in the injector and detector. Elemental analysis (EA) for C, H and N quantifications were performed in LAQV-REQUIMTE Analysis laboratory. For all the compounds, EA calculations required solvent adjustments.

2.4. Ligands synthesis and characterisation

Please refer to Figure 1.11 for the respective structures.

2.4.1. Synthesis of L1

L1 was synthesised following a series of optimizations and according to Sakai *et al.*[41]. A suspension of thiourea (3.00 g, 39.4 mmol) and 2,3-dichloroquinoxaline (1.43 g, 7.18 mmol) was refluxed for 1h in ethanol (25 mL) and followed by TLC. The reaction mixture was cooled to room temperature and the solvent reduced to 5 mL, followed by addition of an aqueous solution

(50 mL) of NaOH (8.53 g, 213.3 mmol). This mixture was refluxed for 1h and cooled to room temperature. The brown solution was filtered and acidified with acetic acid (15 mL) resulting in a brown solid (1.2 g, 6.18 mmol, 86%) that was filtered and washed with water.

^{1}H NMR (400 MHz, DMSO-d_6) chemical shifts, δ (ppm), were as follows (Figures A.1 and A.2): 14.28 (s, 2H, **1**), 7.47 – 7.36 (m, 2H, **2**), 7.33 – 7.22 (m, 2H, **3**).

2.4.2. Synthesis of 2-bromo-1-(4-fluorophenyl)prop-1-en-1-ol

The synthesis of 2-bromo-1-(4-fluorophenyl)propan-1-one (I1; structure in Figure A.3) was performed as previously reported.[42] To a solution of 4'-fluoropropiophenone (2.07 mL, 14.9 mmol) in 11.25 mL of CCl_4 at 0ºC was added dropwise via syringe Br_2 (2.4 mL, 47 mmol). The reaction mixture was reacted for 2 hours at room temperature and diluted with ice. After the ice melt down the mixture was washed with a saturated mixture of $Na_2S_2O_3$ (4×30 mL) until no orange vapour evolution. Afterwards, the mixture was extracted with $CHCl_3$ (3×30 mL) and the organic layers were combined and dried with anhydrous Na_2SO_4. The mixture was filtered and evaporated on vacuum line. The pure product was obtained as a colourless oil (3.278 g, 14 mmol, 95%).

^{1}H NMR (400 MHz, $CDCl_3$) chemical shifts, δ (ppm), were as follows (Figure A.3 and A.4): 8.46 (s, 2H, **2**), 7.14 (s, 2H, **1**), 2.75 (s, 3H, **3**).

2.4.3. Synthesis of 1-(4-fluorophenyl)-1-oxopropan-2-yl dimethylcarbamodithioate

The synthesis of 1-(4-fluorophenyl)-1-oxopropan-2-yl dimethylcarbamodithioate (I2; structure in Figure A.4) was performed as previously reported.[42]A solution of 2-bromo-1-(4-fluorophenyl)propan-1-one (3.278 g, 12 mmol) in diethyl ether (25 mL) was added to refluxing suspension of sodium *N*,*N*-dimethyldithiocarbamate (4.823 g, 34 mmol) in ethanol (23 mL). The reaction was refluxed for 1h and 10 min and cooled until room temperature. The remaining solvents were evaporated on the vacuum line followed by water addition and extractions with CH_2Cl_2 (3×20 mL). All the organic layers were combined and dried with Na_2SO_4 followed by filtration and evaporation of the solvent. The pure compound was obtained as a yellow oil (3.292 g, 12 mmol, 81%) by column chromatography (1:3) (ethyl acetate/*n*-hexane).

^{1}H NMR (400 MHz, $CDCl_3$) chemical shifts, δ (ppm), were as follows: δ 8.10 (dd, *J* = 8.8, 5.5 Hz, 2H, **3**), 7.13 (t, *J* = 8.6 Hz, 2H, **2**), 5.79 (q, *J* = 7.0 Hz, 1H, **6**), 3.55 (s, 3H, **9**), 3.35 (s, 3H, **9**), 1.59 (d, *J* = 7.0 Hz, 3H, **7**). ^{13}C NMR (100 MHz, $CDCl_3$) chemical shifts, δ (ppm), were as follows: 194.77 (**5**), 167.29 (**4**), 164.75 (**1**), 131.71 (**3**), 116.02 (**2**), 51.96 (**6**), 46.07 (**8**), 41.78 (**8**), 17.23 (**7**) (individual spectra in Figures A.5 to A.9).

2.4.4. Synthesis of *N*-(4-(4-fluorophenyl)-5-methyl-1,3-dithiol-2-ylidene)-*N*-methylmethanaminium hydrogen sulfate

The synthesis of *N*-(4-(4-fluorophenyl)-5-methyl-1,3-dithiol-2-ylidene)-*N*-methylmethanaminium hydrogen sulfate (I3; structure in Figure A.10) was performed as previously reported . Sulfuric acid (9 mL, 167.93 mmol) was added to a round bottom flask with 1-(4-fluorophenyl)-1-oxopropan-2-yl dimethylcarbamodithioate (3.292 g, 12 mmol) at room temperature. The mixture was briefly warmed and mixed for 25 minutes. After the mixture was cooled until room temperature was carefully dropwise into diethyl ether (250 mL). The brown precipitate (4.024 g, 95%, 11 mmol) was filtered and washed with diethyl ether.

^{1}H NMR (400 MHz, DMSO-d_6) chemical shifts, δ (ppm), were as follows: 7.63 (dd, J = 8.8, 5.3 Hz, 2H, **3**), 7.42 (t, J = 8.8 Hz, 2H, **2**), 3.52 (d, J = 1.3 Hz, 6H, **9**), 2.38 (s, 3H, **7**). ^{13}C NMR (100 MHz, DMSO-d_6) chemical shifts, δ (ppm), were as follows: 183.69 (**8**), 164.16 (**1**), 131.99 (**3**), 131.09 (**6**), 130.74 (**5**), 125.18 (**4**), 116.79 (**2**), 47.17 (**9**), 46.96 (**9**), 14.74 (**7**). (individual spectra in Figures A.10 to A.14).

2.4.5. Synthesis of L2

In a degassed schlenck, NaOH (2.62 g, 65.5 mmol) was added to a solution of I3 (0.21909 g, 0.62 mmol) in dry MeOH (15 mL). The resulting mixture was refluxed by 90 min under N_2. After cooling until room temperature, the mixture was evaporated until dryness and extracted with CH_2Cl_2 (4×20 mL) and dried with anhydrous Na_2SO_4. The pure product was obtained as a brown precipitate (0.35 mmol, 85.6 mg, 56%).

^{1}H NMR (400 MHz, DMSO-d_6) chemical shifts, δ (ppm), were as follows: 7.53 (dd, J = 7.8, 4.4 Hz, 2H, **3**), 7.33 (t, J = 8.8 Hz, 2H, **2**), 2.22 (s, 3H, **7**). ^{13}C NMR (100 MHz, DMSO-d_6) chemical shifts, δ (ppm), were as follows: 163.86 (**1**), 161.40 (**4**), 132.08 (**3**), 127.45 (**5**), 126.18 (**6**), 116.67 (**2**), 15.28 (**7**) (individual spectra in Figures A.15 to A.19). FTIR vibration modes (ν/cm^{-1}) were as follows: 2924 (C-H), 1643 (C=C), 1507 (C-F), 1215 (C-C). UV-vis bands (nm) were as follows: 418, 275. EA for 3**L2**·4MeOH·H_7NC_2 - calculated (%): C: 43.75, H: 4.89, N: 1.55, S: 21.23; EA - found (%): C: 43.38; H: 4.44; N: 1.07; S: 20.44.

2.4.6. Synthesis of L3

4,4'-Methylenebis(2-chloroaniline) (0.5040 g, 1.88 mmol, 1 equiv) was reacted under Nitrogen atmosphere with 1.6520 g (21.7 mmol, 11.54 equiv) of thiourea in refluxing dry ethanol (30 mL) for 45 min. After cooling to ambient temperature, 13 mL of 5M NaOH (degassed) were added and the solution was refluxed for additional 4.5 hours. Afterwards, the mixture was cooled to the room temperature and the pH adjusted to 5-6 with a 6M solution of HCl and the mixture was extracted with $CHCl_3$ (3×30 mL). The organic layers were combined and dried over Na_2SO_4. The pure compound was obtained in form of a white solid (0.492 g, 1.57 mmol, 84%) by evaporation on the vacuum line and storage under N_2.

^{1}H NMR (400 MHz, DMSO-*d$_6$*) chemical shifts, δ (ppm), were as follows: 6.98 (d, J = 1.7 Hz, 2H, **7**), 6.84 (dd, J = 8.2, 1.7 Hz, 2H, **5**), 6.69 (d, J = 8.2 Hz, 2H, **4**), 5.12 (s, 4H, **2**), 3.58 (s, 2H, **9**). ^{13}C NMR (100 MHz, DMSO-*d$_6$*) chemical shifts, δ (ppm), were as follows: 183.84 (**1**), 142.62 (**3**), 130.53 (**6**), 128.74 (**7**), 127.98 (**5**), 117.02 (**8**), 115.60 (**4**), 38.59 (**9**) (individual spectra in Figures A.20 to A.24). FTIR vibration modes (ν/cm^{-1}) were as follows: 3043(C-H), 2686(S-H), 1647(CH_2), 1622 (C=N), 1589 (C=C), 1312(C-N). UV-vis bands (nm) were as follows: 305. EA for 2**L3**·4NaCl·$4N_2CSH_4$·NH_3 - calculated (%): C: 33.17, H: 4.26, N: 22.75, S: 20.83; EA - found (%): C: 33.30; H: 4.39; N: 21.99; S: 20.44.

2.4.7. Synthesis of L4 and L5

The **L4** and **L5** compounds were already available in our group laboratory and were used after NMR characterisation to confirm the purity of these ligands (individual spectra in Figures A.25 to A:27).**L4:** ^{1}H NMR (400 MHz, $CDCl_3$) chemical shifts, δ (ppm), were as follows: δ 7.95 – 7.70 (m, 8H, **1**), 7.57 – 7.32 (m, 12H, **3/2**), 4.38 (s, 1H, **4**). **L5**: ^{1}H NMR (400 MHz, $CDCl_3$) chemical shifts, δ (ppm), were as follows: δ 13.39 (s, 2H, **1**), 8.59 (s, 2H, **6**), 7.42 (dd, J = 7.6, 1.3 Hz, 2H, **2**), 7.31 (td, J = 8.3, 1.6 Hz, 2H, **5**), 6.87 (dd, J = 12.6, 7.8 Hz, 4H, **3/4**), 3.92 (s, 4H, **7**).

2.4.8. Synthesis of 2,6-bis(chloromethyl)pyridine

The synthesis of 2,6-bis(chloromethyl)pyridine (I4; structure in Figure A.28) was performed with some adjustments according to Reiser *et al*.[43] To a suspension of 2.11 g (15.2 mmol, 1.0 equiv) of 2.6-bis(hydroxymethyl)pyridine in 15 mL dry ether (cooled at 0ºC) was slowly added (dropwise 2.43 mL (33.4 mmol, 3.97 g, 2.2 equiv) of $SOCl_2$. After the complete addition, the mixture was stirred at 0ºC for 1.5 hours, before the ice bath was removed and the stirring continued at ambient temperature for 18 hours. The white solid was collected, washed with Et_2O and dried under vacuum. The hydrochloride present in the solid was removed by dissolving this in 100 mL CH_2Cl_2 and stirring the solution with 100 mL saturated $NaHCO_3$ solution until gas-evolution ceased. After separation, the aqueous layer was extracted with CH_2Cl_2 (3×50 mL). All the organic extracts were combined and dried with Na_2SO_4. The resulting white solid (2.55 g, 15.5 mmol, 95%) was obtained by evaporation of the solvent under reduced pressure.

^{1}H NMR (400 MHz, $CDCl_3$) chemical shifts, δ (ppm), were as follows: 7.79 (t, J = 7.8 Hz, 1H, **3**), 7.46 (d, J = 7.8 Hz, 2H, **2**), 4.69 (s, 4H, **1**) (individual spectra in Figures A.28 and A.29).

2.4.9. Synthesis of L6

L6 was synthesised with some adjustments according to Reiser and co-workers. [43] 2,6-bis(chloromethyl)pyridine (2.55g, 15.5 mmol, 1 equiv) was reacted under a nitrogen atmosphere with 2.36 g (31 mmol, 2.0 equiv) of thiourea in refluxing dry ethanol (30mL) for 45 min. After cooling the reaction mixture to ambient temperature, 13 mL of 5M NaOH (degassed) were added and the solution was refluxed for an additional 4.5 hours. Afterwards, the mixture was cooled to room temperature and the pH was adjusted to 5-6 with a 6M solution of HCl and the mixture was extracted with $CHCl_3$ (3×30 mL). The organic layers were combined and dried over Na_2SO_4. The pure compound was obtained in form of a white solid (1.41g, 8.2mmol, 53%) by evaporation on the vacuum line and storage under N_2.

^{1}H NMR (400 MHz, $CDCl_3$) chemical shifts, δ (ppm), were as follows: 7.78 (t, J = 7.7 Hz, 1H, **4**), 7.33 (d, J = 7.7 Hz, 2H, **3**), 3.94 (d, J = 6.8 Hz, 4H, **2**), 2.33 (s, 2H, **1**) (individual spectra in Figures A.30 and A.31).

2.5. Metal complex synthesis

2.5.1. General synthesis for the mono-substituted metal complexes

To synthesise **M1**, **M3**, **M5** and **M7** (Figure 2.1), the ligand (0.5 mmol) was dissolved in ACN (15 mL) in a nitrogen atmosphere followed by addition of the metal precursor $[Mo(CO)_6]$ (molybdenum hexacarbonyl) (0.6 mmol). The mixture was refluxed overnight, followed by solvent evaporation until dryness and washed with *n*-hexane (3×10 mL).

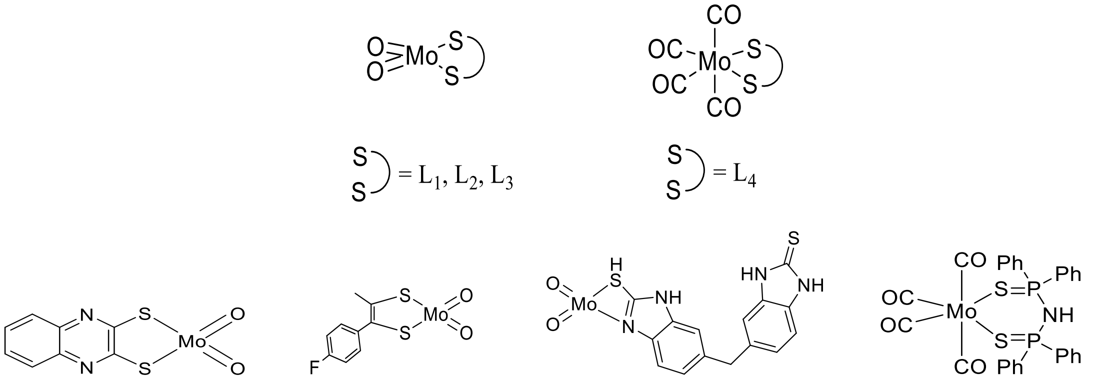

[Mo(L1)(O)$_2$] (**M1**) [Mo(L2)(O)$_2$] (**M3**) [Mo(L3)(O)$_2$] (**M5**) [Mo(L4)(CO)$_4$] (**M7**)

Figure 2.1: Mono-substituted metal complexes prepared in this work.

2.5.1.a. [Mo(L1)(O)$_2$] (M1)

The complex was obtained as a dark brown solid, with a yield of 20% (65.6 mg, 0.20 mmol). ^{1}H NMR (400 MHz, DMSO-*d$_6$*) chemical shifts, δ (ppm), were as follows: 7.86 (m, J = 6.2, 3.4 Hz, 2H, **2**), 7.60 – 7.53 (m, 2H, **1**). ^{13}C NMR (100 MHz, DMSO-*d$_6$*) chemical shifts, δ (ppm), were as follows: 138.24 (**3**), 127.62 (**2/1**), 127.43 (**2/1**). FTIR vibration modes (ν/cm^{-1}) were as follows: 3065 $_{(C\text{-}H)}$, 1613 $_{(C=N)}$, 1522 $_{(C=C)}$, 1174 $_{(C\text{-}N)}$ 949 $_{(Mo=O)}$. UV-vis bands (nm) were as follows: 387 (individual spectra in Figures A.32 and A.39). EA for 4**M1**·MoO$_3$ - calculated (%): C: 26.97, H: 1.13, N: 7.86, S: 18.00; EA - found (%): C: 25.82; H: 1.72; N: 7.13; S: 18.56.

2.5.1.b. [Mo(L2)(O)$_2$] (M3)

The complex was obtained as a black solid. The yield was not calculated since the compound was impure. FTIR vibration modes (ν/cm^{-1}) were as follows: 3065 $_{(C\text{-}H)}$, 1613 $_{(C\text{-}F)}$, 1522 $_{(C=C)}$, 843 $_{(Mo=O)}$.

2.5.1.c. [Mo(L3)(O)$_2$] (M5)

The complex was obtained as a brown precipitate, with a yield of 85% (65.6 mg, 0.14 mmol). ^{1}H NMR (400 MHz, DMSO-*d$_6$*) chemical shifts, δ (ppm), were as follows: 6.98 (s, 2H, **4**), 6.84 (d, J = 8.2 Hz, 2H, **6**), 6.69 (d, J = 8.2 Hz, 2H, **7**), 5.44 (s, 1H, **1**), 5.13 (s, 3H, **2**), 3.58 (s, 2H, **9**). ^{13}C NMR (100 MHz, DMSO-*d$_6$*) chemical shifts, δ (ppm), were as follows: 183.83 (**10**), 142.60 (**8**), 130.47 (**5**), 128.71 (**4**), 127.94 (**6**), 116.97 (**3**), 115.55 (**7**), 38.55 (**9**). FTIR vibration modes (ν/cm^{-1}) were as follows: 2691 $_{(S\text{-}H)}$, 1611 $_{(C=N)}$, 1504 $_{(C\text{-}H,\ methylene)}$, 1290 $_{(C\text{-}N)}$ 958 $_{(Mo=O)}$ (individual spectra in Figures A.41 to A.49). EA for **M5**·$2MoO_3$·N_2CSH_4- calculated (%): C: 23.89, H: 2.01, N: 10.45, S: 11.96; EA - found (%): C: 21.45; H: 2.86; N: 13.57; S: 11.96.

2.5.1.d. [Mo(L4)(CO)$_4$] (M7)

The complex was obtained as a green dark solid, with a yield of 38% (58.54 mg, 0.089 mmol). ^{1}H NMR (400 MHz, DMSO-*d$_6$*) chemical shifts, δ (ppm), were as follows: 7.87 (dd, J = 12.8, 6.7 Hz, 8H, **1**), 7.45 (dd, J = 27.3, 9.3 Hz, 2H, **2/3**) ^{13}C NMR (100 MHz, DMSO-*d$_6$*) chemical shifts, δ (ppm), were as follows: 131.35 (**1**), 128.07 (**2/3**). FTIR vibration modes (ν/cm^{-1}) were as follows: 3052 $_{(C\text{-}H)}$, 2019, 1980, 1939, 1909, 1846 $_{(C=O)}$, 1645 $_{(C=C)}$, 1584 $_{(C\text{-}N)}$, 649 $_{(P=S)}$ (individual spectra in Figures A.50 to A.56). EA for 2**M7**·[Mo(CO)$_6$]- calculated (%): C: 46.74, H: 3.54, N: 1.76, S: 8.48; EA - found (%): C: 47.94; H: 3.59; N: 2.60; S: 8.05.

2.5.2. General synthesis for the di-substituted metal complexes

To synthesise **M2**, **M4**, **M6** and **M8** (Figure 2.2), the ligand (2 mmol) was dissolved in ACN (15 mL) in a nitrogen atmosphere followed by addition of the metal precursor [Mo(CO)$_6$] (molybdenum hexacarbonyl) (1 mmol). The mixture was refluxed overnight followed by solvent evaporation until dryness and washed with *n*-hexane (or ethanol in the case of **M2**) (3×10 mL).

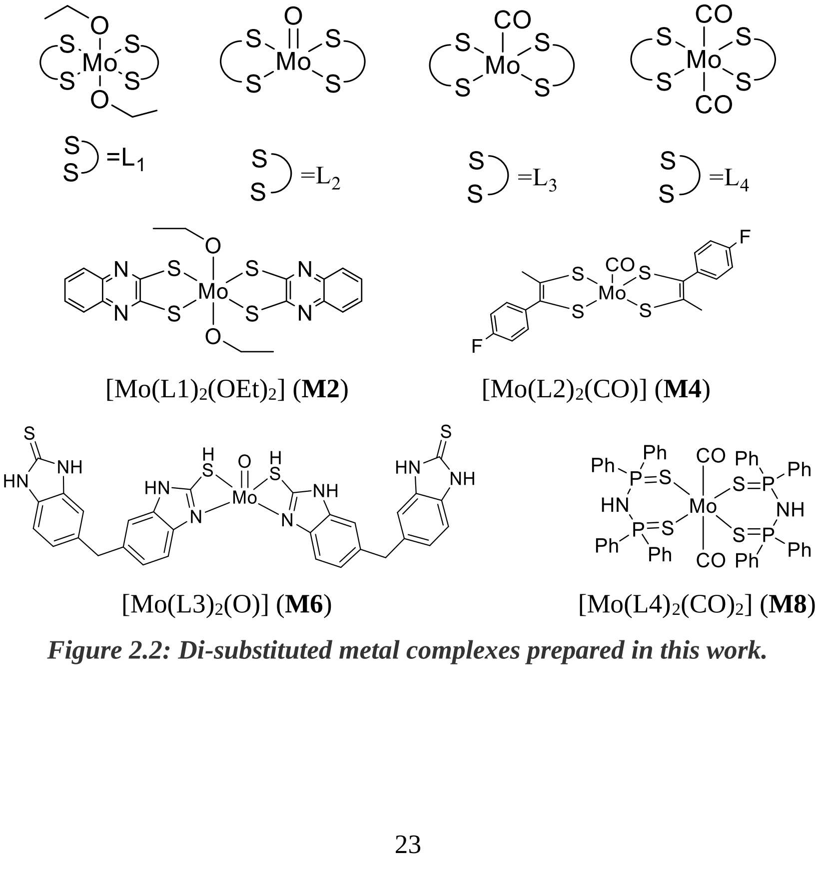

[Mo(L1)$_2$(OEt)$_2$] (**M2**)

[Mo(L2)$_2$(CO)] (**M4**)

[Mo(L3)$_2$(O)] (**M6**)

[Mo(L4)$_2$(CO)$_2$] (**M8**)

Figure 2.2: Di-substituted metal complexes prepared in this work.

2.5.2.a. [Mo(L1)$_2$(OEt)$_2$] (M2)

The complex was obtained as a purple precipitate, with a yield of 5% (16.7 mg, 0.029 mmol). ^{1}H NMR (400 MHz, MeOD) chemical shifts, δ (ppm), were as follows: 7.81 (m, J = 6.3, 3.4 Hz, 2H, **2**), 7.54 (m, J = 6.3, 3.4 Hz, 2H, **1**), 3.11 (q, J = 14.6, 7.3 Hz, 2H, **6**), 1.22 (t, J = 7.3 Hz, 4H, **5**). ^{13}C NMR (100 MHz, MeOD) chemical shifts, δ (ppm), were as follows: 138.19 (**3**), 130.64 (**4**), 128.74 (**1**), 126.95 (**2**), 47.94 (**6**), 9.24 (**5**). FTIR vibration modes (ν/cm^{-1}) were as follows: 3046 $_{(C-H)}$, 1623 $_{(C=N)}$, 1540 $_{(C=C)}$, 1121 $_{(C-O)}$. UV-vis (nm): 395, 556, 618 (individual spectra in Figures A.57 and A.64). EA for **M2**·MoO$_3$·ACN - calculated (%): C: 34.88, H: 3.06, N: 9.24, S: 16.96; EA - found (%): C: 34.85; H: 3.01; N: 8.30; S: 15.90.

2.5.2.b. [Mo(L2)$_2$(O)] (M4)

The complex was obtained as a black solid. The yield was not calculated since the compound was impure. FTIR vibration modes (ν/cm^{-1}) were as follows: 3046 $_{(C-H)}$, 1977 $_{(C=O)}$, 1623 $_{(C-F)}$, 1540 $_{(C=C)}$.

2.5.2.c. [Mo(L3)$_2$(O)] (M6)

The complex was obtained as a brown precipitate, with a yield of 26% (61.72 mg, 0.084 mmol). ^{1}H NMR (400 MHz, DMSO-d_6) chemical shifts, δ (ppm), were as follows: 6.98 (d, J = 1.7 Hz, 4H, **4**), 6.84 (dd, J = 8.2, 1.8 Hz, 4H, **6**), 6.69 (d, J = 8.2 Hz, 4H, **7**), 5.46 (s, 2H, **1**), 5.13 (s, 6H, **2**), 3.58 (s, 4H, **9**). ^{13}C NMR (100 MHz, DMSO-d_6) chemical shifts, δ (ppm), were as follows: 183.81 (**10**), 142.60 (**8**), 130.48 (**5**), 128.71 (**4**), 127.94 (**6**), 116.98 (**3**), 115.56 (**7**), 38.56 (**9**). FTIR vibration modes (ν/cm^{-1}) were as follows: 2089 $_{(S-H)}$, 1622 $_{(C=N)}$, 1415 $_{(C-H,\ methylene)}$, 1317 $_{(C=N)}$, 952 $_{(Mo=O)}$. UV-vis (nm): 350 (individual spectra in Figures A.66 and A.73). EA for **M5**.4MoO$_3$·8N$_2$CSH$_4$·C$_6$H$_{14}$ - calculated (%): C: 24.27, H: 3.30, N: 16.35, S: 18.72; EA - found (%): C: 25.86; H: 2.47; N: 16.30; S: 18.01.

2.5.2.d. [Mo(L4)$_2$(CO)$_2$] (M8)

The complex was obtained as beige solid, with a yield of 18% (21.02 mg, 0.02 mmol). ^{1}H NMR (400 MHz, DMSO-d_6) chemical shifts, δ (ppm), were as follows: 7.85 (dd, J = 13.8, 6.9 Hz, 8H, **1**), 7.53 – 7.37 (m, 12H, **2/3**) ^{13}C NMR (100 MHz, DMSO-d_6) chemical shifts, δ (ppm), were as follows: 131.78 (**1/3**), 128.51 (**2**). FTIR vibration modes (ν/cm^{-1}) were as follows: 3052 $_{(C-H)}$, 2019, 1909, 1846 $_{(C=O)}$, 1647 $_{(C=C)}$, 1447 $_{(N\text{-}H)}$, 647 $_{(P=S)}$. UV-vis bands (nm) were as follows: 467, 392 (individual spectra in Figures A.74 to A.81).

2.5.3. General synthesis for the salen-type and pincer-type metal complexes

2.5.3.a. [$Mo_2(O)_2$(L5)] (M9)

L5 (0.268 g, 1 mmol) was dissolved in ACN (15 mL) in a nitrogen atmosphere followed by the addition of the metal precursor [$Mo(CO)_6$] (molybdenum hexacarbonyl) (0.264 g, 1 mmol). The mixture was refluxed overnight followed by solvent evaporation until dryness and washed with dry dichloromethane (3×10 mL). The complex was obtained as violet solid, with a yield of 35% (0.174 g, 0.35 mmol). FTIR vibration modes (ν/cm^{-1}) were as follows: 3060 $_{(C\text{-}H)}$, 1613 $_{(C=N)}$, 1446 $_{(C=C)}$, 1264 $_{(C\text{-}O)}$, 932 and 906 $_{(Mo=O)}$. EA for **M9** - calculated (%): C: 39.20; H: 2.88; N: 5.71; EA - found (%): C: 40.40; H: 2.78; N: 5.91. (individual spectra in Figures A.85 to A.90)

2.5.3.b. [$Mo(SCN_2H_2)$(L6)] (M10)

L6 (1.5 mmol) was dissolved in dichloromethane (15 mL) in a nitrogen atmosphere followed by the addition of the metal precursor [$Mo(CO)_6$] (molybdenum hexacarbonyl) (1.5 mmol). The mixture was refluxed overnight followed by solvent evaporation until dryness and washed with dry dichloromethane (3×10 mL). The complex was obtained as a black solid, with a yield of 21% (0.107 g, 0.31 mmol). FTIR vibration modes (ν/cm^{-1}) were as follows: 3408 $_{(N\text{-}H)}$, 1627 $_{(C=N)}$, 1502 $_{(C=C)}$, 1383 $_{(C\text{-}H\ methylene)}$. EA for **M10**$\cdot 2MoO_3 \cdot 2N_2CSH_4$ - calculated (%): C: 15.41; H: 2.20; N: 12.58, S: 20.57; EA - found (%): C: 14.31; H: 1.94; N: 11.6; S: 22.00).

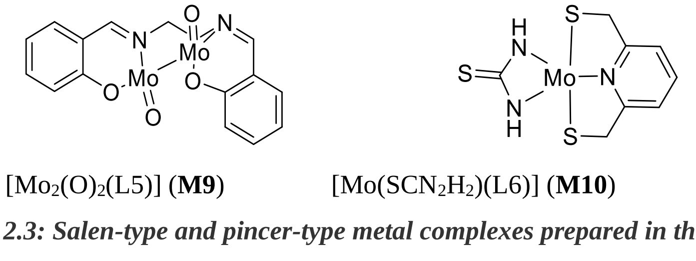

[$Mo_2(O)_2$(L5)] (**M9**)　　[$Mo(SCN_2H_2)$(L6)] (**M10**)

Figure 2.3: Salen-type and pincer-type metal complexes prepared in this work.

3. Results and Discussion

3. Molybdenum complexes as catalysts for CO_2 electroreduction - Results and Discussion

Different electro- and photochemical methodologies have been explored to achieve the CO_2 conversion into added-valued compounds, using a variety of metal complexes as catalysts. Living organisms, on the other hand, use specific enzymes to achieve efficient and selective CO_2 conversion. Hence, it is very tempting to mimic the enzymes active sites to develop innovative and more efficient catalysts for the CO_2 conversion. In this work, we focused on the molybdenum-containing FDH enzymes that catalyse the reversible CO_2 conversion into formate and whose active site harbours a molybdenum ion in a sulfur-rich coordination sphere (Figure 1.7).

Ten molybdenum complexes were prepared, with different ligands inspired in the dithiolene moiety of the pyranopterin cofactor of FDH active site(dithiolene and derivative compounds) and also in different compounds previously described in the literature (pincer-type and salen-type (no sulfur coordination) units) (Figure 1.12). Afterwards, we studied their ability to catalyse the reduction of CO_2 electrochemically. The results obtained will be herein organised by the nature of the complexes: first, the dithiolene and derivative complexes (the ligands (*section 3.1.1.*), the complexes (*section 3.1.2.*) and electrochemical studies, including detection of CO_2 reduction products (*section 3.1.3.*)), followed by the DPPAS$_2$-based complexes (*sections 3.2.1.*, *3.2.2.* and *3.2.3.*) and, finally, the salen-type complex (*sections 3.3.1.* and *3.3.2.*) and pincer-type complex (*sections 3.4.1.*, *3.4.2.* and *3.4.3.*).

3.1. Dithiolene and derivative complexes

3.1.1. Dithiolene and derivative ligands

3.1.1.a. Synthesis

Three dithiolene-type ligands were synthesised, **L1**, **L2** and **L3** (Figure 3.1), by two different methods. The first was based on sulfur insertion in 2,3-dichloro quinoxaline and 4,4'-methylenebis(2-chloroaniline), with thiourea for **L1** and **L3** and sodium dimethyldithiocarbamate hydrate for **L2**.

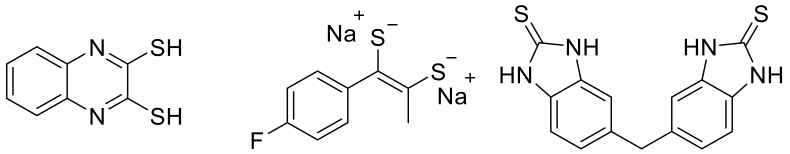

L1 L2 L3

Figure 3.1: Dithiolene ligands used for complex synthesis in this work

L1 was synthesised by a one-pot reaction using thiourea as a precursor for sulfur insertion according to Sakai and co-workers[41] (Scheme 3.1). This reaction can be divided into two steps, the first consists in an aromatic nucleophilic substitution reaction of 2,3-dichloro quinoxaline with thiourea, in a ratio of 1:5.5 equiv (respectively) for 1h forming an isothiouronium ion. The second step consists of the hydrolysis of this ion by the addition of an aqueous solution of sodium hydroxide to the mixture (that was then refluxed for 1h), and an acidification step with acetic acid resulting in **L1** with 85% yield.

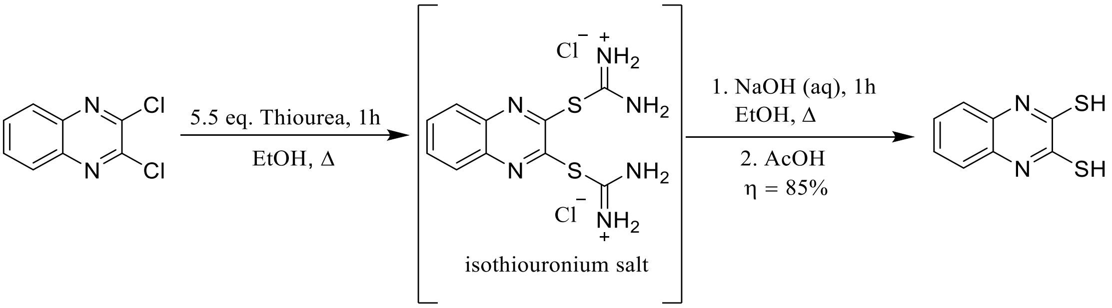

Scheme 3.1: Synthesis of L1.

L2 was synthesised by several steps using sodium dimethyldithiocarbamate hydrate as a precursor to functionalise an *α*-bromo ketone into a dithiolene salt (Scheme 3.2). The last step of the synthesis required inert atmosphere and anhydrous conditions and, for that, Schlenck techniques and dry solvents were used. The synthesis of **L2** starts with a bromination of 4′-fluoropropiophenone in CCl_4 at 0 °C, followed by a nucleophilic substitution reaction with sodium dimethyldithiocarbamate in EtOH. The reaction of this intermediate with H_2SO_4 produces a cyclic organic salt with HSO_4^- as anion through a cyclisation reaction. Finally, the ligand **L2** is obtained by hydrolysis of this cyclic compound with NaOH in dry MeOH under a N_2 atmosphere, leading to the desired dithiolene salt. The last step of this synthesis was very challenging because this reaction was very sensitive to the presence of oxygen and to the acidic work-up resulting in decomposition with the release of sulphydric acid. In Table 3.1, all the conditions tested for the last reaction step in the preparation of **L2** are summarised. Particularising, in two cases (entry 2 and 4) residual amounts of **L2** were identified by NMR spectroscopy, however, it was not possible to perform a purification step due to the reduced amount of compound obtained.

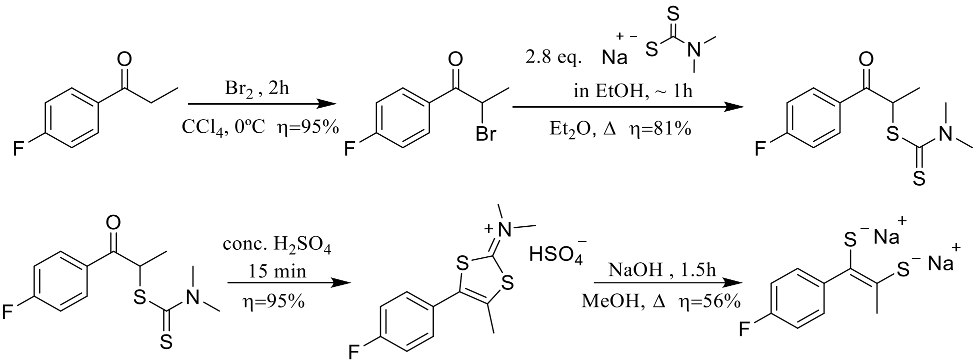

Scheme 3.2: Synthesis of L2.

Table 3.1: Reaction conditions tested for the last step of the synthesis of L2.

#	**Solvent**	**Atmosphere**	**Work-up**	**Purification**	**Yield (%)**
1	MeOH	O_2	✖	Washed with *n*-hexane	✖
2	MeOH	O_2	5M solution of HCl	✖	✖
3	MeOH	O_2	✖	Phase reverse column chromatography	✖
4	MeOH	O_2	✖	✖	✖
5	MeOH	O_2	5M solution of HCl	Column chromatography (Ethyl Acetate/*n*-hexane) (1:5)	20%
6	MeOH	O_2	5M solution of HCl	Column chromatography (Petroleum Ether/Acetone) (10:1)	25%
7	Dry MeOH	N_2	5M solution of HCl	Column chromatography (Petroleum Ether/Acetone) (10:1)	30%
8	Dry MeOH	N_2	✖	✖	56%

L3 was synthesised by reacting thiourea with 4,4'-methylenebis(2-chloroaniline) through a one-pot reaction (Scheme 3.3). The reaction consists in an aromatic nucleophilic substitution followed by cyclisation with thiourea. The product resulting of this synthesis was unexpected since the conditions used in this reaction were very similar to the experimental conditions used in the synthesis of **L1**, being expected one substitution of -Cl by -SH.

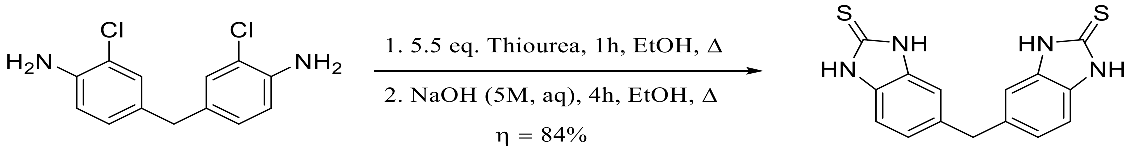

Scheme 3.3: Synthesis of L3.

3.1.1.b. Characterisation

(*To improve reading fluency, most of the spectra of this section and next ones are presented in "Annexes".*)

L1 was synthesised according to the literature[41] and was characterised by NMR (^{1}H and 2D COSY (Figures A.1 to A.2 in "Annexes")). The ^{1}H NMR spectrum of **L1** presents two multiplet signals in the aromatic region (δ = 7.47- 7.36 ppm and δ = 7.33 ppm and 7.22 ppm), corresponding to the aromatic protons in the molecule, and one singlet signal with δ = 14.00 ppm respective to the S-H bond. In the COSY bidimensional experiment, the correlation between the aromatic protons was confirmed.

L2 and **L3** were fully characterised by NMR (Figures A.15 to A.24) and also by FTIR, UV-vis (Figure 3.2 and 3.4). The ^{1}H NMR spectrum of **L2** shows two peaks in the aromatic region, one doublet of doublets between 7.55-7.52 ppm (**3**) and one triplet at 7.33 ppm (**2**) corresponding to the protons of the aromatic ring, and one signal in the aliphatic zone as a singlet at 2.22 ppm (**7**) corresponding to the CH_3. In the COSY bidimensional experience, the correlation between the aromatic protons was confirmed (Figures A.15 and A.16).

The compound was also characterised using 1D and 2D ^{13}C experiments in the NMR. The ^{13}C APT experiment showed that the compound has three signals corresponding to a CH/CH_3 ("in phase") and four corresponding to a CH_2/quaternary carbon ("in anti-phase"). In the signals that are "in phase", two of the peaks on the spectrum can be found in the aromatic zone (~100 to ~150 ppm) while the remaining peak is in the aliphatic zone (~0 to ~50 ppm). The peaks that are anti-phase in the spectrum are corresponding to the quaternary carbons in the molecule (Figure A.17). To determine the overall structure of the ligand, heteronuclear experiments (HSQC and HMBC) were used to evaluate the correlations between ^{13}C-^{1}H. The HSQC experiment gives information on the direct correlations ^{13}C-^{1}H while the HMBC experiment reveals the correlation between ^{13}C-^{1}H that are apart by 2 to 4 bonds (Figure A.18 and A.19). Table 3.2 shows all the chemical shifts and the expected structure as a result of these characterisation experiments.

Table 3.2: NMR characterisation (chemical shifts) of ligand L2.

	^{1}H (ppm)	^{13}C (ppm)
1	-	160.99
2	t (7.33)	116.04/116.26
3	m (7.55-7.52)	131.57/131.68
4	-	163.44
5	-	127.04
6	-	125.77
7	s (2.22)	14.87

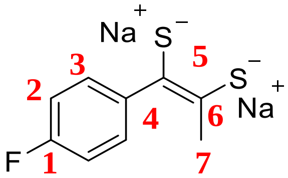

The FTIR spectrum of **L2** confirms the presence of vibrational modes corresponding to the C-F bond (~1507 cm^{-1}), to the aromatic ring (~ 2924 cm^{-1} (C-H), ~1215 cm^{-1} (C-C)) and to the conjugated alkene groups (~1641 cm^{-1} (C=C)) (Figure 3.2).[44] The UV-vis spectrum of the ligand was performed in DMSO with a concentration of 1×10^{-4} mM, and displays two absorbance bands in the UV region (most energetic zone of the spectrum) corresponding to the π-π* transitions (~412 and 276 nm) (Figure 3.2).

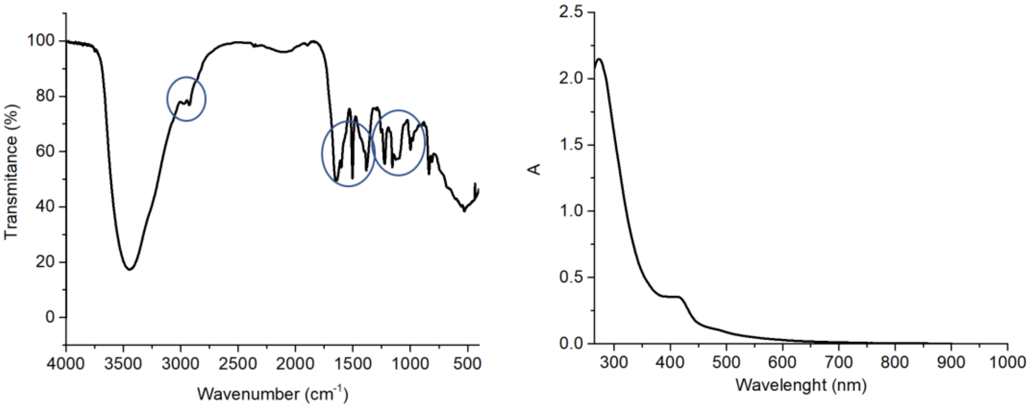

Figure 3.2: FTIR (on left) and UV-vis (on right) spectra of L2. *Highlighted by blue circles are the characteristic vibrational modes discussed in the text.*

The ^{1}H NMR spectrum of **L3** (Figure A.20) presents three aromatic signals, one amine signal and one aliphatic signal. The aromatic signals can be found at 6.98 ppm (doublet) (**7**), 6.85-6.82 ppm (doublets of doublets) (**5**) and 6.70-6.68 ppm (doublet) (**4**), the amine signal at

5.12 ppm (multiplet) (2) and the aliphatic signal at 3.58 ppm (singlet)(9) corresponding to the methylene group. The broad signal at ~ 7.10 ppm is water that was deviated by the amines in the molecule. In the COSY bidimensional experience, the correlation between the aromatic protons (5 and 4) was confirmed, as expected (Figure A.21). The ^{13}C APT experiment for **L3** displayed 3 signals corresponding to CH/CH_3(“in phase”) and 5 signals (“anti-phase”) corresponding to CH_2/quaternary carbons (Figure A.22). All the signals that are in phase are in the aromatic zone (100 to 150 ppm) corresponding to the CH’s of the aromatic ring.

For the attribution and confirmation of the signals in the spectra, heteronuclear experiments (HSQC and HMBC (Figures A.23 and A.24)) were performed to evaluate the correlations between ^{13}C-^{1}H. The HSQC experiment enabled the identification of the direct correlations ^{13}C-^{1}H, while the HMBC experiment revealed the correlation between ^{13}C-^{1}H that are separated by 2 to 4 bonds. Table 3.3 presents all the data treated and the deduced structure by these experiments.

Table 3.3: NMR characterisation (chemical shifts) of ligand L3.

	^{1}H (ppm)	**^{13}C (ppm)**
1	-	183.84
2	m(5.12)	-
3	-	142.69
4	d(6.69)	115.6
5	d.d(6.83)	127.98
6	-	130.53
7	d(6.98)	128.74
8	-	117.02
9	s(3.58)	38.59

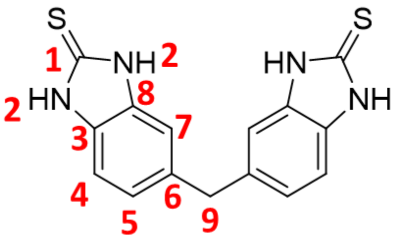

L3 can present two different tautomers, one in the thiol form and the other in the thione form (Figure 3.3). In solution, the compound has a preference for the thione form, as can be observed in the NMR characterisation (Figure A.20 to A.24). Through the analysis of the FTIR spectrum of **L3** (Figure 3.4), it is possible to confirm the presence of the vibrational modes of the aromatic rings (~ 3043 cm^{-1} (C-H), ~1589 cm^{-1} (C=C)), methylene group (~1467 cm^{-1}) and aromatic amines

(~1312 cm^{-1} (C-N), and also reveals the characteristically vibrational modes of imine (~1622 cm^{-1} (C=N)) and thiols (~2686 cm^{-1} (S-H)), which indicates that the compound adopted the thiol form in the solid state.[44] The UV-vis spectrum of **L3** was performed in DMSO with a concentration of 1×10^{-4} mM, and shows one absorbance band in the UV zone (most energetic zone of the spectrum) corresponding to the π-π^* transitions (~280-338) (Figure 3.4).

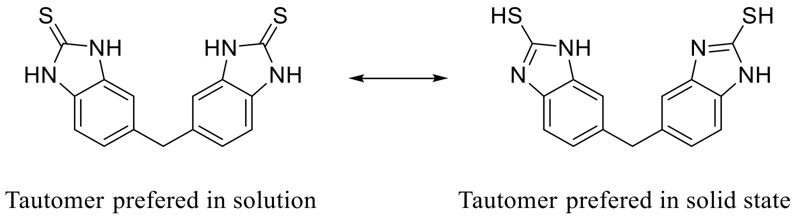

Tautomer prefered in solution

Tautomer prefered in solid state

Figure 3.3: Different L3 tautomers.

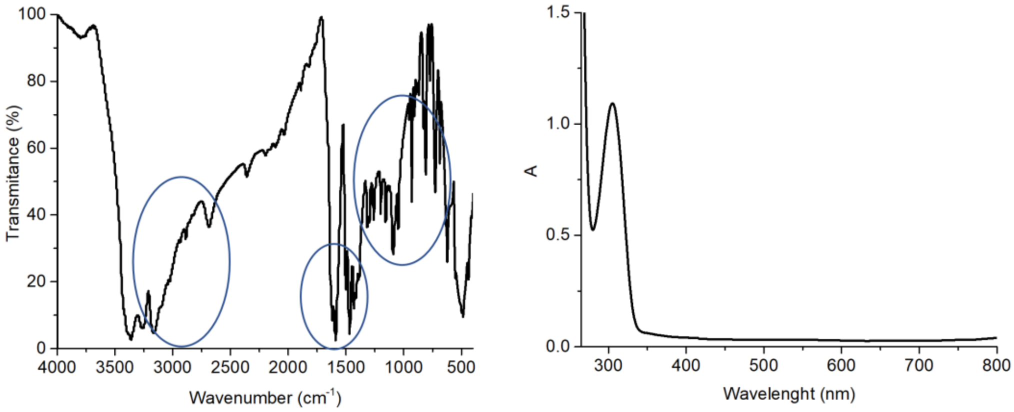

Figure 3.4: FTIR (on left) and UV-vis (on right) spectra for L3. *Highlighted by blue circles are the characteristic vibrational modes discussed in the text.*

In general, all the ligands were obtained as expected and the structures presented for each compound are supported by NMR, FTIR, UV-vis and EA analysis (Figure 1.11). This characterisation was important to understand the different conformations and the purity of the compounds.

3.1.2. Dithiolene and derivative complexes

3.1.2.a. Synthesis

The dithiolene complexes **M1**, **M2**, **M3** and **M4** and derivatives **M5** and **M6**, were synthesised under N_2 by refluxing the ligands **L1**, **L2** or **L3** with molybdenum hexacarbonyl, in ACN overnight (Schemes 3.4 to 3.9). The mono-substituted complexes (**M1**, **M3** and **M5**) were synthesised by reacting the ligands with molybdenum hexacarbonyl in a 1:1 ratio, whereas the di-substituted complexes (**M2**, **M4** and **M6**) were obtained by reacting the ligands with the molybdenum precursor in a 2:1 ratio.

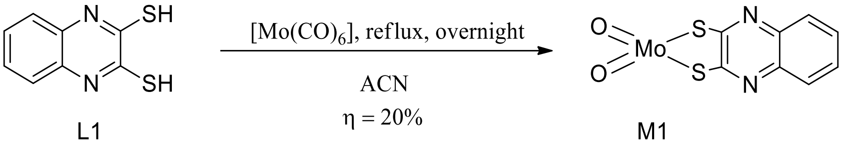

Scheme 3.4: Synthesis of M1.

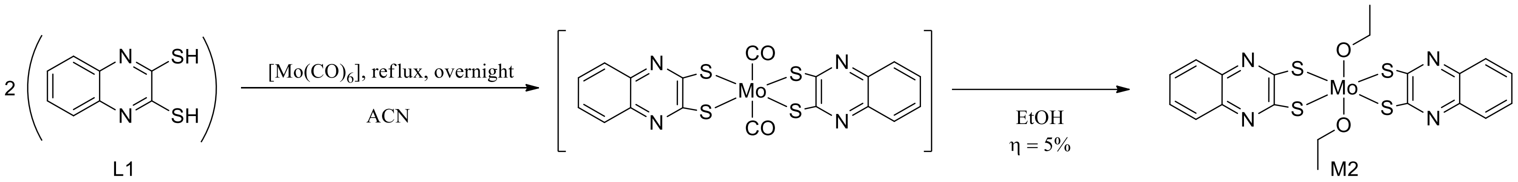

Scheme 3.5: Synthesis of M2.

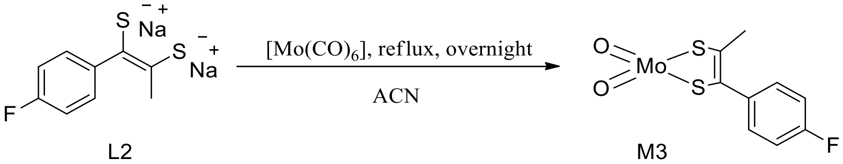

Scheme 3.6: Synthesis of M3.

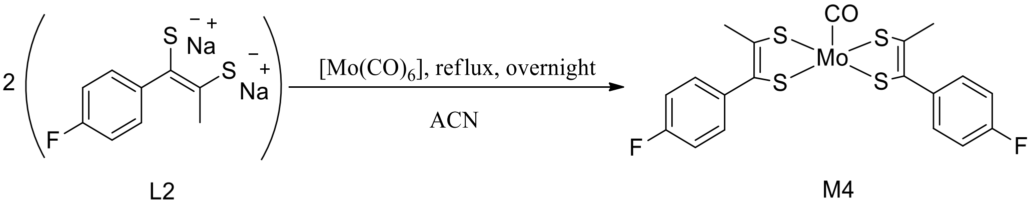

Scheme 3.7: Synthesis of M4.

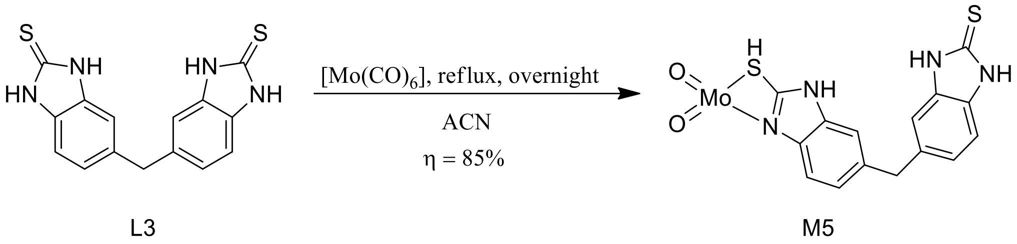

Scheme 3.8: Synthesis of M5.

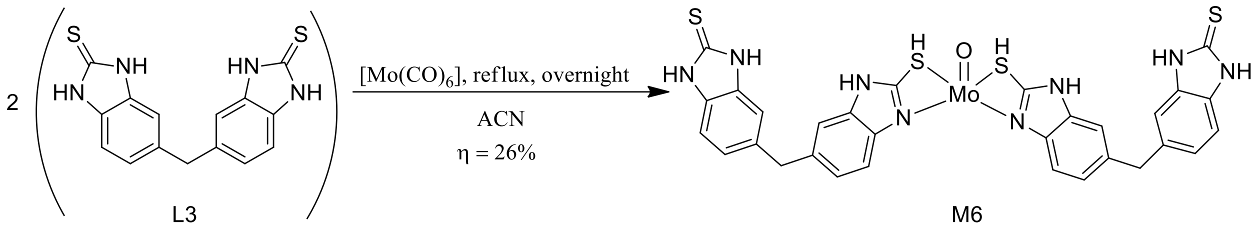

Scheme 3.9: Synthesis of M6.

The **M1** and **M2** complexes were obtained as brown and purple precipitates, with a yield of 20% and 5%, respectively. The respective EA (results presented under "Materials and Methods", section 2.5) showed that the complexes were obtained as solvates and as mixtures of small percentages of decomposed precursors that were not possible to purify. The di-substituted complex **M2** was obtained pure by washing the crude product with ethanol.

The **M3** and **M4** complexes were obtained as black precipitates. Their EA results had to be adjusted with MoO_3, indicating that the compounds initially planned for were obtained only in a very small proportion (when compared to MoO_3), which shows that pure **M3** and **M4** were not obtained. The derivative dithiolene complexes **M5** and **M6** were obtained as brown precipitates, with a yield of 85% and 26%, respectively. Their EA showed that the complexes were obtained with a small proportion of NH_4Cl and thiourea molecules.

3.1.2.b. Characterisation

The complexes were fully characterised by NMR, UV-vis, FTIR and CV (section 3.1.3.a.), except **M3** and **M4** that were not characterised by NMR, due to the low amount of product obtained in the synthesis.

The ^{1}H NMR spectrum of **M1** (Figure A.32; Table 3.4) was characterised in DMSO-d_6 and presents two multiplets in the aromatic region, which correspond to the aromatic protons of the ligand, around ~7.86 (**2**) and ~7.55 (**1**) ppm. The ^{13}C APT spectrum (Figure A.33) displays two signals arising from a CH/CH_3 (~127.18/126.99(**1**/**2**)) ("in phase") and one signal from a

CH_2/quaternary carbon (~137.80 (**3**)) ("anti-phase") (Table 3.4). The HSQC analysis (Figure A.34) confirms that the two signals "in phase" (**2** and **1**) of the ^{13}C APT spectrum correspond to the aromatic protons of the ligand and the other signal corresponds to a quaternary carbon (**3**). The NMR features of **M2** are similar to the ones of **M1** (as expected, since the ligand is the same) (Figure A.57). **M2** was characterised in MeOD and displays two multiplets (~7.82 (**2**) and 7.55 (**1**) ppm) in the aromatic region, corresponding to the aromatic protons of the ligand, and two proton signals in the aliphatic region (~ 3.11 (**6**) and 1.22 (**5**) ppm), corresponding to the protons of the ethanol molecule coordinated to the metal centre. The analysis of the HSQC (Figure A.60) and ^{13}C APT (Figure A.59) spectra indicates that the two signals at 128.74 (**1**) and 126.95 (**2**) ppm arise from the aromatic protons, and the peak at 138.19 (**3**) ppm correspond to the quaternary carbon of the ligand. The signals at 47.94 (**6**) and 9.24 (**5**) ppm correspond to $\underline{C}H_2$ and $\underline{C}H_3$ of the coordinated ethanol molecule.

Table 3.4: NMR characterisation (chemical shifts) of M1 and M2. *Follow atoms numbering in Scheme 3.10.*

	M1		**M2**	
	^1H (ppm)	**^{13}C (ppm)**	**^1H (ppm)**	**^{13}C (ppm)**
1	m(7.55)	127.18/127.99	m(7.55)	128.74
2	m(7.86)	127.18/126.99	m(7.82)	126.95
3	-	137.80	-	138.19
4	-	N/O	-	N/O
5	-	-	t(1.22)	9.24
6	-	-	q(3.11)	47.94

N/O, not observed

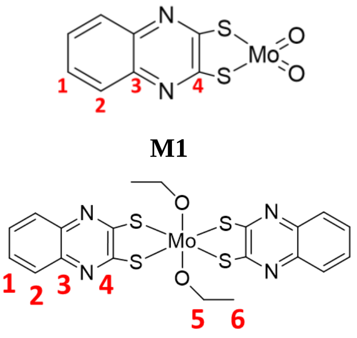

M1

M2

Scheme 3.10: M1 and M2 expected structures.

The ^1H NMR and ^{13}C APT spectra of **M5** and **M6** are very similar (Figures A.41 and A.43 (for **M5**); and Figures A.66 and A.68 (for **M6**); Table 3.5), as expected since the ligand used to synthesise these complexes was the same. In the ^1H NMR spectrum, both complexes show three aromatic signals (two doublets (**6** and **7**) and one singlet (**4**) for **M5**) and (two doublets (**4** and **7**) and one doublet of doublets (**6**) for **M6**), one amine signal (singlet (**2**)), one thiol signal (singlet (**1**)) and one aliphatic signal (singlet (**9**)). These results indicate that the ligand coordinates to the molybdenum when is in the thiol form. The ^{13}C APT spectrum shows three signals that correspond to CH/CH_3 ("in phase") (**4**, **6** and **7**) and five signals that correspond to a CH_2/quaternary carbon (**3**, **5**, **8**, **9** and **10**).

Table 3.5: NMR characterisation (chemical shifts) of M5 and M6.

Follow atoms numbering in Scheme 3.11.

	M5		**M6**	
	^{1}H(ppm)	**^{13}C(ppm)**	**^{1}H(ppm)**	**^{13}C(ppm)**
1	s(5.44)	-	s(5.46)	-
2	s(5.13)	-	s(5.12)	-
3	-	116.97	-	116.98
4	s(6.98)	128.71	d(6.98)	128.71
5	-	130.47	-	130.48
6	d(6.85-6.83)	127.94	d.d(6.85-6.82)	127.94
7	d(6.70-6.68)	115.55	d(6.70-6.68)	115.56
8	-	142.60	-	142.60
9	s(3.58)	38.55	s(3.58)	38.56
10	-	183.81	-	183.81

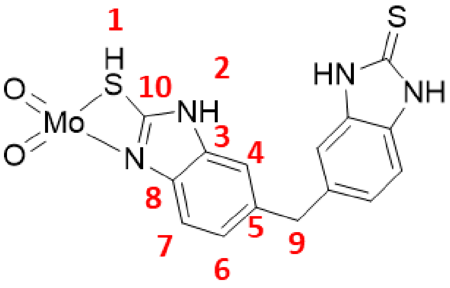

M5

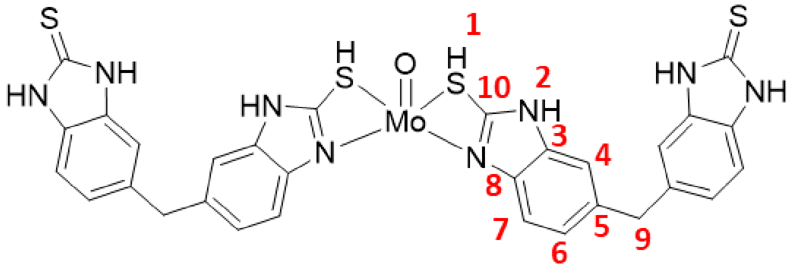

M6

Scheme 3.11: M5 and M6 expected structures.

The compounds were also characterised by FTIR (Figure 3.5) and the most important vibrational modes are summarised in Table 3.6. For **M1** and **M2**, the vibrational modes corresponding to the C=N bond (1613 and 1623 cm^{-1}, respectively), to the aromatic ring ((C-H) and (C=C) bonds) (3065; 1522 cm^{-1} for **M1** and 3046; 1543 cm^{-1} for **M2**, respectively) and to the C-N bond (1174 and 1175 cm^{-1}, respectively) of the ligand were identified. In the case of **M1** complex, it was possible to observe the M=O vibrational modes (949 cm^{-1}) and, in the **M2**, the vibrational modes relative to the C-O bond (1121 cm^{-1}) of ethanol were also observable.[44] For the **M3** and **M4**, it was possible to observe the vibrational modes correspondent to the aromatic ring and C-F bond of the ligand (1613 and 1623 cm^{-1}, respectively). In the case of **M3** complex, it was possible to identify the vibrational modes correspondent to the Mo=O bond (847 cm^{-1}) and, in the **M4** complex, it was detected the C=O vibrational mode of the carbonyl bonded to the metal centre (1977 cm^{-1}). The FTIR analysis of **M5** and **M6** shows the vibrational modes of the aromatic amines and imines (C-N and C=N) (1290; 1611 cm^{-1} for **M5**, and 1317; 1622 cm^{-1} for **M6**, respectively) as long as, the molybdenum-oxygen (Mo=O) (958 and 952 cm^{-1}, respectively) and methylene (C-H) (1504 and 1465 cm^{-1}, respectively) vibrational modes.[44] It was also possible to identify the characteristic vibrational modes of thiols (S-H) (2691 and 2 689 cm^{-1}).

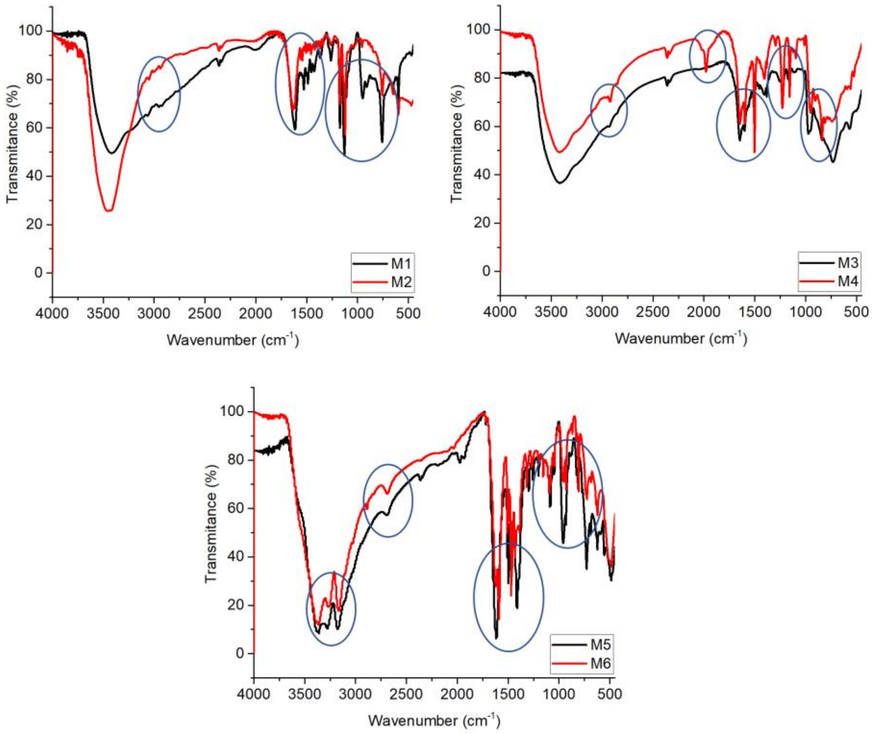

Figure 3.5: FTIR spectra of M1 to M6 compounds. *Highlighted by blue circles are the characteristic vibrational modes discussed in the text.*

Table 3.6: FTIR vibration modes for M1 to M6 complexes (values in cm^{-1}).

	M1	**M2**	**M3**	**M4**	**M5**	**M6**
S-H	-	-	-	-	2691	2689
C-F	-	-	1613	1623	-	-
C-H aromatic	3065	3046	3065	3046	N/O	N/O
C=C	1522	1540	1522	1540	N/O	N/O
C=O	-	1121	-	1977	-	-
Mo=O	949	-	843	-	958	952
C=N	1613	1623	-	-	1611	1622
C-N	1174	1175	-	-	1290	1317
C-H methylene	-	-	-	-	1504	1465
C-O	-	1121	-	-	-	-

N/O, not observed

The UV-vis spectra were obtained in DMSO with the concentrations of 1×10^{-4} mM (**M1** and **M2**) and 1×10^{-6} mM (for **M3**, **M4**, **M5** and **M6**) (Figure 3.6). The UV-vis spectrum of the **M1** complex displays one band in the region of 367-400 nm, arising possibly from the π-π^* transitions of the ligand. The **M2** complex showed three absorbance bands, one in the region of 367-400 nm, that (as in complex **M1**) corresponds to π-π^* transitions of the ligand, and two in the region 492-692 nm that can arise from charge transfer. For complexes **M3** and **M4,** it was not possible to detect absorbance bands on the visible spectrum. The **M5** and **M6** complexes present one absorbance band between 290-350 nm possibly originated by π-π^* transitions of the ligand.

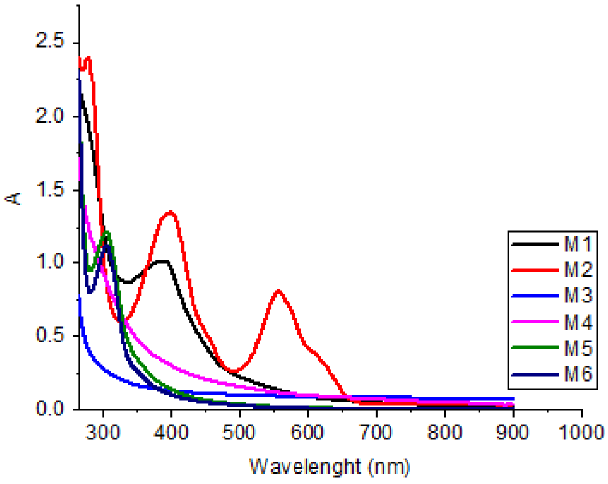

Figure 3.6: UV-vis spectra of M1 to M6 compounds.

Overall, the synthesis procedures implemented were well succeeded. NMR, FTIR, UV-vis and EA characterisation supported that **M1**, **M2**, **M5** and **M6** complexes were obtained with the expected structures (Figure 1.12) and these complexes were tested for their ability to catalyse the CO_2 electroreduction. **M3** and **M4**, on the contrary, were not successfully synthesised (obtained with many impurities) and were not tested for CO_2 conversion.

3.1.3. Electrochemical studies

3.1.3.a. Cyclic voltammetry studies

The complexes **M1, M2, M5** and **M6** were studied by CV, under N_2 and CO_2 atmosphere, to characterise their redox behaviour and to investigate their potential as catalysts of CO_2 electroreduction. (The CV results for **M3** and **M4** would be inconclusive because these compounds were obtained impure, as mixtures dominated by MoO_3, as described in section 3.1.2.a). The ability of these catalysts to electrochemically convert CO_2 was also studied in the presence of water, as a proton source. All values indicated herein are vs Ag/AgCl (0.278V vs NHE).

For **M1**, the CV under N_2 revealed two reduction processes observed around -0.32V and -0.96V, that can be attributed to the redox pairs Mo^{6+}/Mo^{5+} and Mo^{5+}/Mo^{4+},[12,36,45,46] and a reduction process at around -1.70V, that was assigned to the ligand redox behaviour (Figure 3.7 – A and Figure A.39). The studies under CO_2 atmosphere reveal that **M1** is a good candidate as a catalyst for CO_2 electroreduction since the compound shows a gradual increase in current at around -2.1V (Figure 3.7 - B). Moreover, increasing water concentrations gave rise to increasing current values, which is consistent with other studies where the presence of a proton source enhances CO_2 electroreduction[47] (Figure 3.7 - C). The studies under CO_2 with increasing water concentrations revealed that the best water concentration to study the CO_2 electroreduction by CPE is 850 mM. At higher water concentrations, proton reduction (H_2 formation) competes with the CO_2 electroreduction.

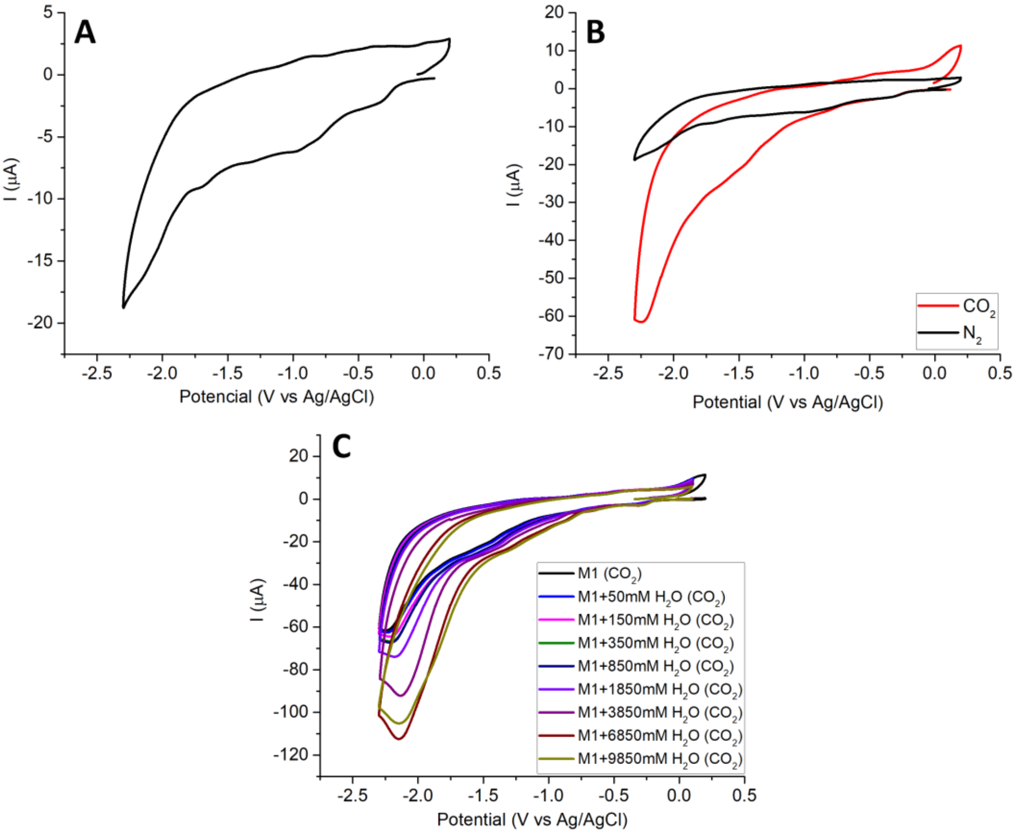

Figure 3.7: CV studies of M1 in DMF (1mM) N_2 or CO_2 saturated solutions. *$TBAPF_6$ was used as supporting electrolyte (0.1 M), at 0.1 mV s^{-1}; glassy carbon (3 mm diameter) was used as working, platinum wire as counter and Ag/AgCl as reference electrodes.* ***(A)*** *CV reduction in N_2 atmosphere.* ***(B)*** *CV overlay in N_2 and CO_2 atmosphere.* ***(C)*** *CV overlay in CO_2 atmosphere with different water concentrations.*

The CV studies of **M2** performed under N_2 showed four reduction processes around -0.1V, -0.59V, -1.17V and -1.32V, which can be indicative of the redox pairs Mo^{4+}/Mo^{3+}, Mo^{3+}/Mo^{2+}, Mo^{2+}/Mo^{1+} and Mo^{1+}/Mo^{0}, respectively.[12,36,45,46] The compound has also one reduction process around -1.65V, similar to **M1**, which suggests that this process is characteristic of the ligand (Figure 3.8 – A and Figure A.64). The experiments under CO_2 atmosphere show that **M2** can be a possible catalyst for CO_2 electroreduction since the compound shows a new peak around -1.5V, which is shifted with the addition of high water concentrations (Figure 3.8 - B and C). The addition of different water concentrations shows a current increase around -2.1V, suggesting CO_2 conversion. As for **M1**, the concentration of H_2O chosen to study the CO_2 conversion by CPE was 850 mM.

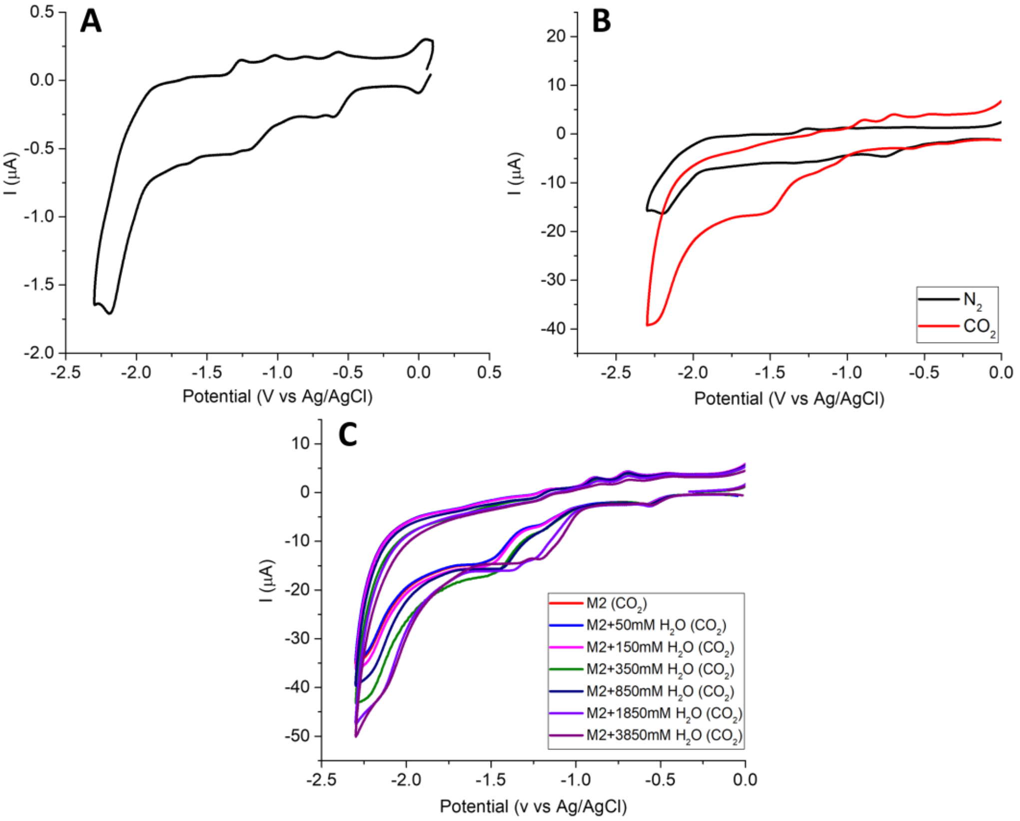

Figure 3.8: CV studies of M2 in DMF (1mM) N_2 or CO_2 saturated solutions. *$TBAPF_6$ was used as supporting electrolyte (0.1 M), at 0.1 mV s^{-1}; glassy carbon (3 mm diameter) was used as working, platinum wire as counter and Ag/AgCl as reference electrodes.* ***(A)*** *CV reduction in N_2 atmosphere.* ***(B)*** *CV overlay in N_2 and CO_2 atmosphere.* ***(C)*** *CV overlay in CO_2 atmosphere with different water concentrations.*

For **M5**, the CV studies under N_2 showed three reduction processes, one around -0.73V, which can be attributed to the ligand (Figure A.49), and two around -1.69V and -1.96V, that can be indicative of the redox pairs Mo^{4+}/Mo^{3+} and Mo^{3+}/Mo^{2+} (Figure 3.9 - A).[12,36,45,46] The experiments under CO_2 atmosphere showed a current increase by water addition, as observed for the other complexes (Figure 3.9 - B and C). The water concentration chosen for CPE experiments was also 850 mM.

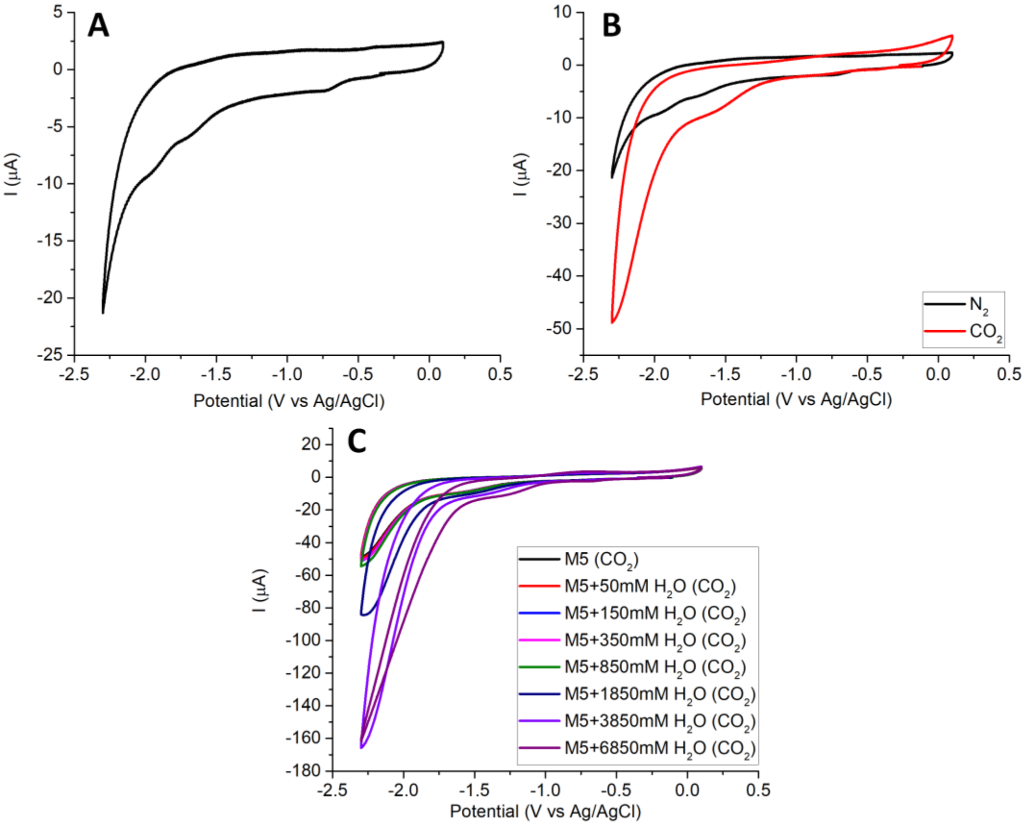

Figure 3.9: CV studies of M5 in DMF (1mM) N_2 or CO_2 saturated solutions. *$TBAPF_6$ was used as supporting electrolyte (0.1 M), at 0.1 mV s^{-1}; glassy carbon (3 mm diameter) was used as working, platinum wire as counter and Ag/AgCl as reference electrodes.* ***(A)*** *CV reduction in N_2 atmosphere.* ***(B)*** *CV overlay in N_2 and CO_2 atmosphere.* ***(C)*** *CV overlay in CO_2 atmosphere with different water concentrations.*

The CV analysis of **M6** under N_2 showed two reduction processes. One process around -0.71V, possibly corresponding to the reduction of the ligand (Figure A.73), and a second process at -1.97V, that can be indicative of the reduction pair Mo^{2+}/Mo^{1+} (Figure 3.10 - A).[12,36,45,46] The redox behaviour under CO_2 atmosphere was completely different from the one observed under N_2 (Figure 3.10 - B). A reduction process around -1.45V appears, suggesting the coordination of CO_2 to the metal centre. Addition of different water concentrations causes a current increase around -2.1V, suggesting CO_2 conversion. The water concentration chosen to perform the CPE experiments was 850 mM (Figure 3.10 - C).

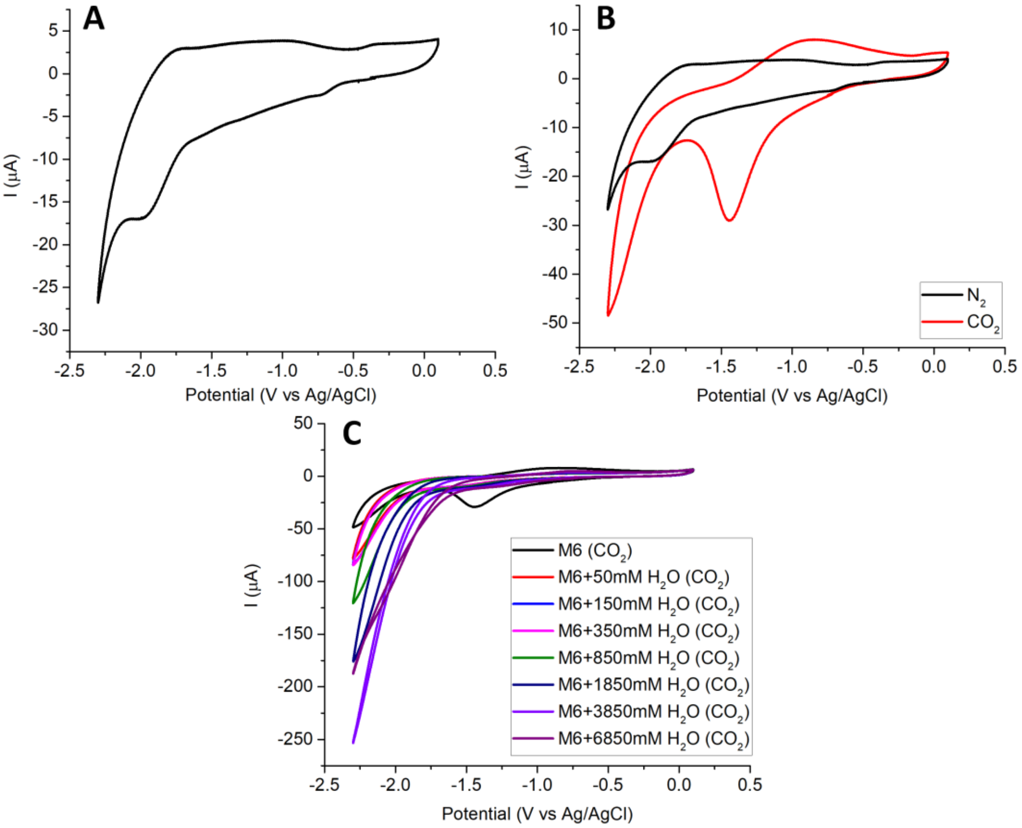

Figure 3.10: CV studies of M6 in DMF (1mM) N_2 or CO_2 saturated solutions. *$TBAPF_6$ was used as supporting electrolyte (0.1 M), at 0.1 mV s^{-1}; glassy carbon (3 mm diameter) was used as working, platinum wire as counter and Ag/AgCl as reference electrodes.* ***(A)*** *CV reduction in N_2 atmosphere.* ***(B)*** *CV overlay in N_2 and CO_2 atmosphere.* ***(C)*** *CV overlay in CO_2 atmosphere with different water concentrations.*

In the assays where water was added, it was observed the evolution of large amounts of gas. To identify the nature of the gas evolved, the gaseous headspace of three vials containing 1 mM of catalyst, 850 mM of water, in DMF, under different atmospheres (N_2, air and CO_2), was analysed (Figure 3.11) The results of this experiment were inconclusive as no gaseous products were detected by GC-TCD. Further studies must be performed to understand this particular phenomenon and identify the gas evolved after the addition of water.

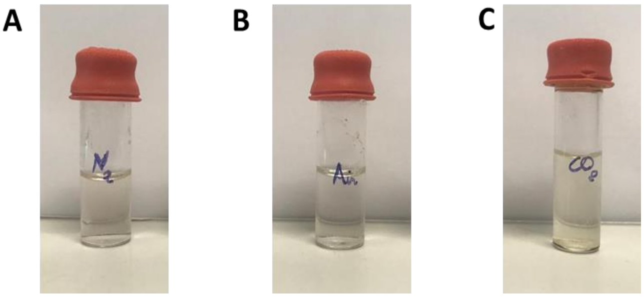

Figure 3.11: *Experimental set-up to determine the nature of the gas (or gases) formed under N_2 atmosphere (A), mimetic of air (N_2+O_2) (B) and CO_2 atmosphere (C).*

3.1.3.b. Controlled potential electrolysis studies

CPE studies were performed to study the ability of **M1, M2, M5** and **M6** to act as catalysts for the CO_2 electroreduction (**M3** and **M4** were not studied, due to their very low purity). The assays were performed at defined potentials, using water (850mM) as proton source, in DMF solutions.

The CPE studies of **M1** and **M2** were performed at -1.89V for 3h in DMF. For **M1**, it is possible to observe a current decrease at the beginning of the experience suggesting catalyst degradation, followed by a small current increase that it is typical of the formation of new active species in solution (Figure 3.12 - A). With **M2**, the current is stable in the first period of the experiment, followed by a small current increase also suggesting the formation of new active species in the CPE cell system (Figure 3.13 - A). CV characterisation of these compounds shows that the complexes redox behaviour changed during the CPE assay (Figure 3.12 - C and Figure 3.13 – C), suggesting that a new electroactive species was formed (Figure A.40 and A.65).

The CPE studies of **M5** and **M6** were performed at -1.86V and -1.83V, respectively, for 3h. For **M5,** the current is stable in the first period of the experiment, followed by a small current increase suggesting the formation of new active species in the CPE cell system (Figure 3.14). CV characterisation shows that the complex redox behaviour changed during the CPE assay (panel C), suggesting that a new electroactive species was formed. **M6** has similar behaviour to **M5** (Figure 3.15).

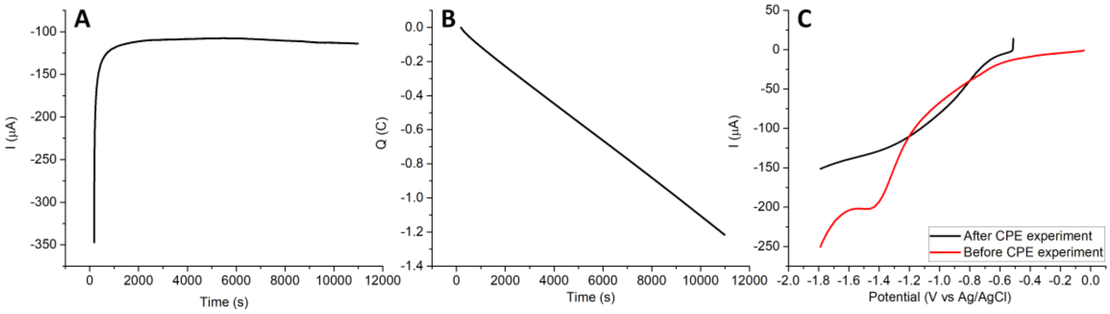

Figure 3.12: Current (A) and charge (B) behaviour during M5 CPE experiment and linear voltammogram before and after CPE assay (C). *Assays were carried out in DMF, using TBAPF$_6$ as supporting electrolyte (0.1 M) at 10 mV s^{-1}; glassy carbon was used as working electrode, platinum wire as counter and Ag/AgCl as reference electrode.*

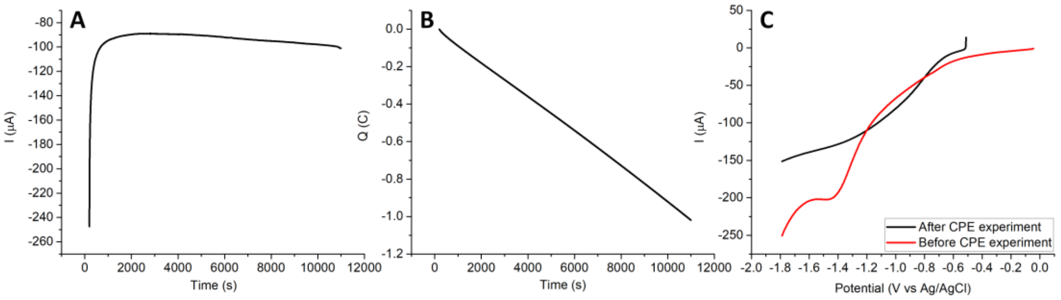

Figure 3.13: Current (A) and charge (B) behaviour during M6 CPE experiment and linear voltammogram before and after CPE assay (C). *Assays were carried out in DMF, using TBAPF$_6$ as supporting electrolyte (0.1 M) at 10 mV s^{-1}; glassy carbon was used as working electrode, platinum wire as counter and Ag/AgCl as reference electrode.*

3.1.3.c. Detection of CO$_2$ reduction products

After the CPE assays, GC-TCD was used to detect gaseous products formed during the assay (present in the apparatus headspace), namely CO and H$_2$ (as described under "Materials and Methods"). For **M1** and **M2**, neither CO nor H$_2$ was detected. Regarding **M5**, the amount of H$_2$ was found to be minimal and no CO was detected (Figure 3.14; gases expected to be eluted at approximately 3.30 and 3.50 min). For **M6**, no CO was detected and residual amounts of H$_2$ were found (Figure 3.17).

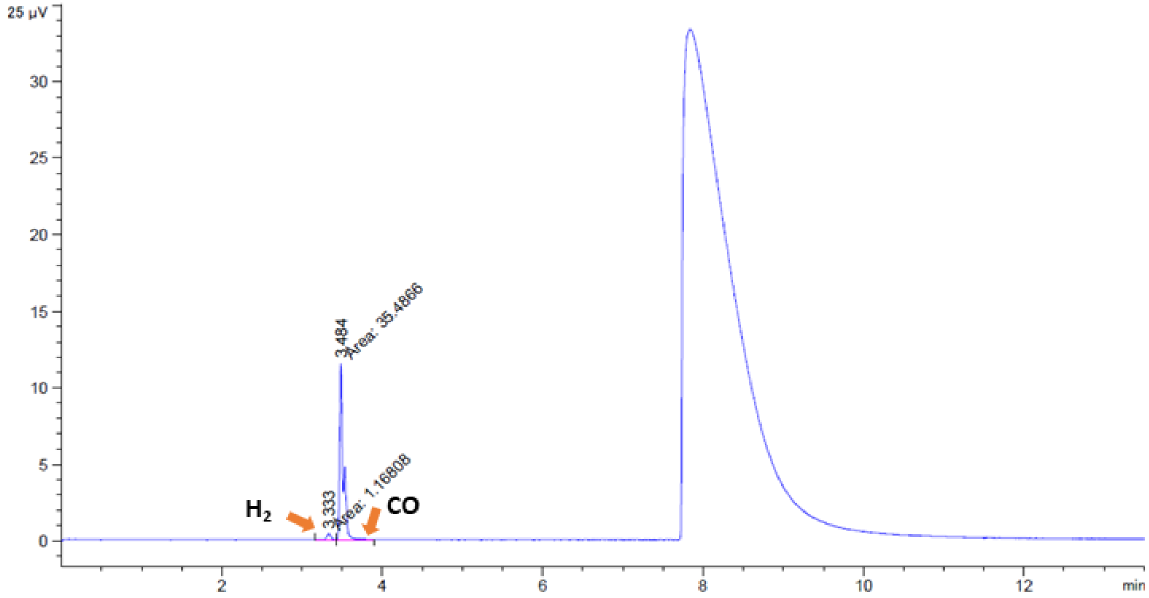

Figure 3.14: GC-TCD chromatogram of M5 reaction mixture headspace after CPE experiment. **Bold**

H_2 and CO are expected to be eluted at 3.30 and 3.50 min, respectively.

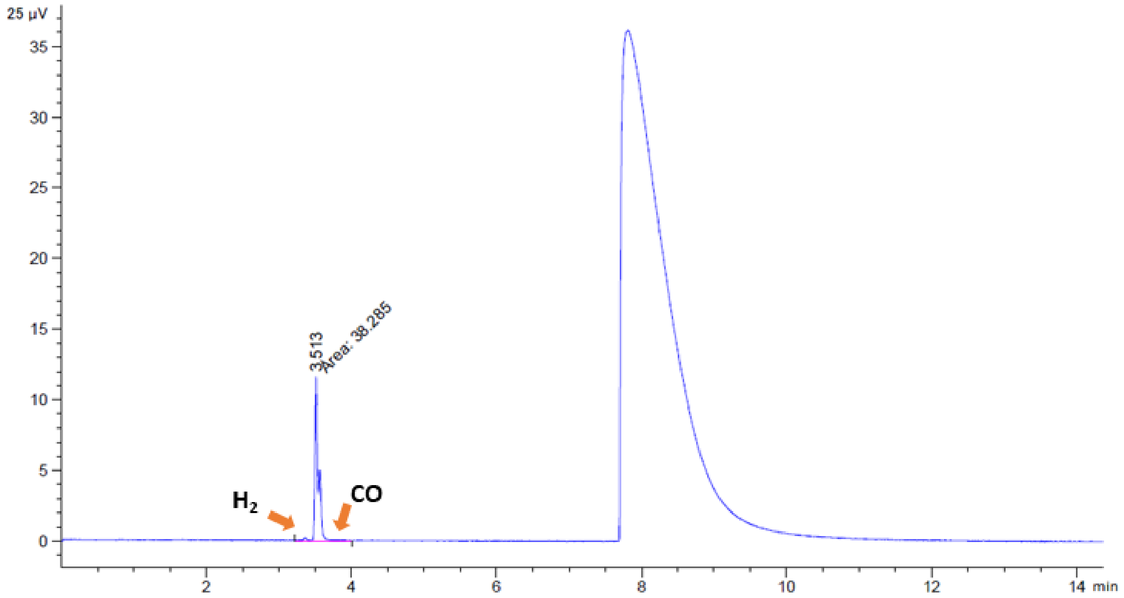

Figure 3.15: GC-TCD chromatogram of M6 reaction mixture headspace after CPE experiment.

H_2 and CO are expected to be eluted at 3.30 and 3.50 min, respectively.

To detect and quantify the formate formed in the bulk solution, a new ^{1}H NMR-based method was developed during this work. The method consists in the calculation of the concentrations of HCOOH using the relative integrals of a standard solution (maleic acid) and a multiple solvent suppression experience, as described under "Materials and Methods". In the NMR spectra of the electrolysis bulk solution (using the multiple solvent suppression experience) it is expected to observe one singlet around 8.3 ppm (respective to the proton of H-C bond of formic acid) and all the solvent signals of DMF and D_2O suppressed. The signal correspondent to the proton of formic acid at 8 ppm can change with the system used, thus a formic acid solution was added to the NMR to confirm the origin of the signal at 8.3 ppm (spiking). Using the GC-TCD and NMR data was possible to calculate the turnover numbers (TONs), turnover frequency (TOFs), selectivity and faradaic efficiency of the different compounds. The following expressions demonstrate the calculations of these parameters using the calculated number of moles of the CO_2 reduction products and H_2.

$$TON = \frac{n_{CO_2 reduction\ products}}{n_{cat}} \qquad TOF = \frac{TON}{time\ (s)}$$

$$Selectivity(\%) = \frac{n_{CO_2 reduction\ desired\ product}}{n(all\ products)} \times 100 \quad F.E(\%) = \frac{n_{CO_2 products} \times F \times n_{e^-}}{(C_e - C_{cat})}$$

$$Q = n \times F \times\ n_{e^-} \qquad n_{e^-} = number\ of\ electrons\ envolved\ in\ the\ reaction$$

$$C_e = electrolysis\ charge \qquad C_{cat} = electrolysis\ charge$$

<u>H_2 calculations</u>

$$V(\mu L) = \frac{I_{Area\ of\ chromatogram}}{37.34} \qquad V_{Headspace} = \frac{V_{(\mu L)} \times 10 \times 3200}{500}$$

$$PV = nRT \qquad n_{H_2} = \frac{V_{Headspace} \times 1 \times 10^{-6}}{298 \times 0.081}$$

$$V_{Total\ Headspace} = 3200\ \mu L \qquad V_{injected} = 500 \mu L$$

For the calculation of the number of moles of HCOOH formed during the electrolysis experiment, was calculated the theoretical concentration of the internal standard in the tube, which was then used to calculate the HCOOH concentration in the tube. These results were used for the calculation of the number of moles of HCOOH (using the following expressions).

$$[HCOO^-] = [HCOOH]$$

$$[Internal\ standart\ in\ the\ tube] = C_{IS} * v_{IS}/v_{tube}$$

$$C_{HCOOH\ in\ tube} = C_{IS\ in\ tube}\left(\frac{\frac{\tau_{HCOOH}}{H_{HCOOH}}}{\frac{\tau_{IS}}{H_{IS}}}\right)$$

$$[HCOOH\ in\ the\ aliquot] = C_{HCOOH\ in\ tube} \times v_{tube}/v_{aliquot}$$

$$[HCOOH\ in\ aliquot] = [HCOOH\ in\ electrolysis\ solution]$$

$$n_{HCOOH} = [HCOOH\ in\ aliquot] \times v_{electrolysis}$$

$$\tau = relative\ integral\ signal\ in\ NMR$$

Using this method, it was found that no formate was formed in the presence of **M1** or **M2**. Yet, **M5** and **M6** were found to produce formate (Figures 3.18, 3.19, 3.20 and 3.21). To prove that the formate formation is, in fact, due to the action of **M5** (or **M6**), the same CPE experiment and formate detection assay were performed in the absence of the metal complex and no formate was detected (Figure A.83 (NMR data) and Figure A.84 (GC data)).

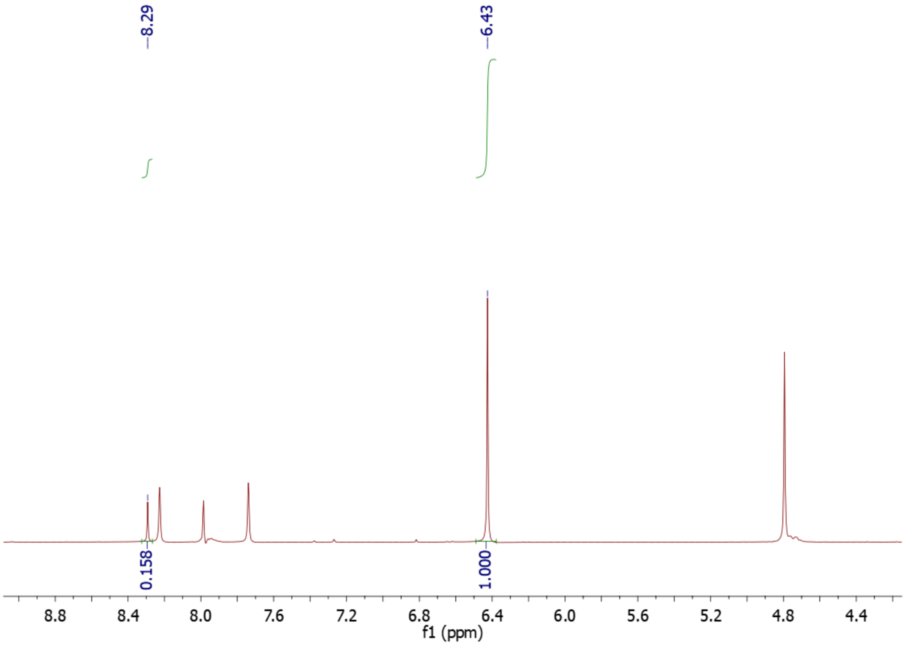

Figure 3.16: ^{1}H NMR spectrum of M5 bulk solution after CPE. *The signals at 8.3 ppm are characteristic of formic acid, and 6.43 ppm of maleic acid used internal standard.*

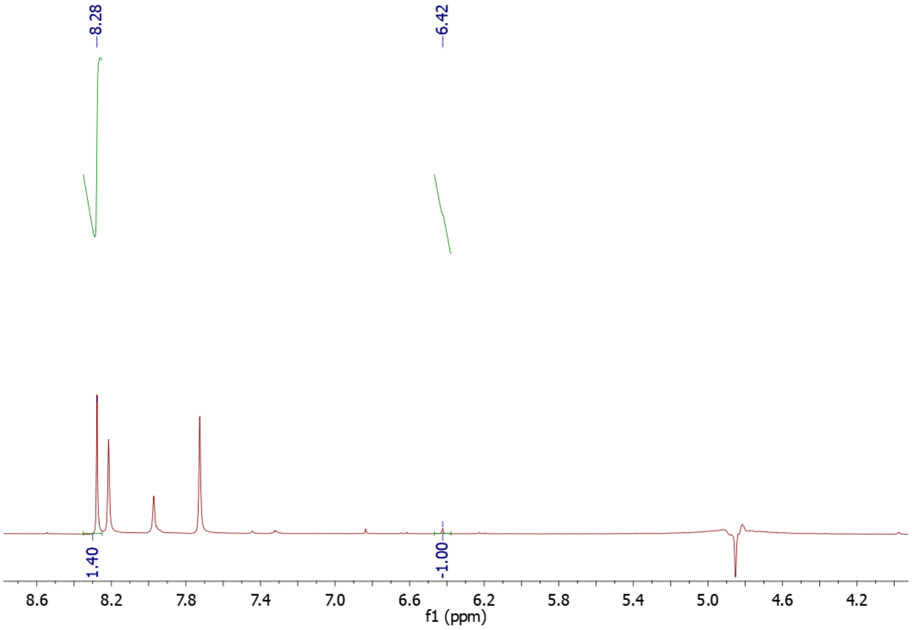

Figure 3.17: ^{1}H NMR spectrum of M5 bulk electrolysis solution after addition of a formic acid solution (spiking). *The signals at 8.28 ppm are characteristic of formic acid, and the 6.42 ppm of maleic acid.*

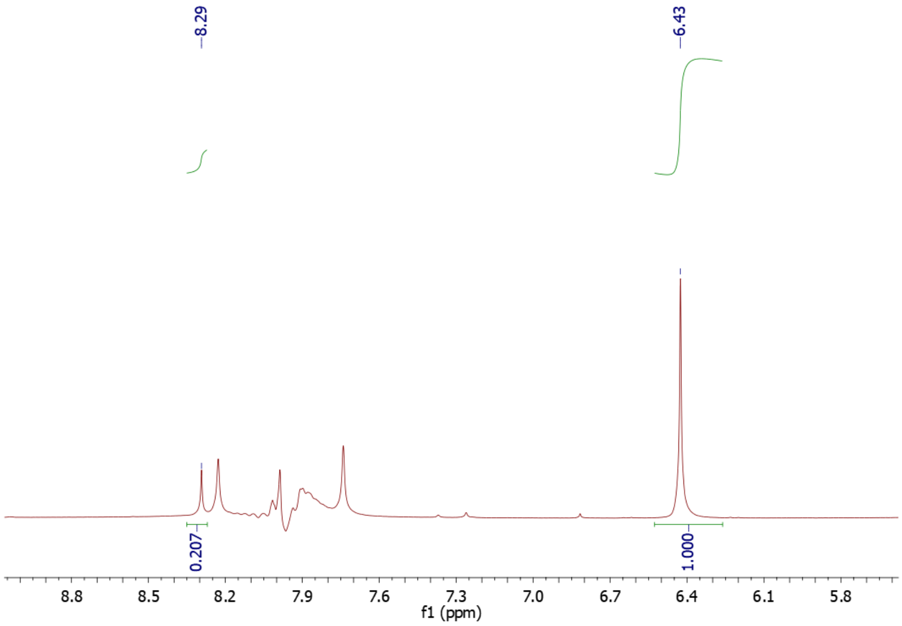

Figure 3.18: ^{1}H NMR spectrum of M6 bulk solution after CPE. *The signals at 8.29 ppm are characteristic of formic acid, and the 6.43 ppm of maleic acid used internal standard.*

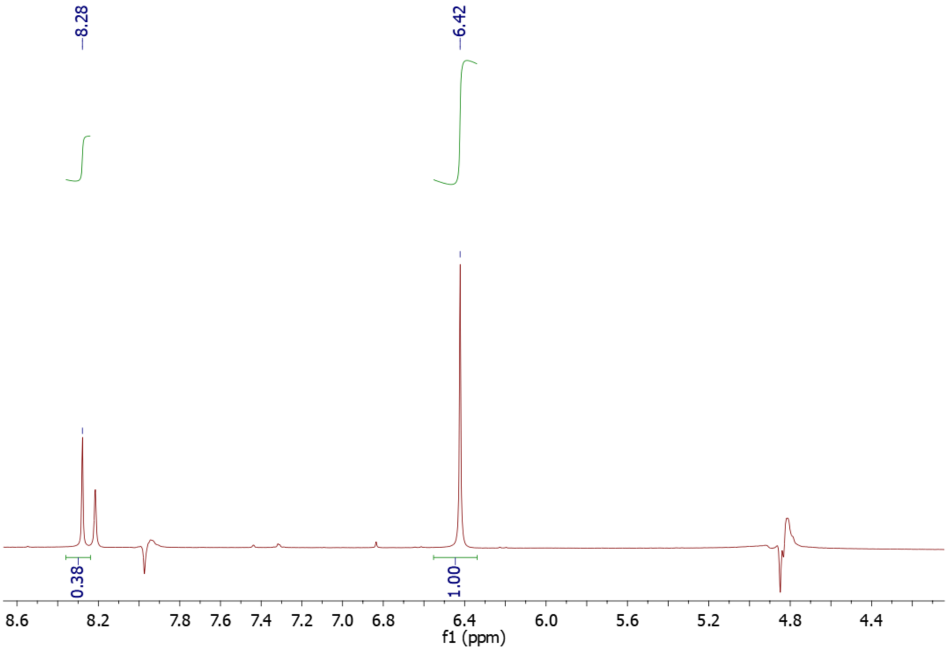

Figure 3.19: ^{1}H NMR spectrum of M6 bulk electrolysis solution after addition of a formic acid solution (spiking). *The signals at 8.28 ppm are characteristic of formic acid, and the 6.43 ppm of maleic acid.*

Using the quantification procedure described, it was found that **M5** produced formate with high selectivity (99%), a TON of 12.8 and a TOF of 1.18×10^{-3} s^{-1} (Table 3.7).

Table 3.7: Products formed by M5 during the CPE experiment.
Reaction conditions: M5 (1mM) in DMF, 850mM H_2O, using $TBAPF_6$ as supporting electrolyte (0.1 M) at $10 mVs^{-1}$; glassy carbon was used as working electrode, platinum wire as counter and SCE as reference electrode.

CAT	n_{cat} (mol)	n_{HCOOH} (mol)	n_{H2} (mol)	HCOOH selectivity (%)	TON	TOF (s^{-1})	FE (%)
M5	5.32×10^{-6}	6.79×10^{-5}	8.29×10^{-8}	99.9	12.8	1.18×10^{-3}	1829

The calculated parameters (Table 3.7) result in a non-sense faradaic efficiency value (ca two thousand percentage), showing that the approach followed is not able to correctly quantify formate.

Overall, **M1**, **M2**, **M5** and **M6** were found to be redox-active, exhibiting redox processes that were assigned to the molybdenum ion and the ligand. However, only the **M5** and **M6** complexes were found to produce formate; we were not able to detect any CO_2 reduction product in the presence of **M1** and **M2**.

3.2. DPPAS$_2$-based complexes

3.2.1. DPPAS$_2$ ligand synthesis and characterisation

DPPAS$_2$ (**L4**) was used in the synthesis of two new molybdenum complexes, **M7** and **M8**. This ligand was previously synthesised in our group, by Liu *et al.*[48], and it was characterised by ^1H NMR and bidimensional COSY to verify the ligand purity (Figures A.25 to A.26).

3.2.2. DPPAS$_2$-based complexes

3.2.2.a. Synthesis

The **M7** and **M8** complexes were synthesised under N_2 by refluxing **L4** with molybdenum hexacarbonyl overnight, using ACN as solvent (Scheme 3.12). The mono-substituted complex (**M7**) was synthesised by reacting **L4** with molybdenum hexacarbonyl in a 1:1 ratio, whereas the di-substituted complex (**M8**) was obtained by reacting the ligand with the molybdenum precursor in a 2:1 ratio. **M7** and **M8** were obtained as dark green and beige solids, with a yield of 38% and 18%, respectively.

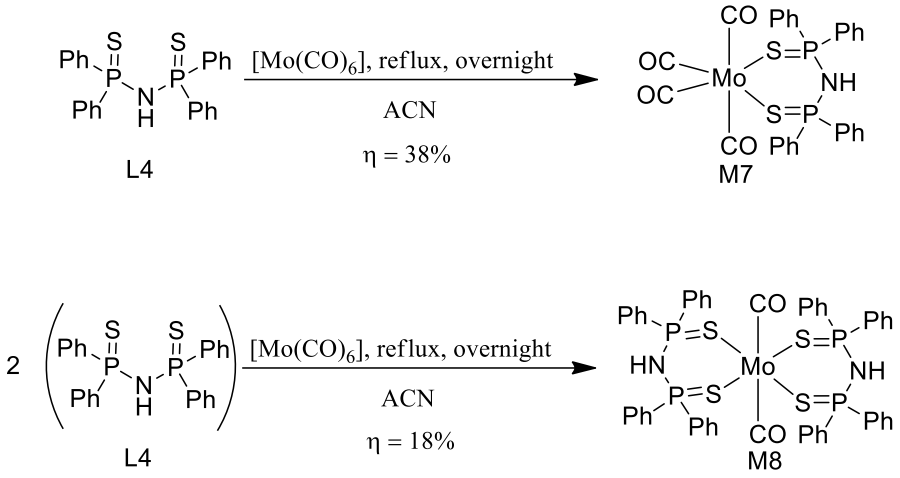

Scheme 3.12: Synthesis of M7 (top) and M8 (bottom).

3.2.2.b. Characterisation

The complexes were fully characterised by NMR, UV-vis, FTIR and CV (section 3.2.3.a.).

The ^{1}H NMR spectra of **M7** and **M8** (Figures A.50 and A.74; Table 3.8) were characterised in DMSO-d_6, and both spectra display two multiplets at ~7.91-7.85(**1**) and 7.50-7.39 (**2**/**3**) ppm (for **M7**) and at 7.98-7.84(**1**) and 7.50-7.43(**2**/**3**) ppm (for **M8**) in the aromatic region, which correspond to the aromatic protons in phenyl groups of DPPAS$_2$. The ^{13}C APT spectrum shows two signals arising from a CH/CH$_3$ (at ~131.75 (**1**) and ~128.07(**2**/**3**) ppm) (for **M7**) and (at ~131.34 (**1**) and ~128.08 (**2**/**3**) ppm) (for **M8**); the quaternary carbons and carbonyl groups were not observed in the NMR spectrum (Figures A.52 and A.76). The HSQC analysis confirmed that two signals of the ^{13}C APT spectrum correspond to the aromatic protons of the ligand (Figure A.53 and A.77). HMBC and COSY experiences helped to understand the overall structure of the molecule (Figures A.54; A.51 and A.78; A.75, respectively).

Table 3.8: NMR characterisation (chemical shifts) of M7 and M8. *Follow atoms numbering in Scheme 3.13.*

	M7		**M8**	
	^{1}H (ppm)	^{13}C APT (ppm)	^{1}H (ppm)	^{13}C APT (ppm)
1	7.91-7.85	131.35	7.89-7.84	131.34
2	7.50-7.39	128.07	7.50-7.43	128.08
3	7.50-7.39	128.07	7.50-7.43	128.08

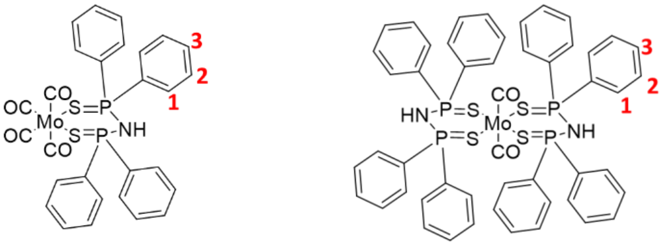

Scheme 3.13: M7 and M8 expected structures.

The complexes were also characterised by FTIR (Figure 3.22) and the most important vibrational modes are summarised in Table 3.9. For **M7** and **M8**, the following vibrational modes were identified: C=O bond (2019; 1980; 1939; 1909; 1846 cm^{-1} for **M7** and 2019; 1909; 1846 cm^{-1} for **M8**), the aromatic ring ((C-H) and (C=C)) (around 3045 and 1645cm^{-1} for both complexes), N-H (1584 and 1447 cm^{-1} respectively) and the P=S bond (647 cm^{-1} for both complexes) of the ligand.[44]

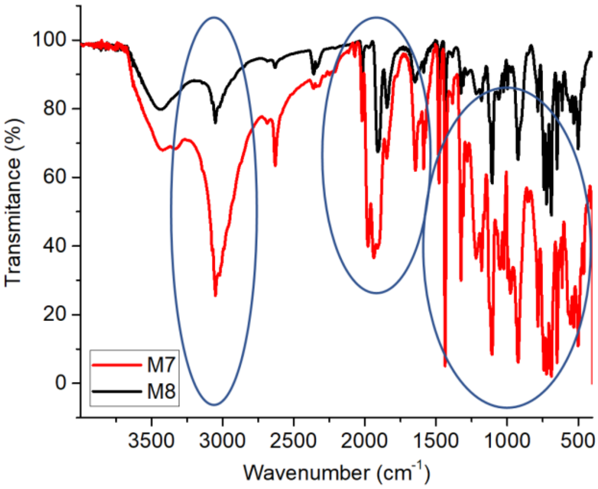

Figure 3.20: FTIR spectra of M7 and M8 complexes. *Highlighted by blue circles are the characteristic vibrational modes discussed in the text.*

Table 3.9: FTIR vibration modes for M7 to M8 complexes.

	M7 (cm^{-1})	**M8 (cm^{-1})**
C=O	~1846;~1909;~1939;~1980; ~2019	~1846;~1909; ~2019
C-H	~3052	~3052
C=C	~1645	~1647
N-H	~1584	~1447
P=S	~649	~647

UV-vis spectra of **M7** and **M8** (Figure 3.23) display one band which can be indicative of π-π^* transitions of the ligand (350-400nm).

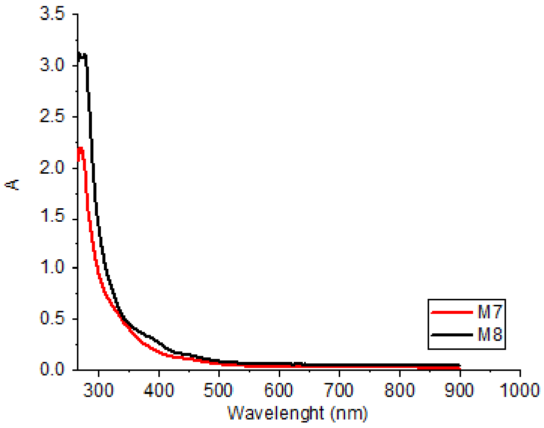

Figure 3.21: UV-vis spectra of M7 and M8 complexes.

Overall, the synthesis of **M7** and **M8** give rise to the expected structures that are supported by NMR, FTIR, UV-vis and EA results (in the case of **M7**, for **M8** elemental analysis was not performed since the compound was yielded in a small amount).

3.2.3. Electrochemical studies

3.2.3.a. Cyclic voltammetry studies

The complexes **M7** and **M8** were studied by CV, under N_2 and CO_2 atmosphere, to characterise their redox behaviour and to investigate their potential as catalysts of CO_2 electroreduction. All values indicated herein are vs Ag/AgCl (0.278V vs NHE). For **M7**, the CV under N_2 revealed two reduction processes around -0.40V and -0.70V, that can be attributed to the ligand redox behaviour, and one another process at -1.13V which can be indicative of a new reduced specie of the complex (Figure 3.22 – A and Figure A.55).[12,36,45,46] The studies under CO_2 atmosphere reveal that **M7** demonstrate a current increase which is characteristic of CO_2 conversion catalysts (Figure 3.24 - B). As previously observed, the addition of water is followed by a current increase (Figure 3.24 - C). For **M8**, the CV under N_2 showed one reduction process around -1.39V, connected to a new reduced specie of the complex (Figure 3.23 – A and Figure A.81).[12,36,45,46] The studies under CO_2 atmosphere showed a current increase suggesting that this compound can be a potential catalyst for CO_2 conversion (Figure 3.25 - B and C). For both complexes the water concentration chosen for CPE experiments was 850 mM since at higher concentrations the current increase in an abrupt form, suggesting proton reduction to H_2.

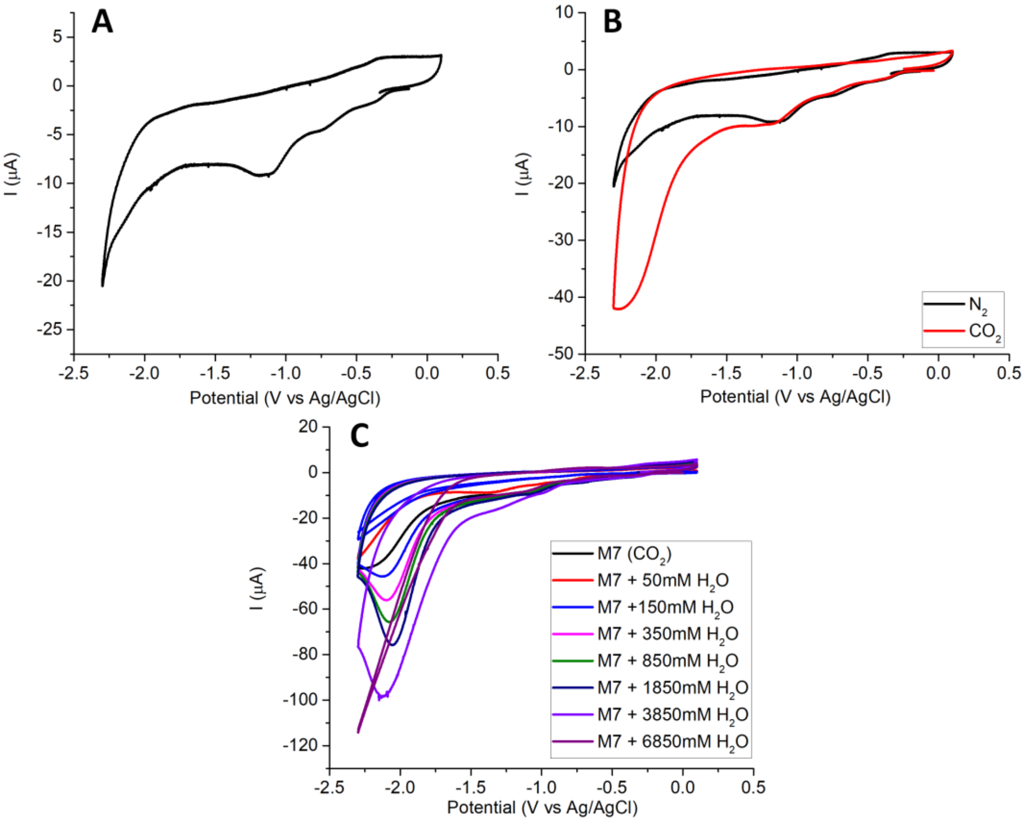

Figure 3.22: CV studies of M7 in DMF (1mM) N_2 or CO_2 saturated solutions. *$TBAPF_6$ was used as supporting electrolyte (0.1 M), at 0.1 mV s^{-1}; glassy carbon (3 mm diameter) was used as working, platinum wire as counter and Ag/AgCl as reference electrodes.* ***(A)*** *CV reduction in N_2 atmosphere.* ***(B)*** *CV overlay in N_2 and CO_2 atmosphere.* ***(C)*** *CV overlay in CO_2 atmosphere with different water concentrations.*

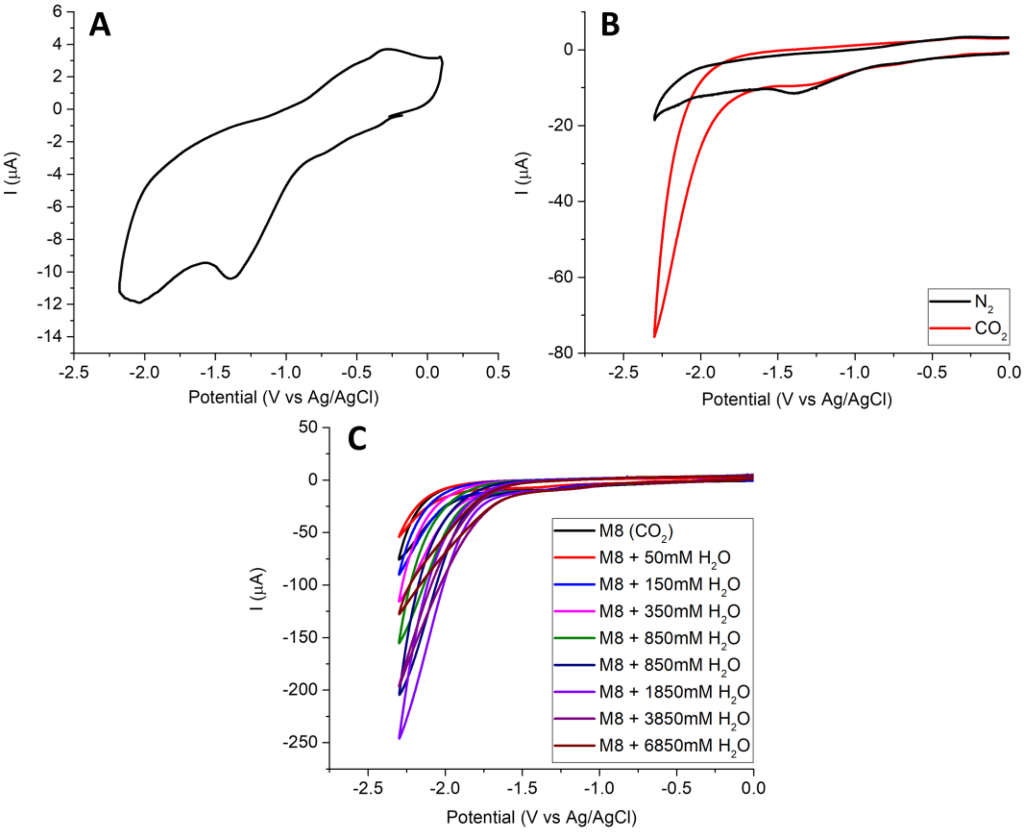

Figure 3.23: CV studies of M8 in DMF (1mM) N_2 or CO_2 saturated solutions. *$TBAPF_6$ was used as supporting electrolyte (0.1 M), at 0.1 mV s^{-1}; glassy carbon (3 mm diameter) was used as working, platinum wire as counter and Ag/AgCl as reference electrodes.* ***(A)*** *CV reduction in N_2 atmosphere.* ***(B)*** *CV overlay in N_2 and CO_2 atmosphere.* ***(C)*** *CV overlay in CO_2 atmosphere with different water concentrations.*

3.2.3.b. Controlled potential electrolysis studies and detection of CO_2 reduction products

The assays were conducted as described in section 3.1.3.b. The CPE studies of **M7** and **M8** were carried out at -1.89V, for 3h. For both compounds, it is possible to observe a current decrease followed by a current stabilisation, suggesting the deactivation of catalyst (Figure 3.26 and 3.27). The CV characterisation, before and after the CPE assay, also corroborates that suggestion (panels C).

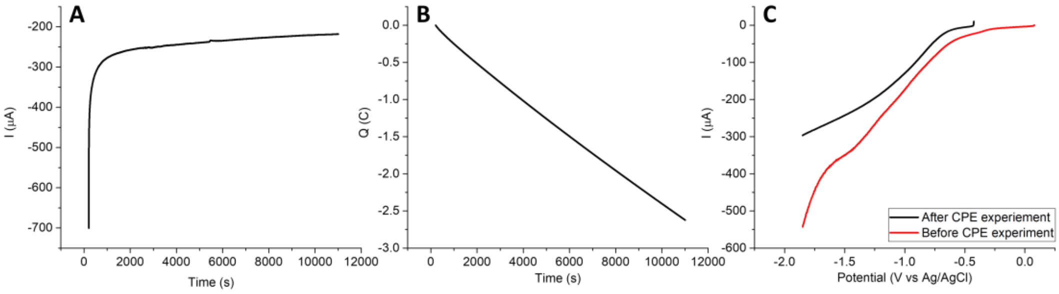

Figure 3.24: Current (A) and charge (B) behaviour during M7 CPE experiment and linear voltammogram before and after CPE assay (C). *Assays were carried out in DMF, using TBAPF*$_6$ *as supporting electrolyte (0.1 M) at 10 mV s*$^{-1}$*; glassy carbon was used as working electrode, platinum wire as counter and Ag/AgCl as reference electrode.*

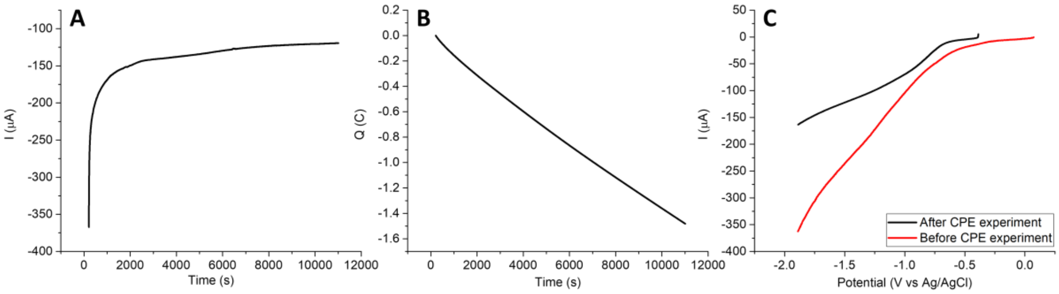

Figure 3.25: Current (A) and charge (B) behaviour during M8 CPE experiment and linear voltammogram before and after CPE assay (C). *Assays were carried out in DMF, using TBAPF*$_6$ *as supporting electrolyte (0.1 M) at 10 mV s*$^{-1}$*; glassy carbon was used as working electrode, platinum wire as counter and Ag/AgCl as reference electrode.*

The **M7** and **M8** bulk solutions and headspaces after CPE experiment were analysed for the presence of CO_2 reduction products, as well as, H_2, by the same method used for **M5** and **M6**. Regarding **M7**, CO was not detected, and residuals amounts of H_2 were observed (Figure 3.28; gases expected to be eluted at 3.50 and 3.30 min). Through NMR experiments was possible to detect formate (Figure 3.29 and 3.30). For **M8**, no CO was detected and the amount of H_2 was found to be minimal (Figure 3.31) also no formate production was detected in the NMR assay. **M8** did not demonstrates formate production since was not possible to detect this product through the NMR experiences (Figure A.82).

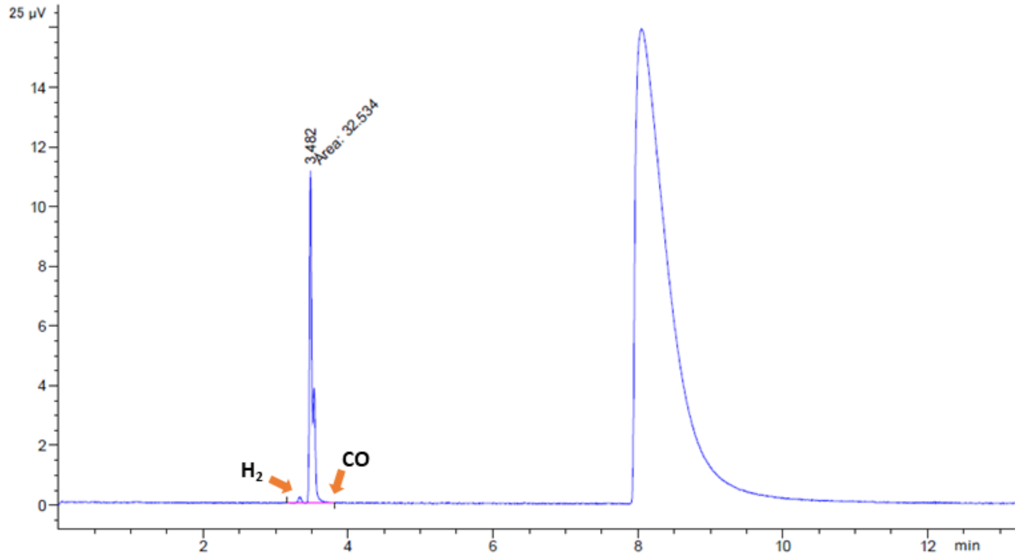

Figure 3.26: GC-TCD chromatogram of M7 reaction mixture headspace after CPE experiment. *H_2 and CO are expected to be eluted at 3.30 and 3.50 min, respectively.*

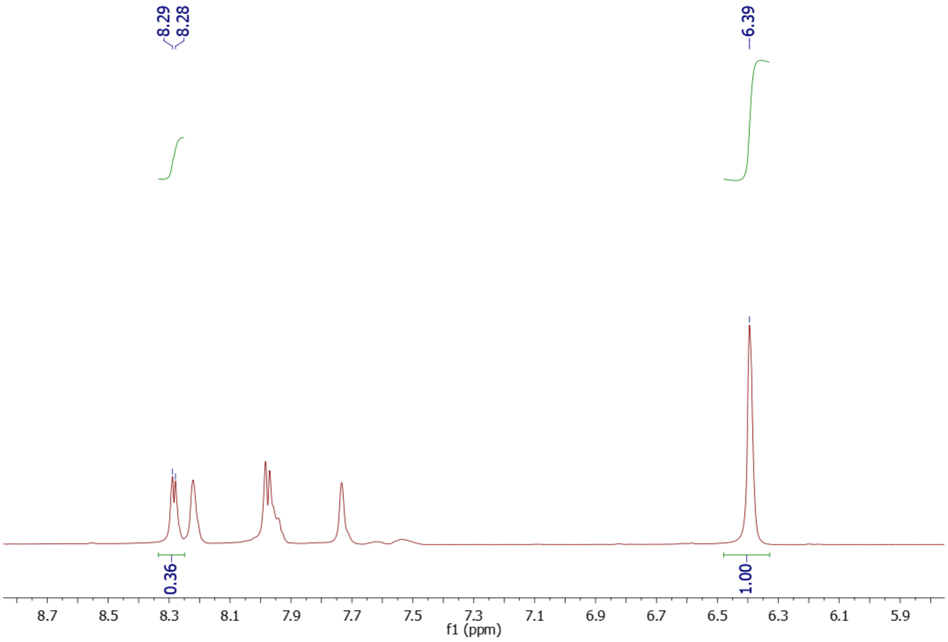

Figure 3.27: ^{1}H NMR spectrum of M7 bulk solution after CPE. *The signals at 8.29 and 8.28 ppm are characteristic of formic acid and formate, and the 6.39ppm of maleic acid used internal standard.*

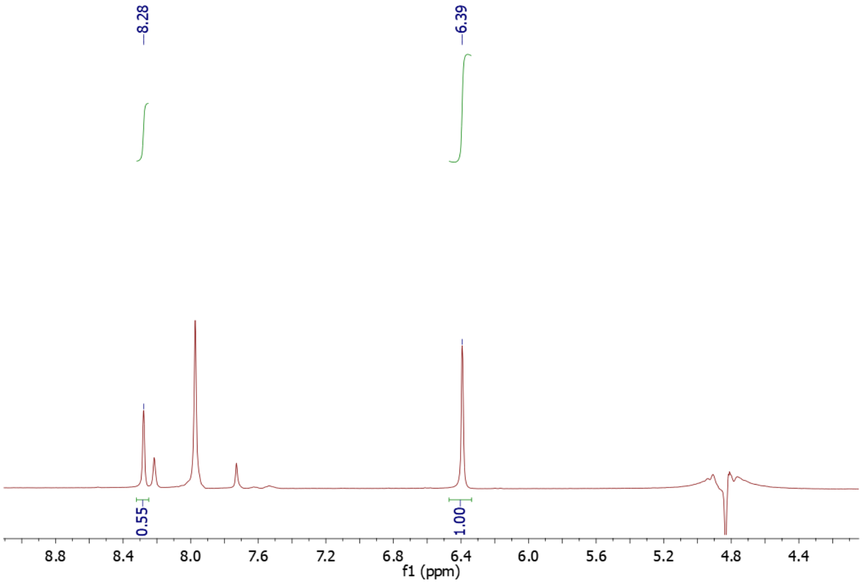

Figure 3.28: ^1H NMR spectrum of M7 bulk electrolysis solution after addition of a formic acid solution (spiking). *The signals at 8.28 ppm are characteristic of formic acid, and the 6.39 of maleic acid.*

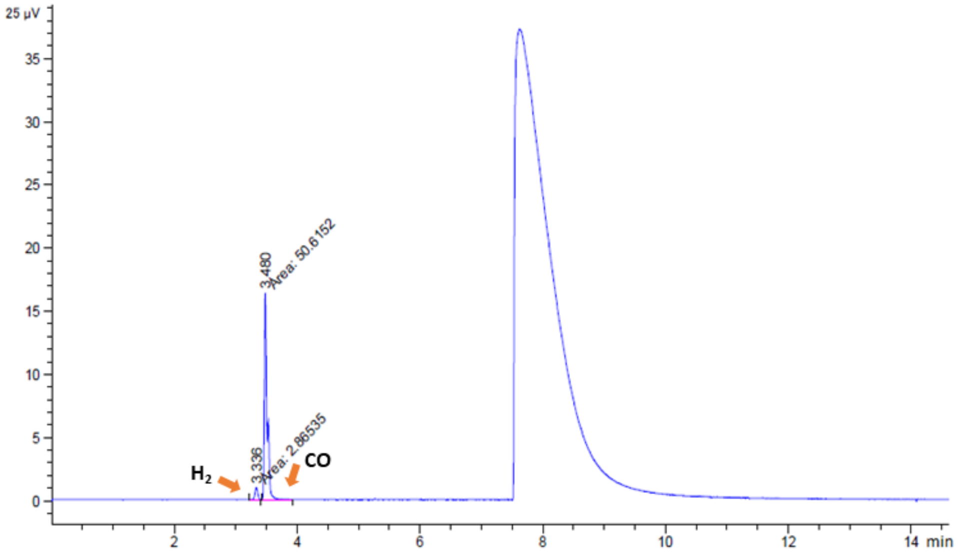

Figure 3.29: GC-TCD chromatogram of M8 reaction mixture headspace after CPE experiment. *H_2 and CO are expected to be eluted at 3.30 and 3.50 min, respectively.*

Both compounds were found to be redox-active, exhibiting redox processes that were assigned to the molybdenum ion and the ligand. For **M8**, were not detected products for CO_2 reduction as expected by the electrochemical studies did in CO_2 atmosphere with different water concentrations. Meanwhile, the compound **M7** produces formate which was detected by the NMR method described above. All the complexes which demonstrate activity should be tested under different conditions to understand if it is possible an improvement of yield for CO_2 conversion for these complexes.

3.3. Salen-type complex

3.3.1. Salen-type complex

3.3.1.a. Synthesis

M9 was synthesised under N_2 by refluxing overnight **L5** with molybdenum hexacarbonyl using ACN as solvent (Scheme 3.14). A purple precipitate was obtained with 35% yield.

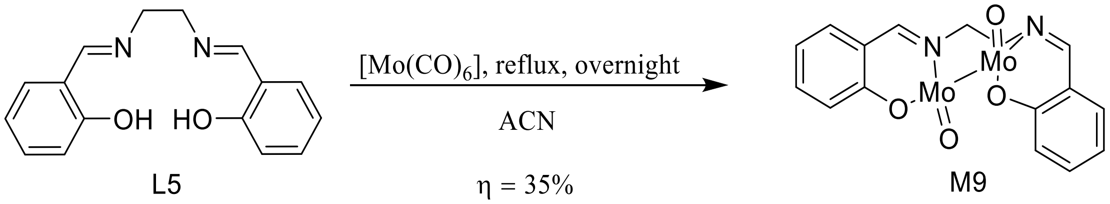

Scheme 3.14: Synthesis of M9.

3.3.1.b. Characterisation

M9 was characterised by NMR, FTIR, UV-vis, EA (in "Materials and Methods") and CV (section 3.3.2.a.)(individual spectra results in Figures A.85 to A.89). The ^1H and ^{13}C NMR spectra, as well as, NMR bidimensional results, demonstrate that **M9** is decomposed in solution, by discoordination of the ligand (the ligand discoordination is clearly observed in Figure A.90, where the ^1H NMR spectra of **L5** and **M9** are superimposed and the ligand signals in the aromatic region are visible).

The complex was also characterised by FTIR (Figure 3.32) and identified the vibrational modes[44] corresponding to the M=O bond (932 and 906 cm^{-1}), to the aromatic ring ((C-H) and (C=C)) (3060 and 1446 cm^{-1} respectively), C=N (1613 cm^{-1}) and to the C-O bond (1264 cm^{-1}) of the ligand. The most important vibrational modes are summarised in Table 3.10. The UV-vis spectra of **M9** and **L5** (1×10^{-4} M in DCM solution) further confirmed the complex decomposition in solution (observe the overlay of the ligand and complex bands around 275-350 nm in Figure 3.33). **M9** UV-vis spectrum shows two bands between 400-600nm, which can correspond to the metal charge transfer bands.

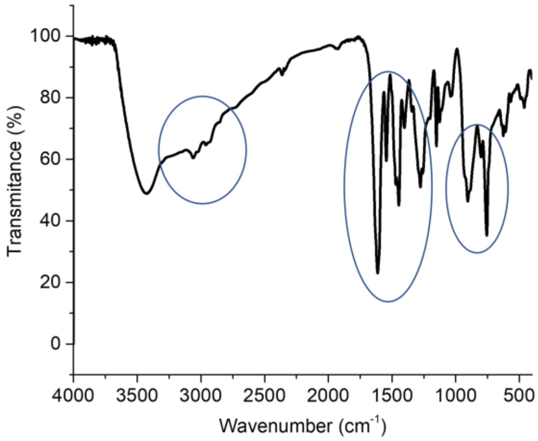

Figure 3.30: FTIR spectrum of M9 complex. *Highlighted by blue circles are the characteristic vibrational modes discussed in the text.*

Table 3.10: FTIR vibration modes for M9 complex.

	M9 (cm^{-1})
Mo=O	~932; ~906
C-H	~3060
C=C	~1446
C=N	~1613
C-O	~1264

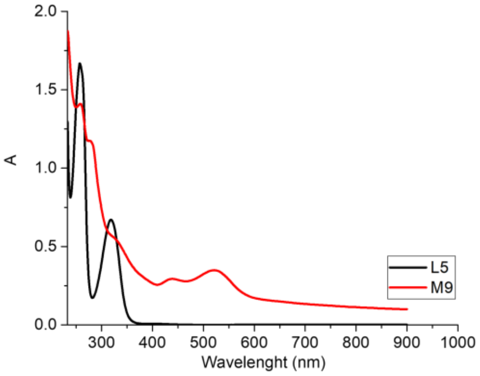

Figure 3.31: UV-vis spectra of L5 and M9 complex.

Overall, the synthesis of **M9** gives rise to an unexpected structure (binuclear complex) that is supported by FTIR and EA results (NMR and UV-vis results were inconclusive since the structure decomposes in solution with air presence). These characterisation techniques also demonstrate that the compound decomposes at air presence.

3.3.2. Electrochemical studies

3.3.2.a. Cyclic voltammetry studies

M9 was studied by CV, under N_2 and CO_2 atmosphere, as previously described for the other complexes. All values indicated herein are vs Ag/AgCl (0.278V vs NHE).

The CV under N_2 revealed three reduction processes at -0.37V, -1.16V and -1.46V that can be attributed to the redox processes of Mo^{4+}/Mo^{3+}, Mo^{3+}/Mo^{2+} and Mo^{2+}/Mo^{+1} (Figure 3.32 - A).[45] **M9** has also a reduction process at -1.86V, which matches to the ligand electrochemical behaviour (Figure A.91). The CV experiments under CO_2 demonstrate a current increase by water addition, which is typical of CO_2 conversion catalysts (Figure 3.34 - B and C). For this compound, the water concentration chosen for CPE experiments was 850 mM.

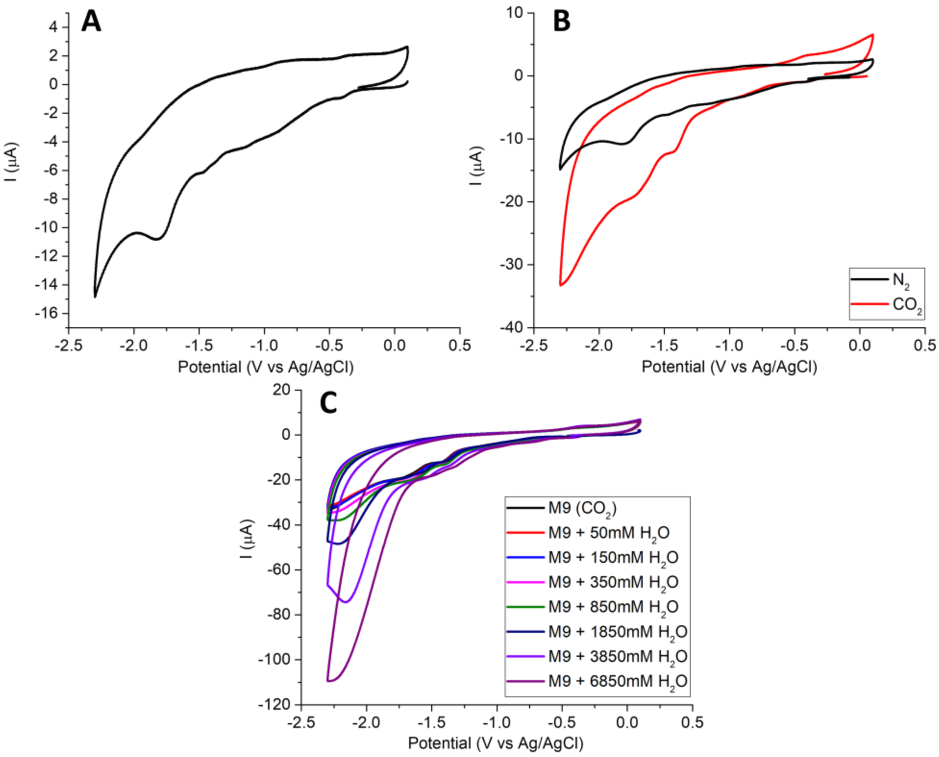

Figure 3.32: CV studies of M9 in DMF (1mM) N_2 or CO_2 saturated solutions. *$TBAPF_6$ was used as supporting electrolyte (0.1 M), at 0.1 mV s^{-1}; glassy carbon (3 mm diameter) was used as working, platinum wire as counter and Ag/AgCl as reference electrodes.* ***(A)*** *CV reduction in N_2 atmosphere.* ***(B)*** *CV overlay in N_2 and CO_2 atmosphere.* ***(C)*** *CV overlay in CO_2 atmosphere with different water concentrations.*

3.3.2.b. Controlled potential electrolysis studies and detection of CO_2 reduction products

The assays were conducted as described for the other complexes, using 850 mM of water as a proton source and performing the CPE assays at -1.86V for 3h. For **M9**, it is possible to observe a current stabilisation followed by a small current increase, suggesting the formation of new active species (Figure 3.35). CV analysis after CPE, suggests the formation of new active species in bulk solution (panel C).

Analysis of bulk solution and gaseous headspace after CPE experiment showed that formate is formed, as well as, a residual amount of H_2 (Figures 3.36 to 3.38).

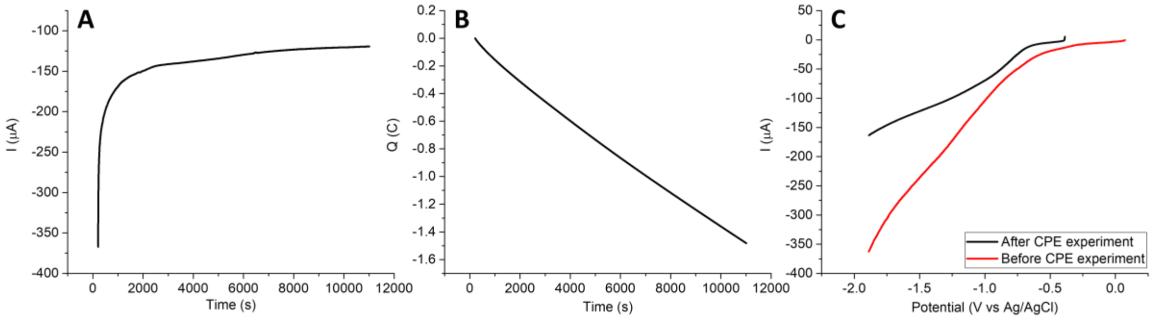

Figure 3.33: Current (A) and charge (B) behaviour during M9 CPE experiment and linear voltammogram before and after CPE assay (C). *Assays were carried out in DMF, using $TBAPF_6$ as supporting electrolyte (0.1 M) at 10 mV s^{-1}; glassy carbon was used as working electrode, platinum wire as counter and Ag/AgCl as reference electrode.*

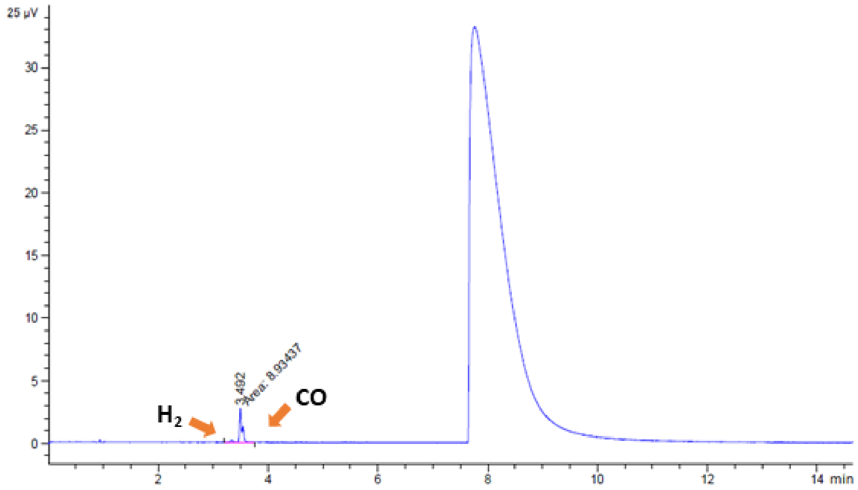

Figure 3.34: GC-TCD chromatogram of M9 reaction mixture headspace after CPE experiment. *H_2 and CO are expected to be eluted at 3.30 and 3.50 min, respectively.*

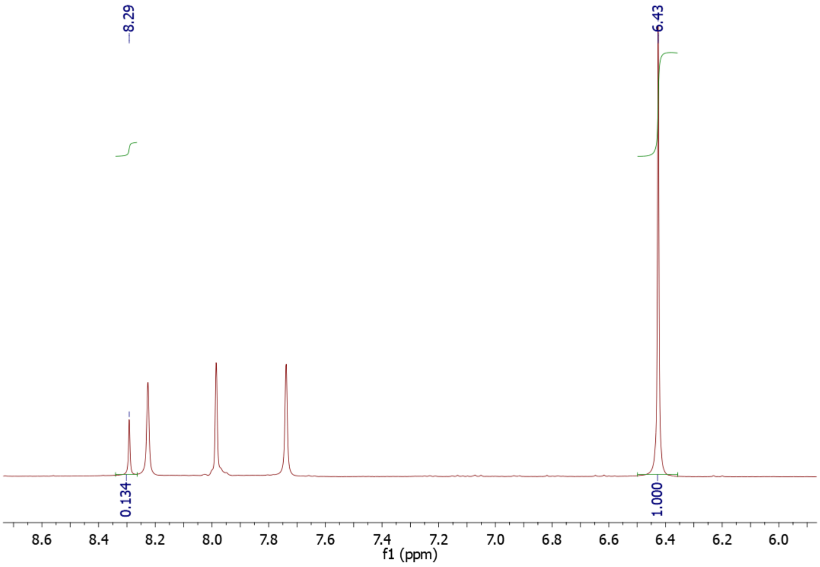

Figure 3.35: ^{1}H NMR spectrum of M9 bulk solution after CPE. *The signals at 8.29 ppm are characteristic of formic acid, and the 6.43 ppm of maleic acid used internal standard.*

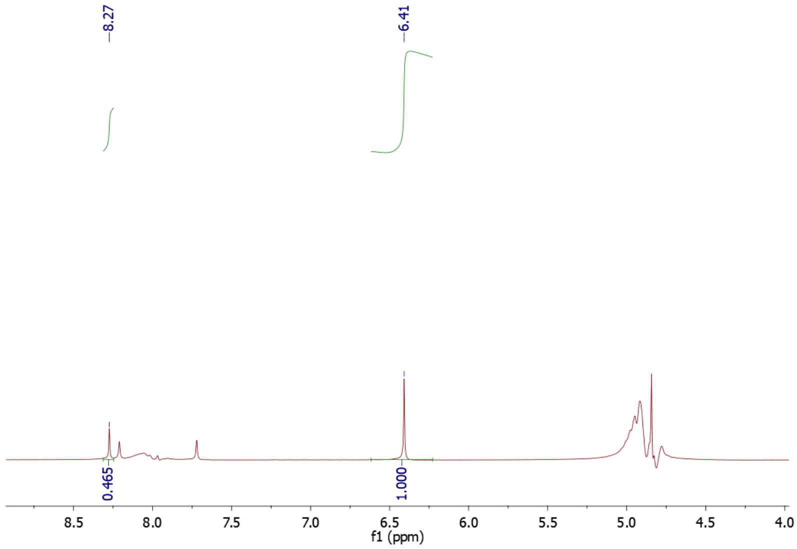

Figure 3.36: ^{1}H NMR spectrum of M9 bulk electrolysis solution after addition of a formic acid solution (spiking). *The signals at 8.27 ppm are characteristic of formic acid, and the 6.41 ppm of maleic acid.*

In general, this complex shows an interesting redox behaviour, demonstrating redox processes which can be characteristic of molybdenum ion and from the ligand. The CV study reveals that this complex can be a promising catalyst for CO_2 electroreduction with H_2O (850mM) as a proton source. **M9** was able to reduce CO_2 to formate (through a CPE experiment and detected by NMR) with no CO production and with residual amounts of H_2 detected by GC-TCD.

3.4. Pincer-type complex

3.4.1. Pincer-type ligand synthesis and characterisation

2,6-Bis(mercaptomehyl)pyridine (**L6**) was used to synthesise complex **M10**. The synthesis of this ligand involved two reactions, with the objective of functionalise 2,6-bis(hydroxymethyl)pyridine into **L6**, as previously described by Reiser and co-workers[43] (Scheme 3.15). The first step consists on a substitution reaction between 2,6-bis(hydroxymethyl)pyridine and thionyl chloride generating 2,6-bis(chloromethyl)pyridine as an intermediary compound (**I5**). The second step of **L6** synthesis is based on a substitution reaction between **I5** and thiourea functionalising the Cl groups into -SH groups.

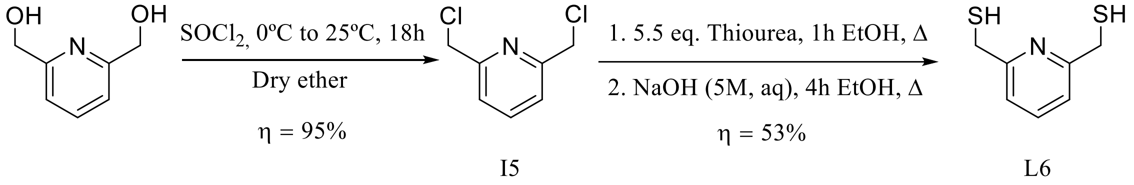

Scheme 3.15: Synthesis of L6.

L6 was obtained as a white precipitate, with a 53% yield. **L6** was characterised by ^{1}H NMR and bidimensional COSY to verify the ligand purity (Figures A.28 to A.29).

3.4.2. Pincer-type complex

3.4.2.a. Synthesis

M10 was synthesised in a similar way to the one described for the other complexes (Scheme 3.16). A black precipitate was obtained in 21% yield. Thiourea is present as a contaminant in the compound **L6** and reacts with molybdenum to form **M10**.

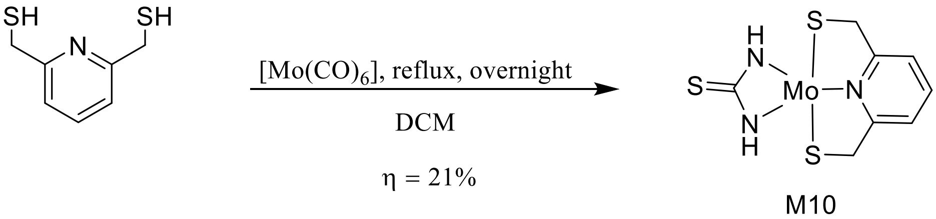

Scheme 3.16: Synthesis of M10.

3.4.2.b. Characterisation

M10 was fully characterised by FTIR, UV-vis, EA (in "Materials and Methods") and CV (section 3.4.3.a.). The FTIR spectrum displays the vibrational modes corresponding to the pyridine ring ((C=C) and C=N) (1502 and 1607 cm^{-1}, respectively), to the amine bond (N-H) (3408 cm^{-1}) and to the methylene groups (C-H) (1383 cm^{-1}) bond of the ligand[44] (Figure 3.39). The most important vibrational modes are summarised in Table 3.11. The UV-vis spectrum of **M10** (5×10^{-6} M in DMSO solution) does not display any bands, not allowing any conclusion to be made (Figure 3.40).

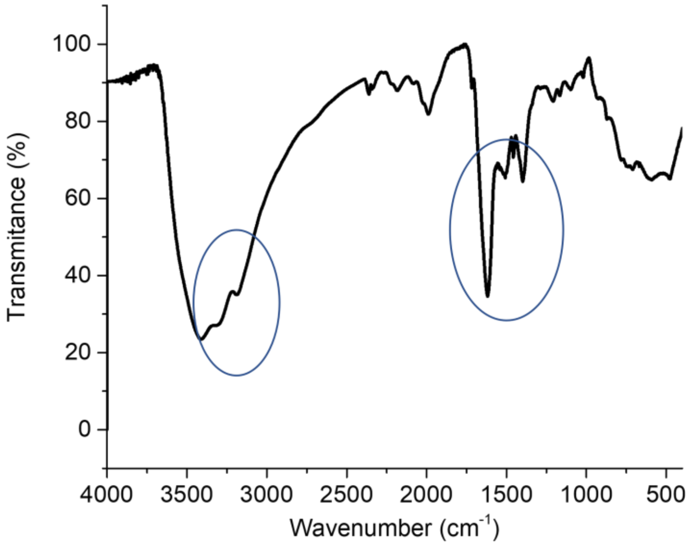

Figure 3.37: FTIR spectrum of M10 complex. *Highlighted by blue circles are the characteristic vibrational modes discussed in the text.*

Table 3.11: FTIR vibration modes for M10 complex.

	M10 (cm^{-1})
C=C	~1502
C=N	~1627
N-H	~3408
C-H (methylene)	~1383

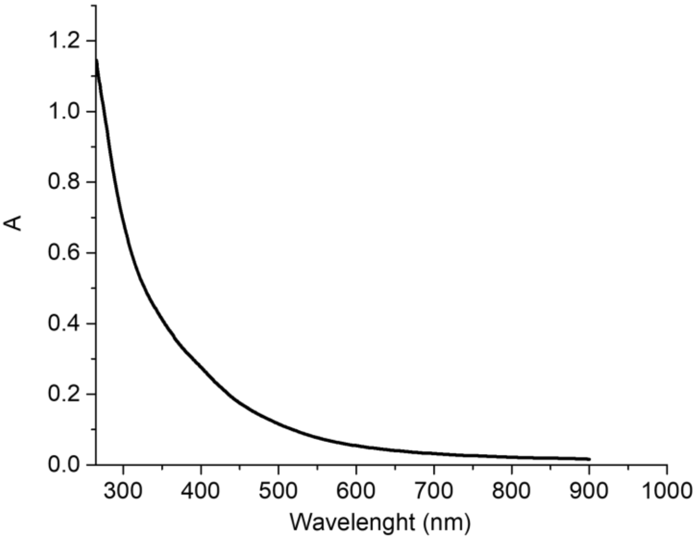

Figure 3.38: UV-vis spectrum of M10 complex.

3.4.3. Electrochemical studies

3.4.3.a. Cyclic voltammetry studies

M10 was studied by CV, under N_2 and CO_2 atmosphere, as previously described for the other complexes. All values indicated herein are vs Ag/AgCl (0.278V vs NHE).

The CV under N_2 revealed three reduction processes observed around -0.37V, -1.16V and -1.46V that can correspond to the redox pairs Mo^{4+}/Mo^{3+}, Mo^{3+}/Mo^{2+} and to the ligand redox processes (Figure 3.39 – A and Figure A.92).[36] As for previous complexes, the assay was also carried out under CO_2 atmosphere (Figure 3.41 - B) and in the presence of increasing concentrations of water (Figure 3.41 - C). For this compound, the water concentration chosen for the CPE experiments was 1850 mM.

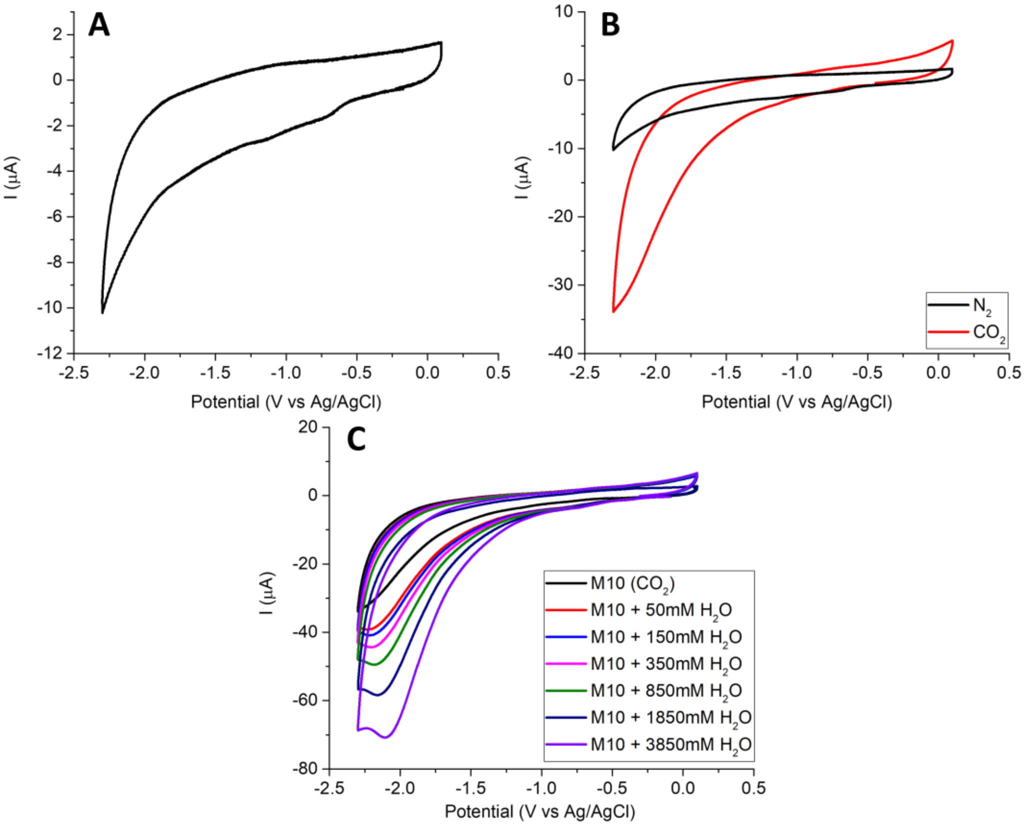

Figure 3.39: CV studies of M10 in DMF (1mM) N_2 or CO_2 saturated solutions. *$TBAPF_6$ was used as supporting electrolyte (0.1 M), at 0.1 mV s^{-1}; glassy carbon (3 mm diameter) was used as working, platinum wire as counter and Ag/AgCl as reference electrodes.* ***(A)*** *CV reduction in N_2 atmosphere.* ***(B)*** *CV overlay in N_2 and CO_2 atmosphere.* ***(C)*** *CV overlay in CO_2 atmosphere with different water concentrations.*

3.4.3.b. Controlled potential electrolysis studies and detection of CO_2 reduction products

The assays were conducted as described for the other complexes, but using 1850 mM of water as a proton source and performing the CPE assay at -1.6V for 3h. For **M10**, it is possible to observe a current stabilisation, followed by a current increase, suggesting the formation of new active species (Figure 3.42). CV analysis after electrolysis demonstrates a new reduction peak (panel C), supporting the formation of new active species in bulk solution or the catalyst decomposition through the air intake on the cell.

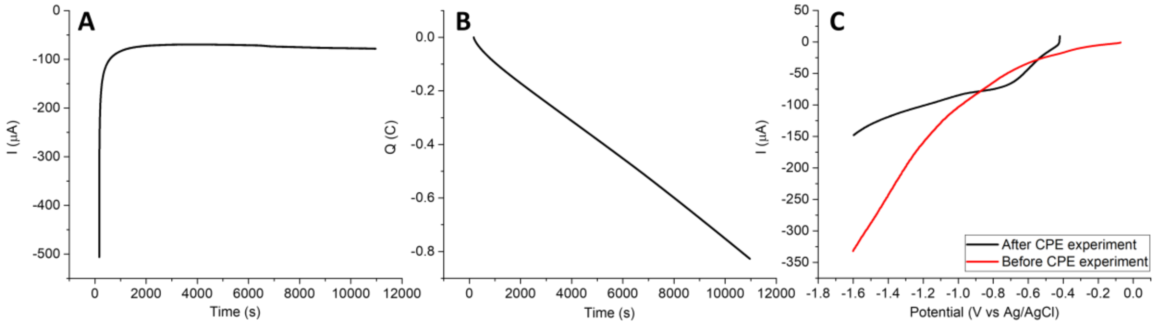

Figure 3.40: Current (A) and charge (B) behaviour during M10 CPE experiment and linear voltammogram before and after CPE assay (C). *Assays were carried out in DMF, using TBAPF*$_6$ *as supporting electrolyte (0.1 M) at 10 mV s*$^{-1}$*; glassy carbon was used as working electrode, platinum wire as counter and Ag/AgCl as reference electrode.*

The **M10** bulk solution and headspace after CPE experiment were analysed for the presence of CO_2 reduction products, as well as, H_2. Under the conditions assayed, **M10** did not show CO_2 conversion and only residual amounts of H_2 were detected (Figure 3.43).

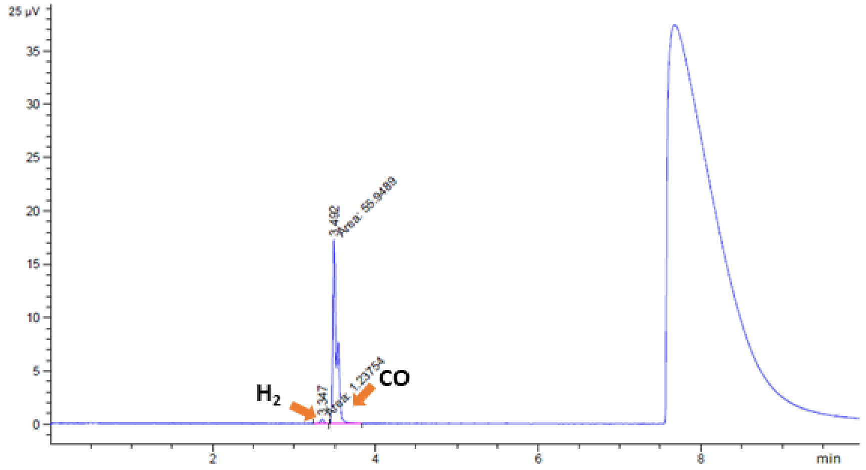

Figure 3.41: GC-TCD chromatogram of M10 reaction mixture headspace after CPE experiment. *H_2 and CO are expected to be eluted at 3.30 and 3.50 min, respectively.*

M10 was found to be redox-active, exhibiting redox processes that were assigned to the molybdenum ion and the ligand. This complex showed to be promising as catalysts for CO_2 reduction in the presence of water (1850 mM), as a proton source. Although, **M10** did not show CO or formate production, just produces minimal amounts of H_2, indicating that with these conditions the complex did reduced CO_2.

4. Conclusions and Perspectives

4. Conclusions and Perspectives

In this work, aiming to mimic the molybdenum-containing FDH active site, several molybdenum complexes were synthesised, characterised and studied for their ability to catalyse the CO_2 reduction electrochemically.

The ligands chosen were inspired in the dithiolene moiety of the pyranopterin cofactor (dithiolene and derivative compounds) and also in different compounds previously described in the literature (pincer-type and salen-type (no sulfur coordination) units). All the complexes synthesised were sensible to the air and "Schlenck techniques" had to be used to handle the complexes, which introduced an additional level of difficulty in the experimental work. Despite the experimental challenges, the ligands synthesised, **L1**, **L2**, **L3** and **L6**, were obtained in good yields and with high purity (86%, 56%, 84% and 53%, respectively). The complexes were divided among four different families, the dithiolene and derivative complexes (**M1-M6**), the $DPPAS_2$-based complexes (**M7** and **M8**), the salen-type complex (**M9**) and a pincer-type complex (**M10**). In general, all the complexes were synthesised with very low yields, however, most were produced in sufficient quantity to perform all the tests required for CO_2 electroreduction and respective characterisation. The only exceptions were the compounds **M3** and **M4** that were not tested in the CO_2 electroreduction, due to their high level of impurities and the very low yield.

M1, **M2**, **M8** and **M10** did not produce CO or formate during CO_2 electroreduction, under the conditions used herein. New experimental conditions (catalyst and water concentrations and applied potentials) will be studied in the future to confirm (or not) the CO_2 catalytic features of these complexes. On the contrary, **M5**, **M6**, **M7** and **M9** catalysed the reduction of CO_2 to formate, in DMF, in the presence of 850 mM of H_2O, with high selectivity. Unfortunately, the correct quantification of the formate produced was not possible. The NMR-based method developed by us during this work for formate quantification was not successful. The method will be improved in the future, as well as, other methods (including HPLC) will be developed and implemented. Also, the synthesis and crystallisation methods will be further improved to obtain high yields of pure catalysts for CO_2 reduction. To understand the mechanism of CO_2 reduction of these catalysts (**M5**, **M6**, **M7** and **M9**) spectro-electrochemical techniques will be used.

5. References

5. References

(1) Anderson, T. R.; Hawkins, E.; Jones, P. D. CO2, the Greenhouse Effect and Global Warming: From the Pioneering Work of Arrhenius and Callendar to Today's Earth System Models. *Endeavour* **2016**, *40* (3), 178–187. https://doi.org/10.1016/j.endeavour.2016.07.002.

(2) Friedlingstein, P.; Jones, M. W.; O'Sullivan, M.; Andrew, R. M.; Hauck, J.; Peters, G. P.; Peters, W.; Pongratz, J.; Sitch, S.; Le Quéré, C.; DBakker, O. C. E.; Canadell1, J. G.; Ciais1, P.; Jackson, R. B.; Anthoni1, P.; Barbero, L.; Bastos, A.; Bastrikov, V.; Becker, M.; Bopp, L.; Buitenhuis, E.; Chandra, N.; Chevallier, F.; Chini, L. P.; Currie, K. I.; Feely, R. A.; Gehlen, M.; Gilfillan, D.; Gkritzalis, T.; Goll, D. S.; Gruber, N.; Gutekunst, S.; Harris, I.; Haverd, V.; Houghton, R. A.; Hurtt, G.; Ilyina, T.; Jain, A. K.; Joetzjer, E.; Kaplan, J. O.; Kato, E.; Goldewijk, K. K.; Korsbakken, J. I.; Landschützer, P.; Lauvset, S. K.; Lefèvre, N.; Lenton, A.; Lienert, S.; Lombardozzi, D.; Marland, G.; McGuire, P. C.; Melton, J. R.; Metzl, N.; Munro, D. R.; Nabel, J. E. M. S.; Nakaoka, S. I.; Neill, C.; Omar, A. M.; Ono, T.; Peregon, A.; Pierrot, D.; Poulter, B.; Rehder, G.; Resplandy, L.; Robertson, E.; Rödenbeck, C.; Séférian, R.; Schwinger, J.; Smith, N.; Tans, P. P.; Tian, H.; Tilbrook, B.; Tubiello, F. N.; Van Der Werf, G. R.; Wiltshire, A. J.; Zaehle, S. Global Carbon Budget 2019. *Earth Syst. Sci. Data* **2019**, *11* (4), 1783–1838. https://doi.org/10.5194/essd-11-1783-2019.

(3) Yaashikaa, P. R.; Senthil Kumar, P.; Varjani, S. J.; Saravanan, A. A Review on Photochemical, Biochemical and Electrochemical Transformation of CO2 into Value-Added Products. *J. CO2 Util.* **2019**, *33* (May), 131–147. https://doi.org/10.1016/j.jcou.2019.05.017.

(4) Mikkelsen, M.; Jørgensen, M.; Krebs, F. C. The Teraton Challenge. A Review of Fixation and Transformation of Carbon Dioxide. *Energy Environ. Sci.* **2010**, *3* (1), 43–81. https://doi.org/10.1039/b912904a.

(5) Zhong, W.; Haigh, J. D. The Greenhouse Effect and Carbon Dioxide. *Weather* **2013**, *68* (4), 100–105. https://doi.org/10.1002/wea.2072.

(6) Moura, J. J. G.; Moura, I.; Maia, L. B. *Enzymes for Solving Humankind's Problems*; Springer Nature Switzerland AG 2021, 2021. https://doi.org/10.1007/978-3-030-58315-6.

(7) Taylor, J. O.; Wang, Y.; Hartl, F. Photo-Assisted Electrocatalytic Reduction of CO2: A New Strategy for Reducing Catalytic Overpotentials. *ChemCatChem* **2020**, *12* (1), 386–393. https://doi.org/10.1002/cctc.201901887.

(8) Ezugwu, C. I.; Asraf, M. A.; Li, X.; Liu, S.; Kao, C.-M.; Zhuiykov, S.; Verpoort, F. Selective and Adsorptive Removal of Anionic Dyes and CO2 with Azolium-Based Metal-Organic Frameworks. *J. Colloid Interface Sci.* **2018**, *519*, 214–223. https://doi.org/10.1016/J.JCIS.2018.02.003.

(9) Qiao, J.; Liu, Y.; Hong, F.; Zhang, J. *A Review of Catalysts for the Electroreduction of Carbon Dioxide to Produce Low-Carbon Fuels*; 2014; Vol. 43. https://doi.org/10.1039/c3cs60323g.

(10) Elgrishi, N.; Chambers, M. B.; Wang, X.; Fontecave, M. Molecular Polypyridine-Based Metal Complexes as Catalysts for the Reduction of CO2. *Chem. Soc. Rev.* **2017**, *46* (3), 761–796. https://doi.org/10.1039/c5cs00391a.

(11) Takeda, H.; Cometto, C.; Ishitani, O.; Robert, M. Electrons, Photons, Protons and Earth-

Abundant Metal Complexes for Molecular Catalysis of CO2 Reduction. *ACS Catal.* **2017**, *7* (1), 70–88. https://doi.org/10.1021/acscatal.6b02181.

(12) Porcher, J. P.; Fogeron, T.; Gomez-Mingot, M.; Derat, E.; Chamoreau, L. M.; Li, Y.; Fontecave, M. A Bioinspired Molybdenum Complex as a Catalyst for the Photo- and Electroreduction of Protons. *Angew. Chemie - Int. Ed.* **2015**, *54* (47), 14090–14093. https://doi.org/10.1002/anie.201505607.

(13) Taylor, J. O.; Veenstra, F. L. P.; Chippindale, A. M.; Calhorda, M. J.; Hartl, F. Group 6 Metal Complexes as Electrocatalysts of CO 2 Reduction: Strong Substituent Control of the Reduction Path of [Mo(η 3 -Allyl)(CO) 2 (x, X′-Dimethyl-2,2′-Bipyridine)(NCS)] (x = 4-6). *Organometallics* **2019**, *38* (6), 1372–1390. https://doi.org/10.1021/acs.organomet.8b00676.

(14) Rudolph, M.; Dautz, S.; Jager, E. G. Macrocyclic [N4/2-] Coordinated Nickel Complexes as Catalysts for the Formation of Oxalate by Electrochemical Reduction of Carbon Dioxide. *J. Am. Chem. Soc.* **2000**, *122* (44), 10821–10830. https://doi.org/10.1021/ja001254n.

(15) Angamuthu, R.; Byers, P.; Lutz, M.; Spek, A. L.; Bouwman, E. Electrocatalytic CO2 Conversion to Oxalate by a Copper Complex. *Science (80-.).* **2010**, *327* (5963), 313–315. https://doi.org/10.1126/science.1177981.

(16) Chapovetsky, A.; Do, T. H.; Haiges, R.; Takase, M. K.; Marinescu, S. C. Proton-Assisted Reduction of Co2 by Cobalt Aminopyridine Macrocycles. *J. Am. Chem. Soc.* **2016**, *138* (18), 5765–5768. https://doi.org/10.1021/jacs.6b01980.

(17) Sampson, M. D.; Nguyen, A. D.; Grice, K. A.; Moore, C. E.; Rheingold, A. L.; Kubiak, C. P. Manganese Catalysts with Bulky Bipyridine Ligands for the Electrocatalytic Reduction of Carbon Dioxide: Eliminating Dimerization and Altering Catalysis. *J. Am. Chem. Soc.* **2014**, *136* (14), 5460–5471. https://doi.org/10.1021/ja501252f.

(18) Torbensen, K.; Han, C.; Boudy, B.; von Wolff, N.; Bertail, C.; Braun, W.; Robert, M. Iron Porphyrin Allows Fast and Selective Electrocatalytic Conversion of CO2 to CO in a Flow Cell. *Chem. - A Eur. J.* **2020**, *26* (14), 3034–3038. https://doi.org/10.1002/chem.202000160.

(19) Costentin, C.; Passard, G.; Robert, M.; Savéant, J. M. Ultraefficient Homogeneous Catalyst for the CO2-to-CO Electrochemical Conversion. *Proc. Natl. Acad. Sci. U. S. A.* **2014**, *111* (42), 14990–14994. https://doi.org/10.1073/pnas.1416697111.

(20) Rao, G. K.; Pell, W.; Korobkov, I.; Richeson, D. Electrocatalytic Reduction of CO 2 Using Mn Complexes with Unconventional Coordination Environments † ChemComm COMMUNICATION. *Chem. Commun* **2016**, *52*, 8010. https://doi.org/10.1039/c6cc03827a.

(21) Nitopi, S.; Bertheussen, E.; Scott, S. B.; Liu, X.; Engstfeld, A. K.; Horch, S.; Seger, B.; Stephens, I. E. L.; Chan, K.; Hahn, C.; Nørskov, J. K.; Jaramillo, T. F.; Chorkendorff, I. Progress and Perspectives of Electrochemical CO2 Reduction on Copper in Aqueous Electrolyte. *Chem. Rev.* **2019**, *119* (12), 7610–7672. https://doi.org/10.1021/acs.chemrev.8b00705.

(22) Fogeron, T.; Retailleau, P.; Gomez-Mingot, M.; Li, Y.; Fontecave, M. Nickel Complexes Based on Molybdopterin-like Dithiolenes: Catalysts for CO 2 Electroreduction. *Organometallics* **2019**, *38* (6), 1344–1350. https://doi.org/10.1021/acs.organomet.8b00655.

(23) Myren, T. H. T.; Alherz, A.; Thurston, J. R.; Stinson, T. A.; Huntzinger, C. G.; Musgrave, C. B.; Luca, O. R. Mn-Based Molecular Catalysts for the Electrocatalytic

Disproportionation of CO2 into CO and CO32-. *ACS Catal.* **2020**, *10* (3), 1961–1968. https://doi.org/10.1021/acscatal.9b04773.

(24) Bourrez, M.; Molton, F.; Chardon-Noblat, S.; Deronzier, A. [Mn(Bipyridyl)(CO)3Br]: An Abundant Metal Carbonyl Complex as Efficient Electrocatalyst for CO2 Reduction. *Angew. Chemie - Int. Ed.* **2011**, *50* (42), 9903–9906. https://doi.org/10.1002/anie.201103616.

(25) Fei, H.; Sampson, M. D.; Lee, Y.; Kubiak, C. P.; Cohen, S. M. Photocatalytic CO 2 Reduction to Formate Using a Mn(I) Molecular Catalyst in a Robust Metal-Organic Framework. *Inorg. Chem.* **2015**, *54* (14), 6821–6828. https://doi.org/10.1021/acs.inorgchem.5b00752.

(26) Chang, C. C.; Li, S. R.; Chou, H. L.; Lee, Y. C.; Patil, S.; Lin, Y. S.; Chang, C. C.; Chang, Y. J.; Wang, D. Y. Photoactive Earth-Abundant Iron Pyrite Catalysts for Electrocatalytic Nitrogen Reduction Reaction. *Small* **2019**, *15* (49), 1–7. https://doi.org/10.1002/smll.201904723.

(27) Shi, J.; Jiang, Y.; Jiang, Z.; Wang, X.; Wang, X.; Zhang, S.; Han, P.; Yang, C. Enzymatic Conversion of Carbon Dioxide. *Chem. Soc. Rev.* **2015**, *44* (17), 5981–6000. https://doi.org/10.1039/c5cs00182j.

(28) Appel, A. M.; Bercaw, J. E.; Bocarsly, A. B.; Dobbek, H.; Dubois, D. L.; Dupuis, M.; Ferry, J. G.; Fujita, E.; Hille, R.; Kenis, P. J. A.; Kerfeld, C. A.; Morris, R. H.; Peden, C. H. F.; Portis, A. R.; Ragsdale, S. W.; Rauchfuss, T. B.; Reek, J. N. H.; Seefeldt, L. C.; Thauer, R. K.; Waldrop, G. L. Frontiers, Opportunities, and Challenges in Biochemical and Chemical Catalysis of CO2 Fixation. *Chem. Rev.* **2013**, *113* (8), 6621–6658. https://doi.org/10.1021/cr300463y.

(29) English, N. J.; El-Hendawy, M. M.; Mooney, D. A.; MacElroy, J. M. D. Perspectives on Atmospheric CO2 Fixation in Inorganic and Biomimetic Structures. *Coord. Chem. Rev.* **2014**, *269* (1), 85–95. https://doi.org/10.1016/j.ccr.2014.02.015.

(30) Müller, E.; Mehlhorn, K. Potentiometrische Verfolgung Der Thiosulfatbildung Aus Alkalisulfid Und Schwefliger Säure. *Angew. Chemie* **1934**, *47* (9), 134–139. https://doi.org/10.1002/ange.19340470905.

(31) Maia, L. B.; Moura, I.; Moura, J. J. G. Molybdenum and Tungsten-Containing Formate Dehydrogenases: Aiming to Inspire a Catalyst for Carbon Dioxide Utilization. *Inorganica Chimica Acta*. Elsevier S.A. January 30, 2017, pp 350–363. https://doi.org/10.1016/j.ica.2016.07.010.

(32) Niks, D.; Hille, R. Molybdenum- and Tungsten-Containing Formate Dehydrogenases and Formylmethanofuran Dehydrogenases: Structure, Mechanism, and Cofactor Insertion. *Protein Sci.* **2019**, *28* (1), 111–122. https://doi.org/10.1002/pro.3498.

(33) Guo, Q.; Gakhar, L.; Wickersham, K.; Francis, K.; Vardi-Kilshtain, A.; Major, D. T.; Cheatum, C. M.; Kohen, A. Structural and Kinetic Studies of Formate Dehydrogenase from Candida Boidinii. *Biochemistry* **2016**, *55* (19), 2760–2771. https://doi.org/10.1021/acs.biochem.6b00181.

(34) Maia, L. B.; Fonseca, L.; Moura, I.; Moura, J. J. G. Reduction of Carbon Dioxide by a Molybdenum-Containing Formate Dehydrogenase: A Kinetic and Mechanistic Study. *J. Am. Chem. Soc.* **2016**, *138* (28), 8834–8846. https://doi.org/10.1021/jacs.6b03941.

(35) Niks, D.; Duvvuru, J.; Escalona, M.; Hille, R. Spectroscopic and Kinetic Properties of the Molybdenum-Containing, NAD+-Dependent Formate Dehydrogenase from Ralstonia Eutropha. *J. Biol. Chem.* **2016**, *291* (3), 1162–1174. https://doi.org/10.1074/jbc.M115.688457.

(36) Sieh, D.; Lacy, D. C.; Peters, J. C.; Kubiak, C. P. Reduction of CO2 by Pyridine Monoimine Molybdenum Carbonyl Complexes: Cooperative Metal-Ligand Binding of CO2. *Chem. - A Eur. J.* **2015**, *21* (23), 8497–8503. https://doi.org/10.1002/chem.201500463.

(37) Fogeron, T.; Retailleau, P.; Chamoreau, L.-M.; Li, Y.; Fontecave, M. Pyranopterin Related Dithiolene Molybdenum Complexes as Homogeneous Catalysts for CO 2 Photoreduction . *Angew. Chemie* **2018**, *130* (52), 17279–17283. https://doi.org/10.1002/ange.201809084.

(38) Chakraborty, S.; Blacque, O.; Berke, H. Ligand Assisted Carbon Dioxide Activation and Hydrogenation Using Molybdenum and Tungsten Amides. *Dalt. Trans.* **2015**, *44* (14), 6560–6570. https://doi.org/10.1039/c5dt00278h.

(39) Zhang, Y.; Williard, P. G.; Bernskoetter, W. H. Synthesis and Characterization of Pincer-Molybdenum Precatalysts for CO2 Hydrogenation. *Organometallics* **2016**, *35* (6), 860–865. https://doi.org/10.1021/acs.organomet.5b00955.

(40) Armarego, W. L. F.; Chai, C. *Common Physical Techniques Used in Purification*; 2013. https://doi.org/10.1016/b978-0-12-382161-4.00001-7.

(41) Aimoto, Y.; Koshiba, K.; Yamauchi, K.; Sakai, K. A Family of Molecular Nickel Hydrogen Evolution Catalysts Providing Tunable Overpotentials Using Ligand-Centered Proton-Coupled Electron Transfer Paths. *Chem. Commun. (Camb).* **2018**, *54* (91), 12820–12823. https://doi.org/10.1039/c8cc07467d.

(42) Rodo, E. C.; Feng, L.; Jida, M.; Ehrhardt, K.; Bielitza, M.; Boilevin, J.; Lanzer, M.; Williams, D. L.; Lanfranchi, D. A.; Davioud-Charvet, E. A Platform of Regioselective Methodologies to Access Polysubstituted 2-Methyl-1,4-Naphthoquinone Derivatives: Scope and Limitations. *European J. Org. Chem.* **2016**, *2016* (11), 1982–1993. https://doi.org/10.1002/ejoc.201600144.

(43) Seitz, M.; Kaiser, A.; Powell, D. R.; Borovik, A. S.; Reiser, O. Predetermined Helical Chirality in Octahedral Complexes with a Novel Pentadentate C2-Symmetrical Chiral Bis(Oxazoline) Ligand. *Adv. Synth. Catal.* **2004**, *346* (7), 737–741. https://doi.org/10.1002/adsc.200404020.

(44) Coates, J. Interpretation of Infrared Spectra, A Practical Approach. In *Encyclopedia of Analytical Chemistry*; John Wiley & Sons, Ltd, 2006. https://doi.org/10.1002/9780470027318.a5606.

(45) Majumder, S.; Pasayat, S.; Panda, A. K.; Dash, S. P.; Roy, S.; Biswas, A.; Varma, M. E.; Joshi, B. N.; Garribba, E.; Kausar, C.; Samir, #; Patra, K.; Kaminsky, W.; Aureíien, ¶; Dinda, R. Monomeric and Dimeric Oxidomolybdenum(V and VI) Complexes, Cytotoxicity, and DNA Interaction Studies: Molybdenum Assisted C□N Bond Cleavage of Salophen Ligands. **2017**, *56*. https://doi.org/10.1021/acs.inorgchem.7b01578.

(46) Porcher, J. P.; Fogeron, T.; Gomez-Mingot, M.; Chamoreau, L. M.; Li, Y.; Fontecave, M. Synthesis and Reactivity of a Bio-Inspired Dithiolene Ligand and Its Mo Oxo Complex. *Chem. - A Eur. J.* **2016**, *22* (13), 4447–4453. https://doi.org/10.1002/chem.201504373.

(47) Dong, Q.; Zhang, X.; He, D.; Lang, C.; Wang, D. Role of H2O in CO2 Electrochemical Reduction As Studied in a Water-in-Salt System. *ACS Cent. Sci.* **2019**, *5* (8), 1461–1467. https://doi.org/10.1021/acscentsci.9b00519.

(48) Liu, H.; Bandeira, N. A. G.; Calhorda, M. J.; Drew, M. G. B.; Félix, V.; Novosad, J.; Biani, F. de F.; Zanello, P. Cu(I) and Ag(I) Complexes of Chalcogenide Derivatives of the Organometallic Ligand Dppf and the Dppa Analogue. *J. Organomet. Chem.* **2004**, *689* (17), 2808–2819. https://doi.org/10.1016/j.jorganchem.2004.06.012.

Annexes

Annexes

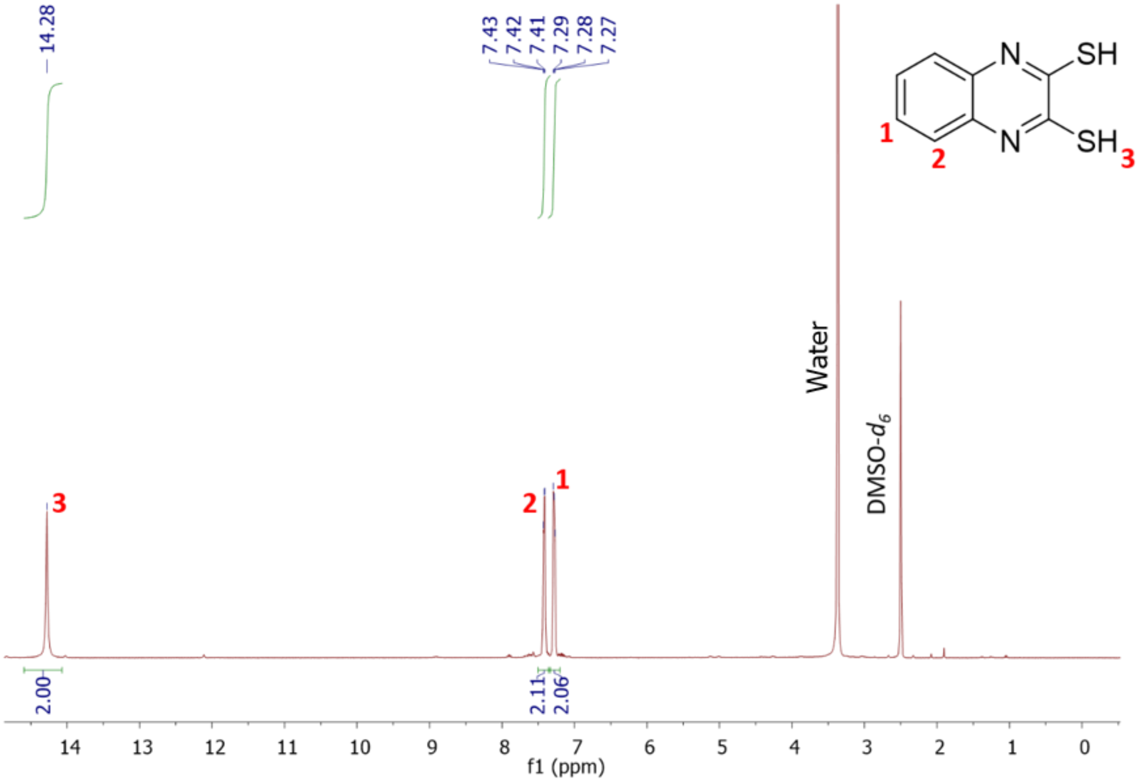

Figure A.1: ^{1}H NMR spectrum of L1, in DMSO-d_6.

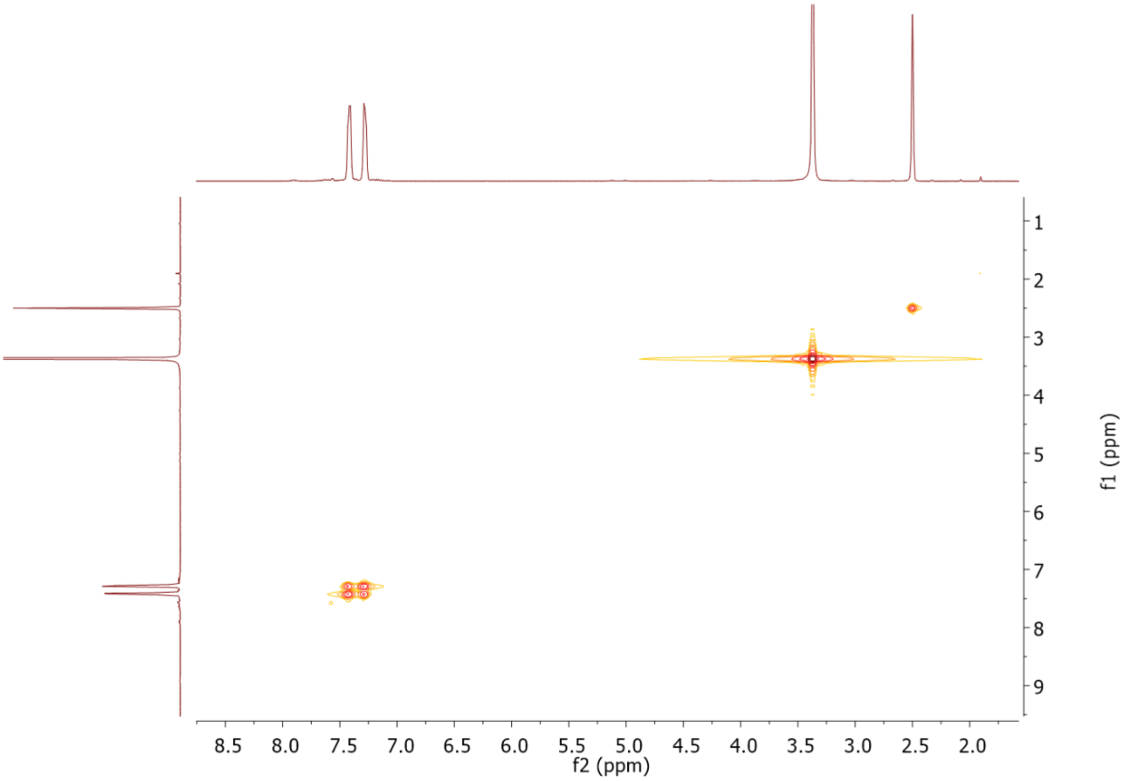

Figure A.2: 2D COSY spectrum of L1, in DMSO-d_6.

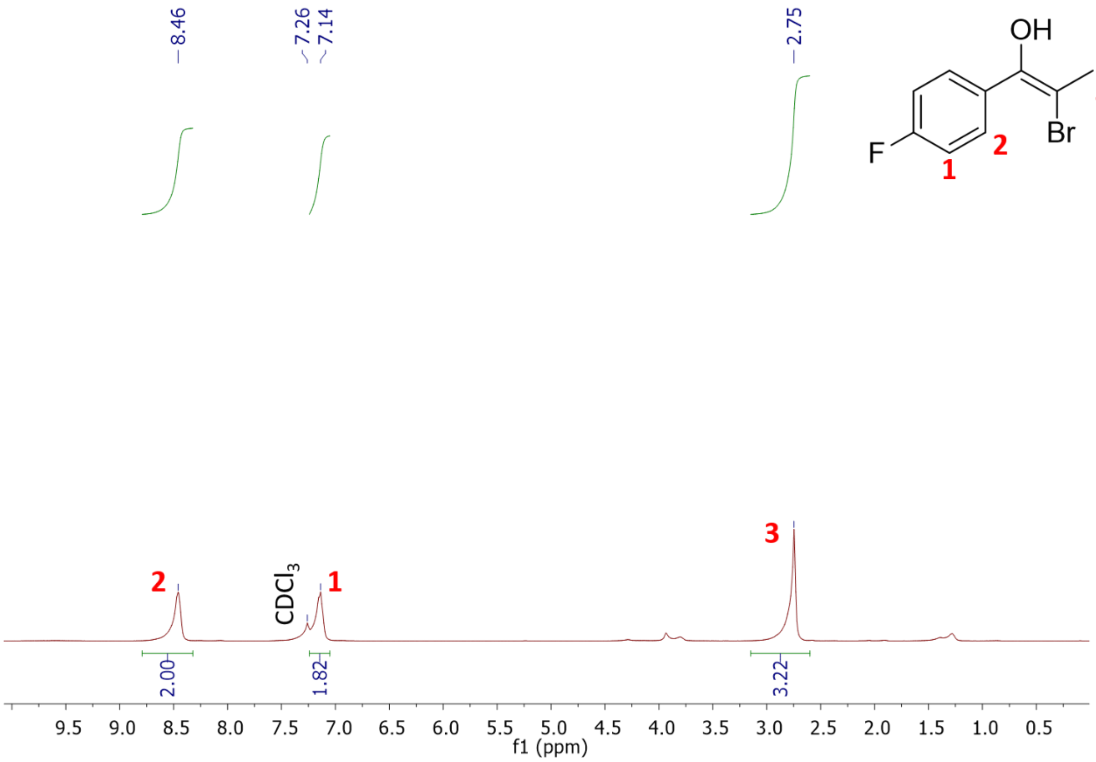

Figure A.3: ^{1}H NMR spectrum of I1, in CDCl$_3$.

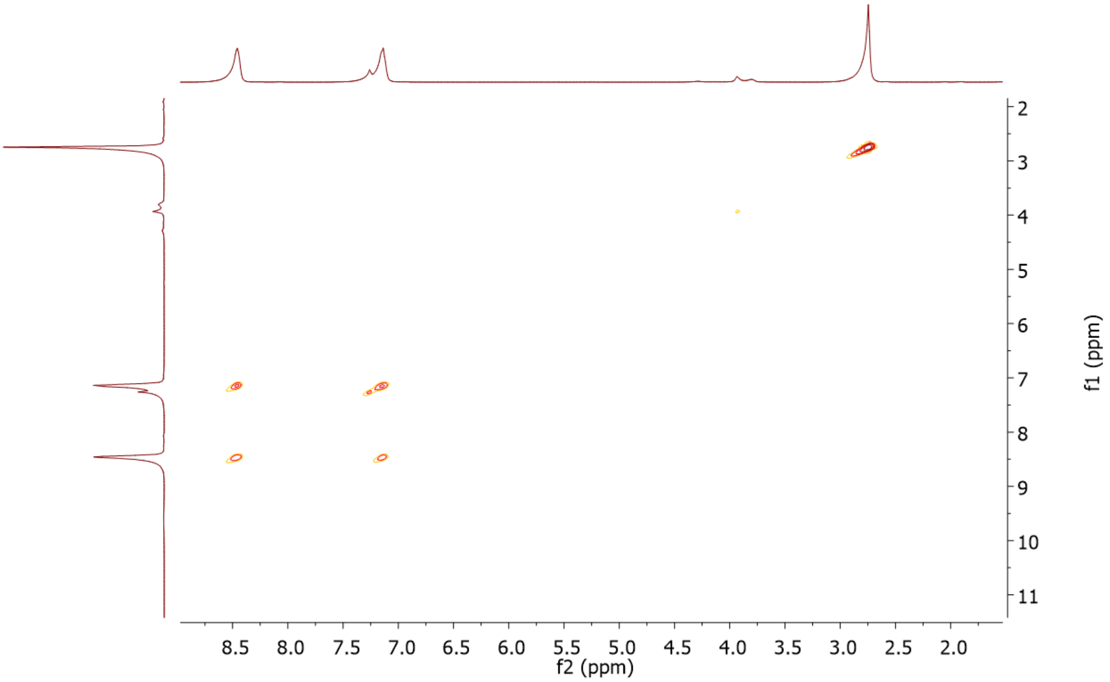

Figure A.4: 2D COSY spectrum of I1, in $CDCl_3$.

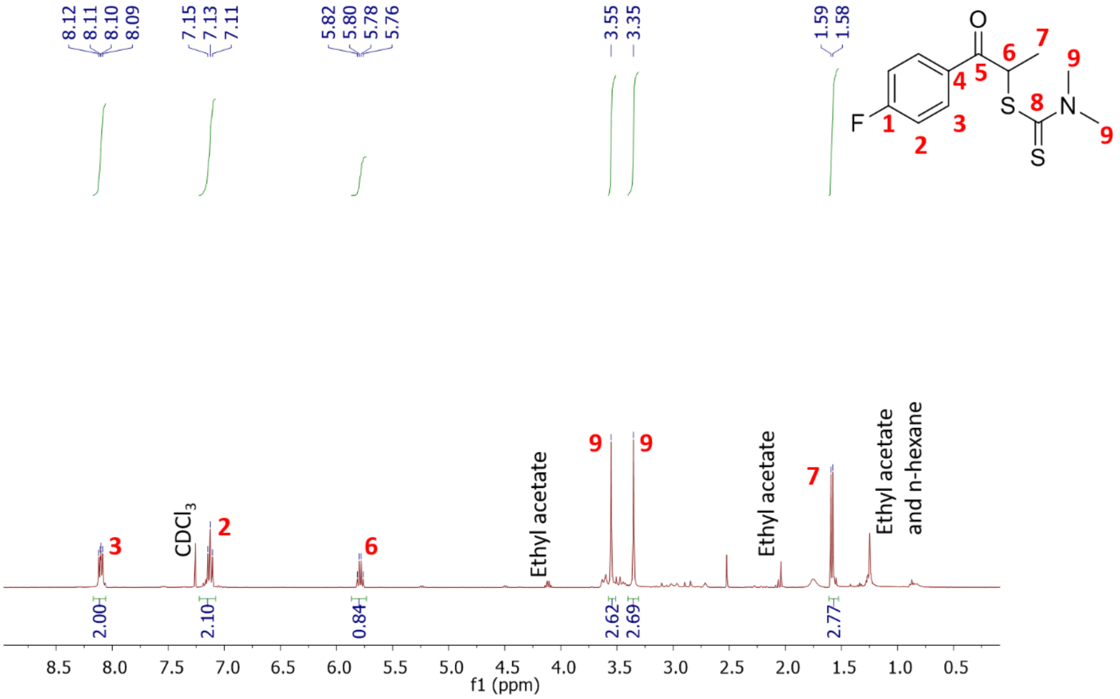

Figure A.5: ^{1}H NMR spectrum of I2, in $CDCl_3$.

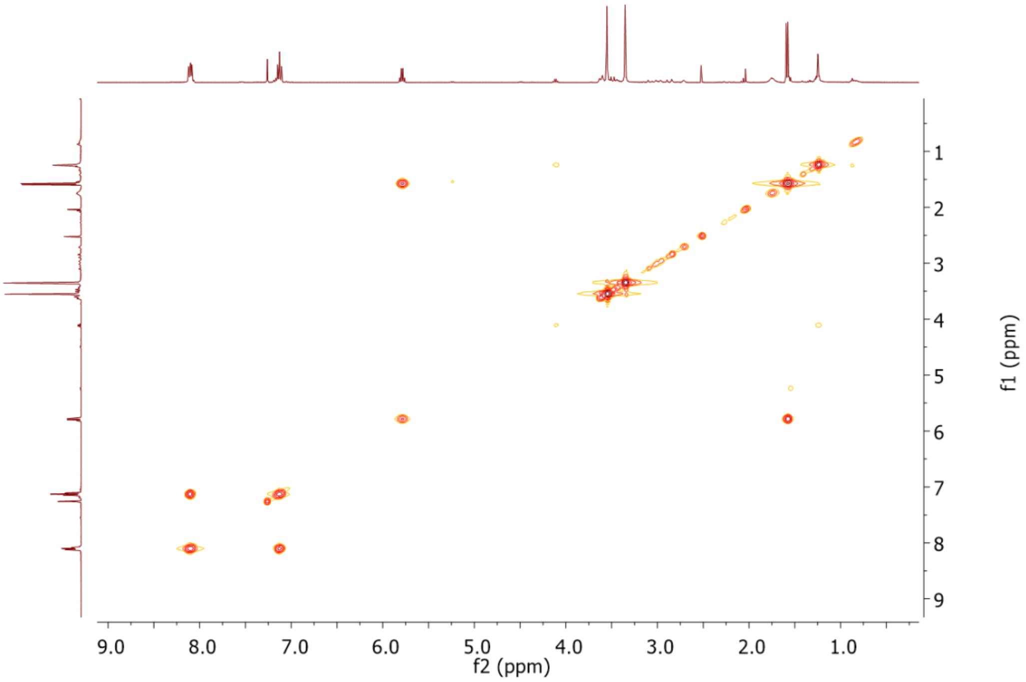

Figure A.6: 2D COSY spectrum of I2, in $CDCl_3$.

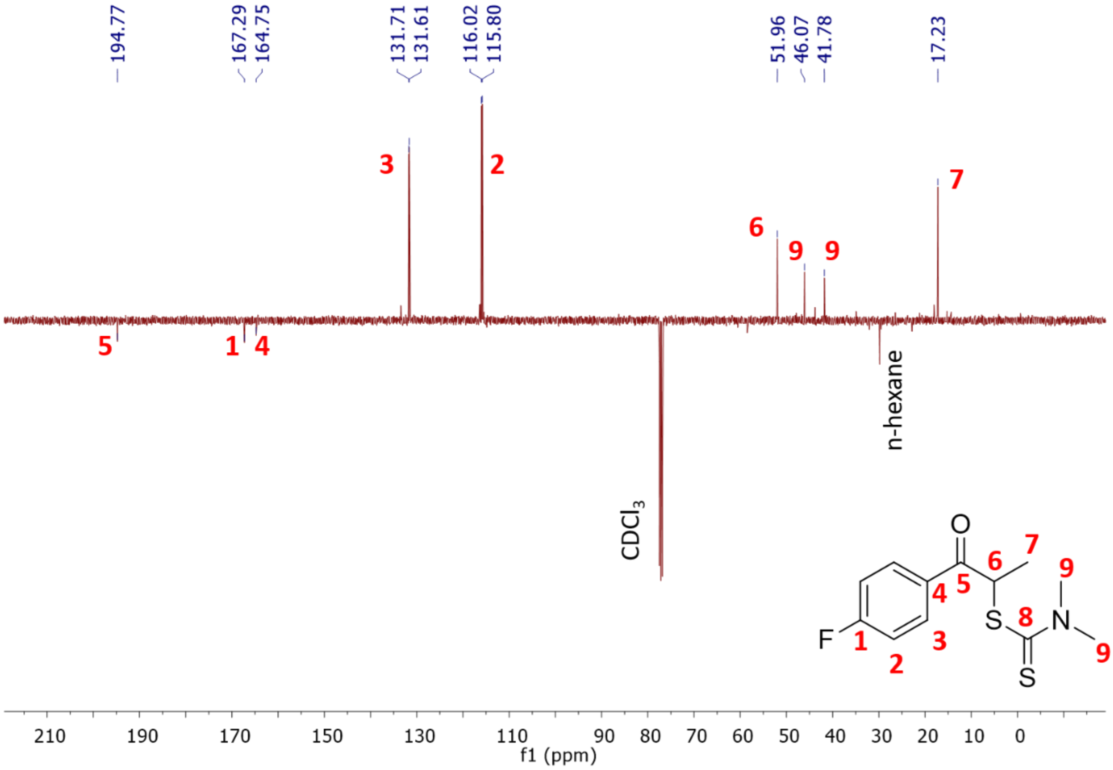

Figure A.7: ^{13}C APT NMR spectrum of I2, in CDCl$_3$.

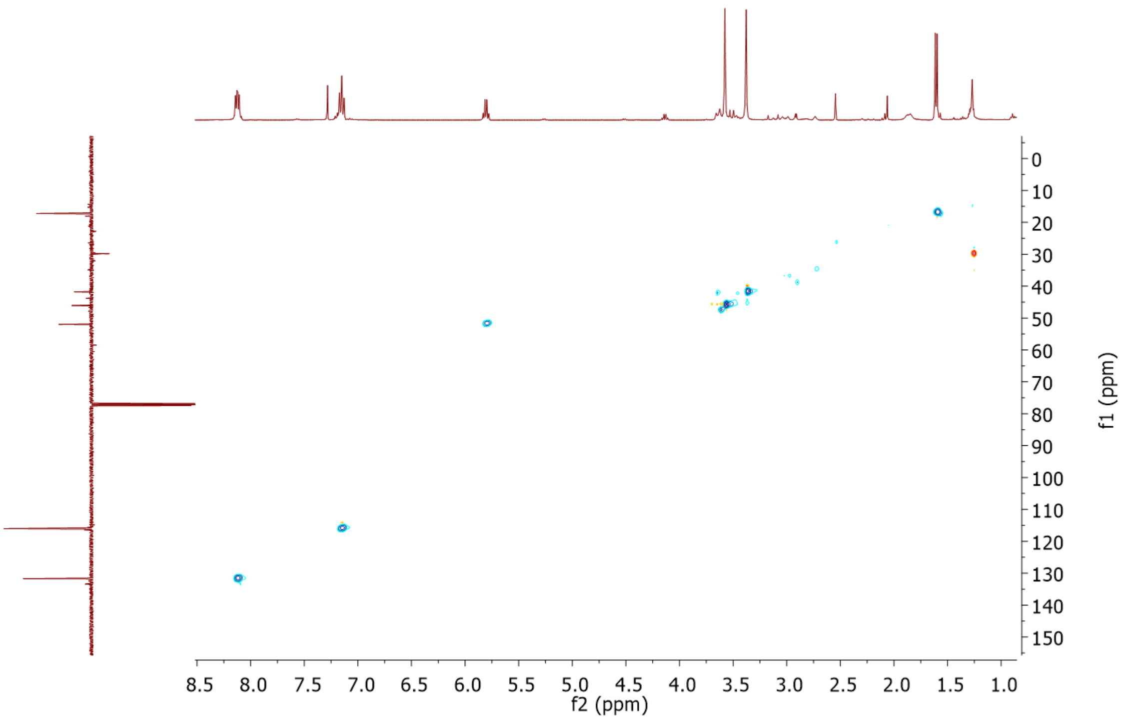

Figure A.8: HSQC spectrum of I2, in $CDCl_3$.

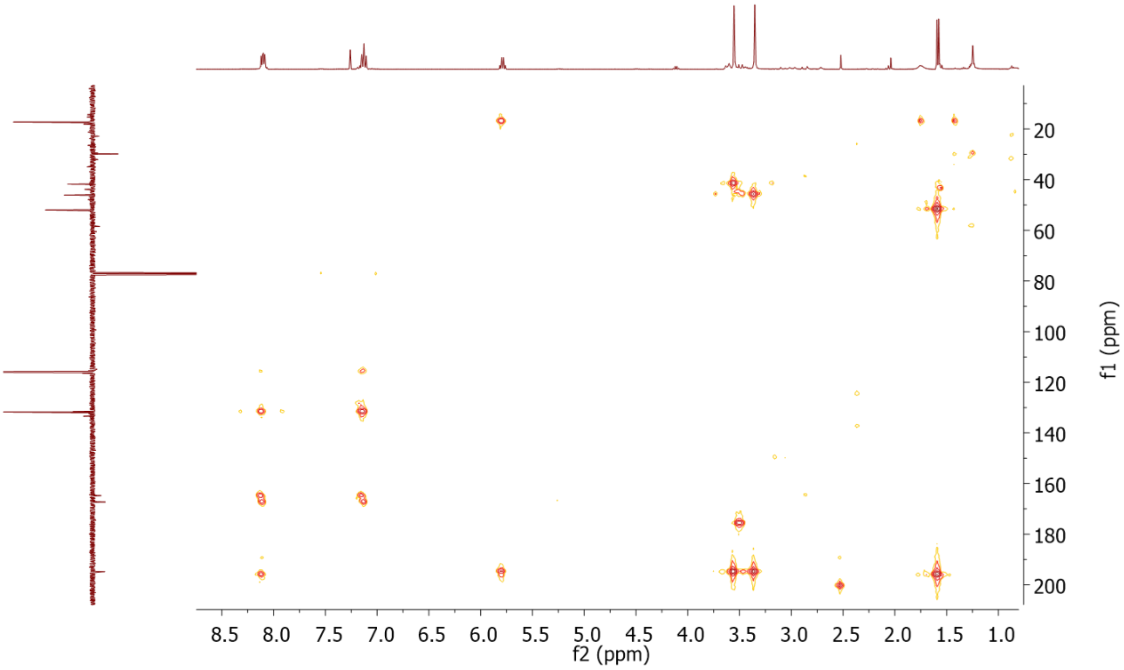

Figure A.9: HMBC spectrum of I2, in $CDCl_3$.

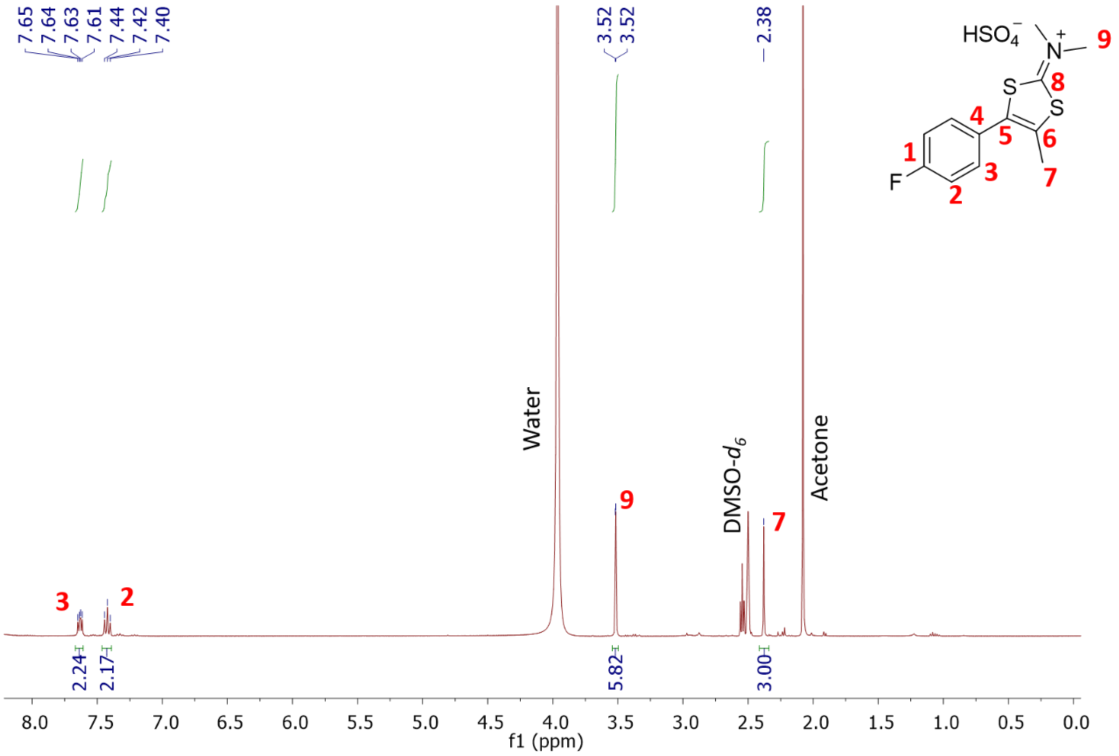

Figure A.10: ^{1}H NMR spectrum of I3, in DMSO-d_6.

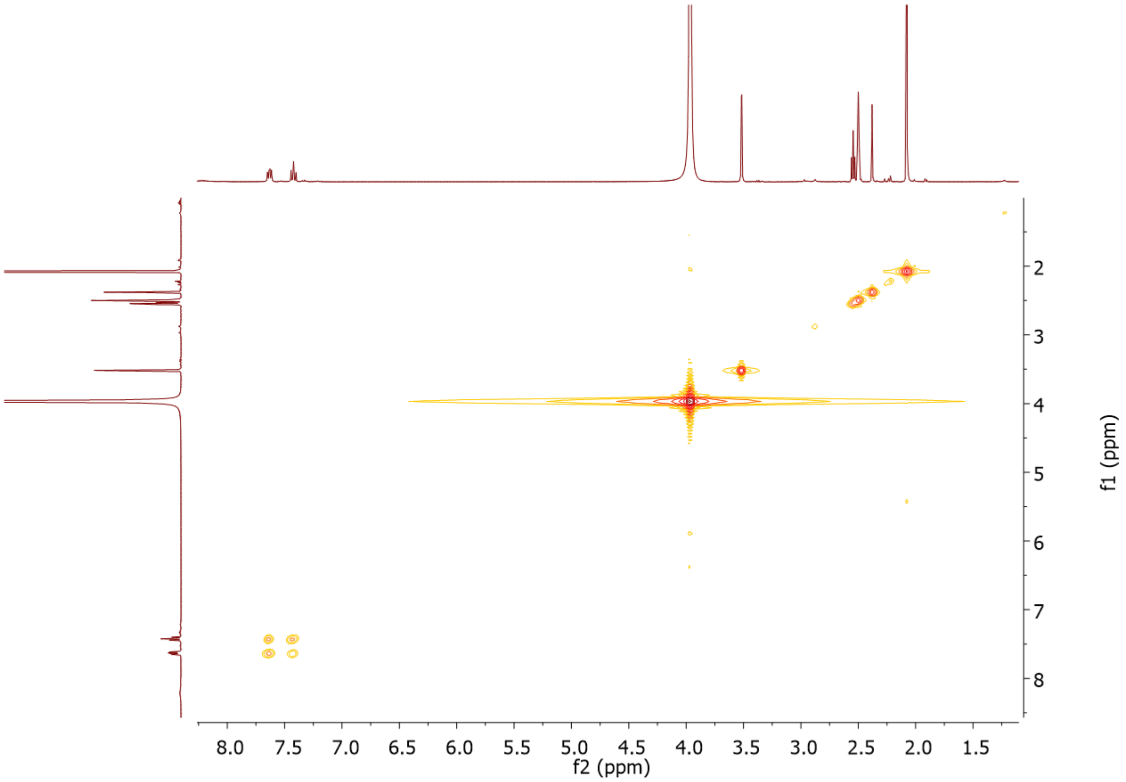

Figure A.11: 2D COSY spectrum of I3 in DMSO-d₆.

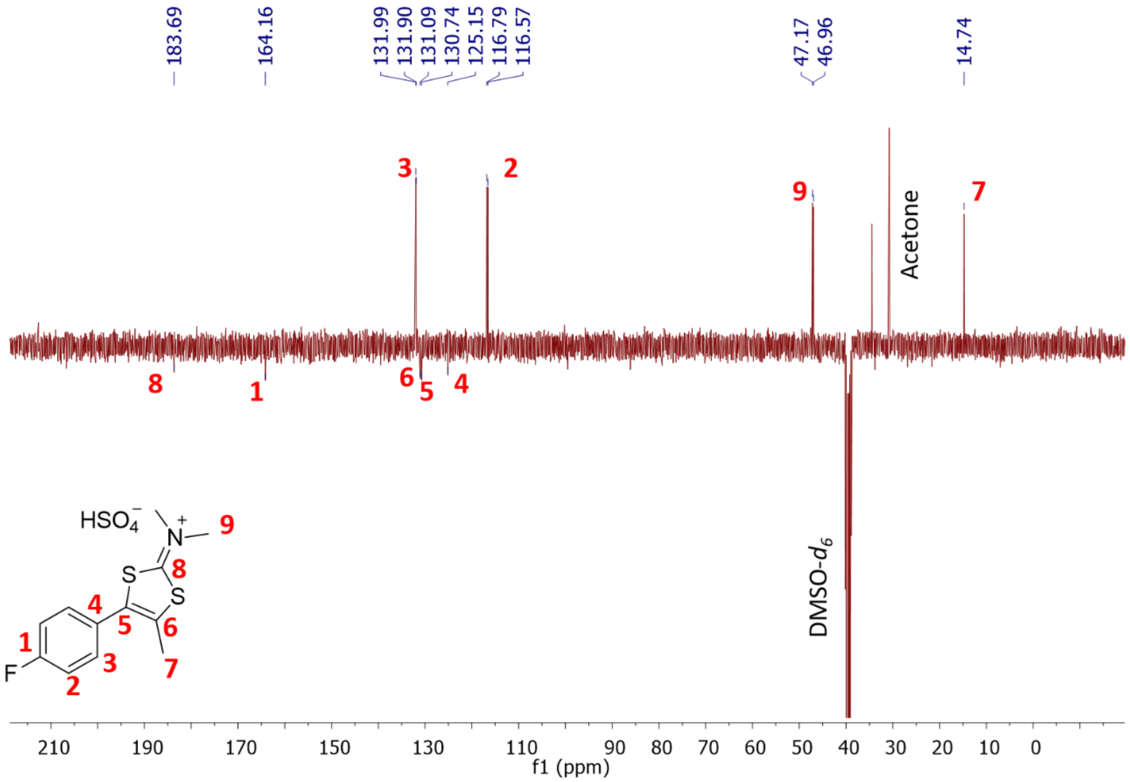

Figure A.12: ***^{13}C APT NMR spectrum of I3, in DMSO-d_6.***

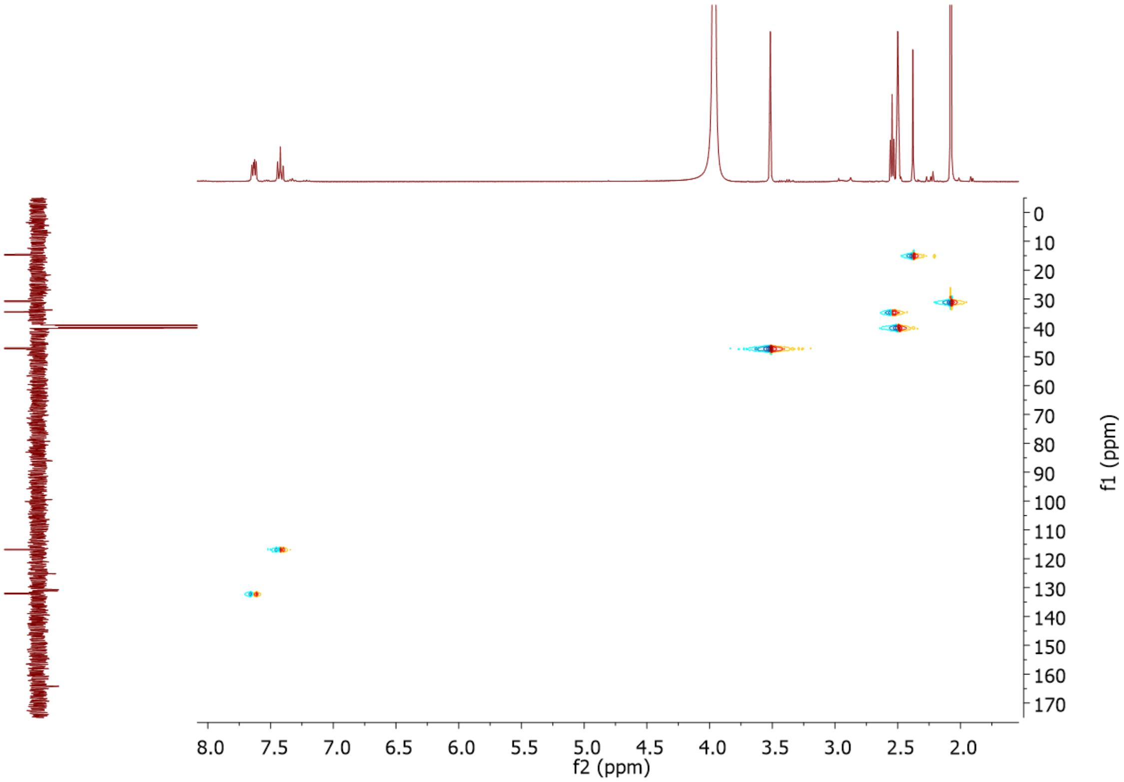

Figure A.13: HSQC spectrum of I3, in DMSO-d_6.

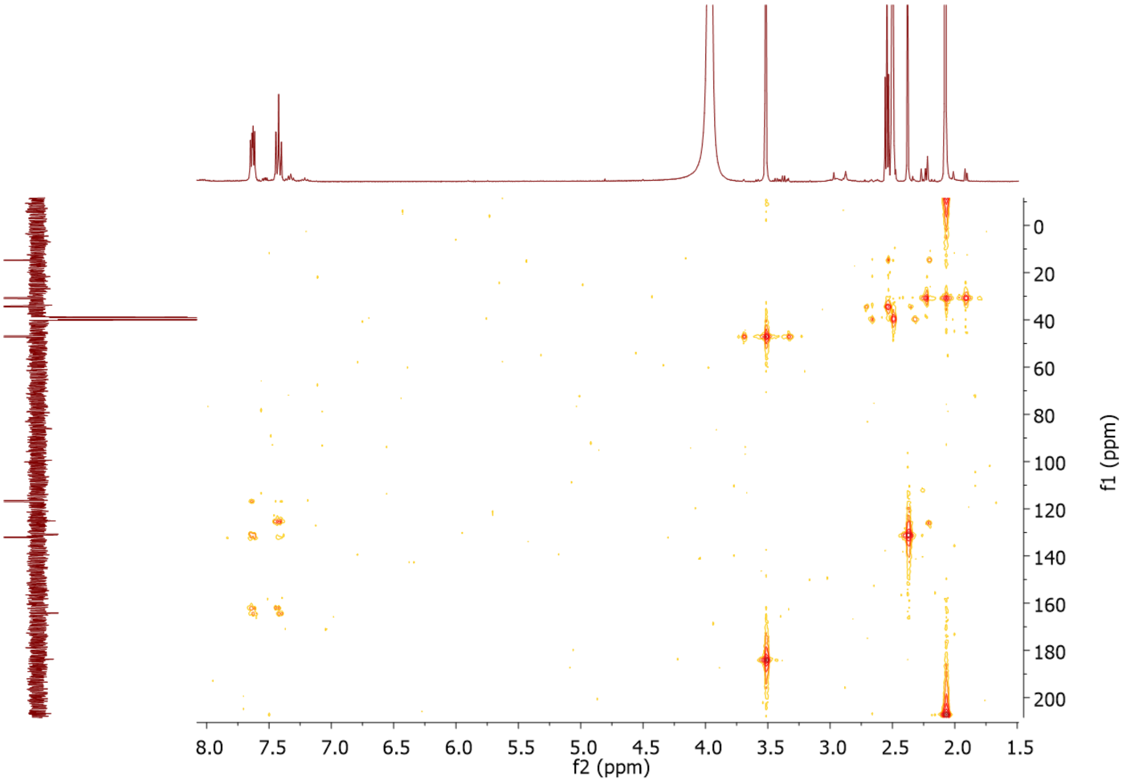

Figure A.14: HMBC spectrum of I3, in DMSO-d_6.

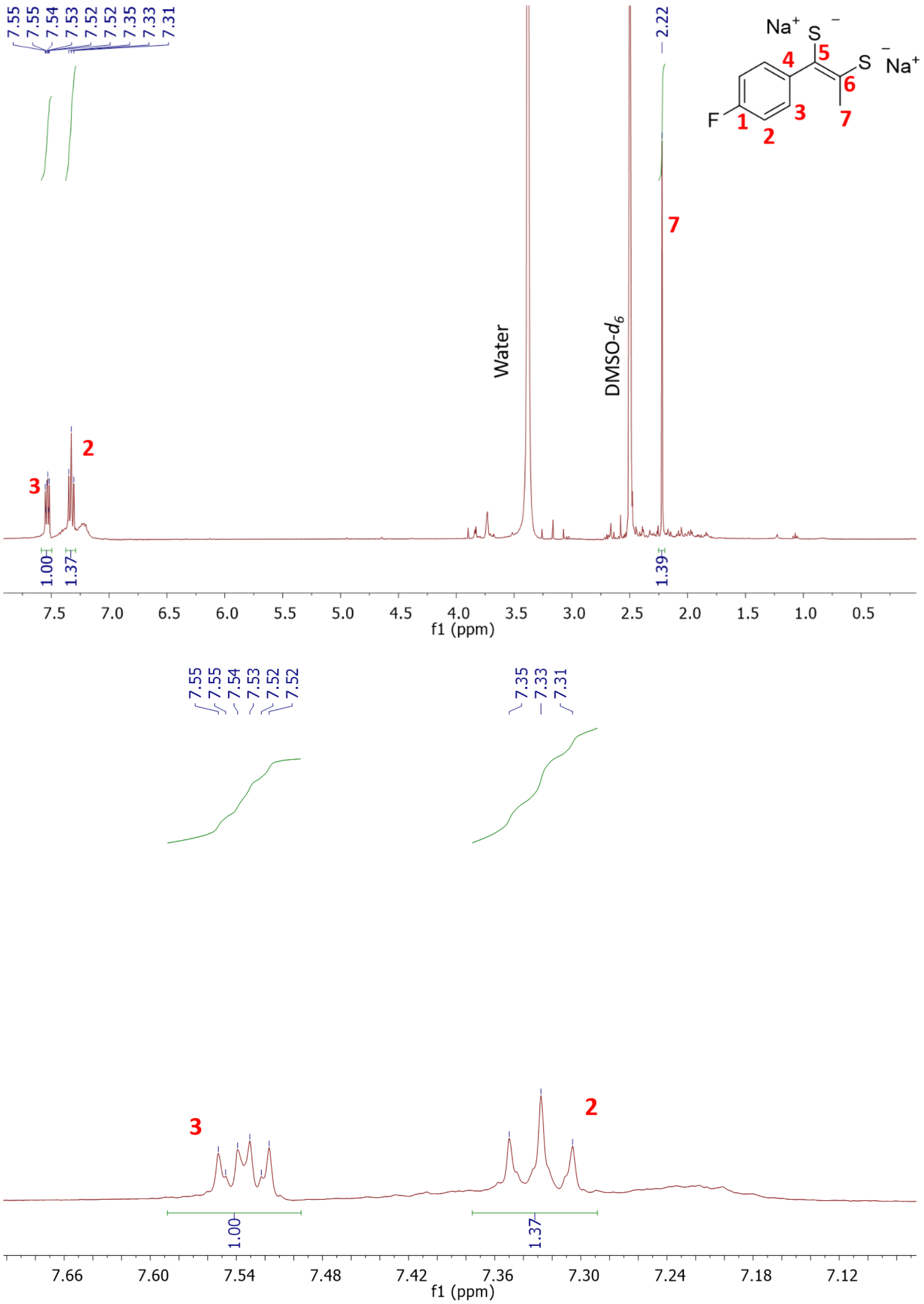

Figure A.15: ^{1}H NMR spectrum of L2 in DMSO-d$_6$ (top) and amplification of aromatic region (bottom).

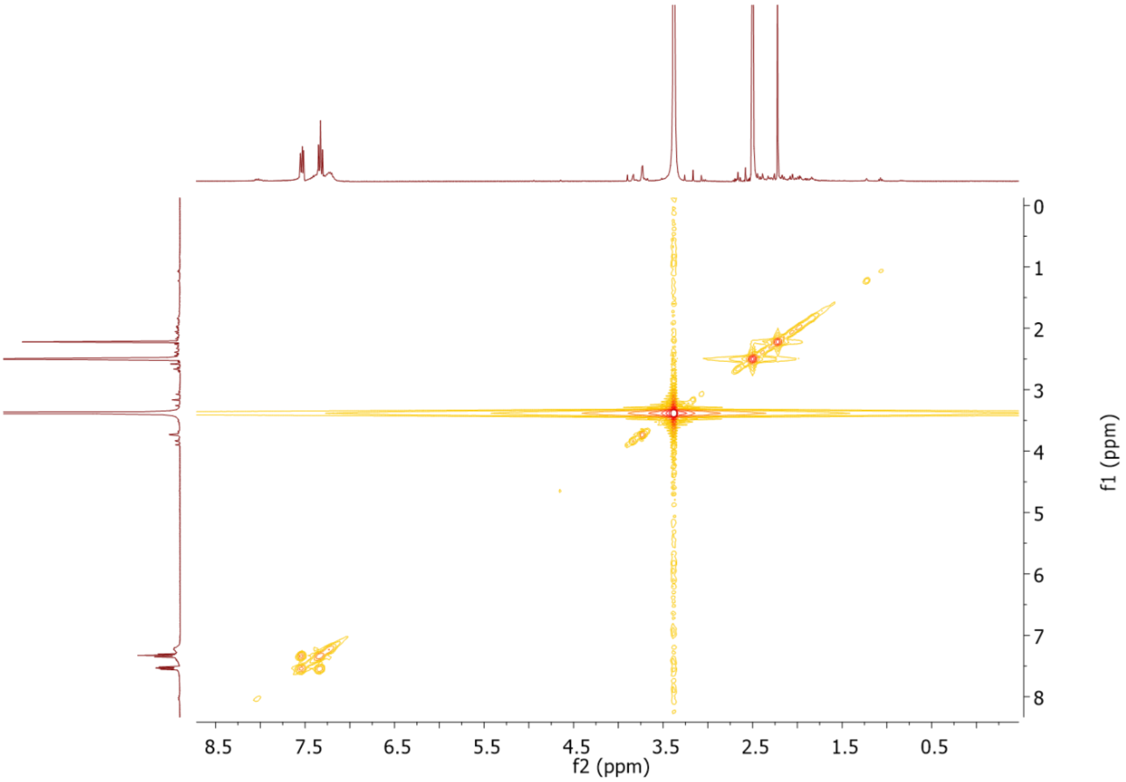

Figure A.16: 2D COSY of L2, in DMSO-d_6.

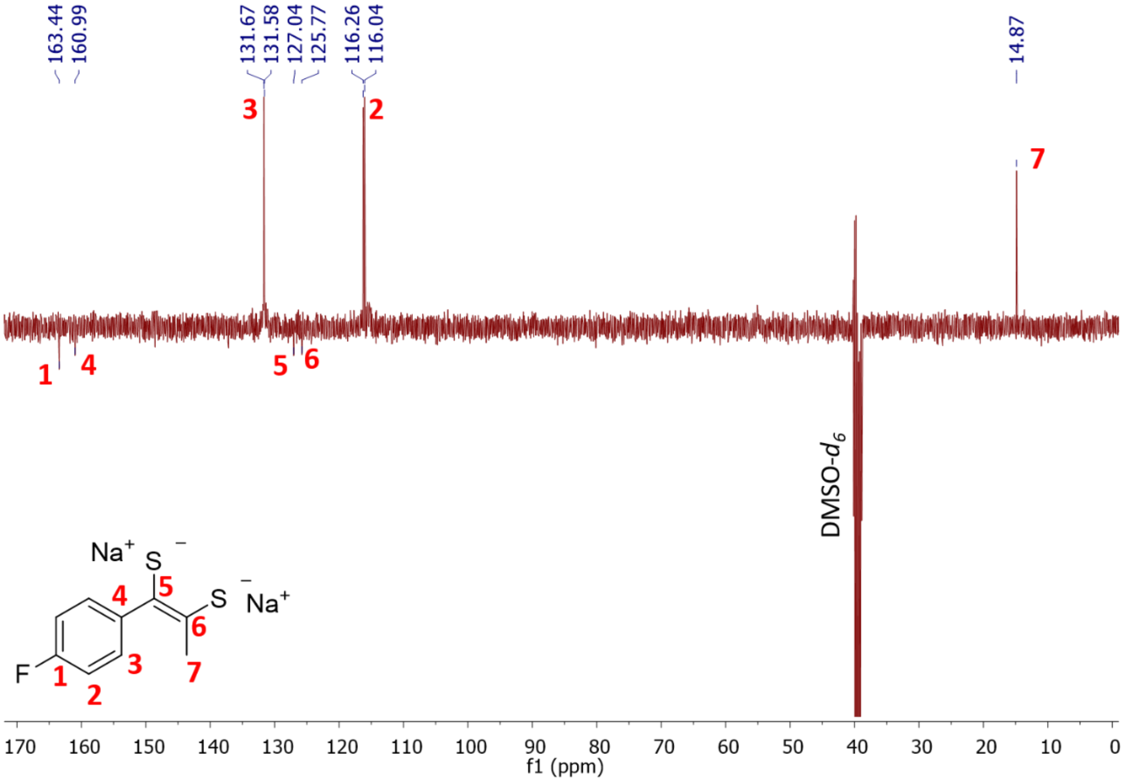

Figure A.17: ***^{13}C APT NMR spectrum of L2, in DMSO-d_6.***

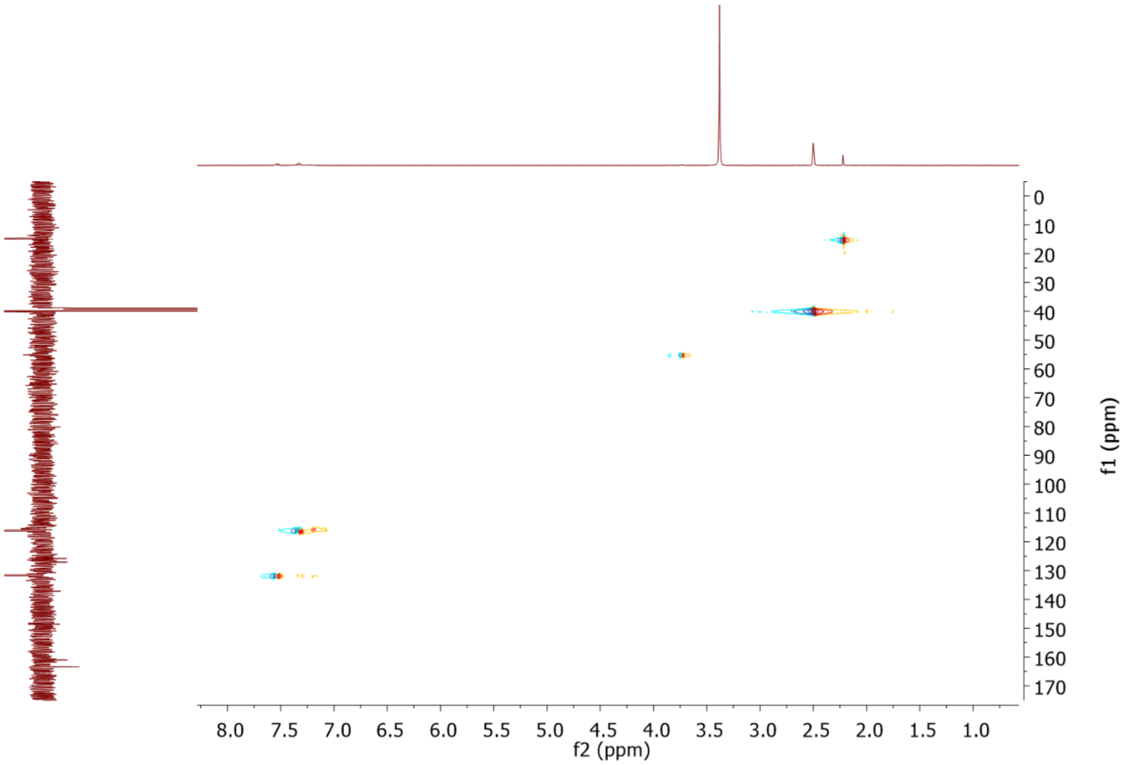

Figure A.18: HSQC spectrum of L2, in DMSO-d_6.

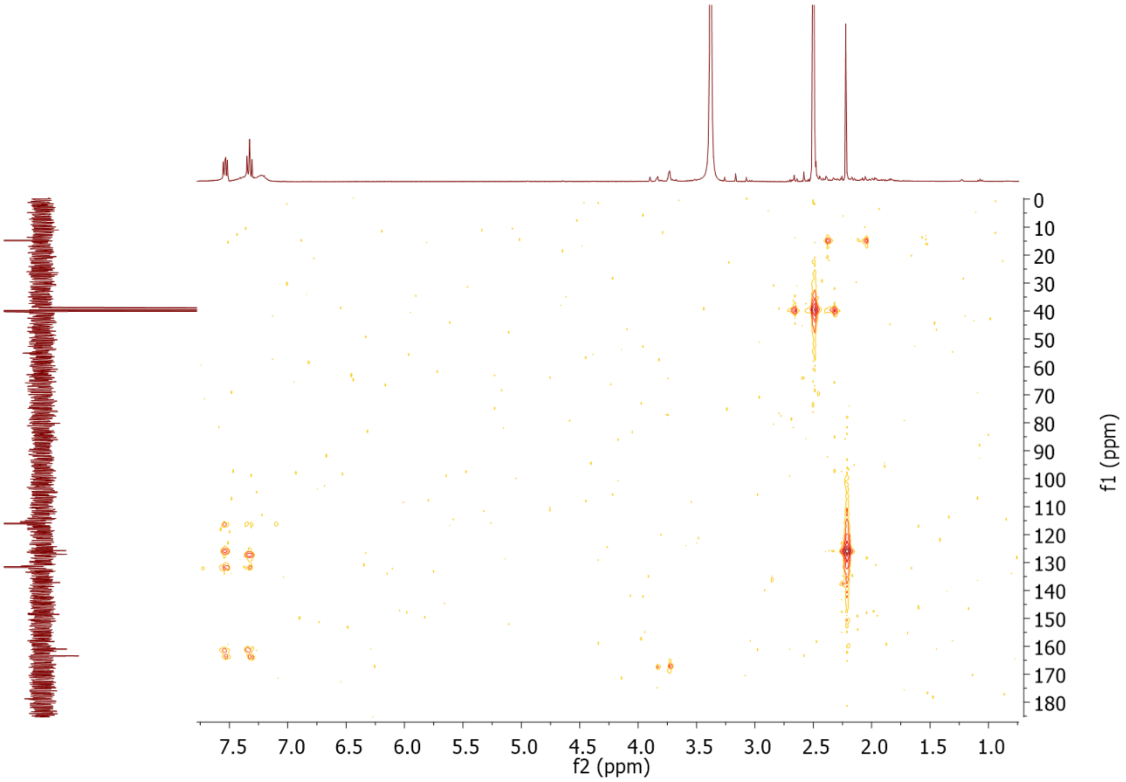

Figure A.19: HMBC spectrum of L2, in DMSO-d_6.

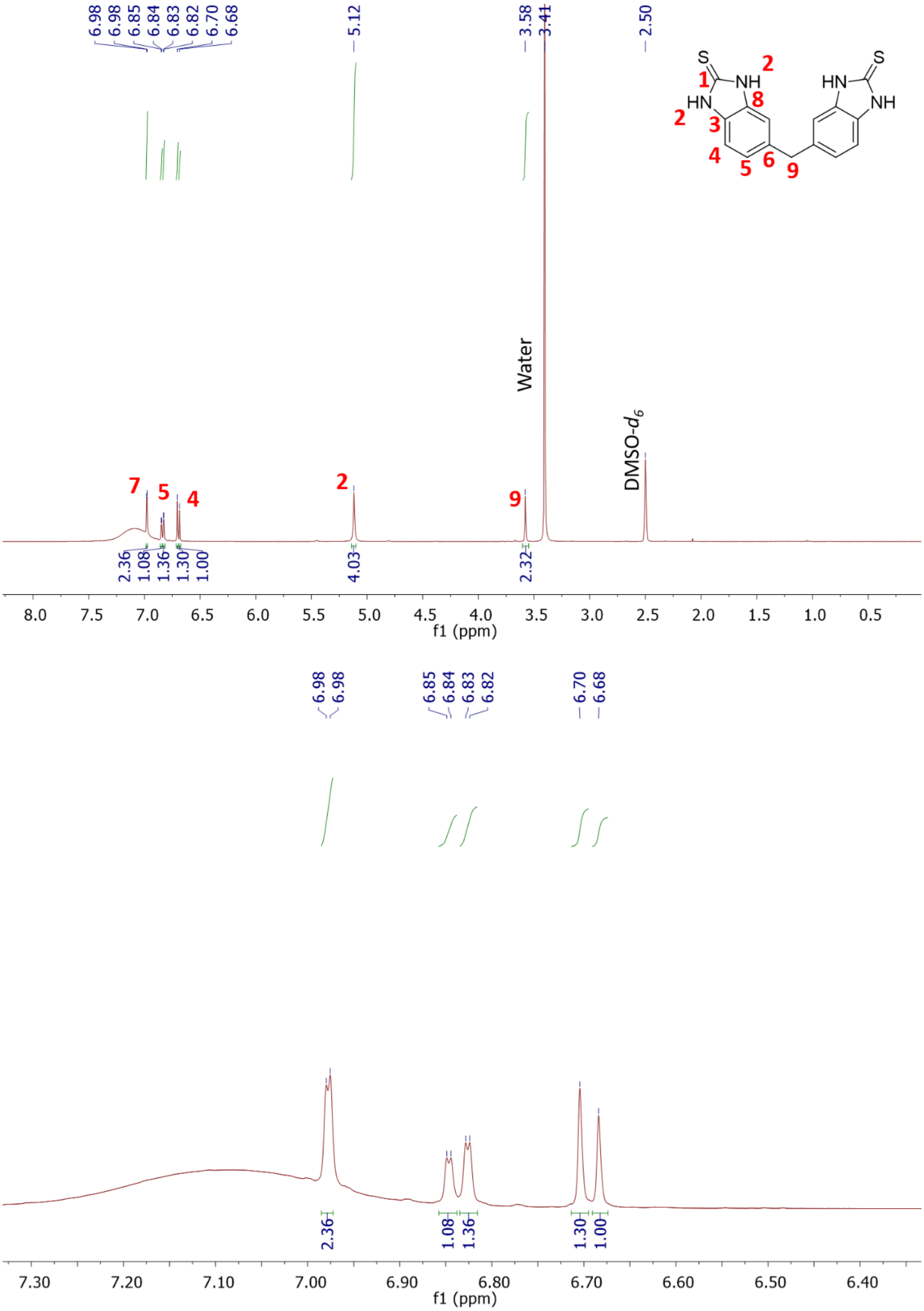

Figure A.20: ^{1}H NMR of L3, in DMSO-d_6 (top) and amplification of aromatic zone (bottom).

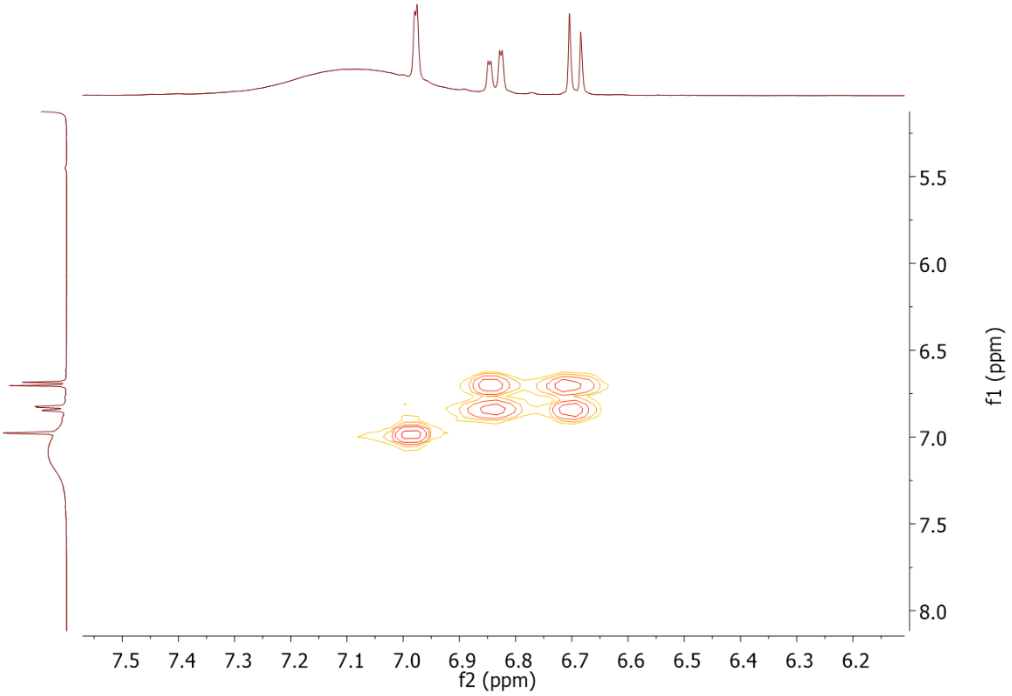

Figure A.21: 2D COSY spectrum of L3, in DMSO-d_6.

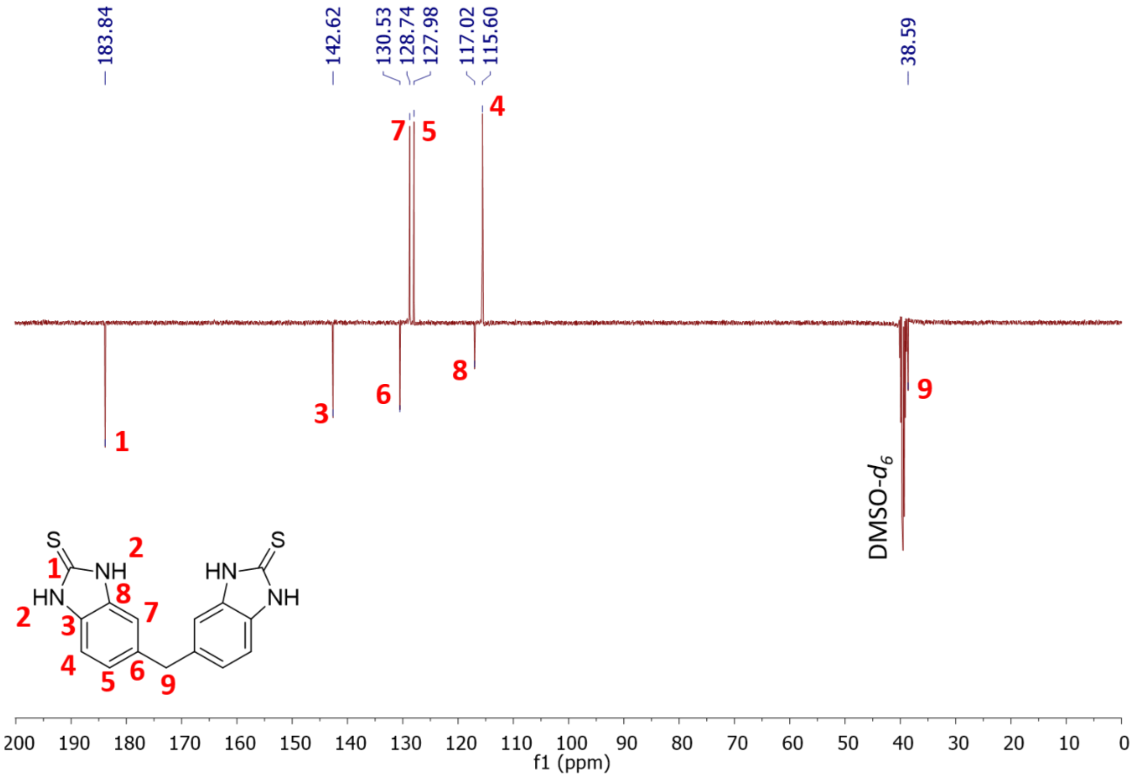

Figure A.22: ^{13}C NMR spectrum of L3, in DMSO-d_6.

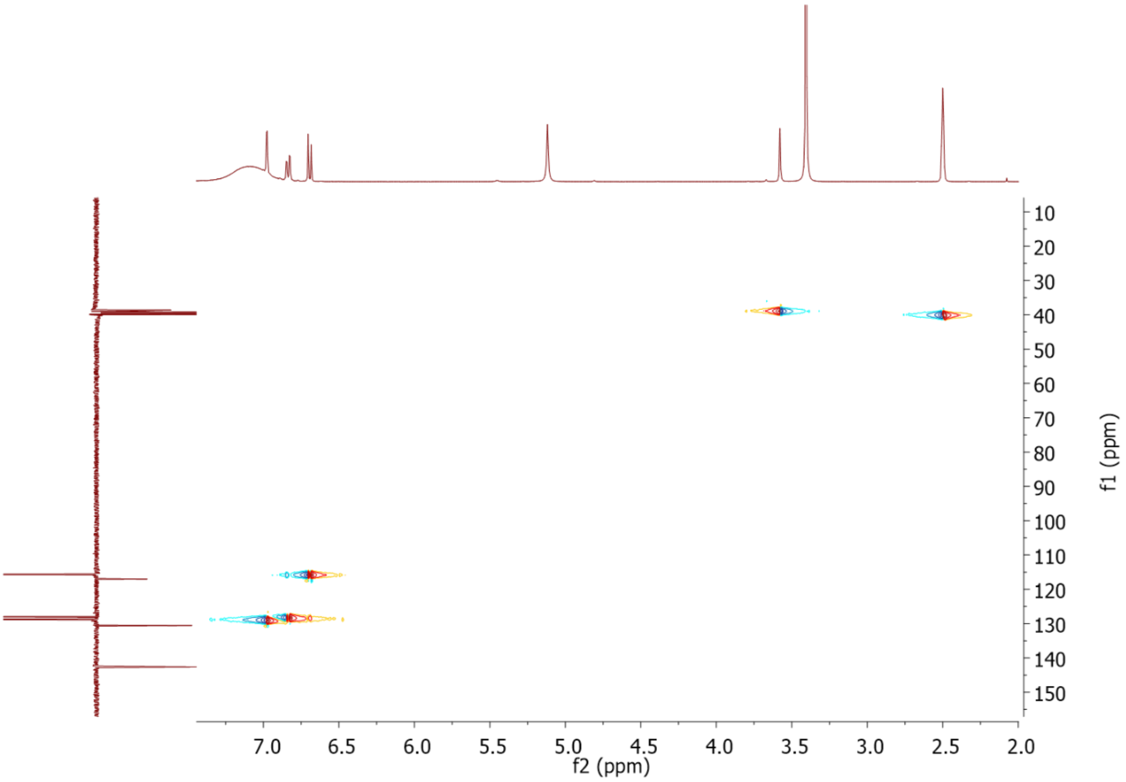

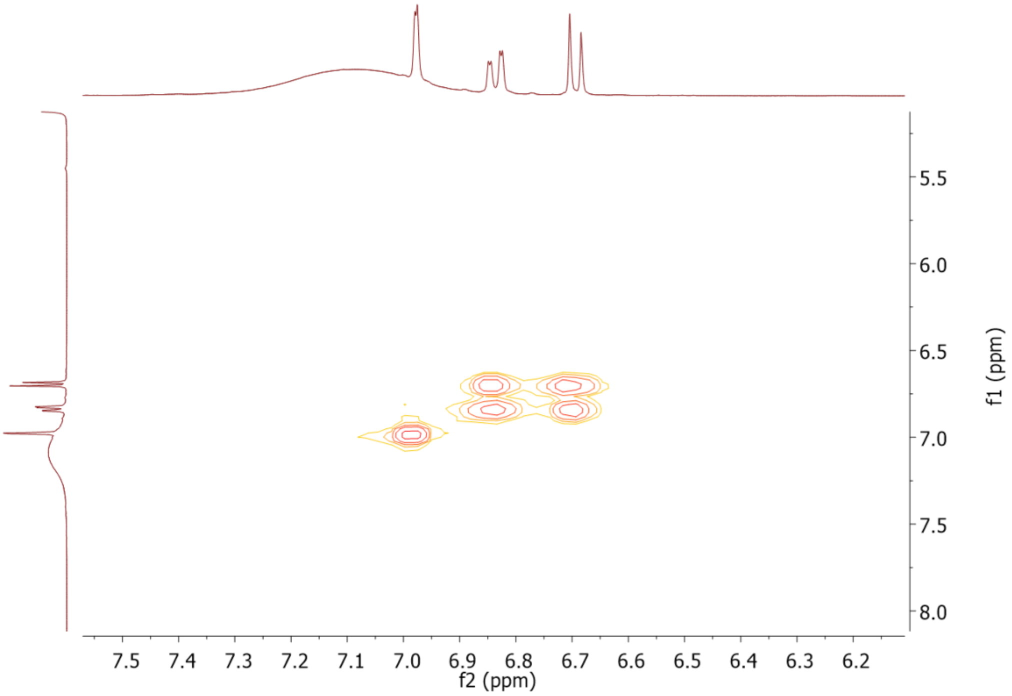

Figure A.23: HSQC spectrum of L3, in DMSO-d₆ (top) and amplification of the aliphatic region (bottom).

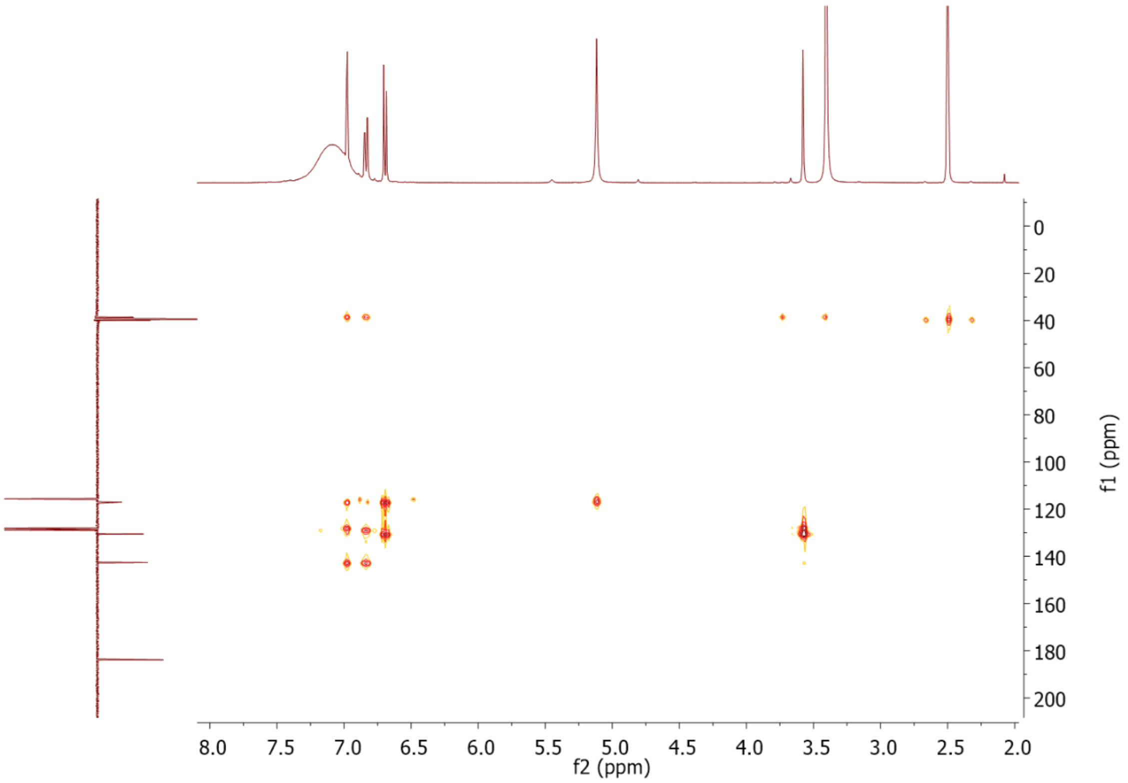

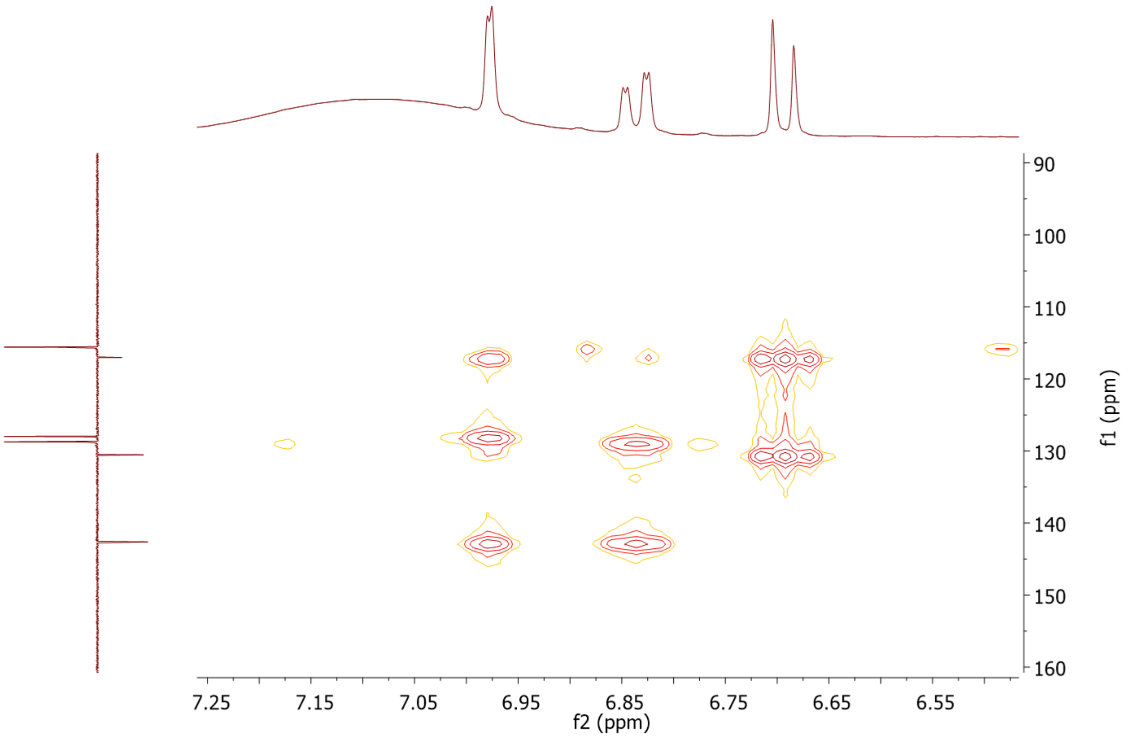

Figure A.24: HMBC spectrum of L3, in DMSO-d_6. (top) and amplification of the aromatic region (bottom).

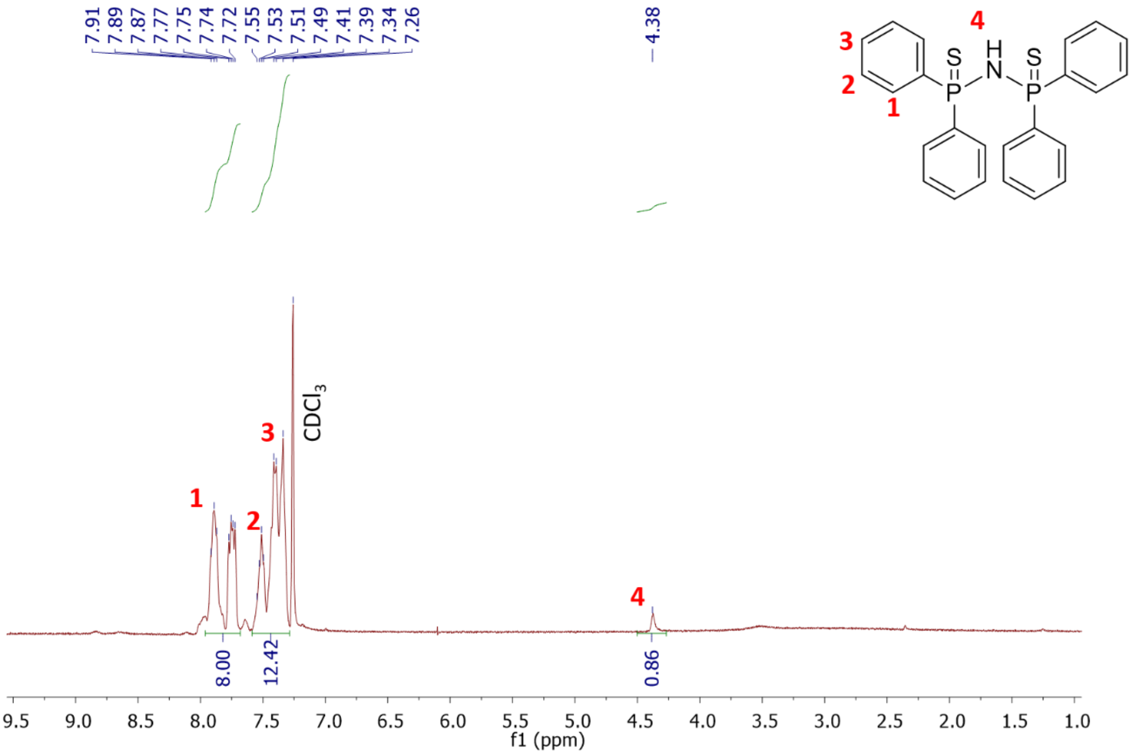

Figure A.25: ^{1}H NMR spectrum of L4, in $CDCl_3$.

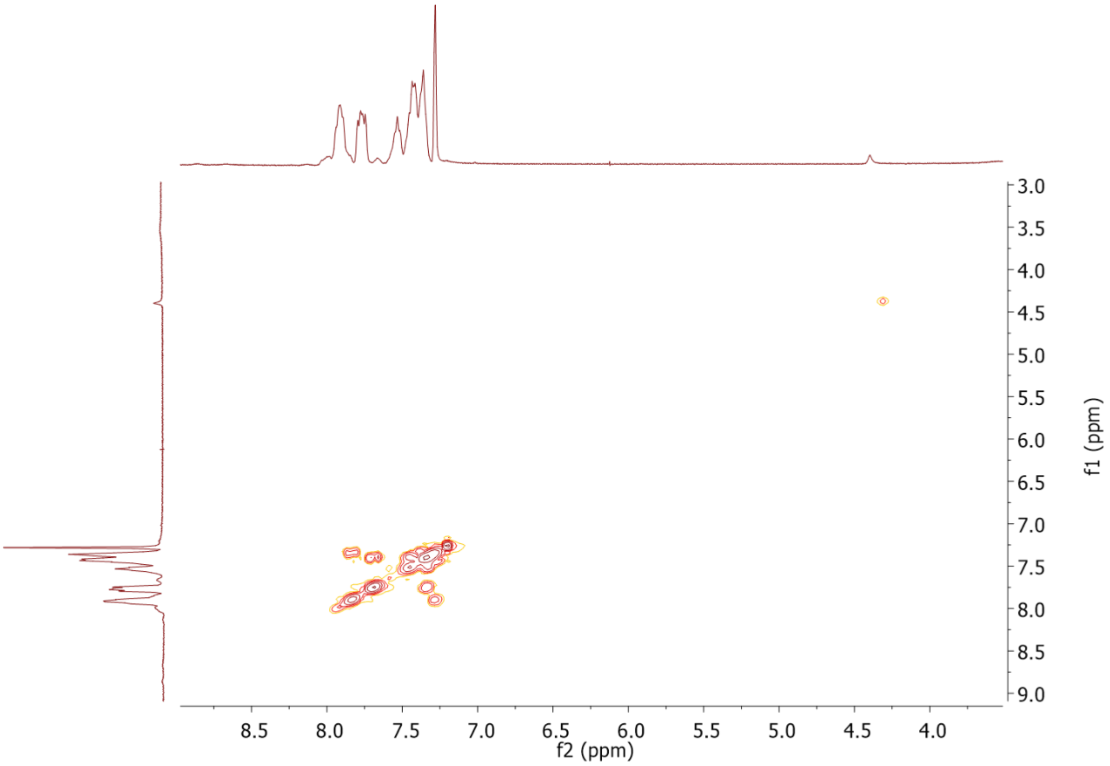

Figure A.26: 2D COSY NMR spectrum of L4, in $CDCl_3$

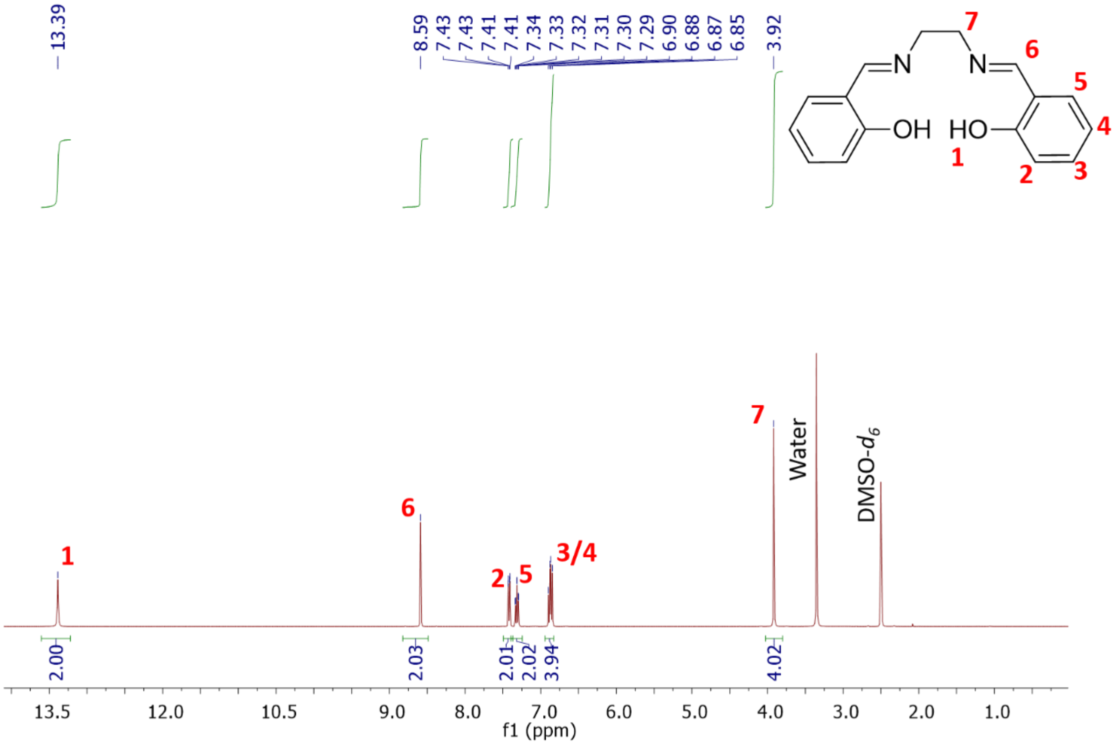

Figure A.27: ^{1}H NMR spectrum of L5, in DMSO-d$_6$.

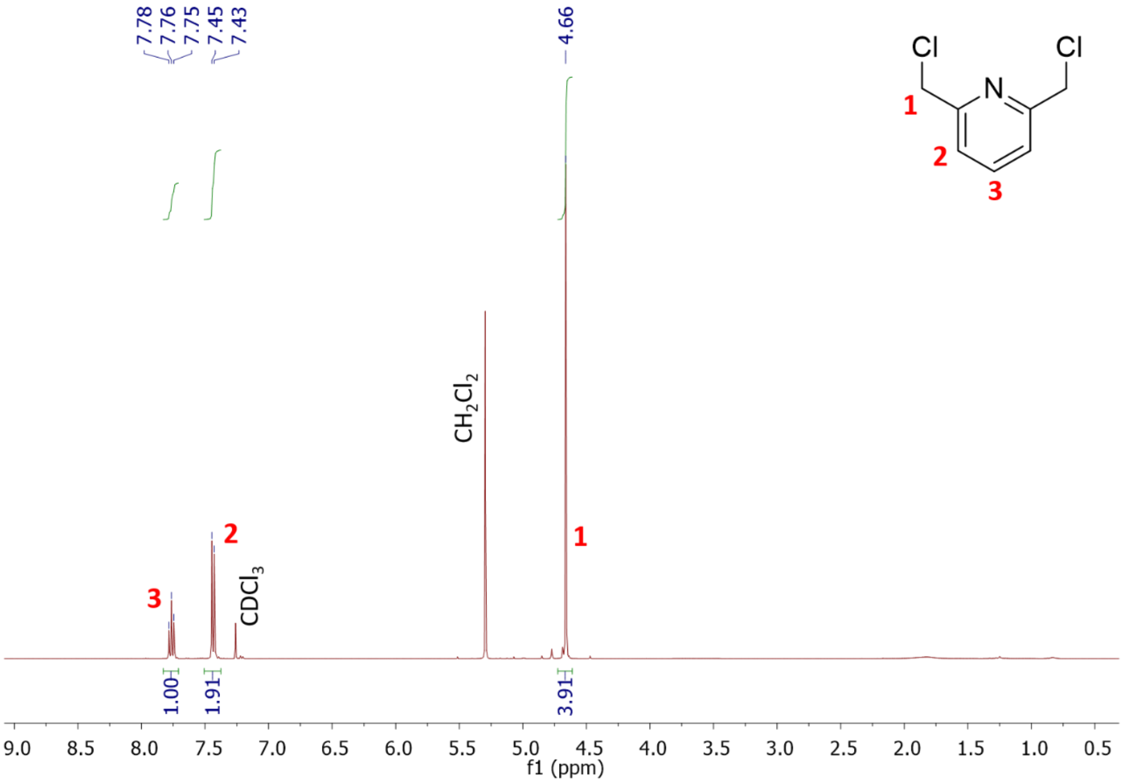

Figure A.28: ^{1}H NMR spectrum of I4, in $CDCl_3$.

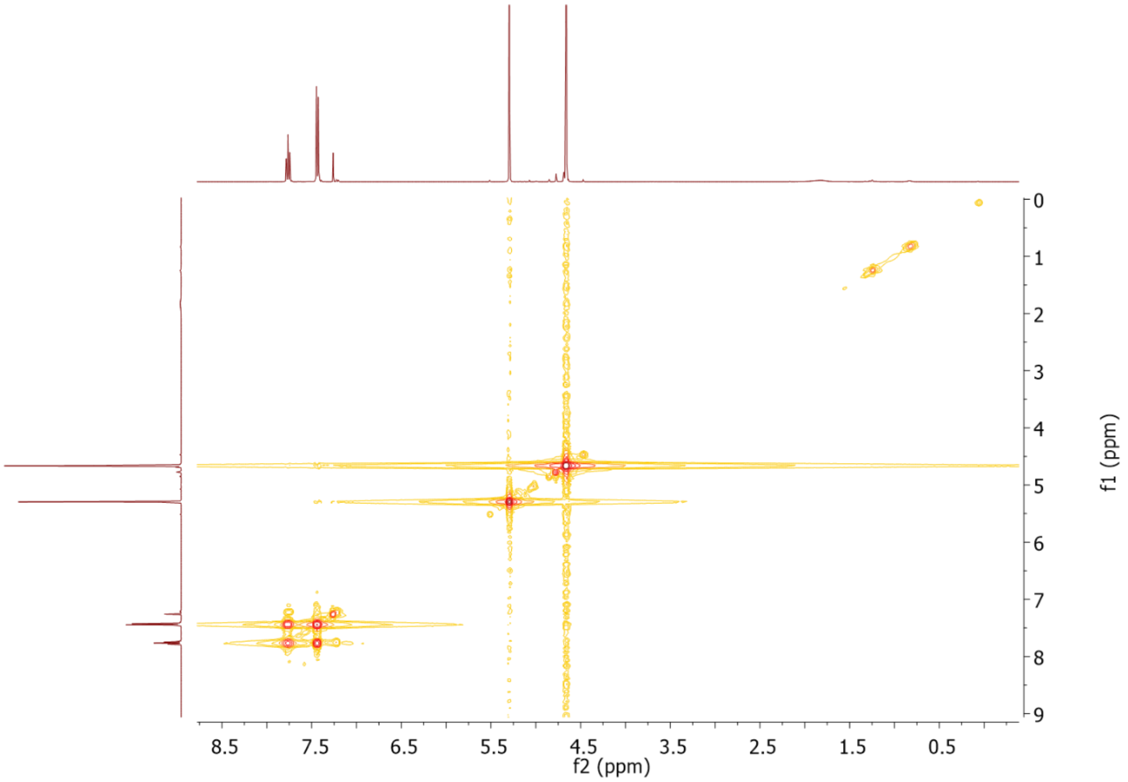

Figure A.29: 2D COSY NMR spectrum of I4, in $CDCl_3$.

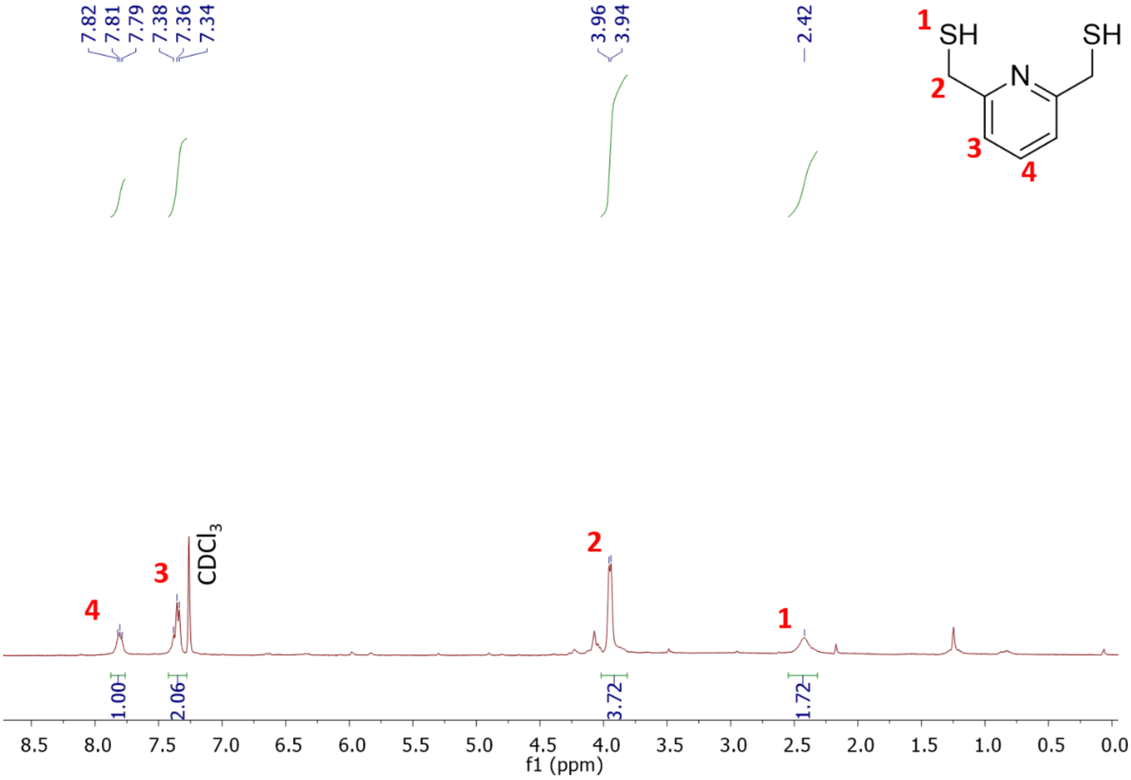

Figure A.30: ^{1}H NMR spectrum of L6, in CDCl$_3$.

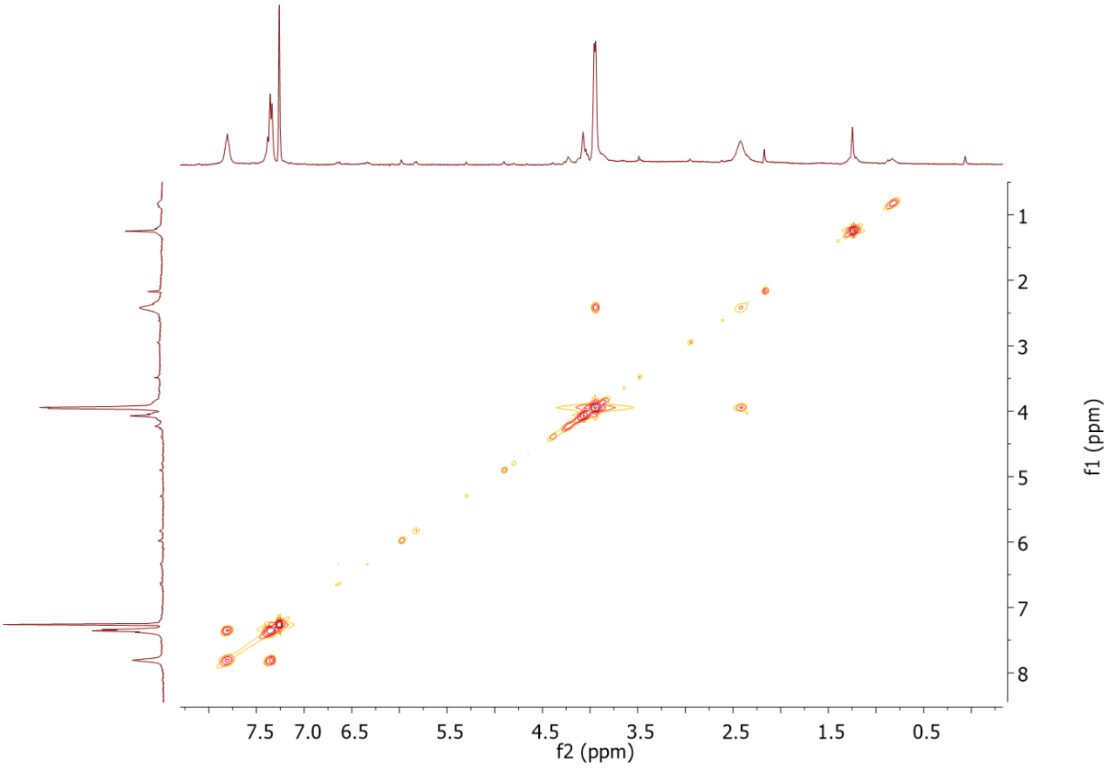

Figure A.31: 2D COSY spectrum of L6, in $CDCl_3$.

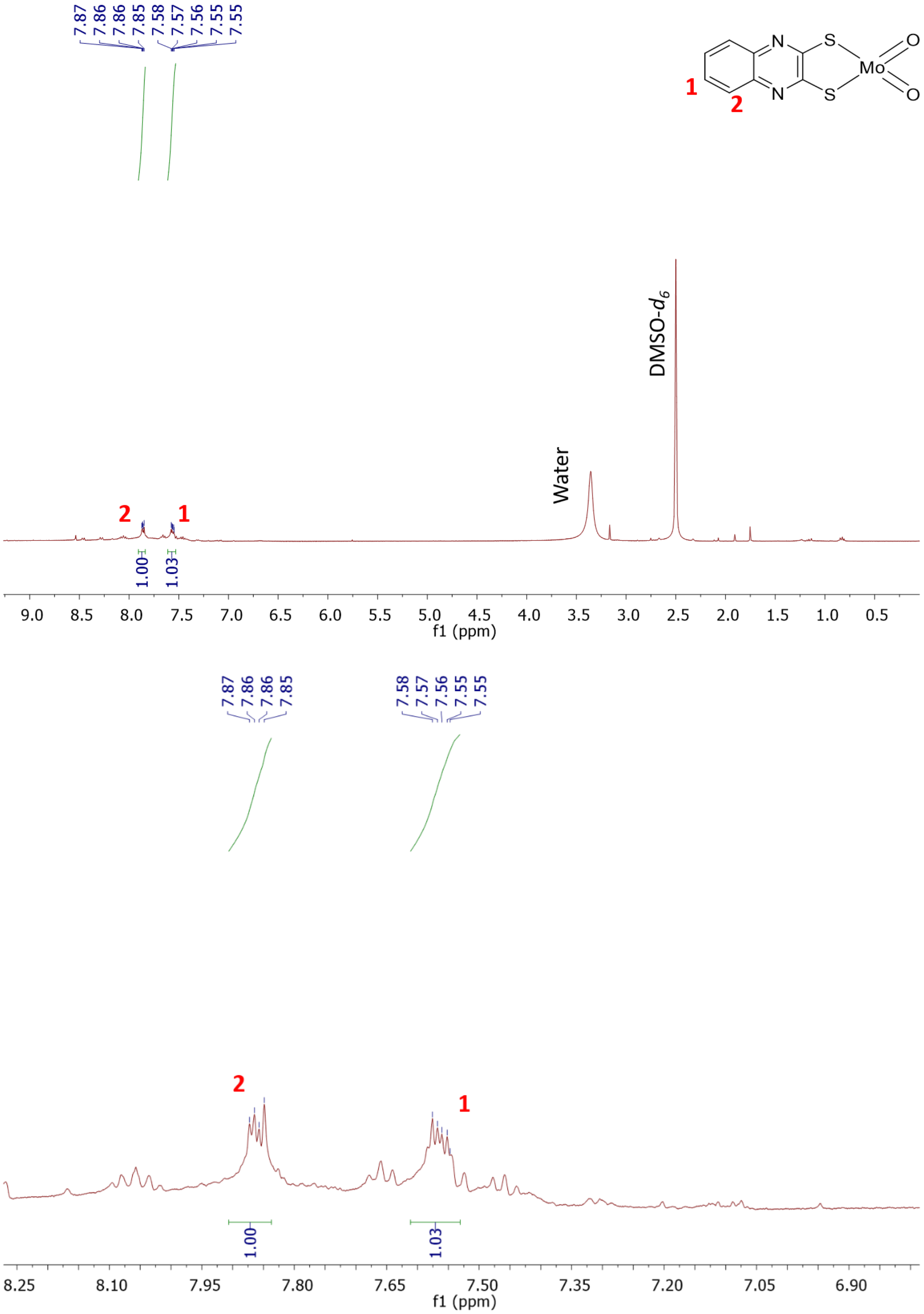

Figure A.32: ^{1}H NMR spectrum of M1 (top) and amplification (bottom)of the aromatic region in DMSO-d_6

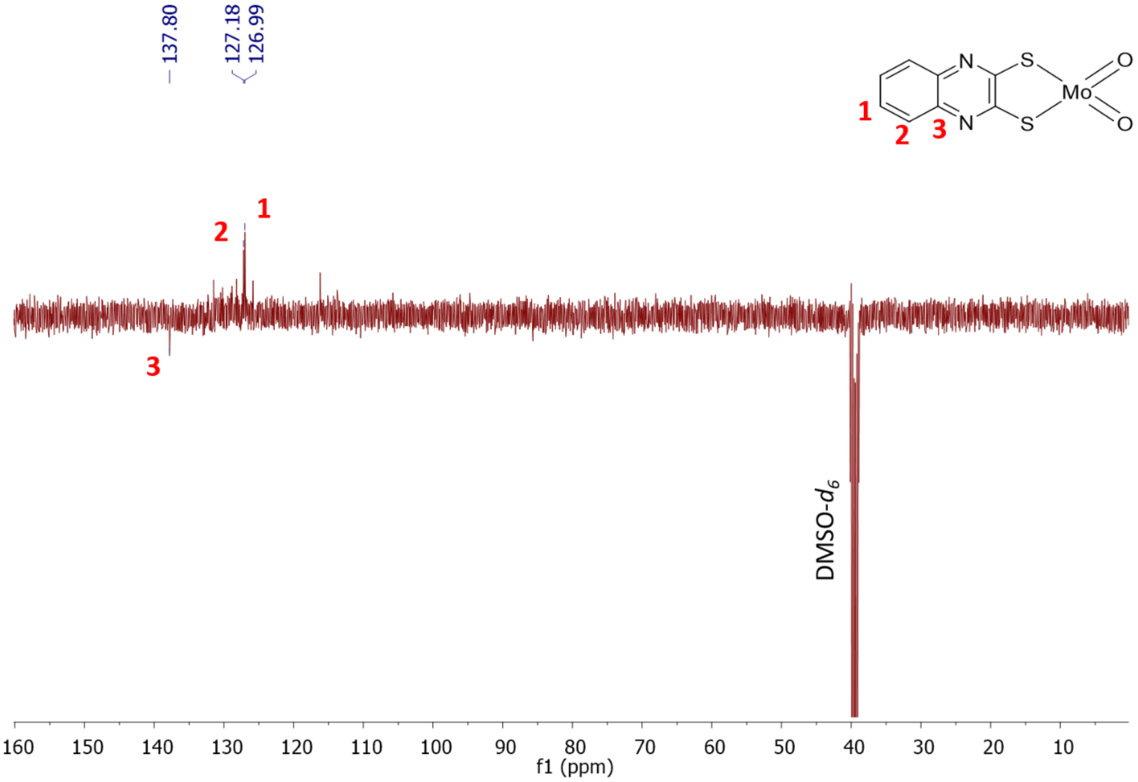

Figure A.33: ***^{13}C APT NMR spectrum of M1 in DMSO-d_6***

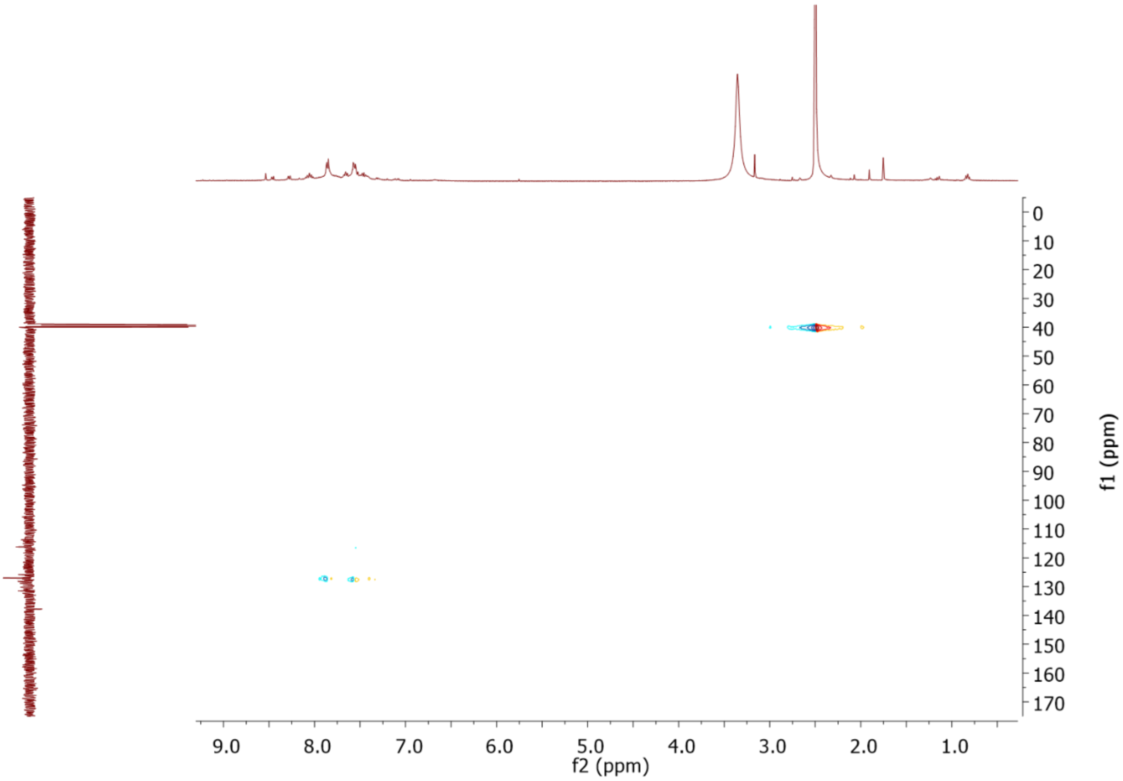

Figure A.34: HSQC spectrum of M1 in DMSO-d_6

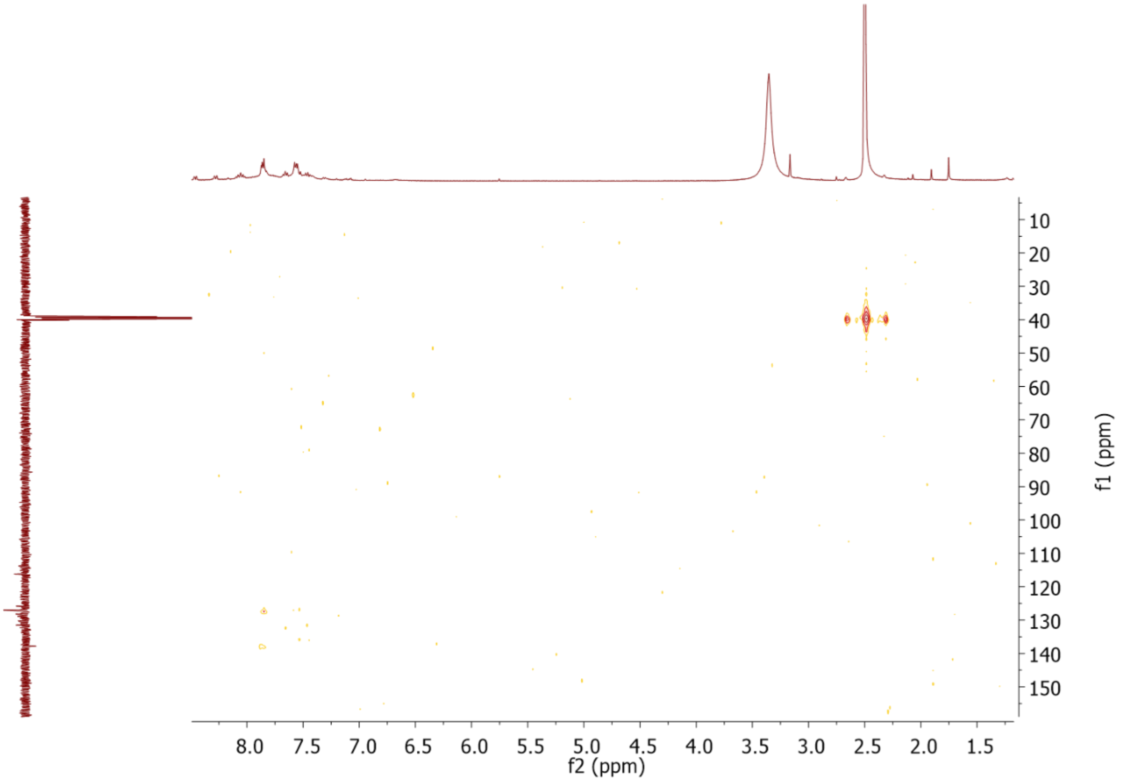

Figure A.35:HMBC spectrum of M1 in DMSO-d_6

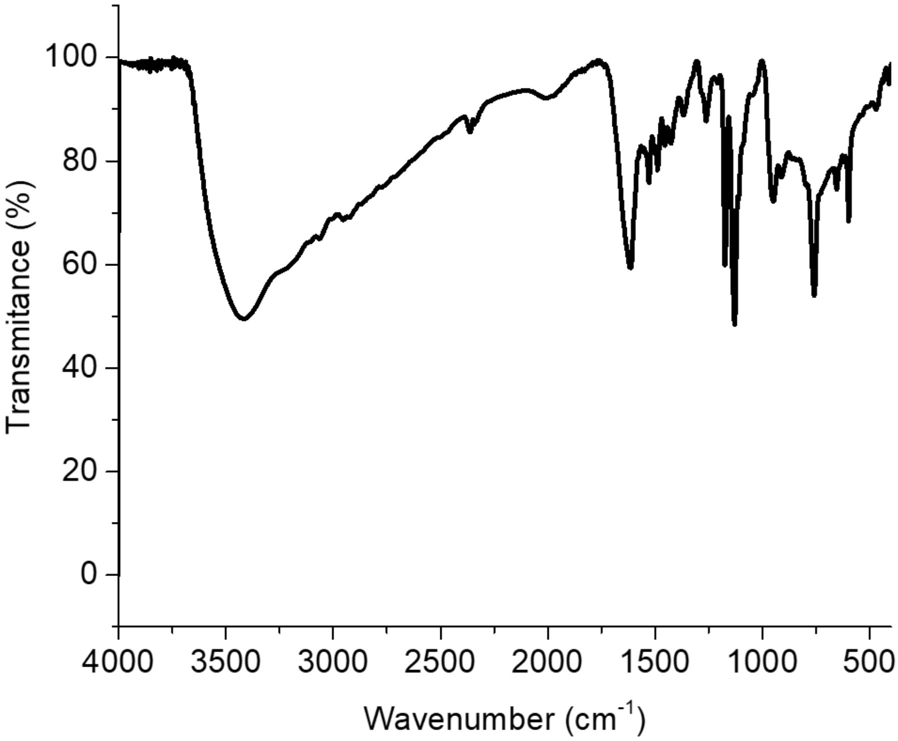

Figure A.36: FTIR spectrum of M1

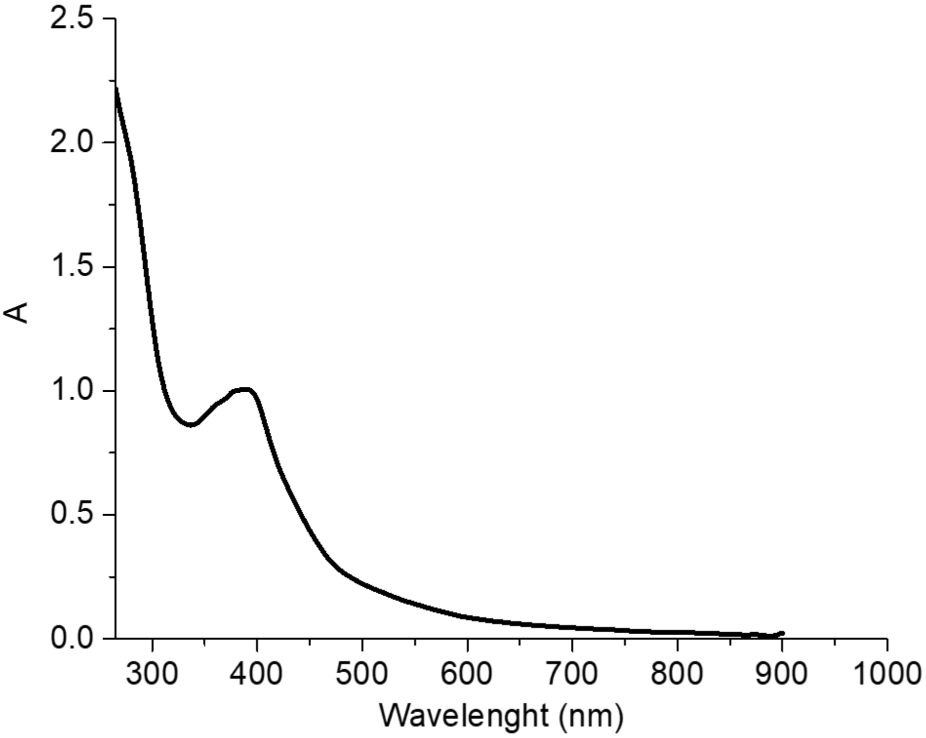

Figure A.37: UV-vis spectrum of M1

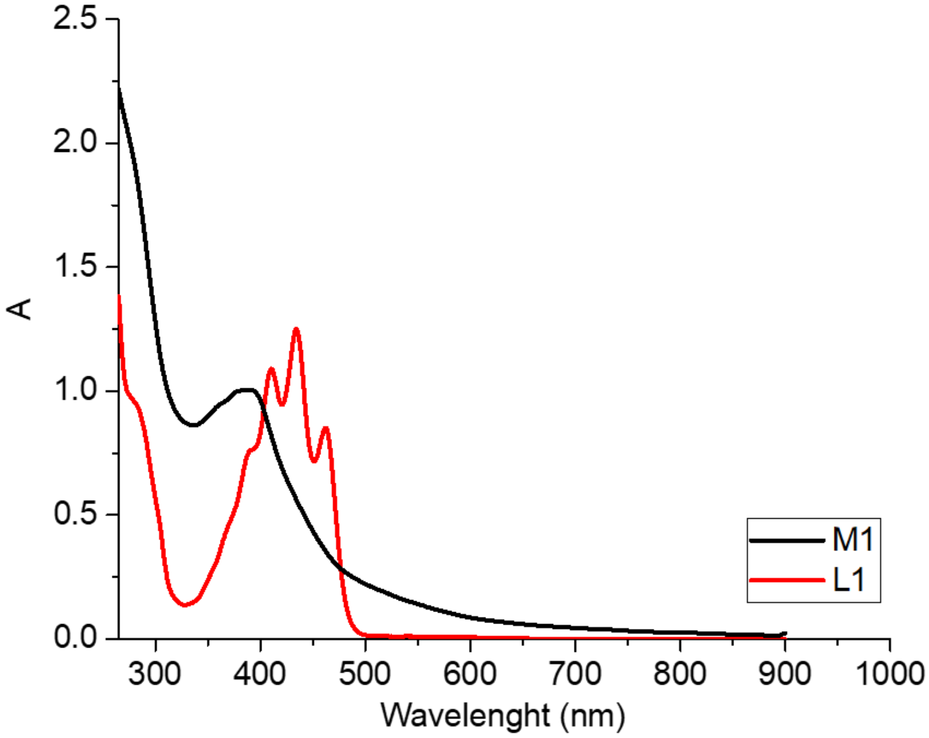

Figure A.38: UV-vis overlay spectrum of M1 and L1

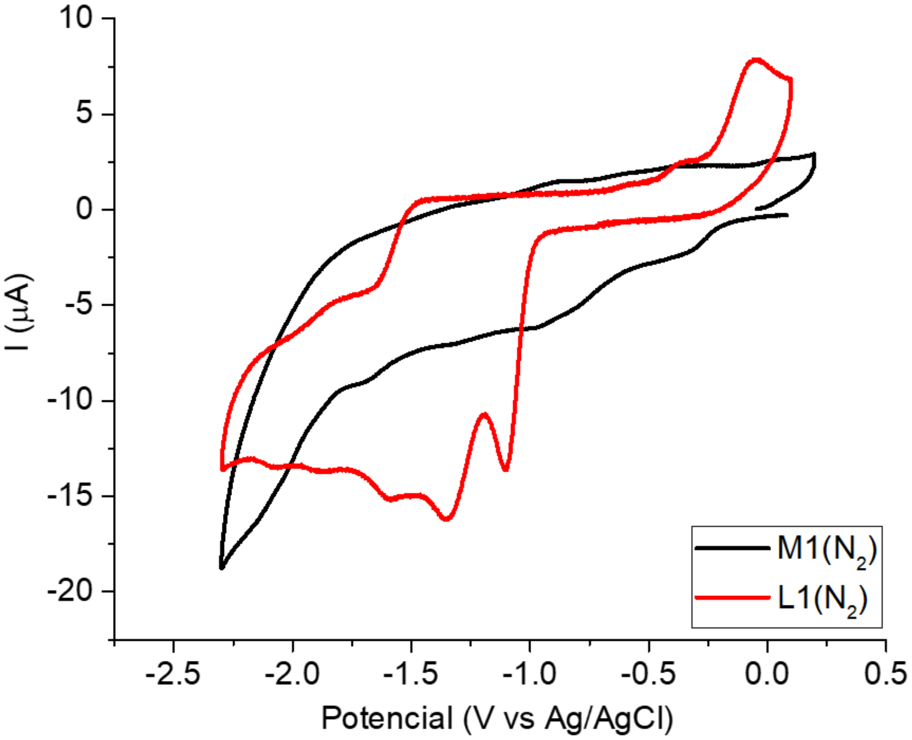

Figure A.39: CV studies overlay of M1 and L1 in DMF(1mM) N_2 saturated solution using $TBAPF_6$ as supporting electrolyte (0.1 M) at 0.1 mV s^{-1}. Glassy carbon (3 mm diameter) was used as working, platinum wire as counter and Ag/AgCl as reference electrodes

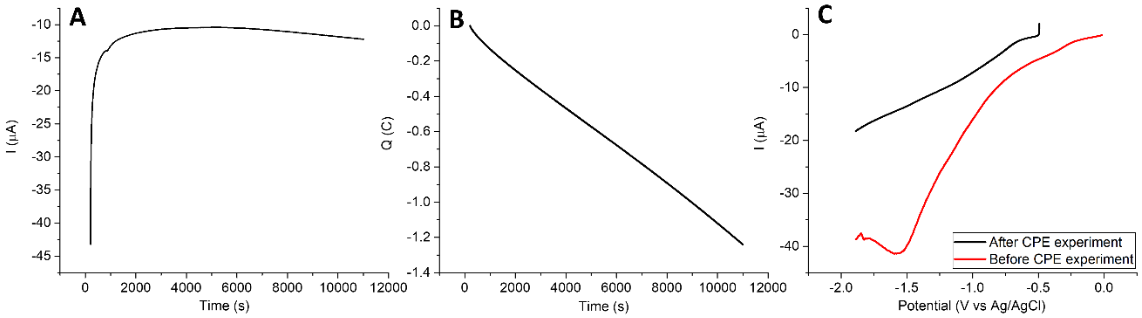

Figure 3.40: Current (A) and charge (B) behaviour during M1 CPE experiment and linear voltammogram before and after CPE assay (C). Assays were carried out in DMF, using TBAPF6 as supporting electrolyte (0.1 M) at 10 mV s-1; glassy carbon was used as working electrode, platinum wire as counter and Ag/AgCl as reference electrode.

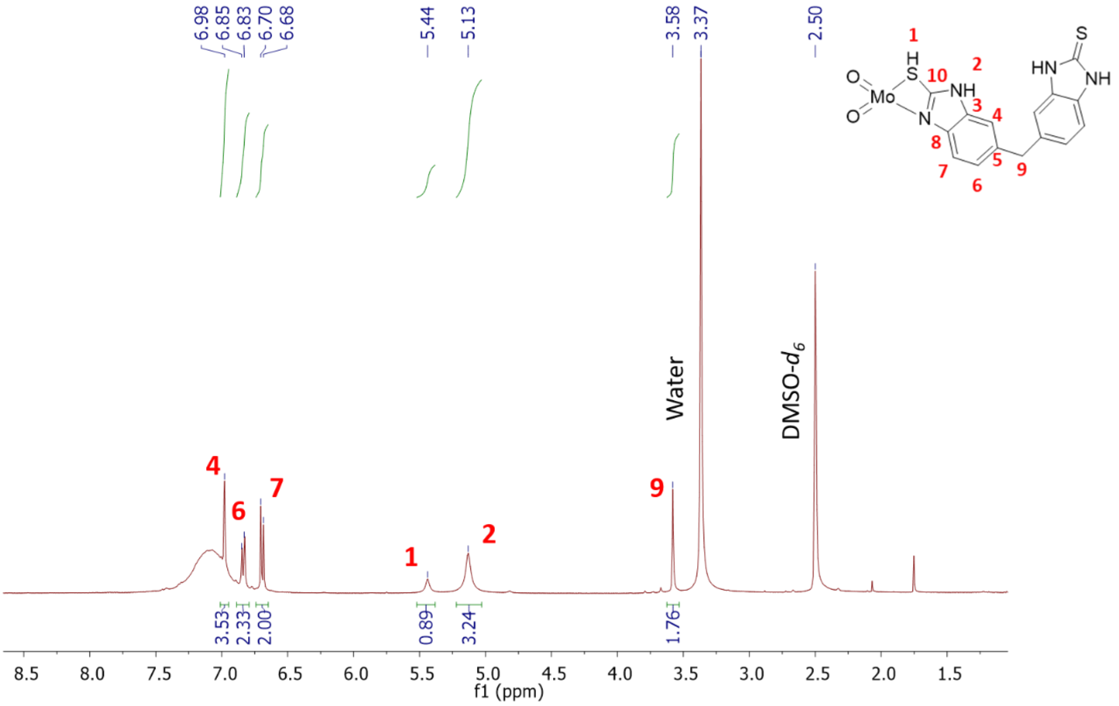

Figure A.41: ^{1}H NMR spectrum of M5 in DMSO-d_6

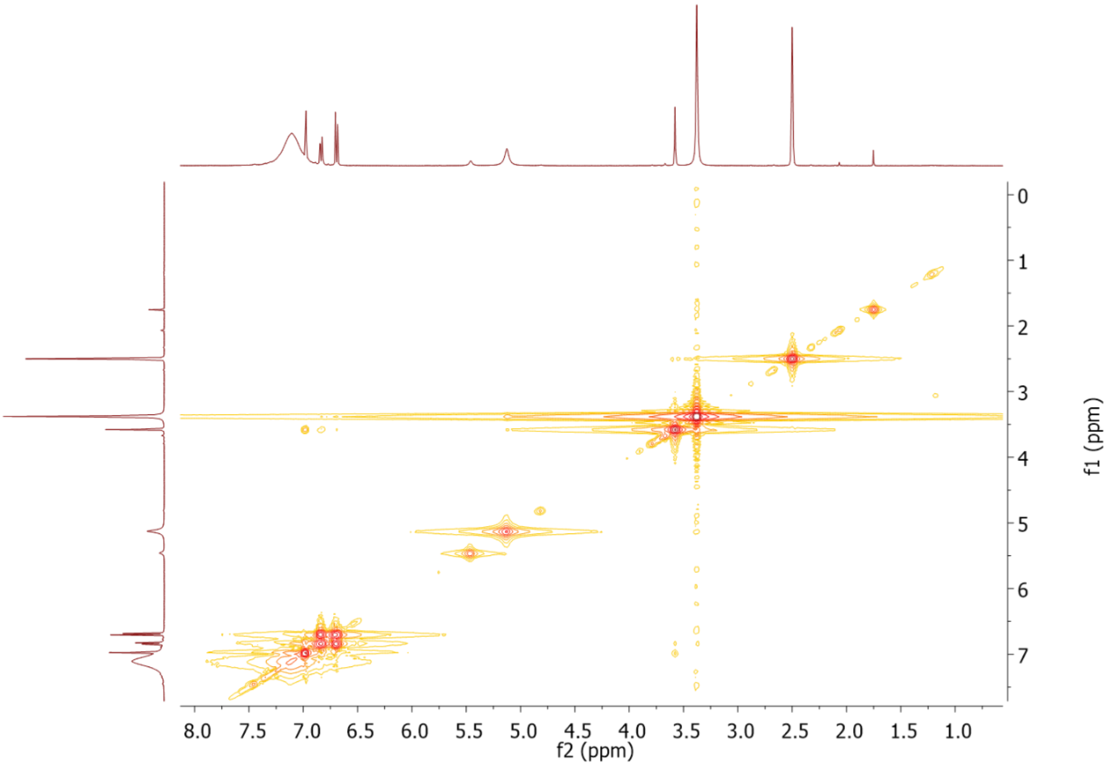

Figure A.42: 2D COSY spectrum of M5

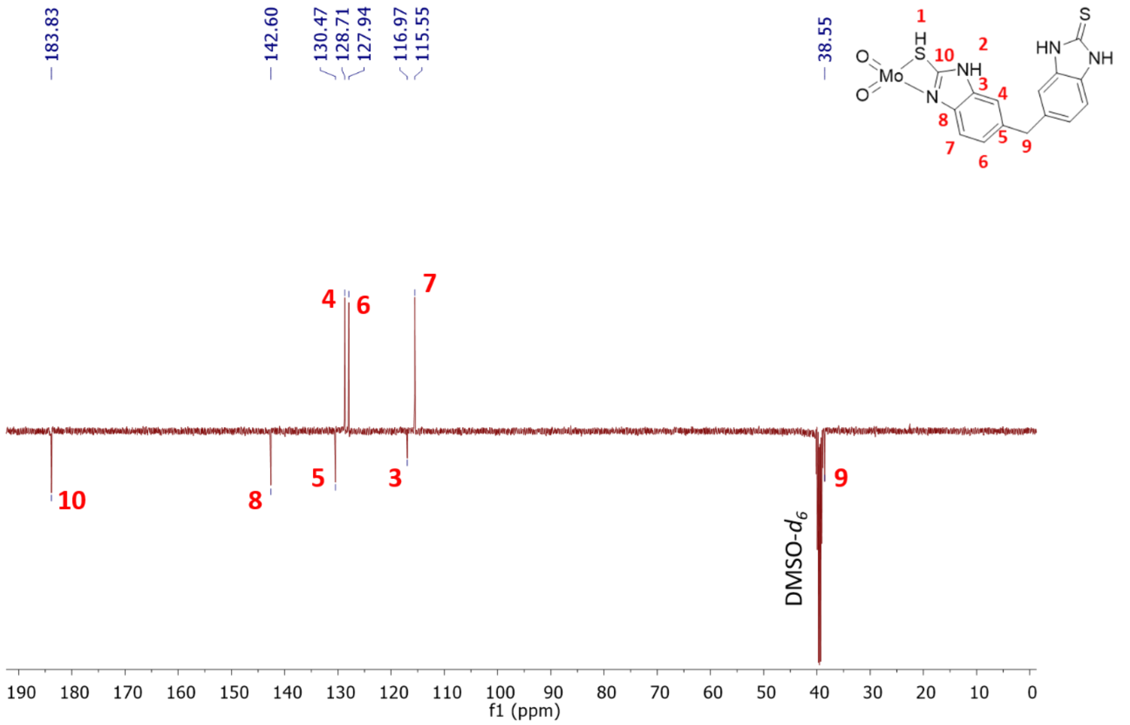

Figure A.43: ^{13}C APT NMR of M5 in DMSO-d_6

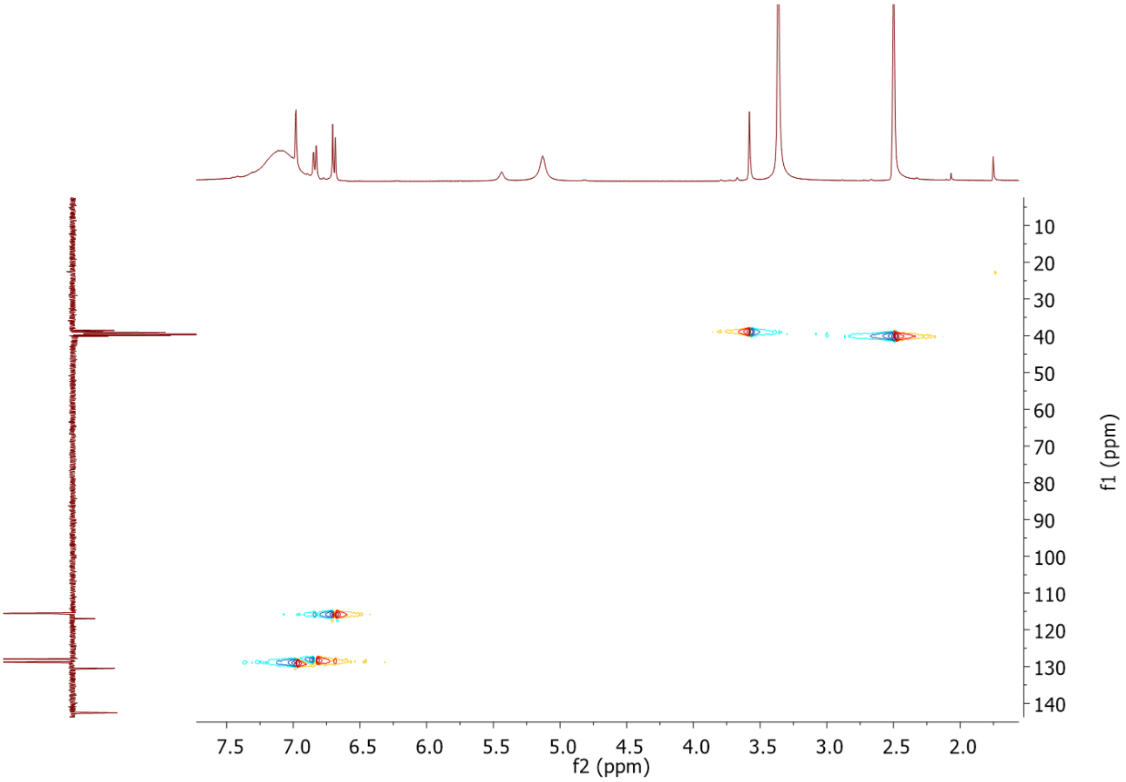

Figure A.44: HSQC NMR spectrum of M5

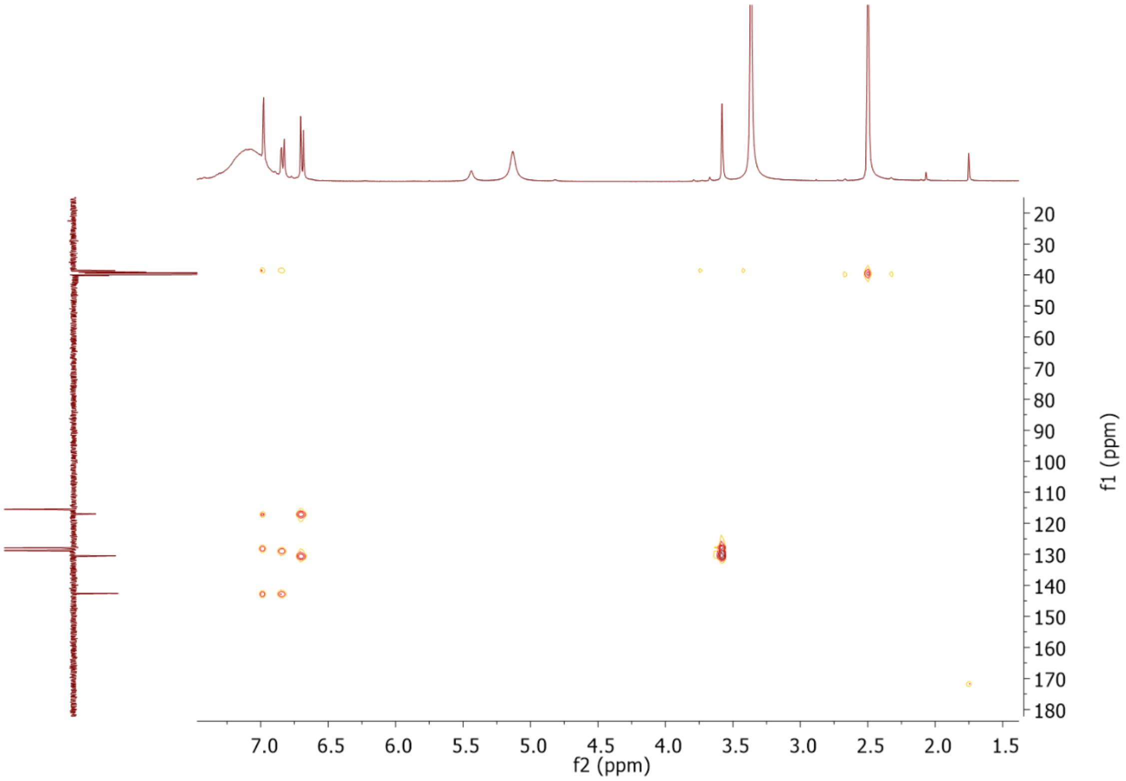

Figure A.45: HMBC spectrum of M5

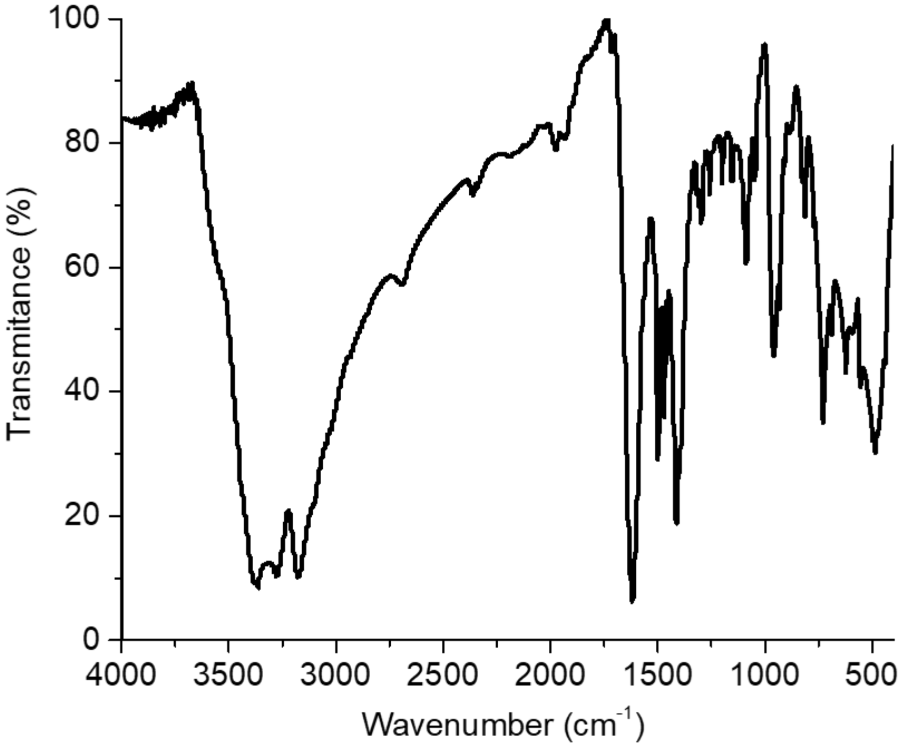

Figure A.46: FTIR spectrum of M5

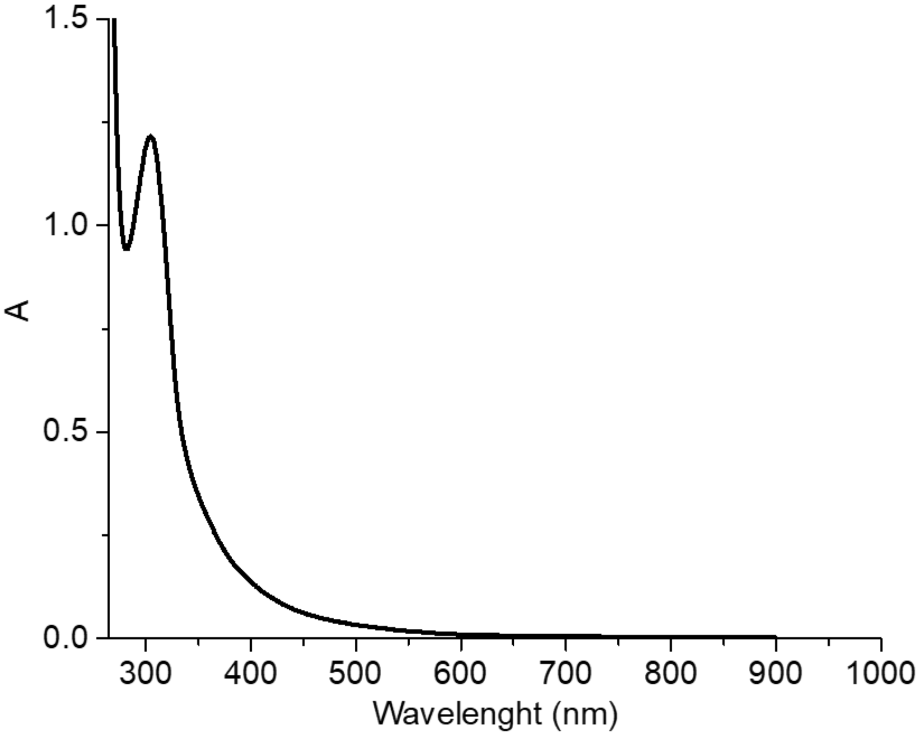

Figure A.47: UV-vis spectrum of M5

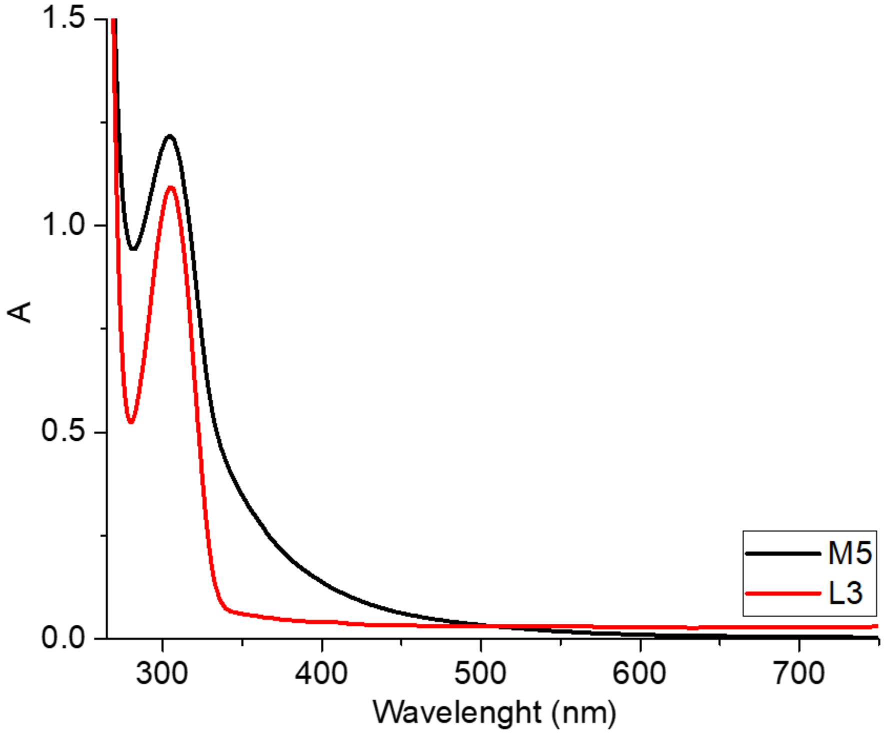

Figure A.48: UV-vis overlay spectrum of M5 and L3

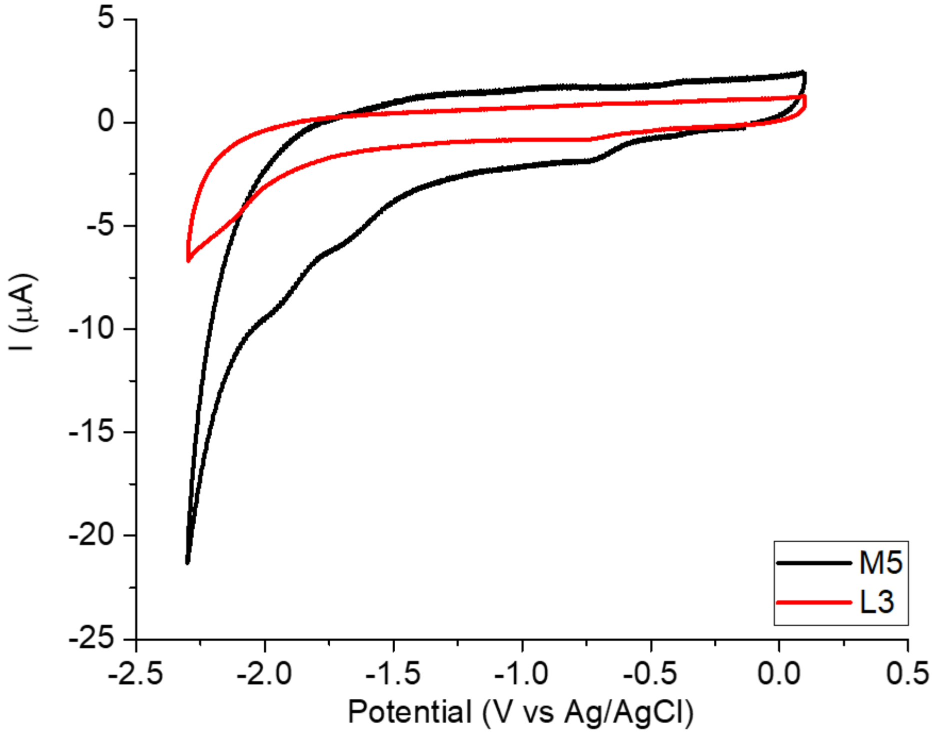

Figure A.49: CV studies overlay of M5 and L3 in DMF(1mM) N_2 saturated solution using $TBAPF_6$ as supporting electrolyte (0.1 M) at 0.1 mV s^{-1}. Glassy carbon (3 mm diameter) was used as working, platinum wire as counter and Ag/AgCl as reference electrodes

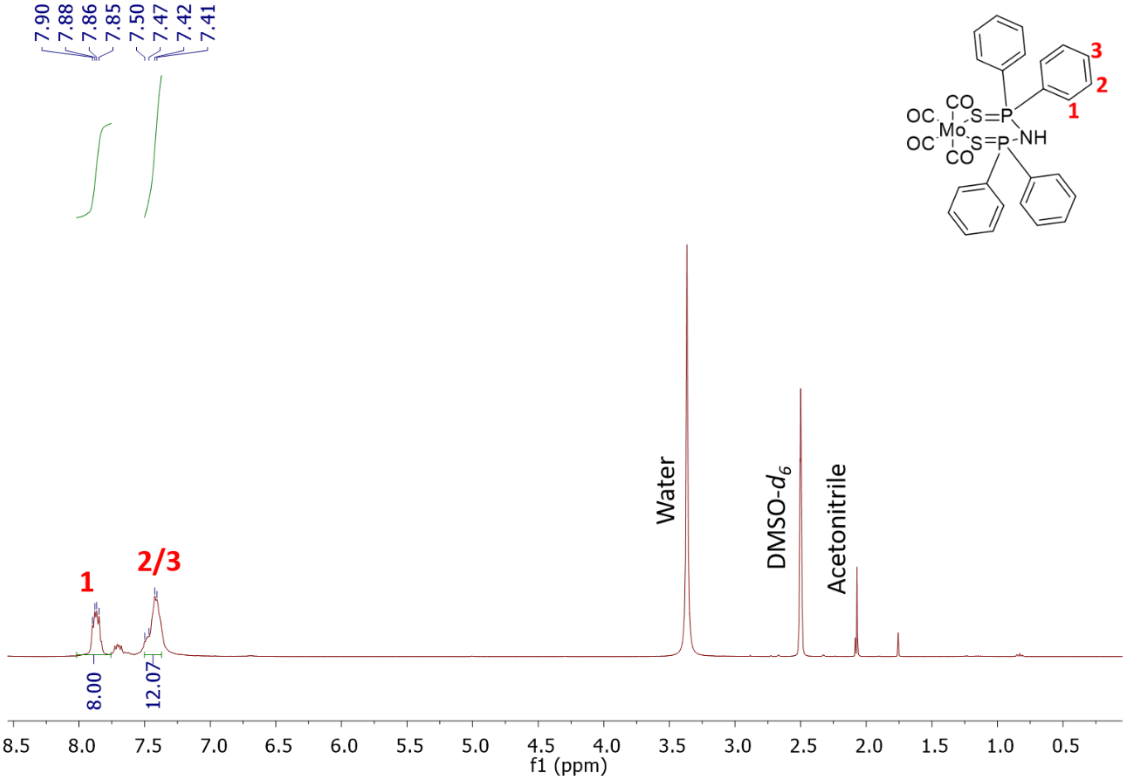

Figure A.50: ^{1}H NMR spectrum of M7 in DMSO-d_6

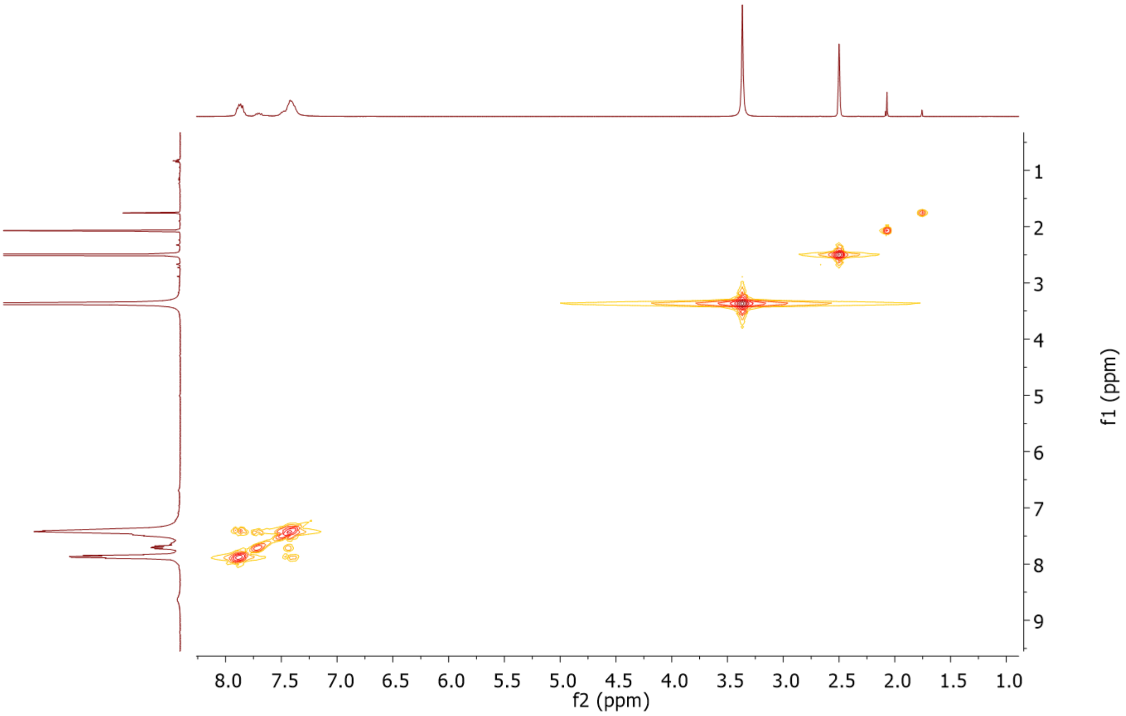

Figure A.51: 2D COSY spectrum of M7 in DMSO-d_6

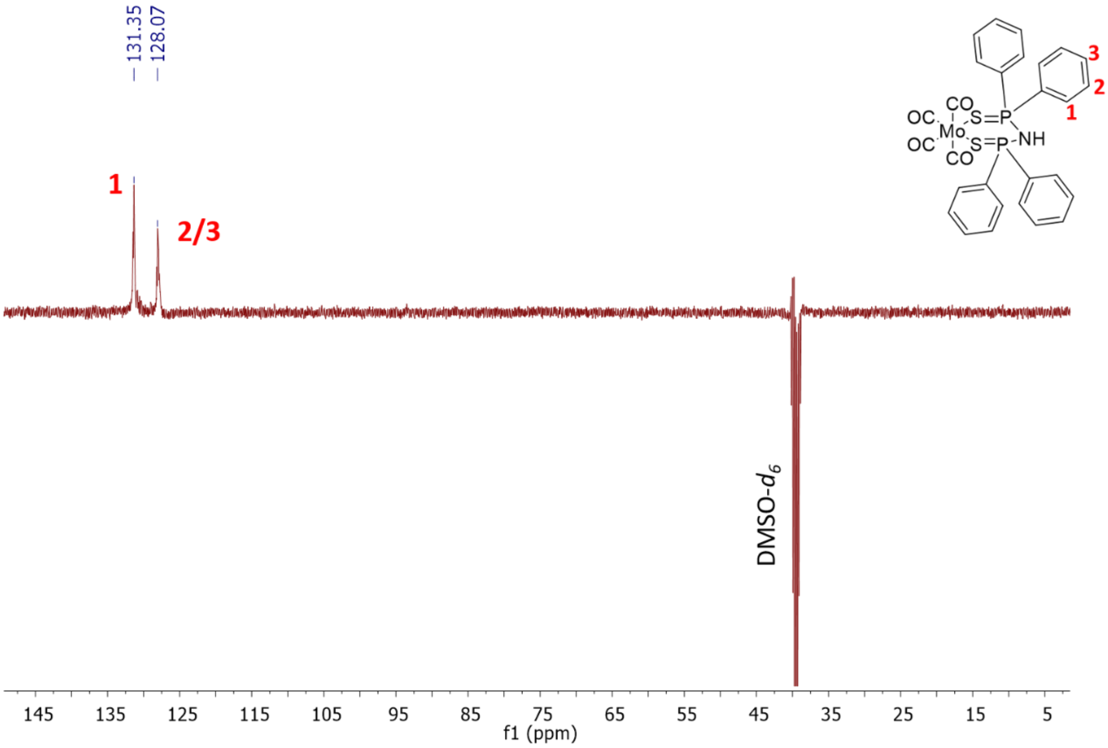

Figure A.52: ^{13}C APT NMR spectrum of M7

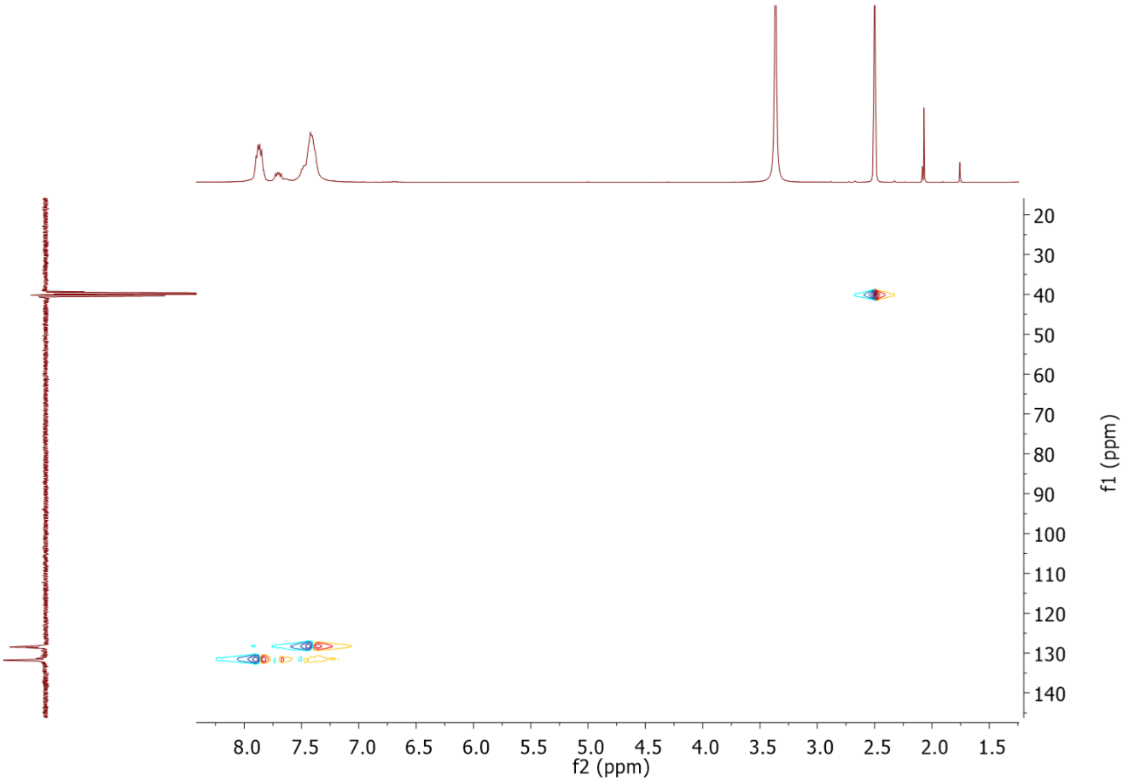

Figure A.53: HSQC spectrum of M7

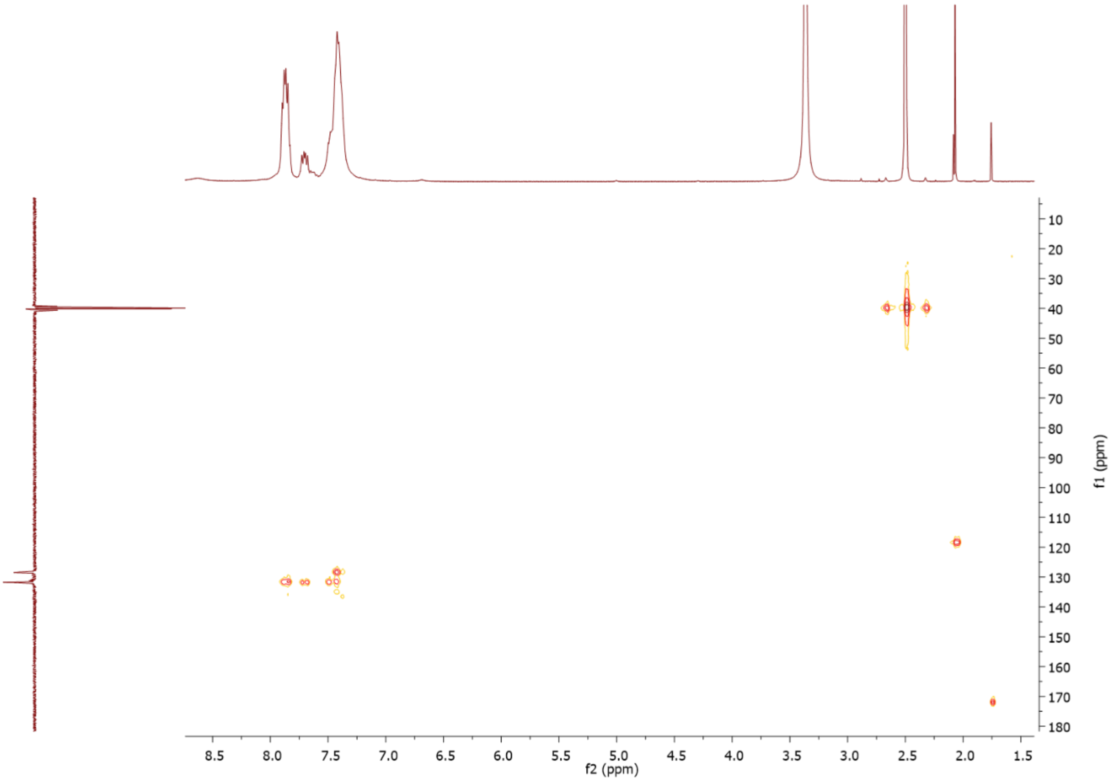

Figure A.54: HMBC spectrum of M7

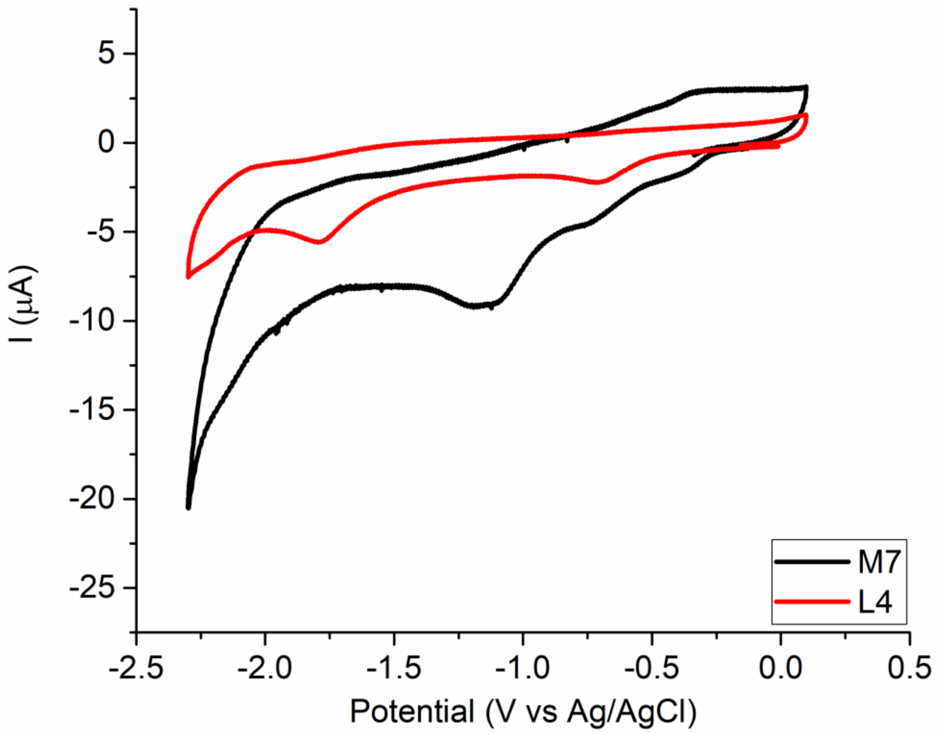

Figure A.55: CV studies overlay of M7 and L4 in DMF(1mM) N_2 saturated solution using $TBAPF_6$ as supporting electrolyte (0.1 M) at 0.1 mV s^{-1}. Glassy carbon (3 mm diameter) was used as working, platinum wire as counter and Ag/AgCl as reference electrodes

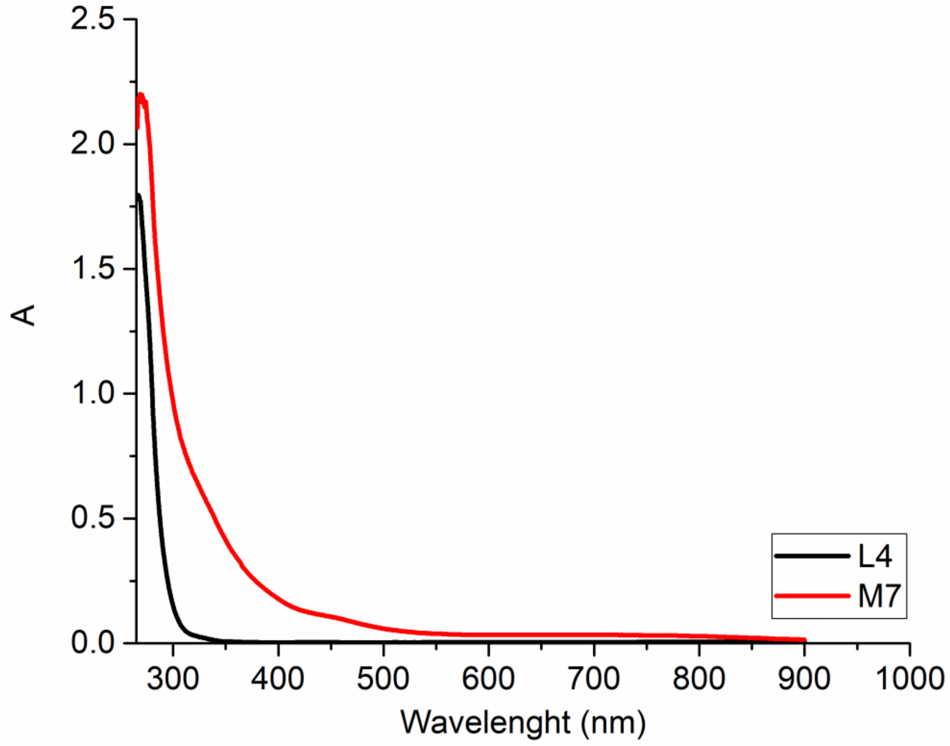

Figure A.56: UV-vis overlay spectra of M7 and L4

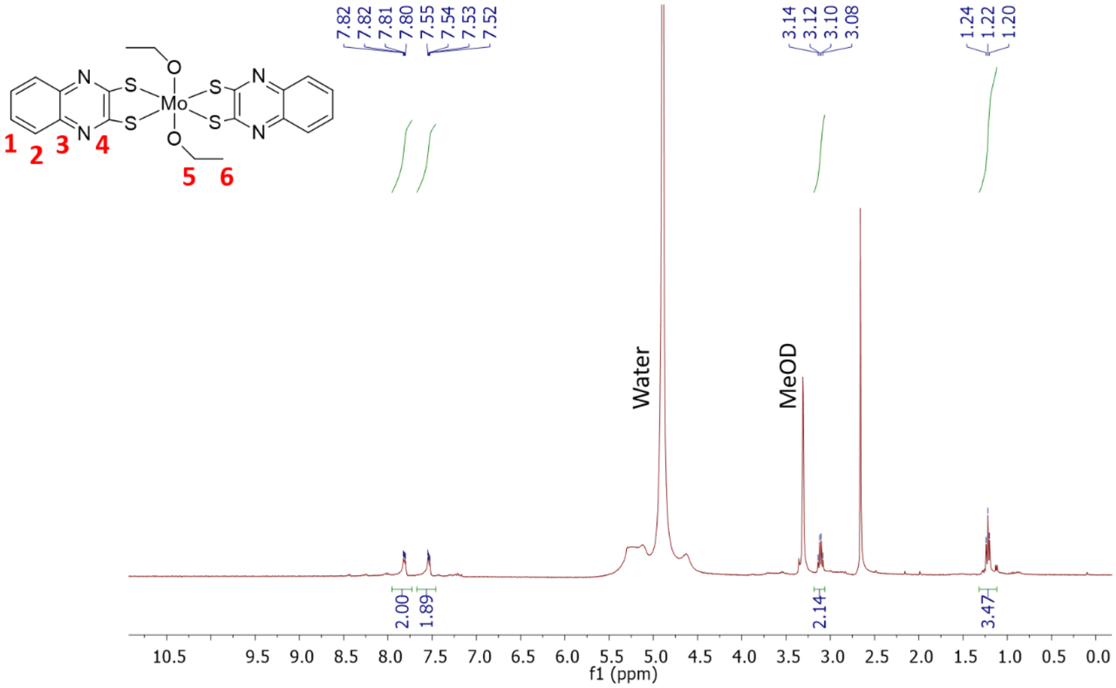

Figure A.57: ^{1}H NMR spectrum of M2 in DMSO-d$_6$

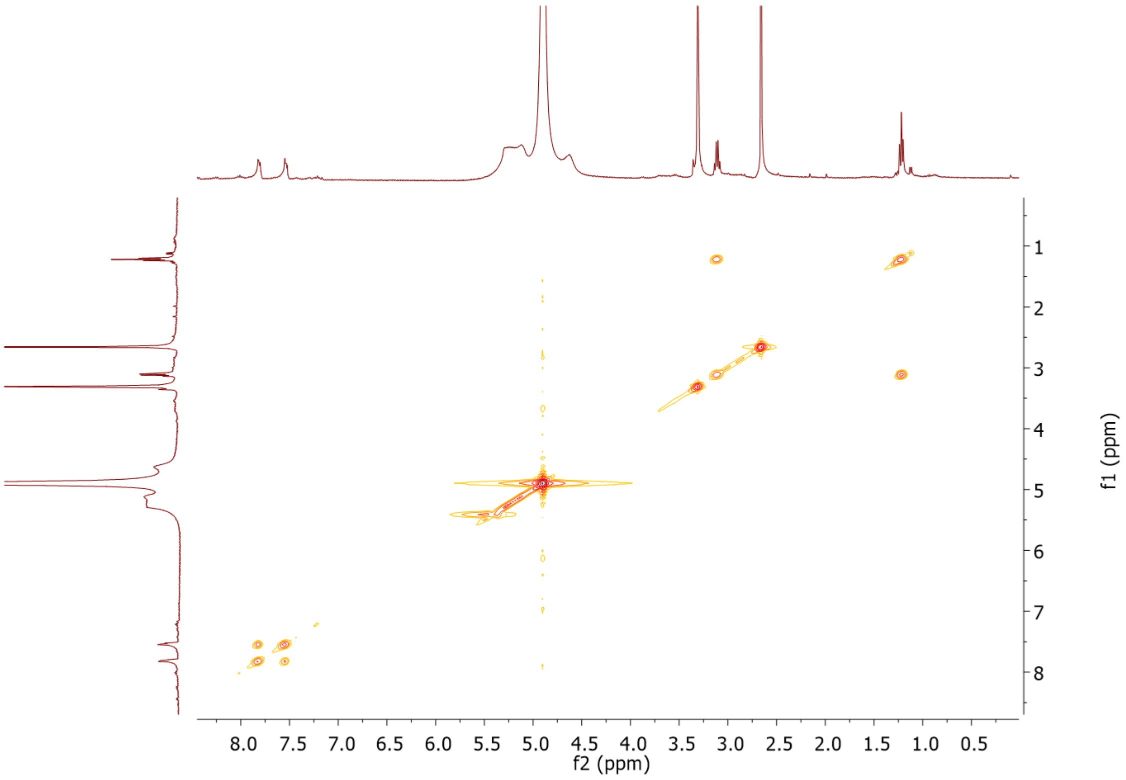

Figure A.58: 2D COSY spectrum of M2 in DMSO-d_6

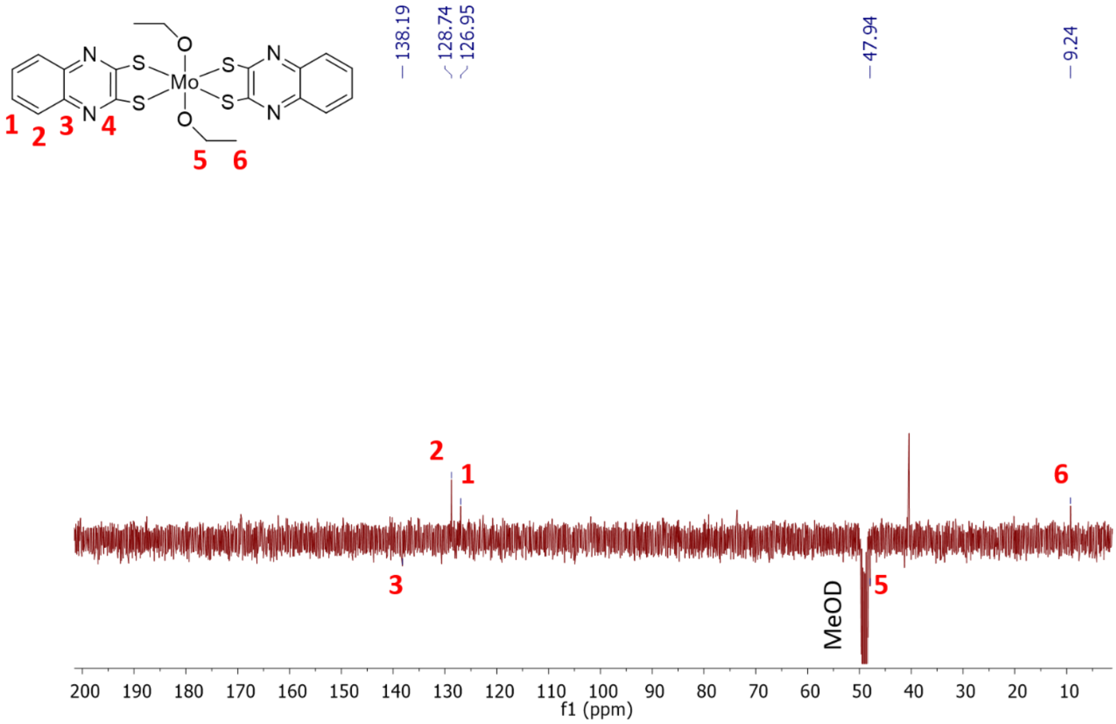

Figure A.59: ^{13}C APT NMR spectrum of M2

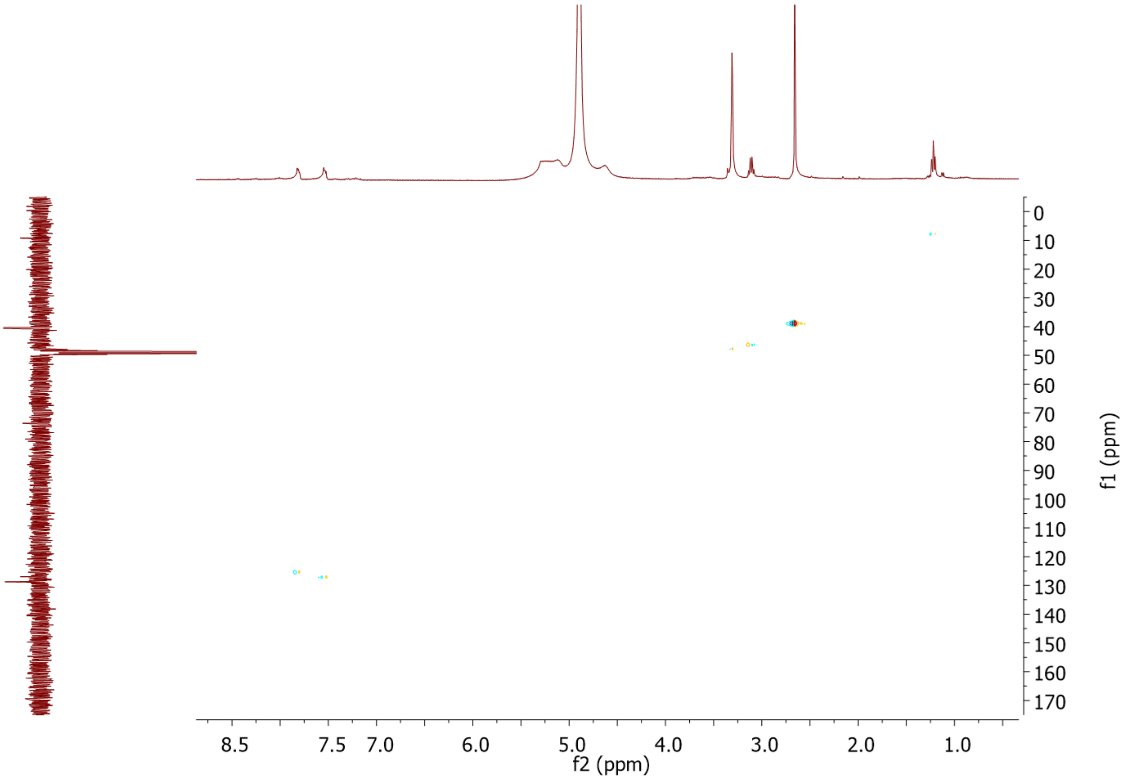

Figure A.60: HSQC spectrum of M2 in DMSO-d_6

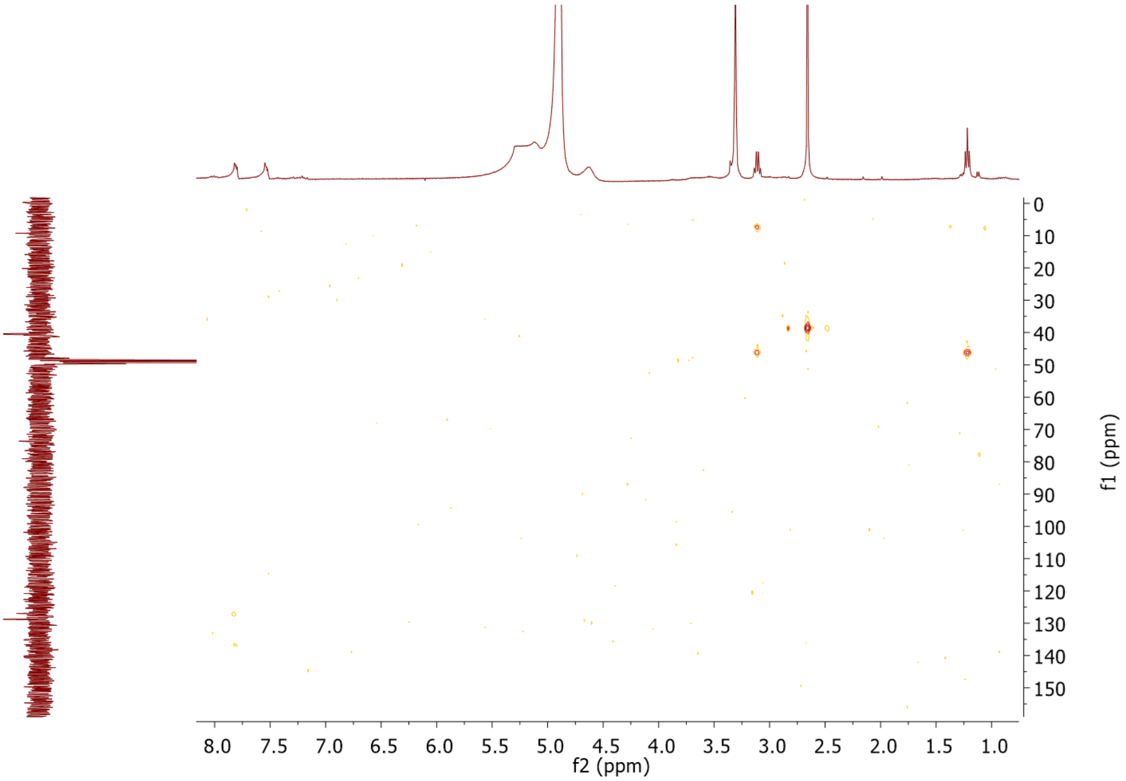

Figure A.61: HMBC spectrum of M2

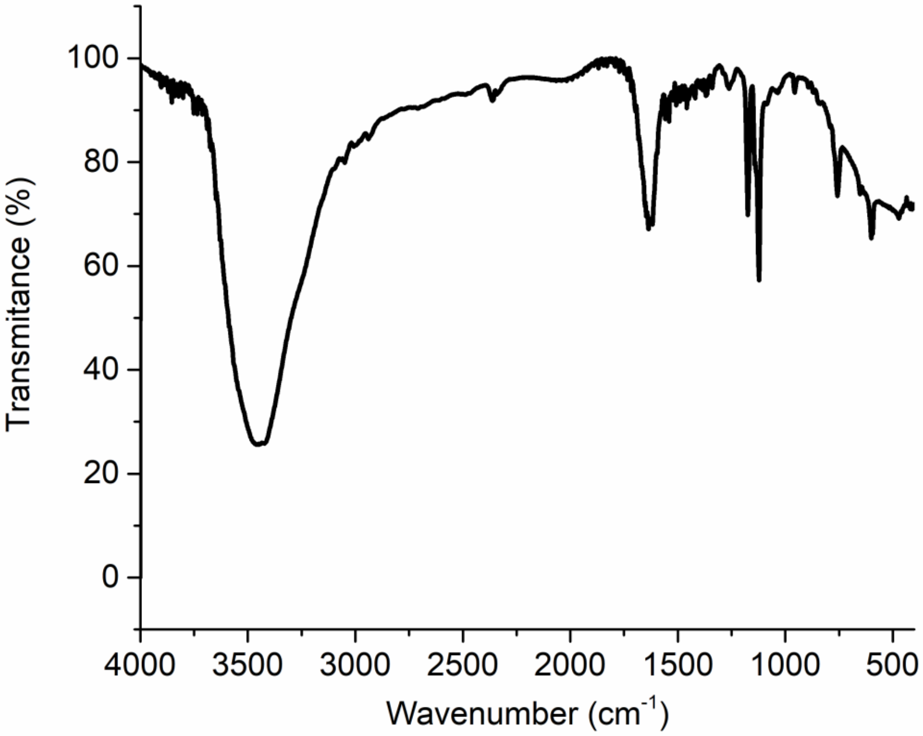

Figure A.62: FTIR spectrum of M2

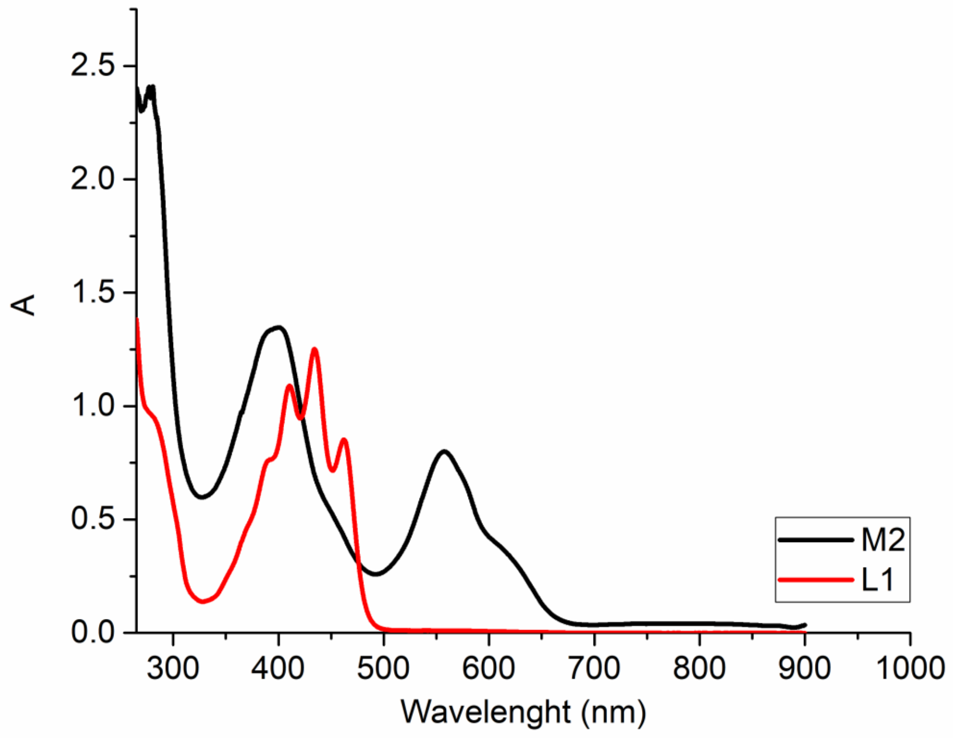

Figure A.63: UV-vis overlay spectra of M2 and L1

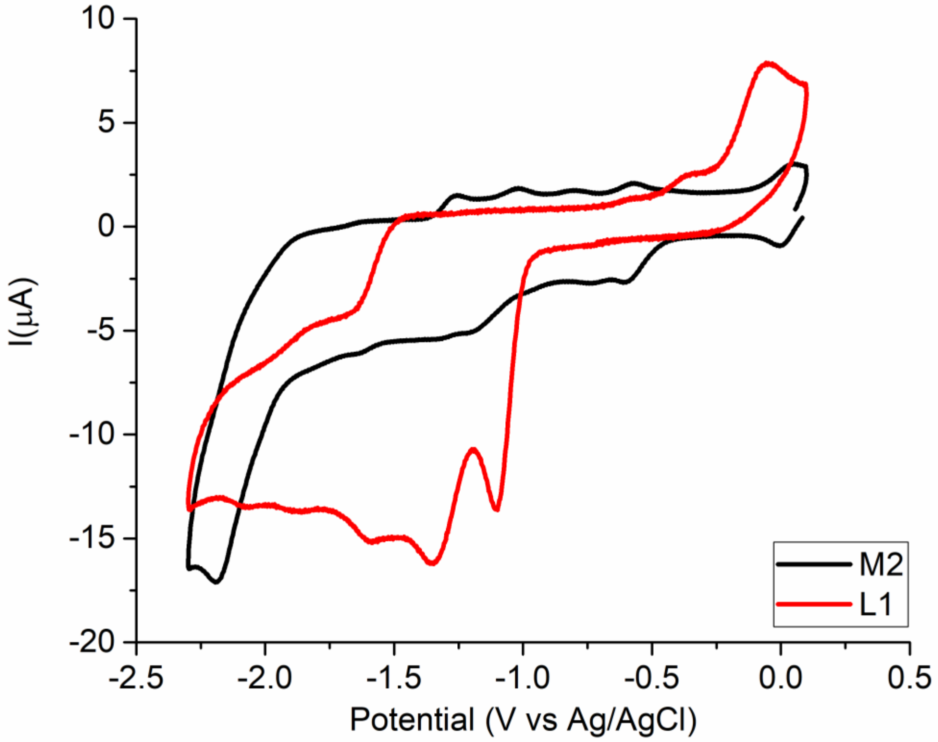

Figure A.64: CV studies overlay of M2 and L1 in DMF(1mM) N_2 saturated solution using $TBAPF_6$ as supporting electrolyte (0.1 M) at 0.1 mV s^{-1}. Glassy carbon (3 mm diameter) was used as working, platinum wire as counter and Ag/AgCl as reference electrodes

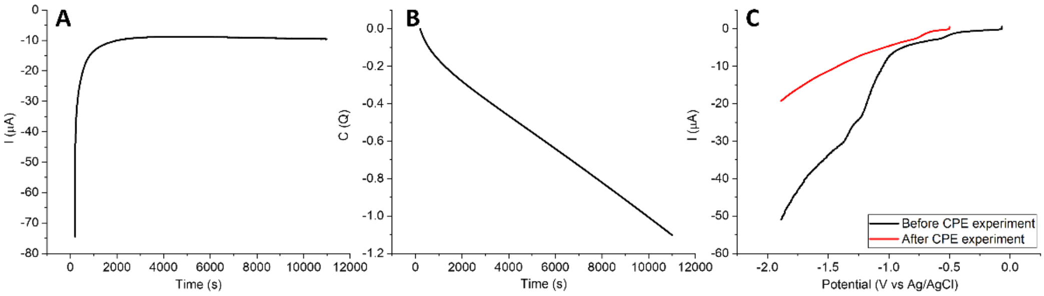

Figure A.65: Current (A) and charge (B) behaviour during M2 CPE experiment and linear voltammogram before and after CPE assay (C). Assays were carried out in DMF, using TBAPF6 as supporting electrolyte (0.1 M) at 10 mV s-1; glassy carbon was used as working electrode, platinum wire as counter and Ag/AgCl as reference electrode.

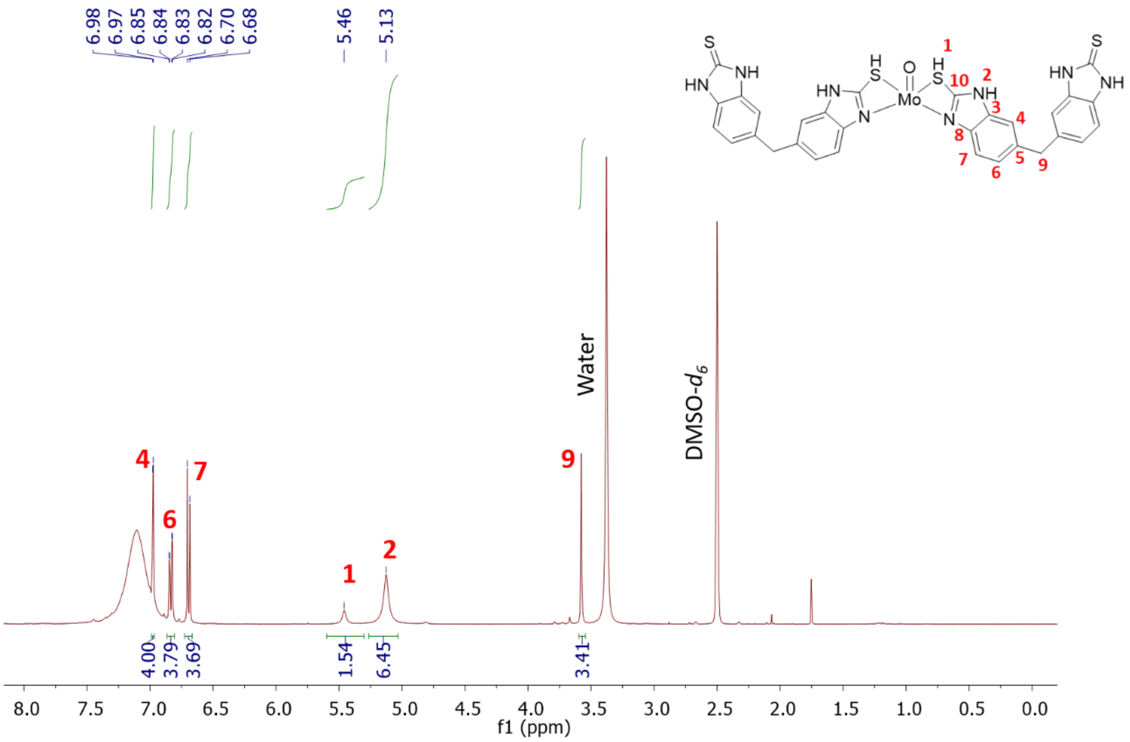

Figure A.66: ^{1}H NMR spectrum of M6 in DMSO-d_6

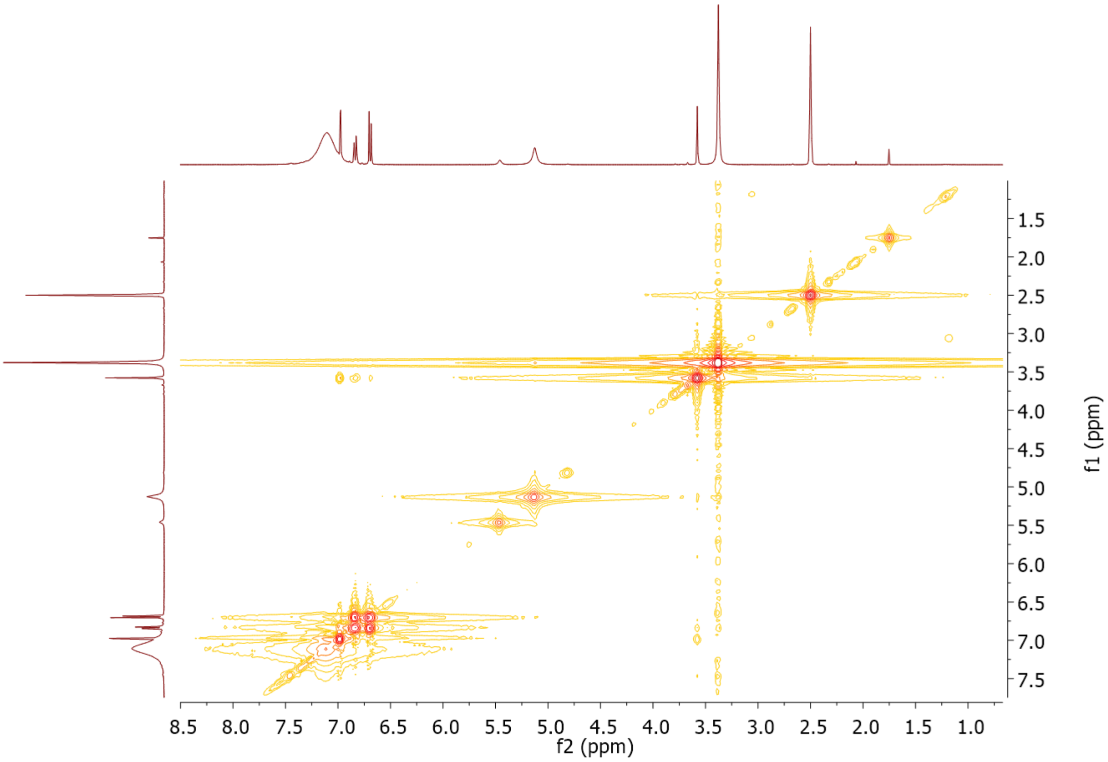

Figure A.67: 2D COSY spectrum of M6

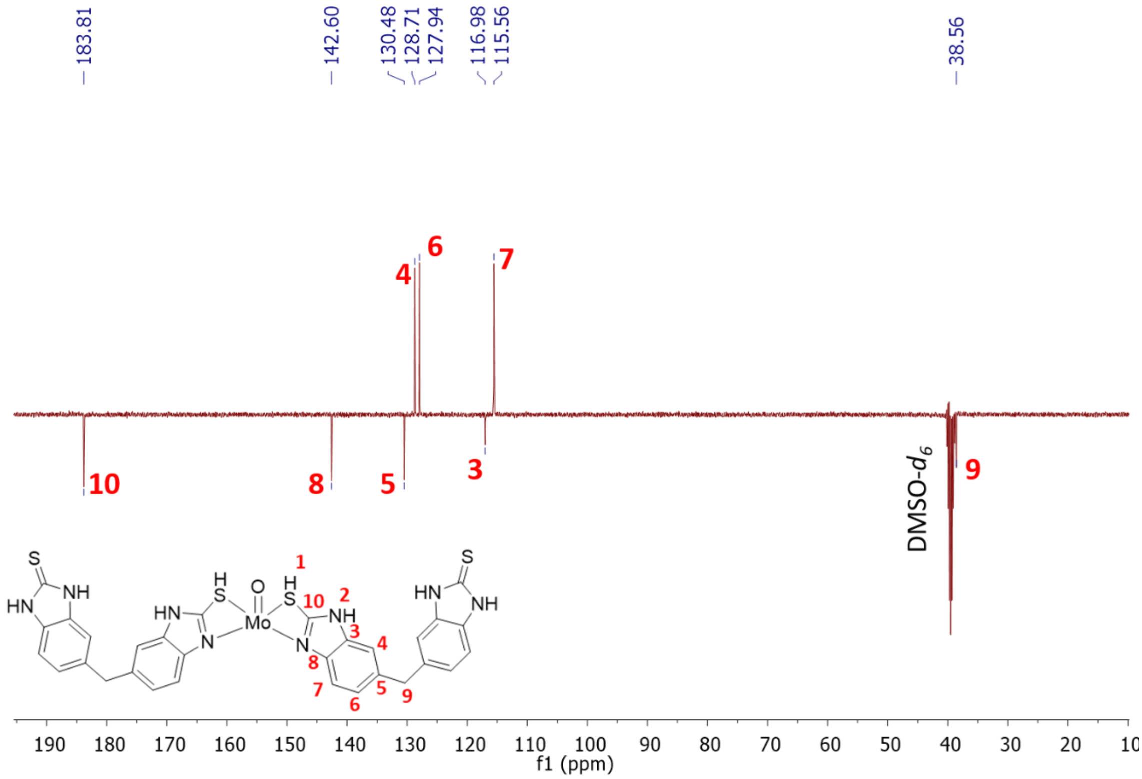

Figure A.68: ^{13}C APT spectrum of M6

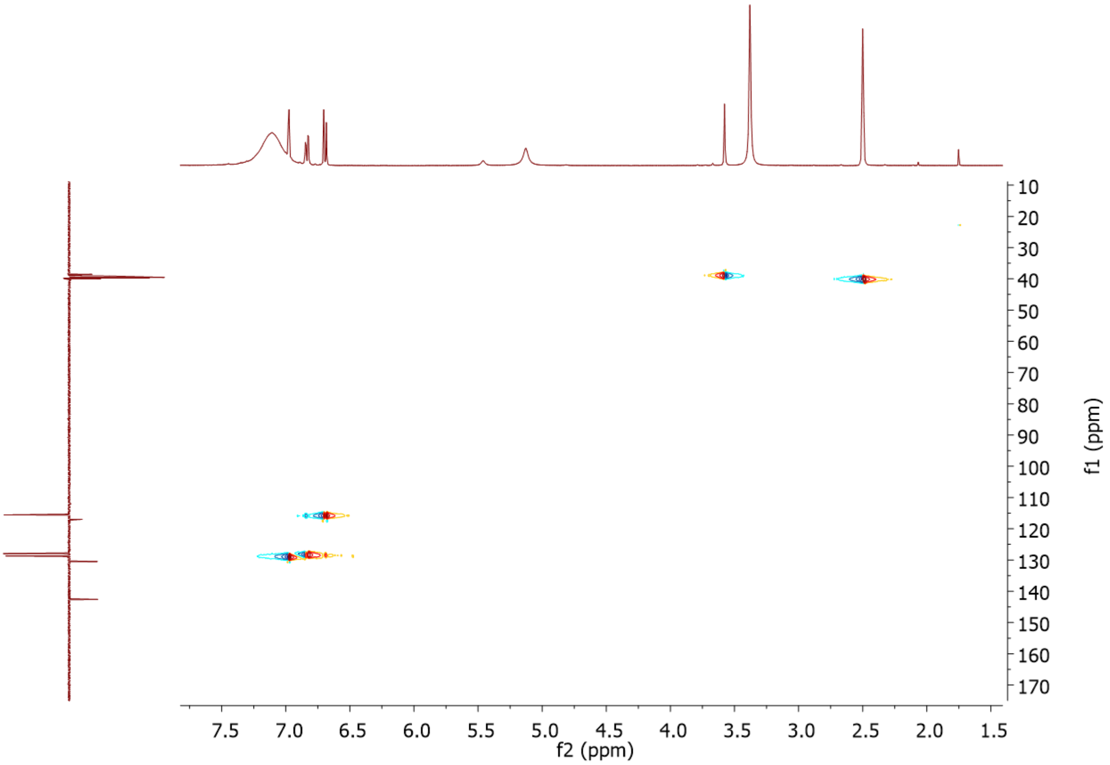

Figure A.69: HSQC spectrum of M6

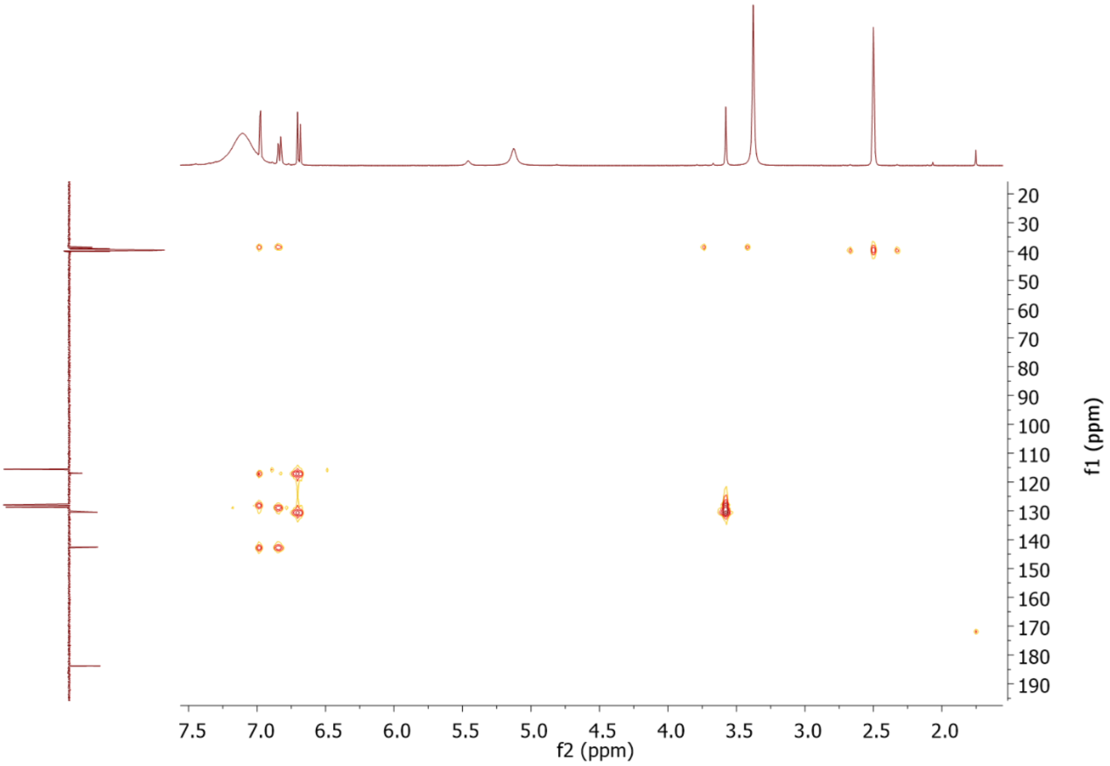

Figure A.70: HMBC spectrum of M6

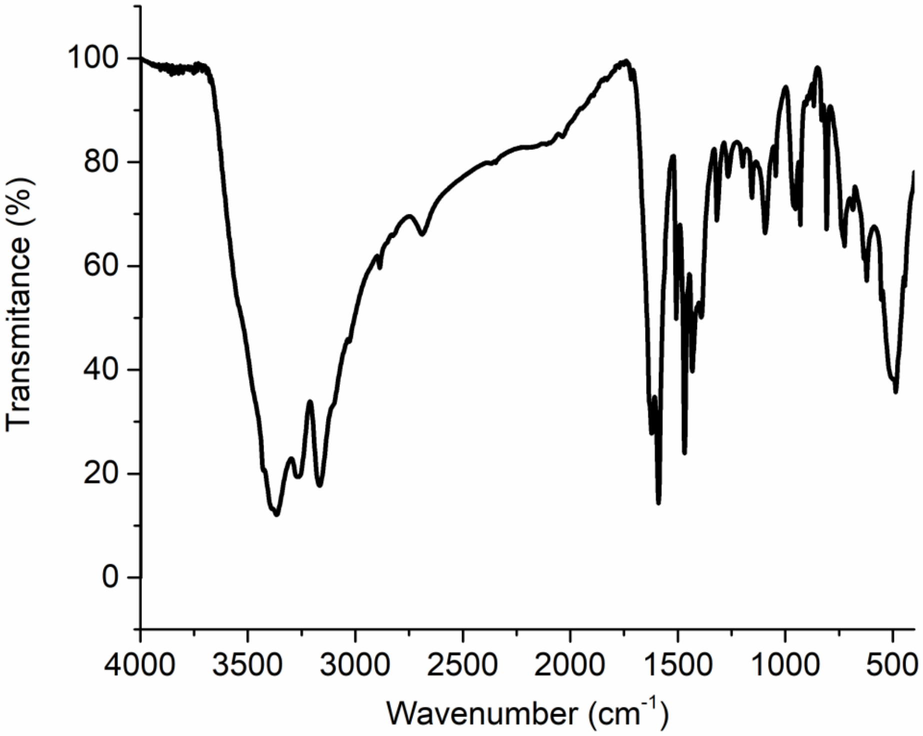

Figure A.71: FTIR spectrum of M6

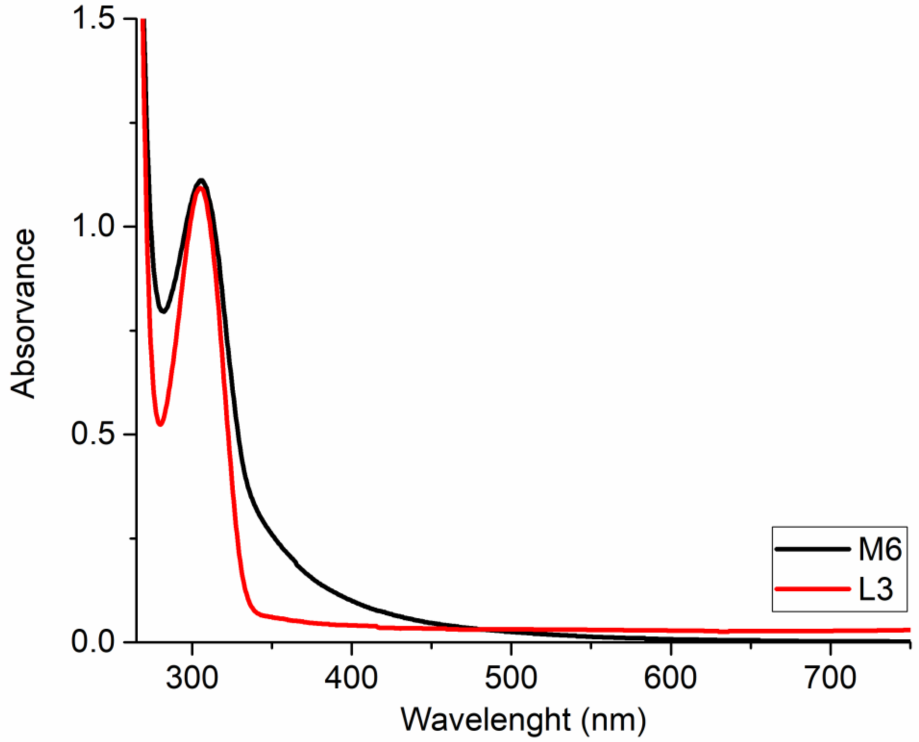

Figure A.72: UV-vis overlay spectra of M6 and L3

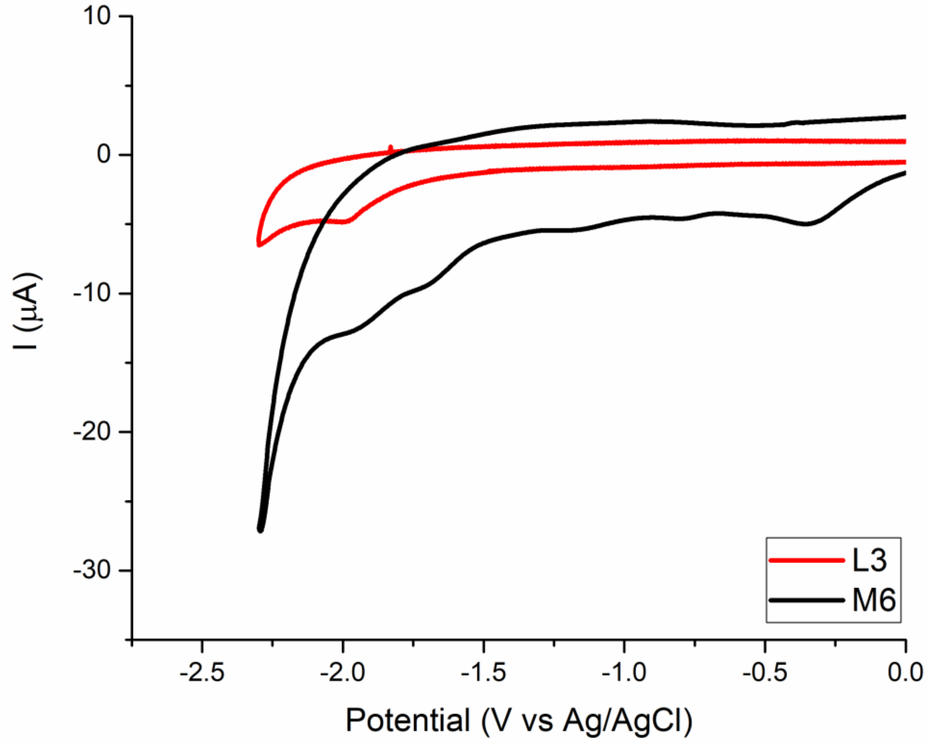

Figure A.73: CV studies overlay of M6 and L3 in DMF(1mM) N_2 saturated solution using $TBAPF_6$ as supporting electrolyte (0.1 M) at 0.1 mV s^{-1}. Glassy carbon (3 mm diameter) was used as working, platinum wire as counter and Ag/AgCl as reference electrodes

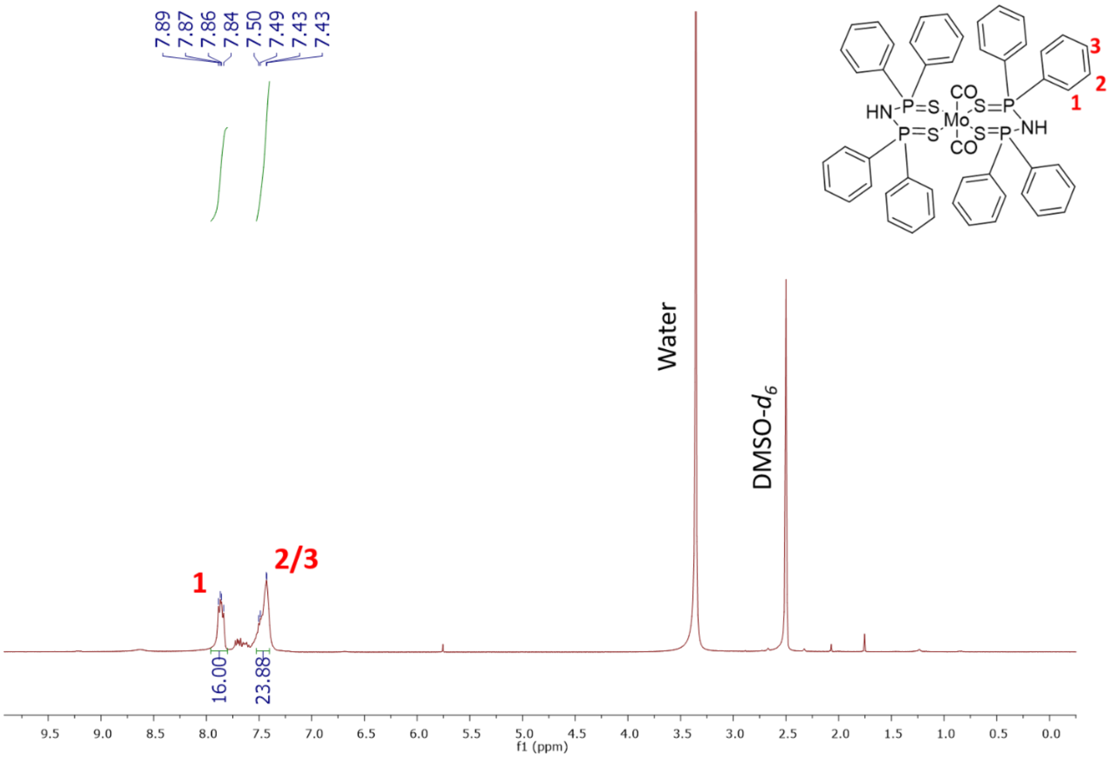

Figure A.74: ^{1}H NMR spectrum of M8 in DMSO-d_6

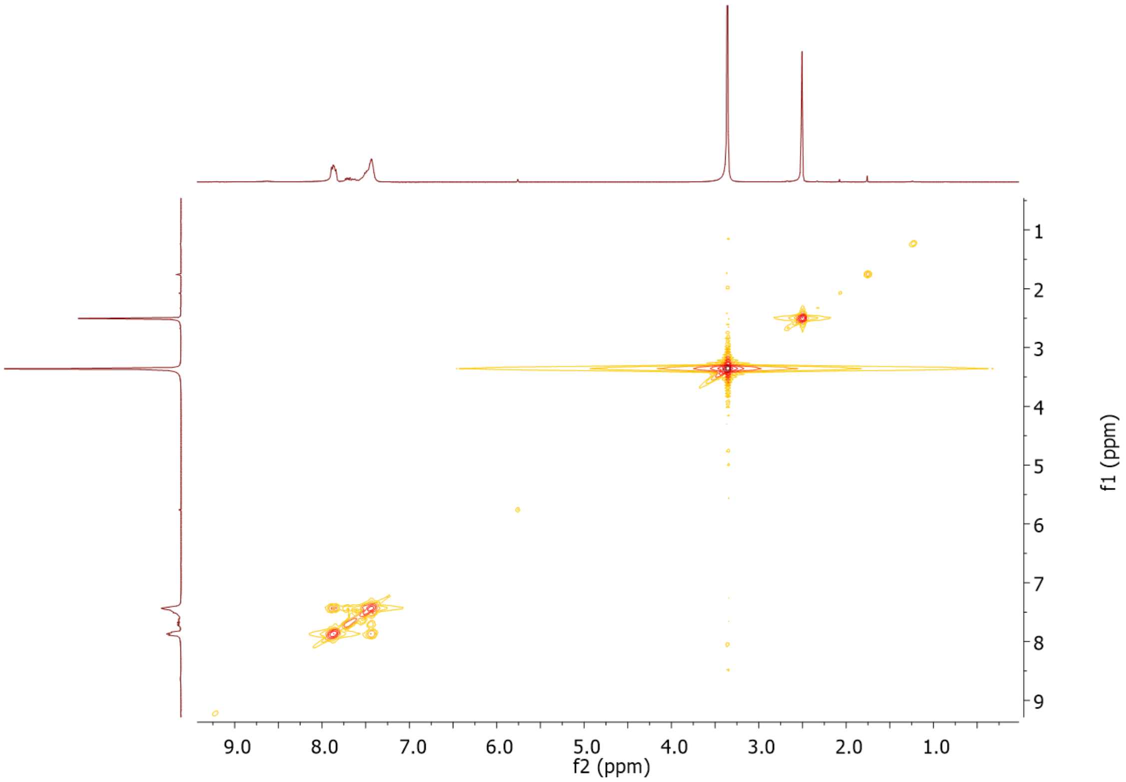

Figure A.75: 2D COSY spectrum of M8

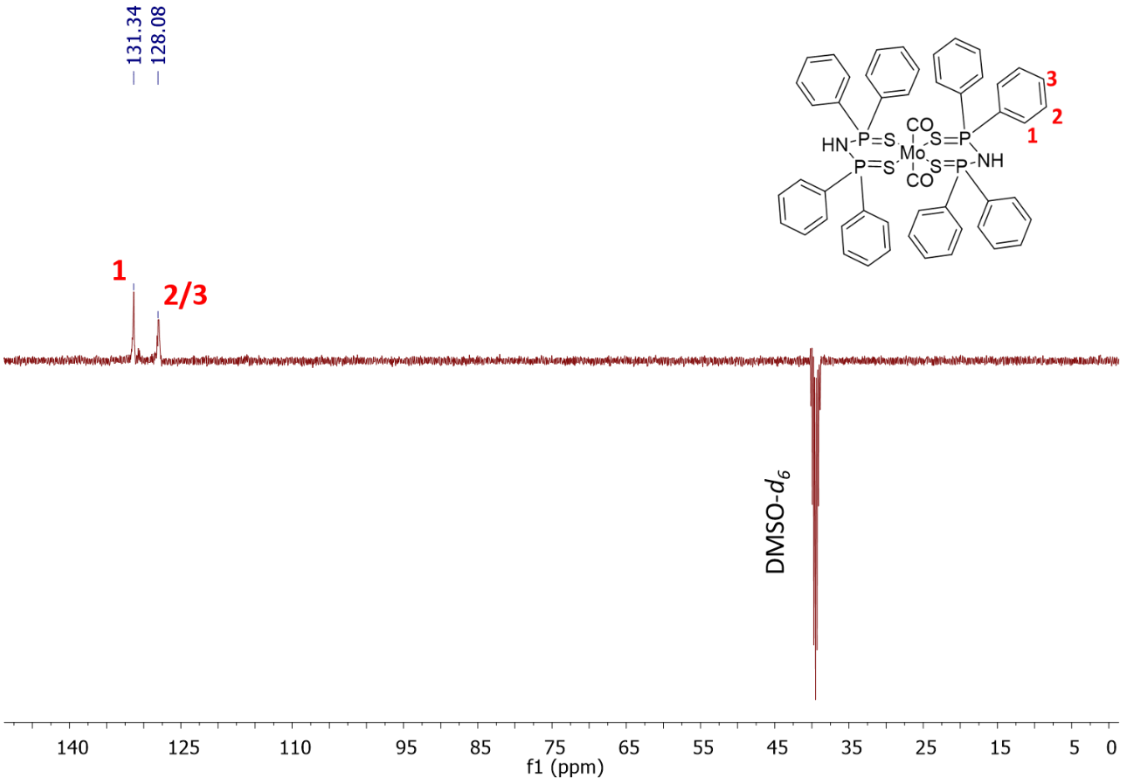

Figure A.76: ^{13}C APT NMR spectrum of M8

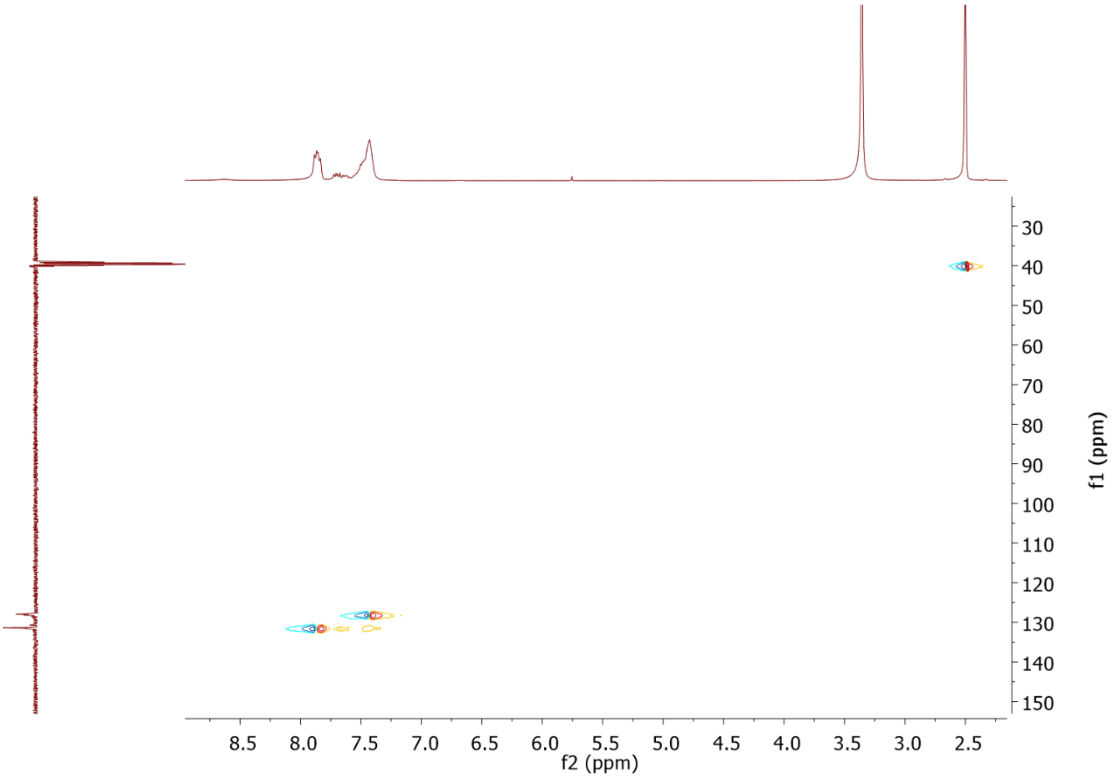

Figure A.77: HSQC spectrum of M8

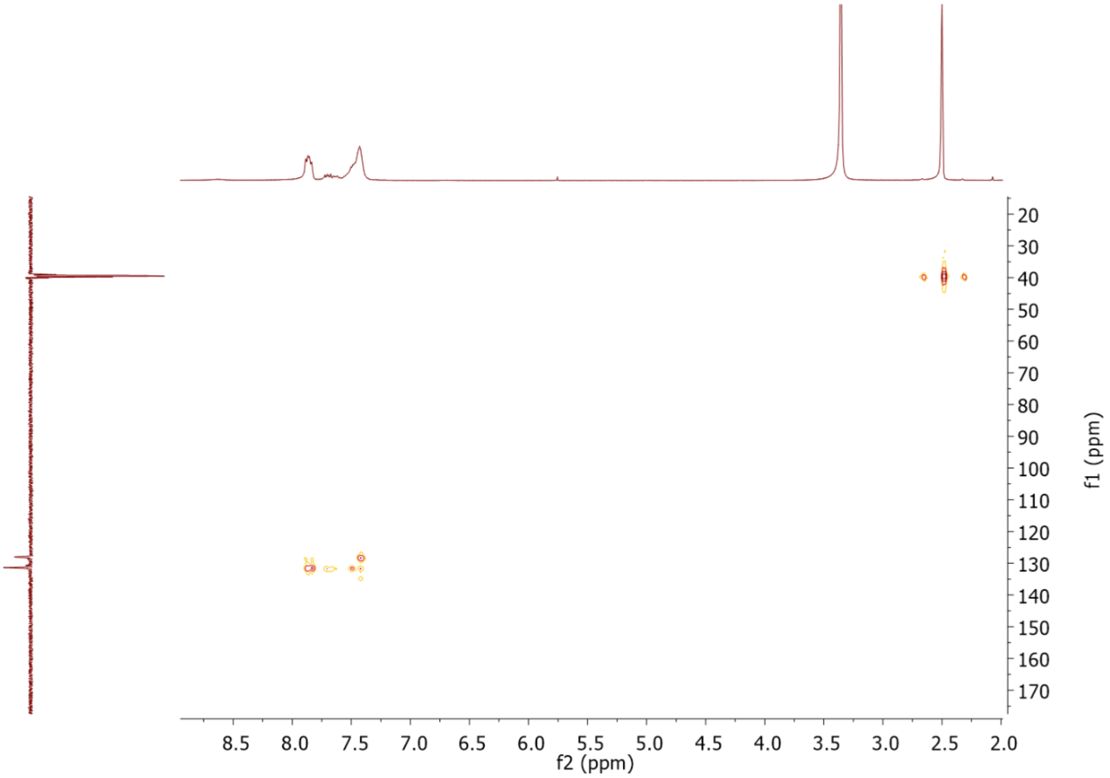

Figure A.78: HMBC spectrum of M8

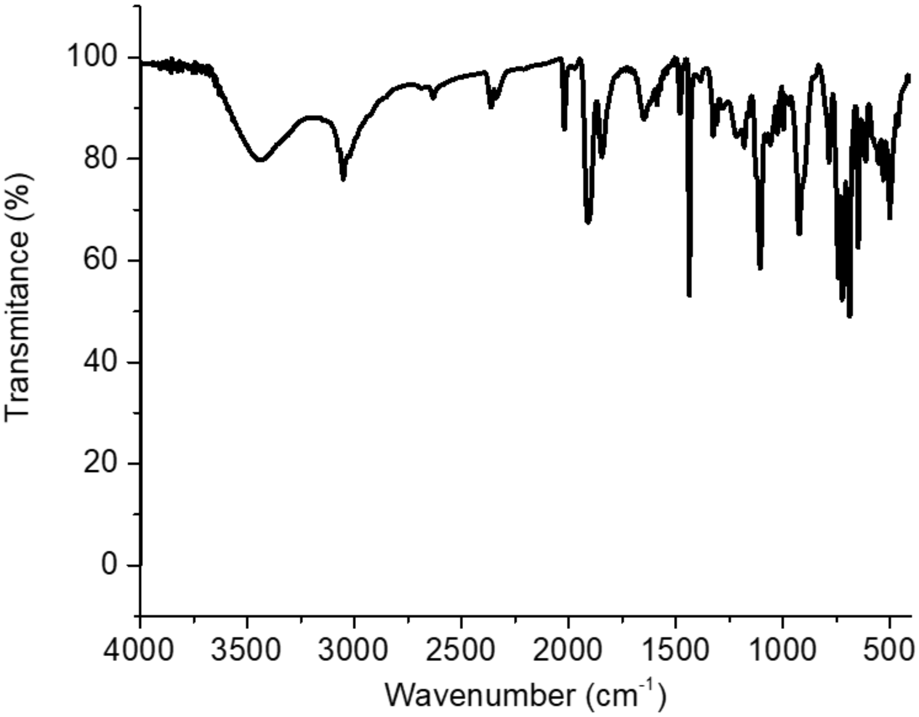

Figure A.79: FTIR spectrum of M8

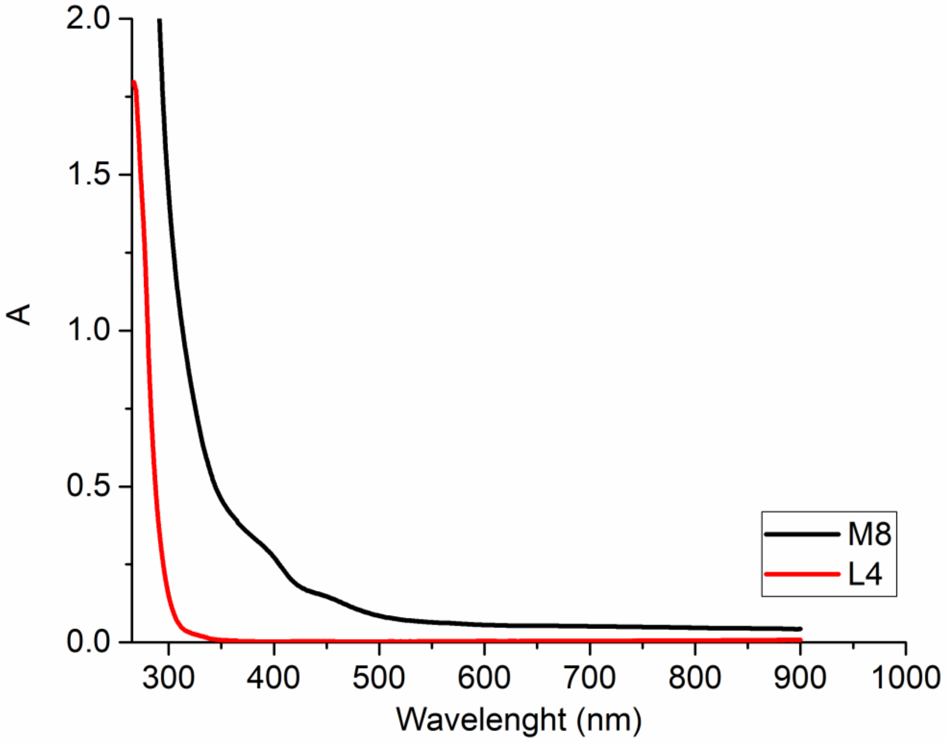

Figure A.80: UV-vis overlay spectra of M8 and L4

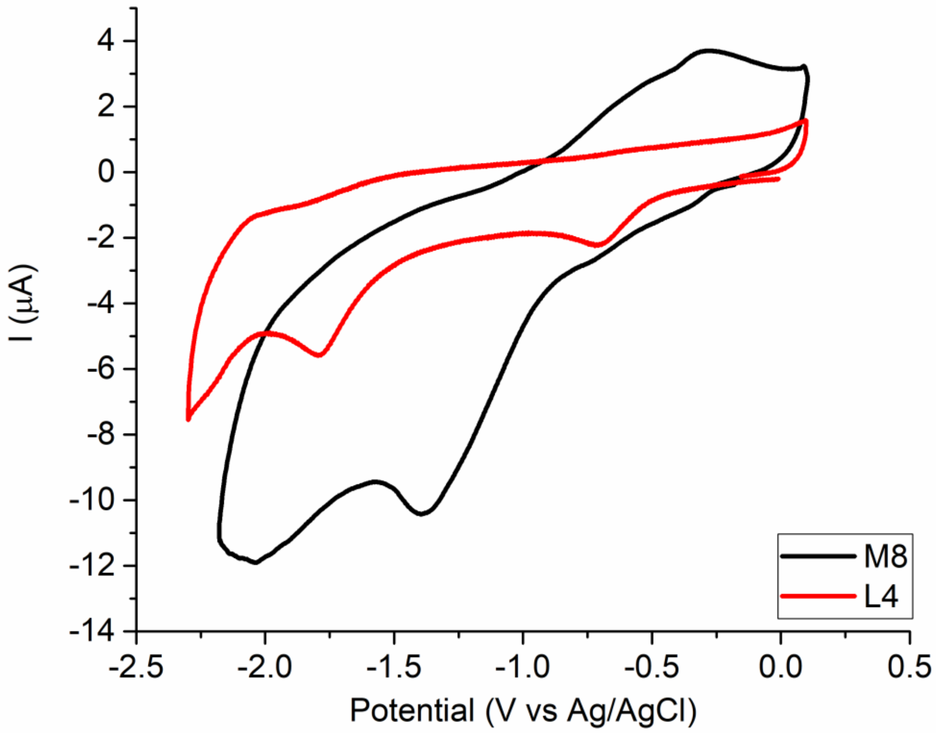

Figure A.81: CV studies overlay of M8 and L4 in DMF(1mM) N_2 saturated solution using $TBAPF_6$ as supporting electrolyte (0.1 M) at 0.1 mV s^{-1}. Glassy carbon (3 mm diameter) was used as working, platinum wire as counter and Ag/AgCl as reference electrodes

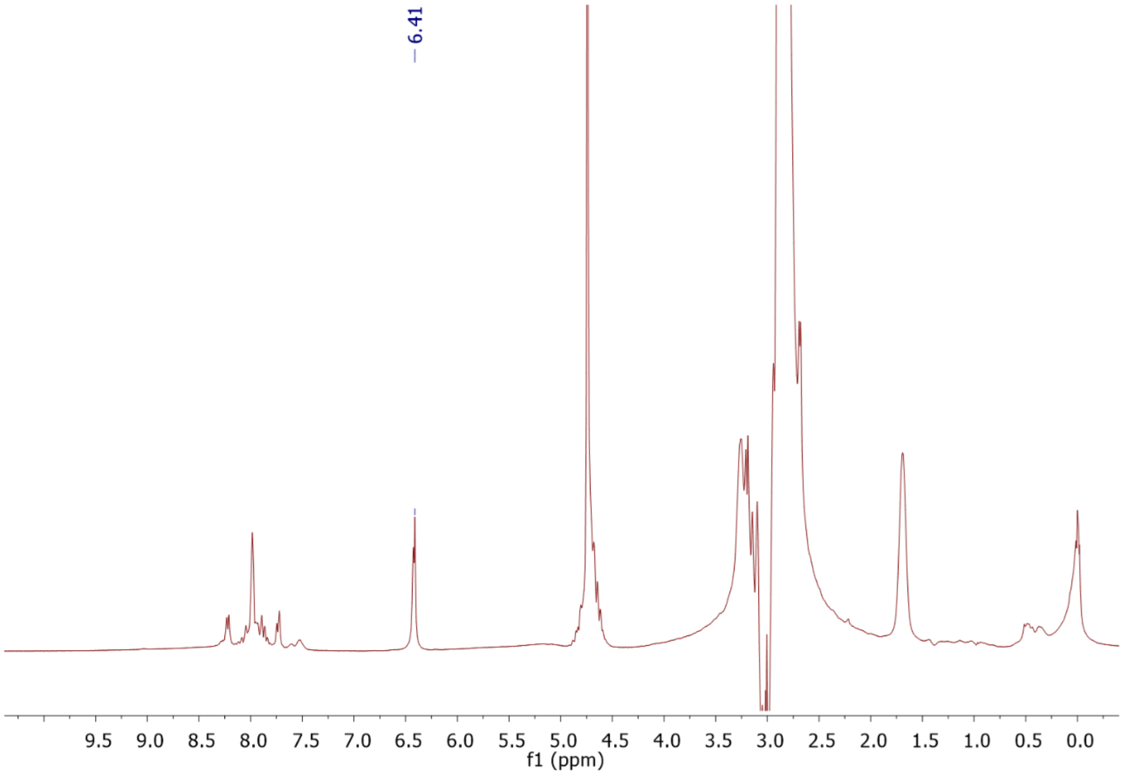

Figure A.82: ^{1}H NMR spectrum of M8 bulk solution after CPE. The signal at 6.41ppm are characteristic of maleic acid used internal standard.

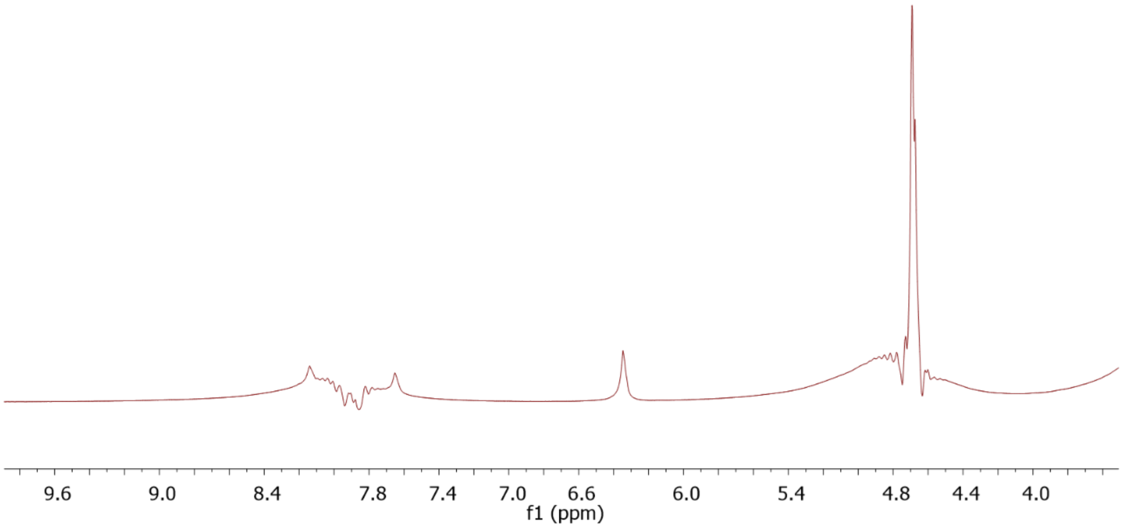

Figure A.83: ^{1}H NMR spectrum of CPE experiement without catalyst

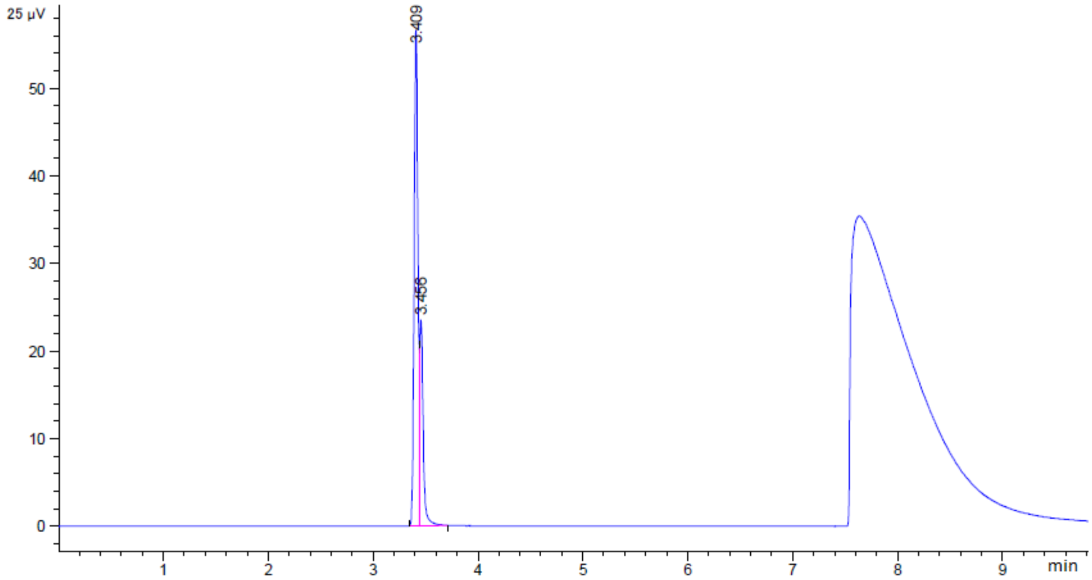

Figure A.84: GC-TCD chromatogram of reaction mixture headspace after CPE experiment without catalyst

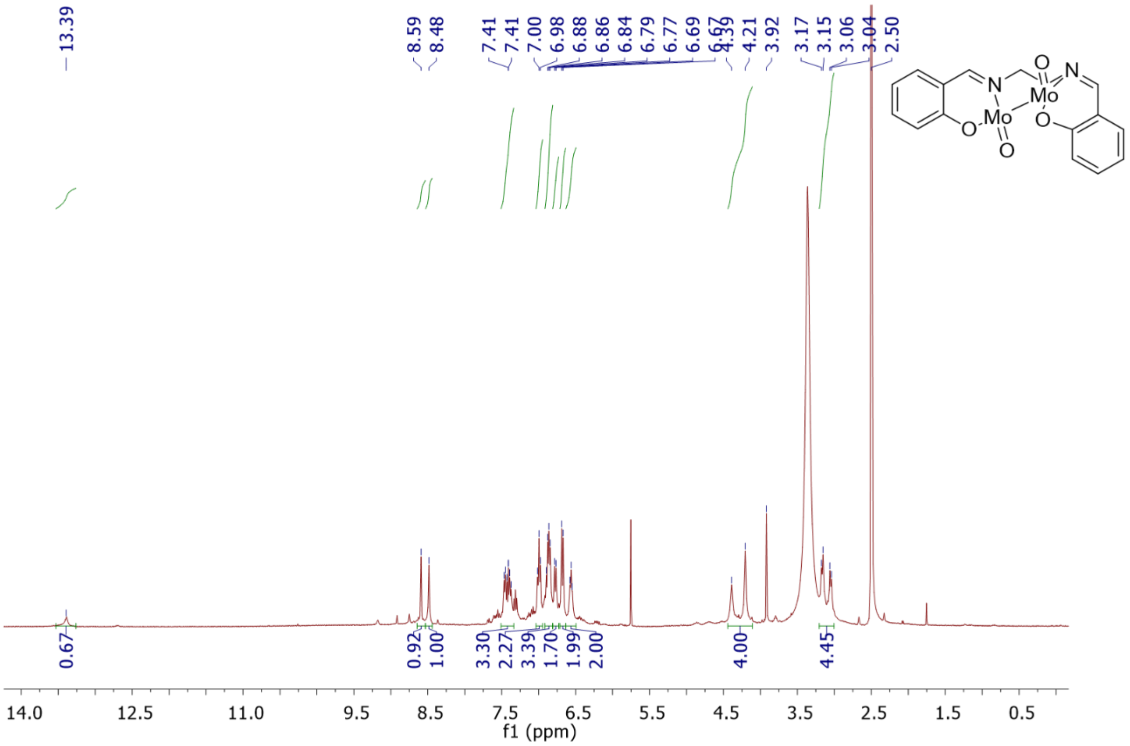

Figure A.85: ^{1}H NMR spectrum of M9 in DMSO-d$_6$

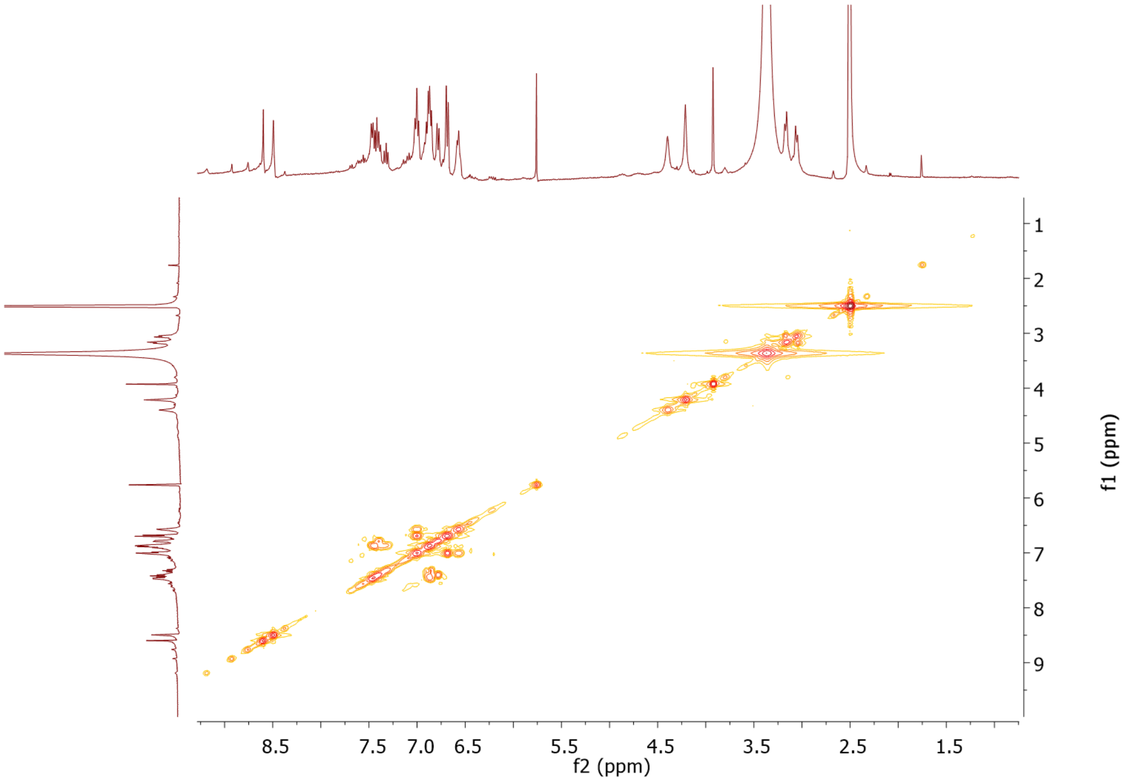

Figure A.86: 2D COSY spectrum of M9

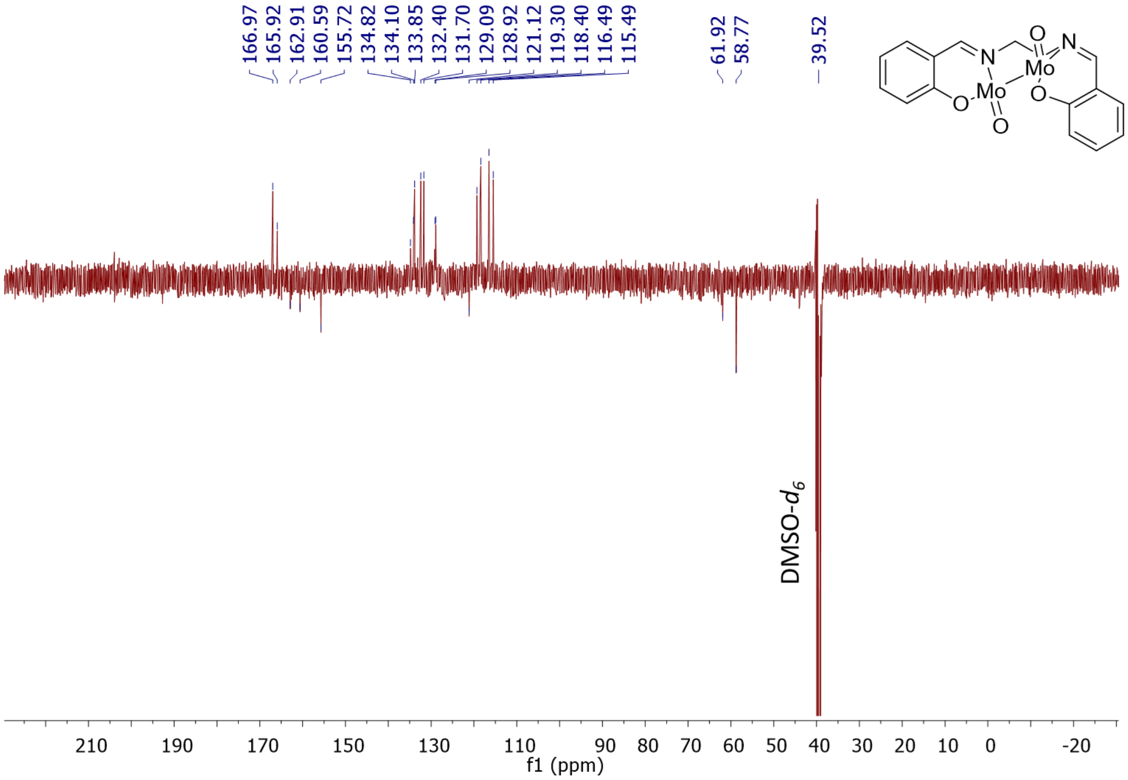

Figure A.87: ^{13}C APT spectrum of M9

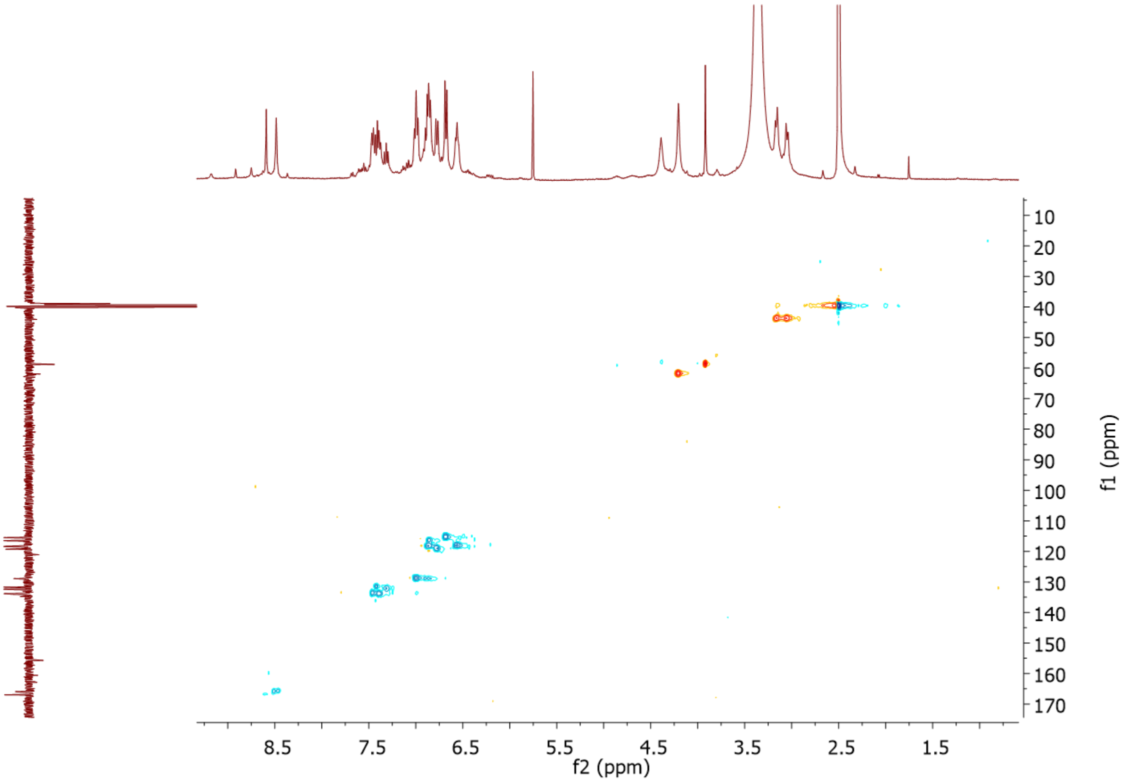

Figure A.88: HSQC spectrum of M9, in DMSO-d_6.

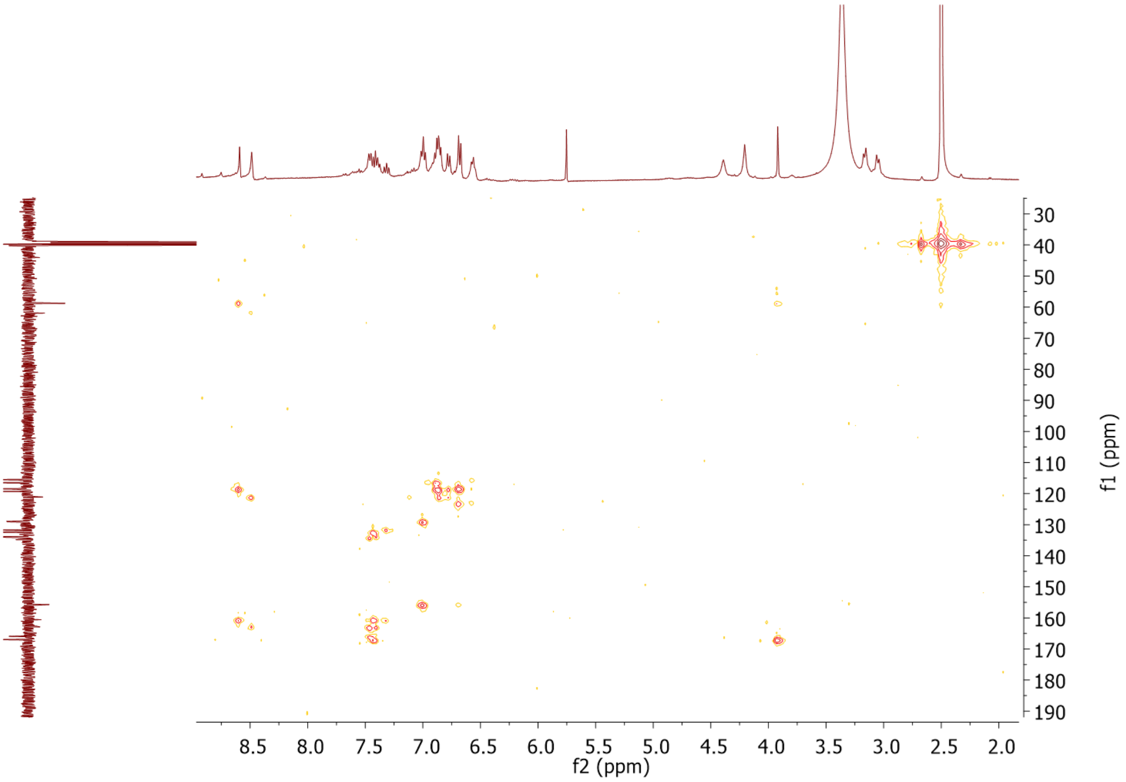

Figure A.89: HMBC spectrum of M9, in DMSO-d_6.

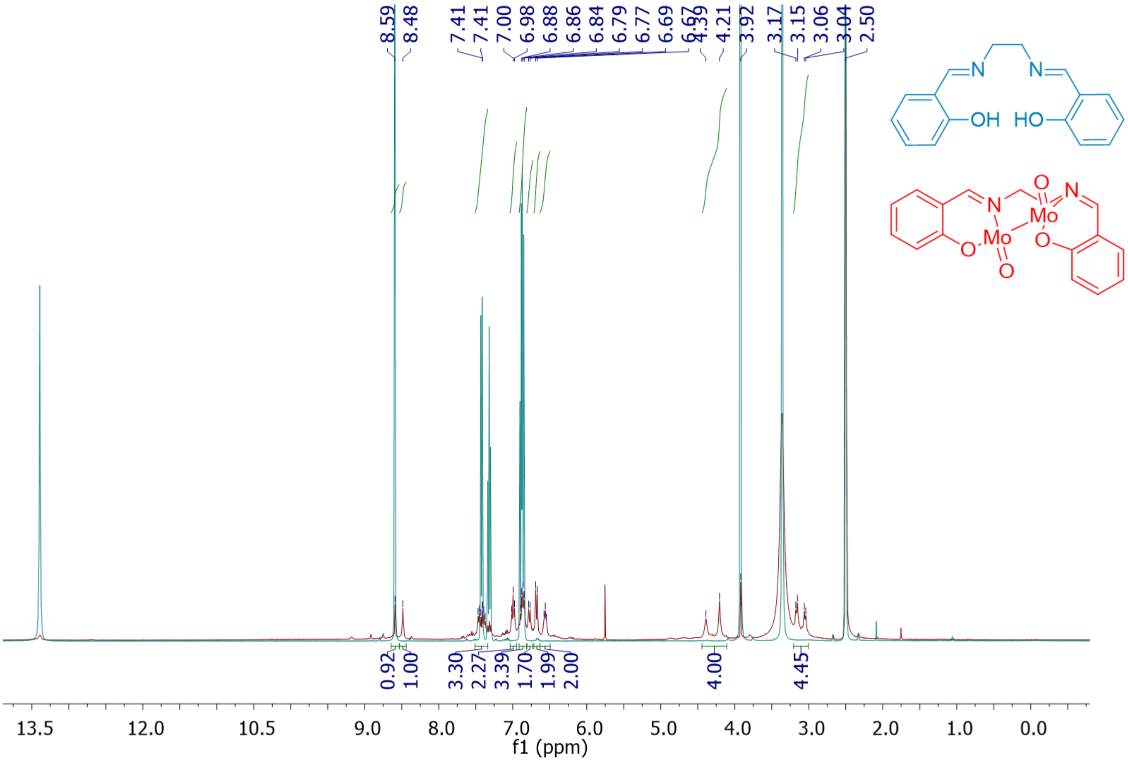

Figure A.90: ^{1}H NMR spectrum overlay of M9(red) and L5(blue) in DMSO-d$_6$

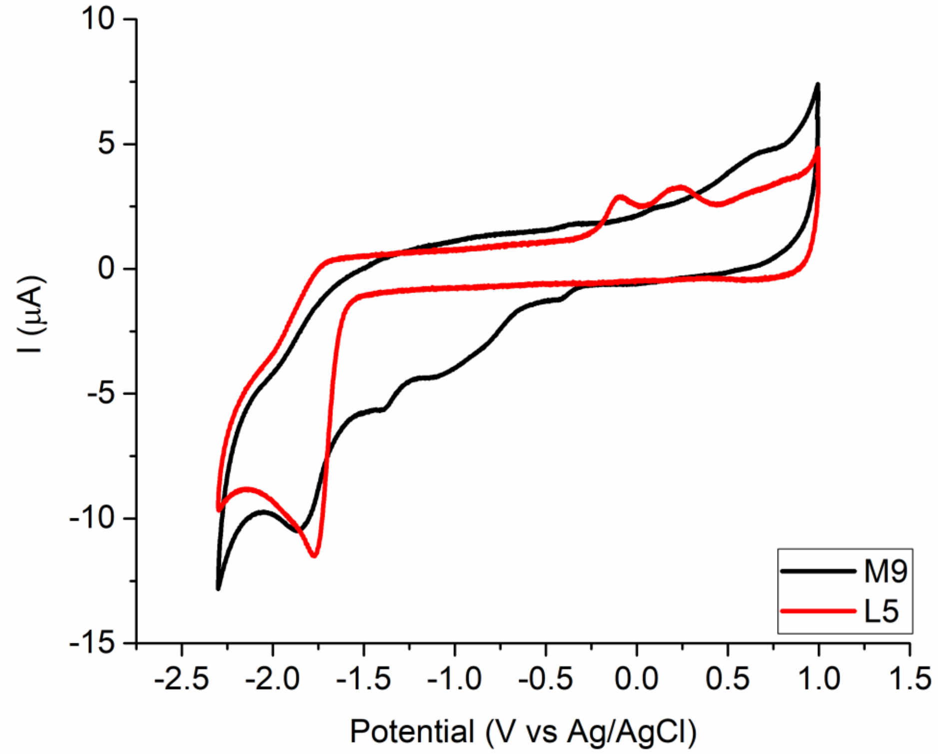

Figure A.91: CV studies overlay of M9 and L5 in DMF(1mM) N_2 saturated solution using $TBAPF_6$ as supporting electrolyte (0.1 M) at 0.1 mV s^{-1}. Glassy carbon (3 mm diameter) was used as working, platinum wire as counter and Ag/AgCl as reference electrodes

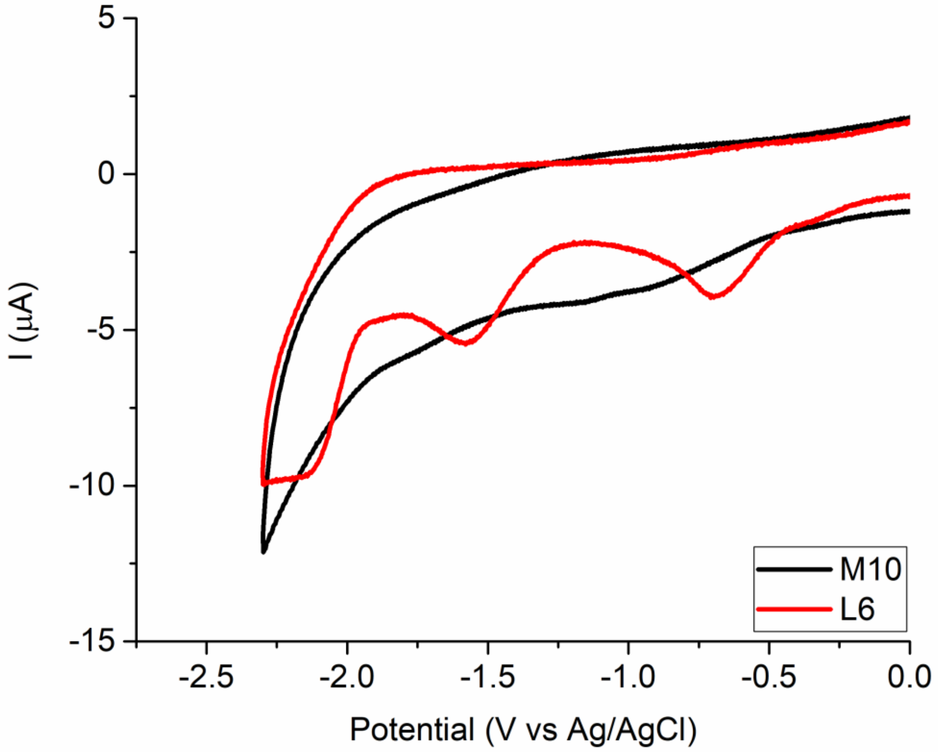

Figure A.92: CV studies overlay of M10 and L6 in DMF(1mM) N_2 saturated solution using $TBAPF_6$ as supporting electrolyte (0.1 M) at 0.1 mV s^{-1}. Glassy carbon (3 mm diameter) was used as working, platinum wire as counter and Ag/AgCl as reference electrodes